# DEVELOPMENT OF MANGANESE BASED NANOMATERIALS FOR ENERGY STORAGE AND PHOTOCATALYTIC APPLICATIONS

*Thesis submitted to the*

*Jadavpur University*

*For award of the degree*

*of*

**Doctor of Philosophy (Science)**

*by*

**Manas Mandal**

Under the guidance of

**Prof. Swapan Kumar Bhattacharya**

**DEPARTMENT OF CHEMISTRY**

**JADAVPUR UNIVERSITY**

**April 2022**

**DEPARTMMENT OF CHEMISTRY**
PHYSICAL CHEMISTRY SECTION
JADAVPUR UNIVERSITY
KOLKATA – 700032, INDIA

**PROF. SWAPAN KUMAR BHATTACHARYA**
Email: skbhatt7@yahoo.co.in
Telephone: 033-2414-6666 Extn. 2458

Index No.: ***109 / 18 / Chem. / 26***

# CERTIFICATE FROM THE SUPERVISOR

This is to certify that the thesis entitled "**Development Of Manganese Based Nanomaterials For Energy Storage And Photocatalytic Applications**" submitted by **Sri Manas Mandal**, who got his name registered on 05th March 2018 for the award of Ph.D (Science) degree of Jadavpur University, is absolutely based upon his own research work under my supervision of **Prof. Swapan Kumar Bhattacharya** and that neither this thesis nor any part of it has been submitted for either any degree/diploma or any other academic award anywhere before.

Bhattacharya

Date: 19/4/2022

Supervisor
Professor of Chemistry
Jadavpur University
Kolkata-700 032

# Declaration

I certify that

a. The work contained in this thesis is original and has been done by myself under the general supervision of my supervisor.

b. The work has not been submitted to any other Institute for any degree or diploma.

c. I have followed the guidelines provided by the Institute in writing the thesis.

d. I have conformed to the norms and guidelines given in the Ethical Code of Conduct of the Institute.

e. Whenever I have used materials (data, theoretical analysis, and text) from other sources, I have given due credit to them by citing them in the text of the thesis and giving their details in the references.

f. Whenever I have quoted written materials from other sources, I have put them under quotation marks and given due credit to the sources by citing them and giving required details in the references.

Manas Mandal.

Signature of the Student

*To My*

*Beloved Son*

*Ishaan*

# Acknowledgements

*At the final stage of this truly memorable journey towards my intellectual destination, it is really hard to list all the people who sincerely helped me and I would like to thank all of them who have made this thesis possible.*

*First of all I would like to express my sincere gratitude to my thesis supervisor* ***Prof. Swapan Kumar Bhattacharya*** *for his kind support, insightful advice and encouragement. I earnestly thank him for his nice guidance, freedom to work, encouragement and inspiration which helped me to enrich myself. I would also like to give sincere gratitude to my research advisory committee (RAC) members, Prof. Chittaranjan Sinha (former HOD, Chemistry) and Dr. Sachindranath Das, Dept. of Instrumentation Science, Jadavpur University for their advices and suggestions. I am also grateful to Prof. A. Mahapatra, Prof. A. Gayen, Prof. N. K. Chattopadhyay, Prof. P. P. Parui, Prof. S. Chattopadhyay, and Prof. S. Das for their continuous supports and nice lectures during PhD coursework.*

*I would like to express my sincere gratitude to my M.Tech thesis supervisor Late Professor Chapal Kumar Das, IIT Kharagpur under whose supervision I stepped into my research life.*

*I would like to thank the Principal of Sree Chaitanya College for giving permisssion to carry out the reseacrh. I would also like to thank all of my faculty collegues especially, Debasish Da, Reena Di, Sachin Da, Atanu Da, Sushanta Da, Swapan Da, Harasit Da, Buddhadeb Da, Ivy, Sanchita, Tulika Di, Soumik, Debasree, Deeptanil Da and Dhiman.*

*I extend my gratitude to my beloved parents Mr. Samir Kumar Mandal and Mrs. Mamata Mandal whose endless love and inspiration has always been strength for me. Their eternal blessing and constant support has guided me this far and positively, this will take me far forward in future to achieve the success they dreamt of. I am thankful to my parents-in-law Mr. Pradip Chatterjee and Mrs. Kalyani Chatterjee whose endless blessing and supports helped me a lot to reach the milestone. I would also like to convey my gratitude to my beloved elder sister Munmun, brothers-in-law Kartick and Koushik for always being there by my side. Further, no words would be sufficient to express my feelings to my Wife* ***Krishna****, whose affection and care have so luxuriously continued to enrich every fraction of my life. I want to thank her for her moral support and advice which gave me strength to do what I wanted. She has*

*always been there to support and encourage me even in frustrating and difficult times of my life, for which I wish to put forward my hearty gratitude to her. I express my love to my beloved son* ***Ishaan*** *who always inspires me to be more curious and passionate about learning new things. I feel truly blessed to have them in my life.*

*I would like to convey special thanks to my friends-cum-collaborators Dr. Debasis Ghosh (JAIN University), Dr. Sarbaranjan Paria (JeonBuk National University), Dr. Dipanwita Majumdar (Chandernagore College), Dr. Kalyan Ghosh (Brno University of Technology), Dr. Subhadeep Dutta (IACS) for their constant support and encouragement.*

*I take this opportunity to thank lab members and friends Malay, Sujit Da, Kamal, Anupam, Bappa Da, Partha Sarathi Da, Mousumi, Pradip Da, Senjuti, Ankita, Kalyan, and Akbar for their co-operation and inspiration in my research work, without which it would not, been easy to complete the PhD thesis.*

*Finally I am thankful to Jadavpur University for infrastructural facility for my research work.*

Date: 19·04·2022

Place: Kolkata

Manas Mandal.

(Manas Mandal)

# List of Abbreviations

| Abbreviations | Descriptions |
|---|---|
| EDLC | Electrochemical Double Layer Capacitor |
| CNT | Carbon Nanotube |
| MWCNT | Multi Walled Carbon Nanotube |
| AC | Activated Carbon |
| FESEM | Field Emission Scanning Electron Microscopy |
| FTIR | Fourier Transform Infrared Spectroscopy |
| HRTEM | High resolution Transmission Electron Microscopy |
| TEM | Transmission Electron Microscopy |
| XRD | X-Ray Diffraction |
| BET | Brunauer–Emmett–Teller |
| CV | Cyclic Voltammetry |
| GCD | Galvanostatic Charge Discharge |
| EIS | Electrochemical Impedance Spectroscopy |
| ESR | Equivalent Series Resistance |
| GO | Graphene oxide |
| rGO | reduced Graphene Oxide |
| SCE | Saturated Calomel Electrode |
| SAED | Selected Area Electron Diffraction |

# Abstract

Index No. ***109 / 18 / Chem. / 26***

**"DEVELOPMENT OF MANGANESE BASED NANOMATERIALS FOR ENERGY STORAGE AND PHOTOCATALYTIC APPLICATIONS"**

Submitted by: **Manas Mandal**

Supercapacitor, also known as electrochemical capacitor or ultracapacitor, has attracted great attention from the material-researchers due to its unique properties like high specific power, moderate specific energy, short charging time, high cyclic stability, etc. Based on their charge-storage mechanism supercapacitors are classified into two types. The electrical double layer capacitor (EDLC) is the one which mainly stores the charge electrostatically. Another one is pseudocapacitor in which the capacitance originates from fast Faradaic redox reactions. Carbonaceous materials like activated carbon, graphene, carbon nanotube etc. are used as capacitive materials. On the other hand, transition metal oxides, hydroxides, sulfides and conducting polymers are used as pseudocapacitive materials. Manganese-based nanomaterials are promising in the area of energy research. Being a second row transition element Mn can implement some properties like electron mobility, good conductivity, excellent charging-discharging profile and high cycle life.

In this thesis manganese oxides such as $MnO_2$, $Mn_3O_4$, bimetallic hydroxide $MnSn(OH)_6$, bimetallic sulfides (MnCoS) and co-ordination complex like $Mn[Fe(CN)_6]$ have been described and their electrochemical performances have been investigated. The as-synthesized materials were structurally characterized by XRD, FTIR, XPS techniques; the morphology was identified with the help of FESEM and TEM images; the surface area and porosity was measured form the BET study. Finally, the electrochemical performances were investigated in terms of CV, GCD and EIS study. Due to low conductivity of the manganese oxide, it was combined with highly conductive material such as carbon nanotube to synthesize a composite. An assymetric supercapacitor has been constructed using $Mn_3O_4$-MWCNT and rGO. The as-fabricated capacitor has achieved high specific energy with high power delivery rate along with high cyclic stability. A combinatorial transition metal oxide also has

been used to get high electroactive surface area and the high electrochemical performances thereof. The electrochemical performances of a supercapacitor device not only depend on the active electrode materials solely, but also on the electrolyte, separator, and design of the supercapacitor fabrication also. Therefore, a redox system has been incorporated in conventional electrolyte. This redox system surpluses the electron density of the mother electrolyte and enhances the charge storage also. The bimetallic sulfides have also been prepared on nickel foam via electrodeposition. The electrodeposition is a single step technique by which large area nanostructured materials can be synthesized without going through a harsh reaction condition. Additionally, the nickel foam can be directly used as current collector. Although carbonaceous materials are used as negative electrode of supercapacitor, these materials suffer from low capacitance. Few pseudocapacitive materials like $V_2O_5$, $Mn_3O_4$ have shown the efficiency to be the promising negative electrode for supercapacitor. A bimetallic hydroxide such as $MnSn(OH)_6$ has been prepared and its electrochemical performance has been investigated as negatrode for the supercapacitor. Recently, the coordination complexes like metal hexacyanoferrates have gained attention due to their semiconducting nature with narrow band gap. Hence these compounds show promising applications in energy storage and conversion, photocatalysis, ion sensing etc. Manganese hexacayanoferrates along with some other metals like cobalt, copper and zinc have been prepared and their electrochemical performances and photocatalytic activity on the reduction of highly toxic Cr(VI) have been studied. The as-synthesized materials have been used for photocatalytic reduction of Cr(VI) and it showed good reducing capability.

It has been realized how the electrochemical activity of different manganese-based nanomaterials depends on the nature, architecture, dimension and electrolyte. Hope the obtained results will be useful in practical application in the field of supercapacitors.

# Content

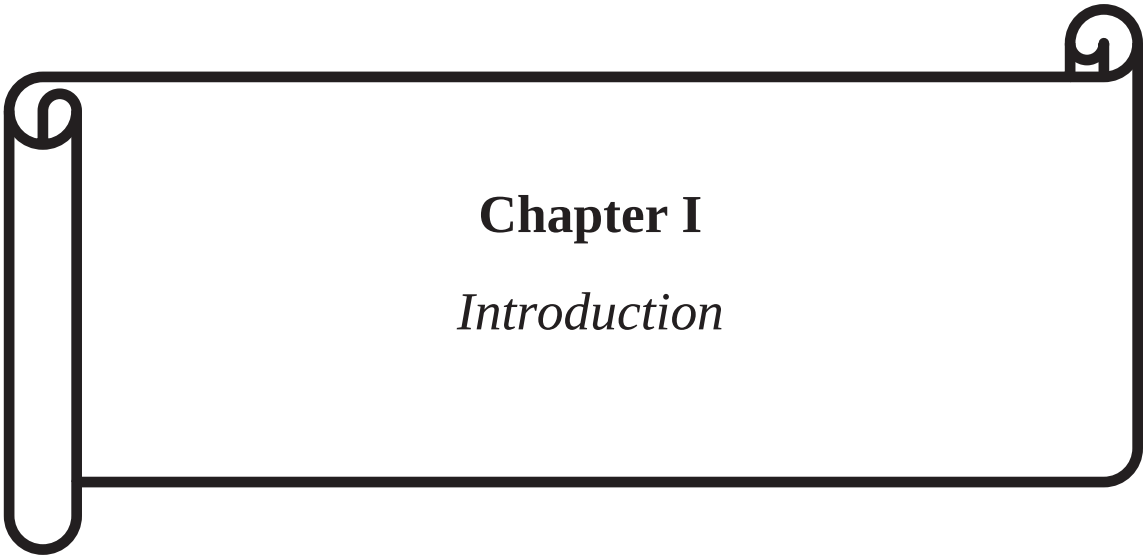

# Chapter I

*Introduction*

# Introduction

The day to day discovery of portable electronics and smart technologies needs further breakthroughs to accomplish high power and energy, and definitely long-running energy storage strategies [1]. With environmental consciousness, the advancement of energy conversion and storage has been a great challenge for the fulfillment of the enormous energy demand of our modern society. An environmentally friendly energy resource, alternative to the fossil fuel, is urgently required for the fulfillment of this huge demand [2]. The primitive alternative energy sources such as solar energy and the wind energy could not fulfill the criteria due to their intermittent nature [3, 4]. This problem can be overcome with the help of the energy storage technologies by storing the energy for anytime availability. This not only help to develop civilization but also makes it economically, ecologically, and environmentally sustainable [5]. Now-a-days, the world is targeting to the maximum replacement of fuel cars by electric vehicles having net-zero emission [6, 7]. Therefore, the major research has been devoted to the advancement and more breakthroughs in the field of energy storage. Since the last century lithium ion batteries and capacitors are extensively used in the consumer portable electronic devices (Figure I.1) [8, 9]. The lithium ion batteries store energy through electrochemical reactions and provide excellent specific energy. Some of the significant drawbacks are: it takes long charging time, very low specific power and low cycle life (Table I.1). On contrary the conventional capacitors store charge electrostatically and provide capacitance in the range of picofarads to microfarads. The major problem with these capacitors is production of very low capacitance and specific energy. Therefore, an alternative energy storage system is

still required which will be able to achieve high specific energy, high specific power and high cyclic stability.


**Figure I.1** Applications of supercapacitors.

**Table I.1:** Comparison between batteries, capacitors and supercapacitors

| Properties | Battery | Capacitor | Supercapacitor |
|---|---|---|---|
| **Charging time** | 1 – 5 h | $10^{-3}$ – $10^{-6}$ s | 0.3 – 30 s |
| **Discharging time** | 0.3 – 3 h | $10^{-3}$ – $10^{-6}$ s | 0.3 – 30 s |
| **Capacitance** | - | 10 pF to 2.2 mF | 100 mF to 1500 F |
| **Specific Energy** | 10 – 100 Wh/kg | <0.1 Wh/kg | 1 – 10 WH/kg |
| **Specific Power** | 50 – 200 W/kg | >10 kW/kg | 1000 W/kg |
| **Life Cycles** | 500 – 2000 | >500000 | >100000 |

# I.1 Supercapacitor

A conventional capacitor is a charge storage device having low specific energy whereas a Li-ion battery is an energy storage device with low specific power. In that context, an electrochemical capacitor also known as supercapacitor has attracted significant attention of the materials scientist community for its some unique features like high specific power, moderate specific energy, fast charging capacity, and high life cycle [10]. Therefore, supercapacitors overcome not only those prior mentioned drawbacks, but it can also act as a bridge between a conventional capacitor and

battery [11]. The comparative analysis among the batteries, capacitors and supercapacitors are depicted in Table I.1 with respect to the different properties [12]:

## I.1.1 Taxonomy of supercapacitor

Based on the mechanism of charge storage phenomena supercapacitors can be categorized into three types (Figure I.2): electrochemical double layer capacitors (EDLCs), pseudocapacitors, and hybrid capacitors [13].

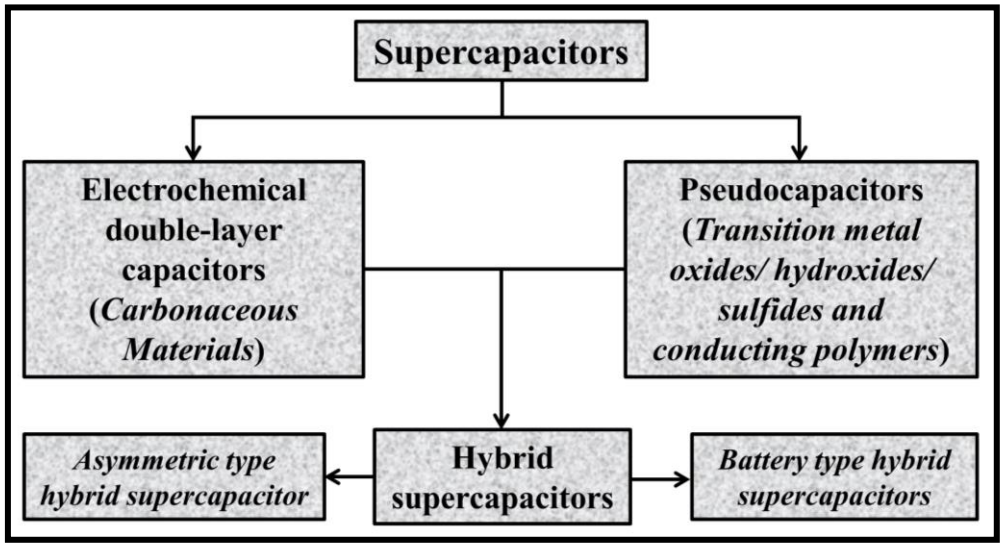


**Figure I.2** Taxonomy of supercapacitors.

### *I.1.1.1 Electrochemical double layer capacitors (EDLCs)*

In electrochemical double layer capacitors the charge accumulation occurs at the interface of electrode/electrolyte resulting in the capacitance [14-17]. In spite of using any dielectric material like capacitors, it uses only electrolyte in which the active electrodes are soaked into and a separator is placed between two electrodes which prevent short circuit. The electrolyte ions move to the oppositely charged electrodes up on applying the voltage and get selectively absorbed on the surface of the solid

electrode (Figure I.3a). Thus two oppositely charged ions line up on the boundary between electrode and electrolyte forming the electrical double layer.

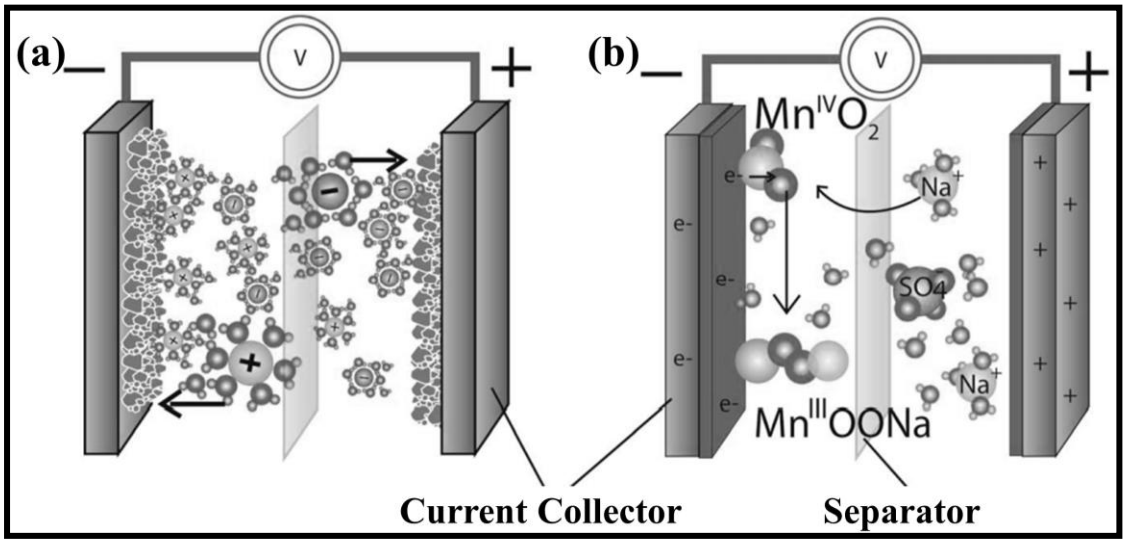


**Figure I.3** Basic schematics for an (a) EDLC, and (b) a pseudocapacitor ($MnO_2$ depicted center) [18].

## *Advantages of EDLCs*

(i) EDLCs store charge (in order of Farad) which is many times more compared to the conventional capacitors.

(ii) EDLCs achieve higher specific energy than conventional capacitors.

(iii) These capacitors can survive millions of charging-discharging cycles as no chemical reactions are involved; only adsorption/desorption of electrolyte ions occurs.

(iv) Unlike battery, overcharging does not affect the life cycle of EDLCs.

(v) EDLCs have a large working temperature range and no special charging-discharging circuits are needed.

(vi) The rate of charge-discharge is very high.

*Disadvantages of EDLCs*

(i) Very high rate of self-discharge than batteries.

(ii) Achieve lower specific energy than batteries.

***I.1.1.2 Pseudocapacitors***

Pseudocapacitors store charges via fast faradaic reversible redox reactions between electrode and electrolyte ions (Figure I.3b) [18, 19]. Unlike an ideal EDLC, the charge transfer in pseudocapacitors is voltage dependent phenomenon.

*Advantages of pseudocapacitors*

(i) Pseudocapacitors give very high specific capacitance compared to that of EDLCs and batteries.

(ii) They give high specific energy than EDLCs.

*Disadvantages of pseudocapacitor*

(i) Low specific power.

(ii) Self-discharge due to uncontrollable Faradaic reactions from the impurities.

***I.1.1.3 Hybrid supercapacitors***

EDLCs and pseudocapacitors have their own pros and cons. Therefore, a hybrid type of capacitor can be fabricated taking the advantages from both EDLCs and pseudocapacitors [20-22]. The EDLC part which stores charge electrostatically, increases the specific power whereas the pseudocapacitor part improves the specific energy by storing the charge electrochemically. Thus a hybrid capacitor can supply high specific power with high specific energy and long cycle life. Depending up on

the electrode configuration, hybrid supercapacitor can be categorized into two types, such as asymmetric type and battery type hybrid supercapacitor.

### *Asymmetric type hybrid supercapacitors*

In asymmetric type hybrid electrode mainly pseudocapacitive transition metal or bimetallic oxides/ hydroxides/ sulfides or it's composite with conducting polymer or carbonaceous materials is used as positive electrode and the carbonaceous materials such as activated carbon, graphene, reduced graphene oxide (rGO), carbon nanotubes (CNTs) are mainly used as negative electrode [23, 24]. Thus this type of hybrid supercapacitor consists of both faradaic and non-faradaic processes which help to increase specific energy and specific power, respectively, along with the life cycle.

### *Battery type hybrid supercapacitors*

Due to the reversible electrochemical reactions lithium ion battery gives high specific capacitance as well as high specific energy. But it is unable to supply high specific power due to its slow ion diffusion and involved electrochemical reaction-based charge transfer process. The electrochemical reactions also reduce the cycle life. On contrary EDLCs offer high specific power but low specific energy. Therefore, a hybrid type electrode resulting from the combination of a battery type electrode and an EDLC electrode can be proficient to supply high specific power and high specific energy as well [25-27]. The battery type hybrid supercapacitor also offers high cycle life and fast charging process.

## I.1.2 Electrode materials for supercapacitor

There are mainly three types of electrode materials for supercapacitor such as carbonaceous materials, pseudocapacitive materials and their composites.

### *I.1.2.1 Carbonaceous materials*

Carbon nanomaterials have been extensively employed in energy storage application because of its different architectures and tunable surface chemistry. Furthermore, it has high electrical conductivity, high electrochemical stability, excellent mechanical properties, and wide operating temperatures [28-30]. However, the most important criterion is the high specific surface area (SSA) of carbon materials for enhanced gravimetric capacitance. The different types of carbon-based materials with high SSA and high conductivity are depicted in Table I.2 **[**31**]**.

**Table I.2** Various types of carbon-based materials with their properties. Reprinted with permission from Simon et al. [31]. Copyright 2013 American Chemical Society

| Material | Carbon onions | Carbon nanotubes | Graphene | Activated carbon | Carbide derived carbon | Templated carbon |
|---|---|---|---|---|---|---|
| Dimensionality | 0-D | 1-D | 2-D | 3-D | 3-D | 3-D |
| Conductivity | High | High | High | Low | Moderate | Low |
| Volumetric Capacitance | Low | Low | Moderate | High | High | Low |
| Cost | High | High | Moderate | Low | Moderate | High |
| Structure | 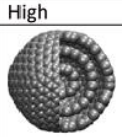 | 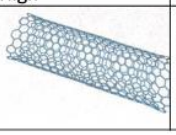 | 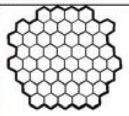 | 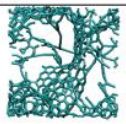 | 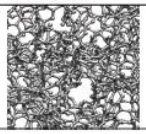 |  |

Every material has its unique structure and distinctive electrochemical properties. Such as zero- and one-dimensional carbon materials allow fast adsorption/desorption of the electrolyte ions on their surface, indicating high power density. On contrary, two-dimensional graphene can deliver high charging/discharging rate and volumetric energy density. Porous 3D carbon materials

acquire higher surface areas and mesoporous structure, providing higher energy densities [32].

### *Activated carbon*

Activated carbon (AC) has been widely used as active material for EDLCs because of the excellent properties such as high specific surface area (~3000 $m^2/g$), high electrical conductivity (1000 to 3000 S/m), and low cost [33]. Generally, porous carbon prepared by carbonization-activation method is called activated carbon. Carbonization is a method by which a carbonaceous residue of organic or natural substances (pyrolysis) is produced by thermal decomposition under an inert atmosphere. A large number of different kinds of reactions like dehydrogenation, condensation, hydrogen transfer, crosslinking and isomerization simultaneously occur during this process [34]. These reactions help to release the volatile materials leaving behind the nonporous carbonaceous residue. This residue is also called as coal char or biochar. In the activation step the nonporous carbonaceous residue is treated with activating agents, also known as pore-forming agents or porogens. With activating agents nonporous residue undergoes oxidation reactions to create required pores into it. Based on the activating agents used in activation methods, these are categorized as either chemical or physical activation method [35]. The chemical activation process uses KOH, NaOH, $Na_2CO_3$, $K_2CO_3$, $ZnCl_2$, or $H_3PO_4$ as activating agents, whereas $CO_2$, $O_2$, air, or steam are used in physical activation. Both the processes have several advantages and disadvantages as well. The chemical activation is comparatively low-temperature process which produces highly mesoporous carbon with high mass of yields and BET (Brunauer–Emmett–Teller) surface area. On contrary, physical activation requires high activation temperatures with longer operation time, producing

relatively lower yields of compounds with small pore sizes and low specific surface area (SSA). In spite of these disadvantages, physical activation process is more feasible and useful for industrial scale production than chemical activation, as it exhibits low corrosion. AC can be able to give the maximum capacitance of 300 F/g with a potential window of 0.9 V in aqueous electrolyte [36]. However in organic electrolyte it gives a maximum capacitance of 100 F/g with a large potential window of 2.7 V.

### *Graphene*

Graphene is a two-dimensional new allotrope of carbon, having monoatomic thick hexagonal (honeycomb) lattice structure with carbon-carbon distance of 1.42 Å. In other words, it is a single layer of graphite having $sp^2$ hybridized carbon atoms. Graphene is the building block of all other graphitic materials such as, three dimensional (3D) graphite, one dimensional (1D) carbon nanotubes and zero dimensional (0D) fullerenes [37]. Due to its attractive physical and chemical properties such as very high surface area, excellent electronic and thermal conductivities, superior mechanical and electrochemical stability, good transparency, graphene has grabbed a great scientific and technological interest in recent years [38]. Moreover, graphene can be easily produced in large scale by the reduction of graphene oxide. Because of the remarkable properties as well as ease of synthesis of graphene, it has been widely used in many fields such as polymer nanocomposites, energy storage and conversion (e.g. supercapacitors, batteries, fuel cells and solar cells), chemical sensors, flexible electronic and optical devices [39-44]. Graphene shows double layer capacitance, which results from the charge or ion accumulation on the surface of electrode/electrolyte interface.

Intrinsic (undoped) graphene behaves like a semi-metal or zero gap semiconductors. It exhibits amazing electronic and mechanical properties such as, extremely high charge carriers (electrons and holes) mobility = 230000 $cm^2$/Vs at room temperature, thermal conductivity = 3000 W/mK, mechanical stiffness =1 TPa with large surface area 2600 $m^2$/g [45]. Graphene is also transparent material, which can absorb 2.3% light of the optical region. In the year 2010, Andre K. Geim and Konstantin S. Novoselov were awarded Nobel Prize for "groundbreaking experiments regarding the two dimensional material graphene". They successfully synthesized free-standing graphene film for the first time by using an effective mechanical exfoliation method with a scotch tape and silicon substrate [46]. In graphite, adjacent graphene layers are bonded via weak interaction between $p_z$ orbitals. This interaction between $p_z$ orbitals restricts the complete separation of bulk graphite layers into individual graphene sheets under mechanical actions. Mechanical exfoliation of graphite results in either stacks of sheets, or a small amount of detached sheets. This depends on the condition of mechanical exfoliation. Chemical oxidation followed by reduction of graphite oxide results in graphene like materials termed as reduced graphene oxide (rGO) which contains defects and residual oxygen-containing functionalities attached at the periphery of the sheets. Graphene has been considered as an efficient electrode for EDLCs due to its high SSA (2630 $m^2$/g), high electrical conductivity (>1700 S/m) [47], and high theoretical specific capacitance (550 F/g) [48].

## *Carbon nanotubes*

Carbon nanotubes (CNTs) are the one-dimensional carbon nanomaterials which have been extensively used for energy storage application due to its high SSA (500 -1600

$m^2/g$), mechanical and electrical properties ($10^6$ S/m) [49]. On the basis of the number of walls present in the nanostructure, it can be categorized into two types such as single-walled carbon nanotubes (SWCNTs) and multi-walled carbon nanotubes (MWCNTs). CNTs are generally synthesized by the catalytic decomposition of hydrocarbons. Although it has high specific surface area, the hydrophobicity nature of the nanotube restricts its specific capacitance in between 20 to 80 F/g. Modified CNTs with some pseudocapacitive functional groups can improve the specific capacitance but it reduces the cyclic stability [50, 51].

### *I.1.2.2 Pseudocapacitive electrode materials*

Transition metal oxides are excellent pseudocapacitive electrode materials because of their variable oxidation states [52-57]. To be a good pseudocapacitive electrode, it must possess at least three important characteristics for supercapacitor applications [58]. Firstly, it should have an appreciable conductivity to exhibit high magnitude of gravimetric capacitance and large specific energy density. Secondly, the crystalline phase/morphology of the compound must not change during oxidation state change to have high electrochemical reversibility. Finally, the smaller ions of electrolyte can easily intercalate into the lattice of metal compounds to possess long cycle life. The charge storage mechanism of these transition metal oxides involves the chemisorption/desorption of electrolyte cations into the active electrode. Due to the small size and high mobility of $H^+$ ion, concentrated $H_2SO_4$ was considered as most suitable electrolyte. But most of the metal oxides are not stable in that electrolyte except $RuO_2$. $RuO_2$ shows the excellent electrochemical stability in $H^+$ medium and achieves high specific capacitance [59]. However, the less availability and very high cost of $RuO_2$ restricted its use. Recently, $MnO_2$, $Mn_3O_4$, NiO, $Co_3O_4$, etc. have been

investigated as pseudocapacitive electrodes [60-63]. Mixed metal oxides are used to enhance the efficiency of the electrode materials by increasing the electroactive redox sites. There have been plenty of research works exploring the same idea. Apart from the oxide, bimetallic hydroxides have been investigated as pseudocapacitive electrode due to their high electroactive redox sites, easy synthetic method and high theoretical specific capacitance [64-65].

Systematic investigation of the electrochemical performances of various transition metal sulfides, an important class of inorganics, such as MnS [66-68], CoS [69, 70] and NiS [71, 72] reported those as high performances materials. Recently, binary metal sulfides such as Mn-Ni-S [73-75], Co-Ni-S [76-79], and Mn-Co-S [80-83] have attracted enormous attention due to their large number of redox active sites, high thermal stability and electrical conductivity compared to that of their corresponding unitary metal sulphide [84].

### *Conductive polymers*

Conductive polymers such as polyaniline, polypyrrole, polythiophene and their derivatives are promising candidates for pseudocapacitor application due to their excellent conductivity owing to the extensive conjugation, fast charge-discharge kinetics and ease of synthesis [85, 86]. During charging-discharging, the reversible redox reactions mainly involve doping and de-doping of ions to or from the backbone of polymer. The doping process can be two types, such as p-doping and n-doping. The p- and n-doping refers to the doping with anion counterpart ($A^-$) and cation counterpart ($C^+$), respectively.

$$CP \leftrightarrow CP^{n+}(A^-)_n + ne^- \qquad \text{(p-doping)} \qquad (1)$$

$$CP + ne^- \leftrightarrow (C^+)_nCP^{n-} \qquad \text{(n-doping)} \qquad (2)$$

The forward and backward reactions are corresponded to the charging and discharging process, respectively. The pseudocapacitive conductive polymers provide high specific capacitance due to the fast faradaic redox reactions.

#### *I.1.2.3 Composite materials*

Current research on the electrode materials for supercapacitor is focused to design the composite materials by combining both the electrical double layer capacitive and the pseudocapacitive active materials [87]. Therefore, the composite materials resulting from the combination of the carbonaceous material having high specific surface area and the highly redox active pseudocapacitive materials is capable of storing charge electrostatically as well as electrochemically. However, better compatibility gives better synergistic interaction between the components and shows enhanced electrochemical performance than the pristine components. Such as a superior synergistic interaction between graphene or CNTs with metal oxides like $MnO_2$ or the conducting polymer like polyaniline give high electrochemical activity than any single component [88-90].

## I.1.3 Electrolytes for supercapacitor

Apart from the active material the electrochemical performance of a supercapacitor greatly depends on the electrolyte. The electrolyte determines the working potential window of the device and it's capacitance as well. Electrolyte ions are soluble either in aqueous or non-aqueous solvent. These electrolyte ions play the key role whether to form the double layer in EDLCs or to conduct the reversible faradaic redox reaction in case of pseudocapacitor. Furthermore, electrolyte is the only conductive connection

between the positrode and negetrode which are separated by a separator. In nutshell, an ideal electrolyte should have (i) broad potential window, (ii) high chemical and electrochemical stability, (iii) high ionic conductivity along with chemical and electrochemical inertness to the other components such as active materials, separator current collectors of the device, (iv) wide operating temperature range, (v) low equivalent series resistance, viscosity, volatility and flammability, and (vi) should be cheap and environmentally benign [91, 92]. Primarily liquid electrolyte can be categorized into two types such as aqueous and non-aqueous electrolyte. Aqueous electrolyte consists of inorganic solutes and water as solvent. The high ionic mobility and low equivalent series resistance are the main advantage of using aqueous electrolyte. One major disadvantage is that the devices can be operated only up to 1.2 V in traditional aqueous electrolyte as the decomposition potential of water is 1.23 V. Therefore, high specific energy cannot be achieved using aqueous electrolyte. Depending upon pH, aqueous electrolytes are acidic ($H_2SO_4$), neutral ($Na_2SO_4$) and basic (KOH) in nature [93]. To improve the conductivity of conventional aqueous electrolytes and charge storage, foreign redox system like $K_3[Fe(CN)_6]$/ $K_4[Fe(CN)_6]$ can be added to it [94]. Non-aqueous electrolytes used in supercapacitor are organic electrolytes ($TEABF_4$/PC) and ionic liquids ($EMIMBF_4$) [95]. The main advantage of using non-aqueous electrolyte is the broadening of potential window range which leads to improved specific energy. Solid or quasi-solid state electrolytes are solid in nature. The examples are gel polymer electrolyte (PVA/$H_2SO_4$-$H_2O$), solid polymer electrolyte (PEO/LiCl) and inorganic electrolyte ($Li_2S$-$P_2S_5$).

## I.1.4 Separator

A separator is a permeable membrane sandwiched between two electrodes of a supercapacitor. The separator acts as an inactive component which plays a vital role in controlling the energy storage device performance [96]. It mainly acts as a physical barrier between the two electrodes, thus facilitating transport of the ionic charge carriers via the interconnected pores of the separator avoiding short circuits. Highly porous nature of the separator easily permits the electrolyte ions and hence the equivalent series resistance decreases. Depending up on the nature of electrolyte, separators are chosen. For example, ceramic or glass fiber separators are commonly employed in aqueous electrolytes, whereas paper or polymer separators are preferred in organic electrolyte.

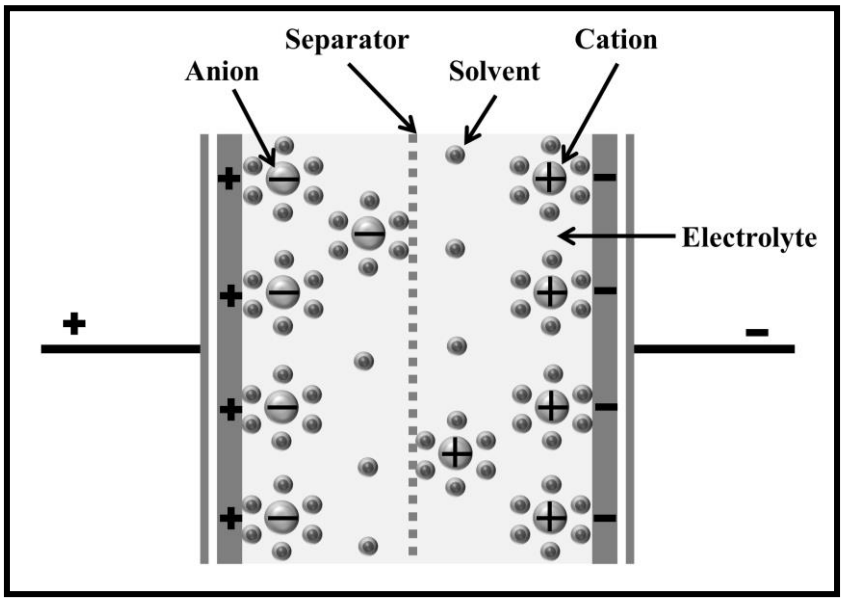


**Figure I.4** Construction of supercapacitor.

### I.1.5 Construction of supercapacitor

Supercapacitors assemble with two electrodes viz. positrode and negetrode immersed in an aqueous or non-aqueous electrolyte, and an electrolyte ion permeable porous membrane separator in between them (Figure I.4) [12]. The electrodes are prepared by pasting or depositing the active materials such as carbonaceous or pseudocaoacitive materials, or their composites on the surface of the current collector. If both the electrodes are of same active materials then the fabricated supercapacitor is known as symmetric supercapacitor otherwise fabricated supercapacitor is called asymmetric supercapacitors.

### I.1.6 Application of supercapacitor

Supercapacitors have wide range of applications as it can overcome the limitations of the conventional capacitors and batteries [97, 98]. These can be used as a backup power system for static random-access memory, microcomputer, measuring and communication device, digital tuning system, etc. Supercapacitors are also used as a power source in various high power applications such as electronic toy, display light, gas igniter, load lifting, etc. It can also provide the starting power to the electrical vehicle in start and stop systems. Supercapacitor can be used in a micro source system connected to micro-grid. It can also be used in wind turbines where it helps to smooth out the intermittent power supplied by the wind.

## I.2 Techniques of materials preparation

The synthetic routes not only influence the architecture of the nanomaterials but also affect the performance of the desired product in various applications. A large number

of methods have been developed for the synthesis of nanomaterials having electrochemically active high SSA. The simple and highly used techniques are hydrothermal method, precipitation method and electrochemical deposition technique.

## I.2.1 Hydrothermal method

The term 'hydrothermal' refers to the involvement of water and heat. This process involves growth of the crystals from aqueous solution within Teflon-coated stainless-steel autoclave at high temperature under high pressure [99]. When other solvent instead of water is used, the method is termed as solvothermal. In the last few years, hydrothermal method has attracted great interest from the researchers of different disciplines for the preparation of nanostructured materials. This method has several advantages such as its efficiency to produce high yield of products with standardization in nucleation, growth and aging (which affects size, morphology and aggregation) and reproducibility. Moreover, it is eco-friendly in nature and needs low energy consumption over other available conventional fabrication techniques. A large number of metal oxides, hydroxides and sulfides have been synthesized using hydrothermal technique for various applications reported elsewhere.

## I.2.2 Precipitation method

The chemical precipitation method is more suitable and common method for the synthesis of nanomaterials with various architecture and porosity due to simplicity, reproducibility and cost-effectiveness [100]. In this process a substance of a solution converts itself into an insoluble form and separate out from the solution. Generally, a precipitating agent like hydroxide is added to the homogeneous solution of desired metal salt. This type of reactions undergo in room temperature or little high

temperature. Chemical precipitation routes are categorized into the direct precipitation (the solution contain on cation only) and co-precipitation (multi-cations are present in the mixed solution) method [101].

### I.2.3 Electrodeposition technique

The electrodeposition method exploits the creation of different kinds of materials with desired surface morphologies directly from electrochemical reactions in liquid phase with substrate materials. Unlike some other methods which involve multistep and complicated process, electrochemical deposition is a simple, low cost, highly effective and convenient method to fabricate a uniformly extended nanostructure with large-area coverage in aqueous electrolyte [102]. The main advantage is that it does not need any harsh condition. Moreover, the morphology and thickness can be tuned easily by controlling the deposition parameters, such as, concentration of electrolytic solution, electrodeposition scan rate, current density, and time. The fast nucleation and growth on a large variety of conducting substrates like Ni foam [68] or wire [103], Cu foam [104], stainless steel [105], ITO coated glass [106], carbon cloth [107] or fiber [108] facilitates its use in energy storage devices directly as binder free electrode.

## I.3 Techniques of materials characterizations

The as-synthesized material is characterized structurally, morphologically and electrochemically.

## I.3.1 Electrochemical characterization

The electrochemical performance of a material is investigated in terms of cyclic voltammetry (CV), galvanostatic charge-discharge (GCD) and electrochemical impedance spectroscopy (EIS) using a potentiostat (Figure I.5) [109].

### *I.3.1.1 Cyclic voltammetry (CV)*

CV is an extensively used electrochemical method which gives the basic information about potential window, charge transfer reaction (if any), specific capacitance and cycle life of an active material. CV measures the current that develops in an electrochemical cell as the voltage is swept over a potential window. This can be performed using a three- or two- electrode system cell. The three electrode system cell consists of working, reference and counter electrode. Working electrode is made of the active materials, whereas the reference electrode is a standard electrode with constant electrochemical potential such as saturated calomel electrode or Ag/AgCl electrode. Counter electrode is used to complete the circuit of the electrochemical cell. Generally inert metal like Pt is used as counter electrode for single electrode study.


**Figure I.5** Potentiostat for electrochemical measurement

The nature of the CV curves is different for the EDLCs and pseudocapacitive materials. A rectangular CV curve is obtained for EDLCs whereas for a pseudocapacitive material a deviation is shown from its ideal behavior. The specific capacitance of the electrode materials can be calculated from CV curve using eq. 1.

$$C_s = \frac{\int_{V1}^{V2} i(V)dV}{2(V2-V1)vm} \quad \ldots\ldots (1)$$

where, $\int_{V1}^{V2} i(V)dV$ is the area of the CV curve, $\Delta V = (V2 - V1)$ is the potential window (V), $v$ is the scan rate (mV/s) and m is the mass (g) of the active materials.

### *I.3.1.2 Galvanostatic Charge-Discharge (GCD)*

GCD curve helps to understand the electrochemical performance more accurately towards real-field performance. In GCD test the cell is charged and discharged in the specified potential range at a constant applied current. Like CV curves, the nature of GCD curve is different depending upon the nature of electrode materials. Ideal EDLC gives linear voltage response with triangular-shaped GCD curve, whereas nonlinear GCD curve indicates pseudocapacitive nature of the electrode. From GCD curve coulombic efficiency (η), specific capacitance ($C_s$), specific energy (E) and specific power (P) can be calculated using following equations:

$$\eta = (t_d/t_c) \times 100\% \qquad (2)$$

$$C_s = \frac{i \times \Delta t}{m \times \Delta V} \qquad (3)$$

$$E = ½\, C_s \times (\Delta V)^2 \qquad (4)$$

$$P = E/\Delta t \qquad (5)$$

where $t_d$, and $\Delta t$ represents the discharging time (s), $t_c$ is charging time (s), ($i/m$) is the measurement of the mass normalized current (A/g), and $\Delta V$ is the potential window (V).

#### *I.3.1.3 Electrochemical Impedance Spectroscopy (EIS)*

EIS is also an equally important electrochemical method which gives the idea about the various resistive effects happen in the active material during the electrochemical process [110]. A real versus imaginary part of the complex impedance of an electrode is plotted, known as Nyquist plot, from EIS. After fitting the curve with an equivalent electrical circuit various parameters like charge transfer resistance ($R_{ct}$), solution resistance ($R_s$), double layer capacitance ($C_{dl}$), Warburg impedance (W), and constant phase element (CPE) can be obtained. As these parameters are related to ESR and therefore they effect on electrochemical performance of an electrode material in an electrolyte.

## I.3.2 Structural characterization

#### *I.3.2.1 X-ray diffraction (XRD) analysis*

The XRD analysis helps to examine the crystallographic structure or chemical composition of a material [111]. When monochromatic X-rays are passed through a crystalline sample the microcrystals diffract the X-rays due to constructive interference. The diffracted X-rays from the sample produce a characteristic pattern of rings on the detector screen. This pattern is analyzed to get insight into the crystallinity and the phase purity of the sample being analyzed. The working principal of diffractometer is governed by the Braggs law. From the diffractometer the diffraction patterns are obtained as absolute intensity *vs.* 2θ.

### *I.3.2.2 Fourier Transform Infrared Spectroscopy (FTIR)*

FTIR is an important analytical tool used to identify the functional groups present in organic and inorganic materials [112]. Every molecular bond vibrates at a characteristic frequency depending up on the constituent atoms and the type of bond. A molecule absorbs the infrared radiation to excite itself to the higher vibrational state. The wavelength of the absorbed light is a function of the energy difference and also characteristic of the particular functional moiety. This spectroscopic method records percent transmittance versus wavenumber. The term 'Fourier Transform' means a mathematical algorithm, which is essential to transform the raw data to the actual spectrum.

### *I.3.2.3 Raman Spectroscopy*

Raman spectroscopy is another important analytical tool used to get information about the chemical and structural information of a sample [113]. When a single wavelength laser excites the bonds of a molecule to the higher vibrational level a measurable scattered light is produced. In an inelastic scattering also known as Raman scattering process, a transfer of energy between the molecule and scattered photon occurs. If the scattered photon transfers energy to the molecule, then its wavelength increases due to decreasing the energy, which is called Stokes Raman scattering.

### *I.3.2.4 X-ray Photoelectron Spectroscopy (XPS)*

XPS is an important spectroscopic technique which mainly gives the idea about elemental composition of the sample surface [114]. The sample surface is irradiated with monochromatic x-rays and the kinetic energy of the photoelectrons emitted from the surface is measured.

## I.3.3 Morphological characterization

### *I.3.3.1 Field Emission Scanning Electron Microscopy (FESEM)*

The surface morphology can be examined by the electron microscopy like FESEM. This produces images of the sample surface by using focused beam of electrons instead of light. The FESEM analysis can provide largely magnified images with higher resolution at a lower voltage compared to that obtained from the conventional SEM method. The main difference between the SEM and FESEM is the use of different electron generation system.

### *I.3.3.2 High Resolution Transmission Electron Microscopy (HRTEM)*

In HRTEM, the focused beam of electrons transmits through the sample to form the image. It can provide highly magnified images with lattice fringes which are really difficult to get by normal TEM. The HRTEM uses both the transmitted and the scattered beams to create an interference image.

## I.3.4 Surface area measurement

### *I.3.4.1 Brunauer-Emmett-Teller (BET) analysis*

BET surface area analysis provides the specific surface area ($m^2/g$) of a sample trough gas adsorption analysis. An inert gas like nitrogen is constantly run over a solid sample and the formation of a monolayer of gas molecules is used to determine the specific surface area of the sample.

# I.4 Literature Review

The energy storage research in terms of supercapacitor application is mainly focused on finding the best electrode material which can deliver high specific energy at high rate of specific power. Therefore, the materials researchers have been using pristine or choosing the best combination among capacitive and pseudocapacitive materials. In this section, the electrode materials of supercapacitor based on transition metal oxides/hydroxides/sulfides, rGO/graphene, CNT and their hybrids/composites have been reviewed to focus the scope of the present work.

Among pseudocapacitive transition metal oxides, manganese oxides have some advantages like, high natural abundance, variable oxidation states, high theoretical specific capacitance, low cost and environmentally benign nature [115]. Generally manganese has four stable oxides such as $Mn_3O_4$, $Mn_2O_3$, $MnO_2$ and MnO. Among them $Mn_3O_4$ is one of the stable spinal oxides ($Mn^{II}Mn^{III}{}_2O_4$). Due to variable oxidation states of Mn, the charge storage mechanism is governed by the fast faradaic redox reaction by adsorption of the electrolyte cations on the surface of $Mn_3O_4$. Therefore, the pseudocapacitive $Mn_3O_4$ shows exceptionally high theoretical specific capacitance of about 1400 F/g [116].

B. Gnana Sundara Raj et al. have reported $Mn_3O_4$ nanoparticles prepared by a simple chemical precipitation method [117]. The active material exhibited maximum specific capacitance of 322 F/g at areal current density of 0.5 $mA/cm^2$ in 1 M $Na_2SO_4$ electrolyte. It exhibited high capacitance retention of 77% over 1000 cycles. Y. Luo et al. have reported $Mn_3O_4$ cubes prepared by a simple dissolution evaporation method followed by calcination [118]. The 3D hierarchical architecture with interlocking structure and higher conductivity of the as-synthesized materials exhibited high

electrochemical performance. The electrode material showed maximum specific capacitance of 583 F/g at specific current of 1 A/g in 6 M KOH electrolyte accompanied with good capacitance retention of 71.8% over 1200 cycles. B. Li et al. have reported ultrafine $Mn_3O_4$ nanoparticle which exhibited maximum specific capacitance of 260 F/g at specific current of 1 A/g [119]. They fabricated an aqueous asymmetric supercapacitor activated carbon//$Mn_3O_4$ which was able to deliver high specific energy of 40.2 Wh/kg at a power delivery rate of 500 W/kg accompanied with good capacitance retention of 70.8% over 5000 GCD cycles.

One major drawback of $Mn_3O_4$ is poor conductivity ($10^{-7}$ to $10^{-8}$ S/cm) [120]. The combination with highly conductive material such as rGO/graphene/CNTs can overcome this intrinsic problem [121]. X. Cui et al. have reported $Mn_3O_4$ nanoparticles deposited on carbon nanotube array (CNTA) for electrochemical energy storage [122]. They first synthesized CNTA via catalytic chemical vapor deposition technique and then the $Mn_3O_4$-CNTA composite via dip-casting process followed by annealing. The composite exhibited maximum specific capacitance of 143 F/g at 2 mV/s scan rate, indicating high areal capacitance of 1.70 F/cm$^2$ in 0.5 M $Na_2SO_4$ electrolyte. R. Poon et al. have reported $Mn_3O_4$-MWCNT composite prepared by wet chemical synthesis [123]. The as-prepared composite exhibited remarkably high areal capacitance of 3.52 F/cm$^2$ at scan rate of 2 mV/s. V. Hiremath et al. have reported CNT threaded $Mn_3O_4$ nanocomposites prepared by hydrothermal method [124]. In composite CNTs were well decorated on the surface of $Mn_3O_4$ nanoclusters. CNTs improved the conductivity of the composite whereas $Mn_3O_4$ provided more electroactive sites. Due to the synergistic effect of the component materials, the composite exhibited high specific capacitance of 81.9 F/g at a specific current of 0.6 A/g with good cycle life.

To increase the specific energy, an asymmetric device can be fabricated using $Mn_3O_4$ based composite and carbonaceous material as positive and negative electrode, respectively. Y. Hu et al. have reported super flexible $Mn_3O_4$-rGO nanohybrid paper prepared by a simple hydrothermal route followed by electrochemical reduction [125]. A well dispersion of highly redox active $Mn_3O_4$ on the amply conductive rGO made the hybrid nanocomposite exceptionally electrochemical active. A flexible asymmetric supercapacitor fabricated using $Mn_3O_4$-rGO paper and rGO paper as positive and negative electrodes, respectively, was able to provide remarkably high volumetric capacitance of 54.6 F/cm$^3$ accompanied with high energy density (0.0055 Wh/cm$^3$) and power density (10.95 W/cm$^3$). Y. Xiao et al. have reported an asymmetric supercapacitor using $Mn_3O_4$@GR and activated carbon (AC) as positive and negative electrodes, respectively [126]. It exhibited maximum specific energy of 34.6 Wh/kg at a power delivery rate of 500 W/kg in 1 M $Na_2SO_4$ electrolyte.

Another very stable oxide of manganese, $MnO_2$, is also abundant, cheap, and environmentally benign [121]. $MnO_2$ has some remarkable electrochemical properties such as exceptional theoretical specific capacitance of 1370 F/g [127], large electrochemical potential window, and ability to perform in mild aqueous electrolytes. C. Wu et al. have reported hydrothermal synthesis of plate-like $MnO_2$ deposited on nickel foam as a binder free electrode for supercapacitor [128]. Due to the 3D architecture it achieved high surface area and also remarkable electrochemical performance. $MnO_2$ showed maximum specific capacitance of 583.5 F/g at specific current of 1 A/g accompanied with good (~91.2%) capacitance retention and 100% coulombic efficiency even after 4000 cycles. A. Xia et al. have reported δ-$MnO_2$ nanosheets prepared by a simple hydrothermal method [129]. The active material

exhibited maximum specific capacitance of 332.7 F/g at specific current of 0.5 A/g with capacitance retention of 93.7% after 10000 cycles.

Copper oxide (CuO) is also a promising pseudocapacitive candidate due to its abundance, chemical stability, ease of synthesis of numerous nanostructure, good electrochemical performance, non-toxicity and environmental friendliness. J. Ye et al. have reported porous CuO nanoflowers on flexible Cu foil prepared by a simple chemical deposition process [130]. The active material exhibited maximum specific capacitance of 284.5 F/g at areal current of 0.5 $mA/cm^2$ accompanied with 80 % capacitance retention after 1000 cycles. S.K. Shinde et al. have reported CuO thin films prepared by chemical bath deposition method using different ionic liquids [131]. Among them CuO nanosheets synthesized using 2-dimethylimidazolium chloride exhibited maximum capacitance of 464 F/g at 5 mV/s in 1 M $Na_2SO_4$ electrode. To improve the shortcomings like limited specific surface area and comparatively low electrical conductivity, CuO is often combined with other metal oxide (e.g. MnO2) resulting in a hybrid material having improved specific capacitance. Y. Xin Zhang et al. have reported CuO-$MnO_2$ nanocomposites prepared by hydrothermal method [132]. In composite the highly porous $MnO_2$ nanosheets nicely covered the CuO nanoflowers. The maximum specific capacitance of 167.2 F/g was calculated for the composite at a specific current of 0.3 A/g in 1 M $Na_2SO_4$ electrolyte. M. Huang et al. reported CuO@$MnO_2$ composite prepared using CuO nanotubes and $MnO_2$ nanosheets [133]. The highly porous structure with high SSA of the material improves redox faradic reactions by enhancing the rate of ion transfer and surface adsorption of electrolyte cations. They fabricated an asymmetric device using CuO@$MnO_2$ and activated microwave exfoliated graphite oxide (MEGO) as positive and negative electrode, respectively. The device exhibited high specific energy 22.1 Wh/kg with

power delivery rate of 85.6 kW/kg accompanied with high cycling stability. Z. Zhang et al. have reported hollow dandelion-like CuO wrapped with MnO nanosheets [134]. The active material exhibited maximum specific capacitance of 228 F/g with good cycling stability.

Apart from the combinatorial metal oxides, the bimetallic sulfides also have attracted enormous attention due to their large number of redox active sites, high thermal stability and electrical conductivity [84]. N. Ahmed et al. reported 3D interconnected Mn−Ni−S nanosheets on Ni foam prepared by a single step electrodeposition process [73]. The Mn−Ni−S exhibited remarkably high specific capacitance of 2849 F/g at specific current of 1 A/g with high rate capability. The fabricated asymmetric supercapacitor using Mn−Ni−S nanosheets as positive and $Fe_3O_4$-GR as negative electrode achieved high specific energy 40.44 Wh/kg with power delivery rate 800 W/kg accompanied with high capacitance retention. Y. Li et al. have reported Ni–Co sulfide nanowire on Ni foam prepared by hydrothermal technique [135]. The self-supported Ni-Co-S exhibited maximum capacitance of 2415 F/g at the areal current 2.5 mA/cm$^2$. The fabricated asymmetric supercapacitor using Ni-Co-S nanowire as positive and $Fe_3O_4$-GR as negative electrode achieved high specific energy 40.44 Wh/kg with power delivery rate 800 W/kg accompanied with high capacitance retention. G. Li et al. have reported electrochemically co-deposited three-dimensinal hierarchical porous Mn-Co sulphide nanosheets on Ni foam [81]. The binder free electrode exhibited areal capacitance of 1.724 F/cm$^2$ at 1 mA/cm$^2$ areal current.

The charge storage properties of the binary metal hydroxides have also been considered as a recent research topic due to their interconnected arrangement and high

SSA. The $MnSn(OH)_6$ has been chosen for electrochemical application due to its high electron mobility, good conductivity, excellent charging-discharging profile and high cycle life due to the transition metal (Mn) along with the robustness achieved from the post transition metal (Sn). B. Jansi Rani et al. have reported $MnSn(OH)_6$ nanocubes prepared by solvothermal method [136]. The oriented fine edge morphology and oxygen vacancies in the active material were helpful to improve the electrochemical performance. A maximum specific capacitance of 525 F/g at the scan rate of 5 mV/s was achieved.

To increase the specific energy, enhancement of capacitance and the working potential window of an electrode is very essential according to the equation; $E = 0.5C_{sp}V^2$. Fabrication of an asymmetric supercapacitor with a pseudocapacitive electrode (positrode) as the energy source and a capacitive electrode (negatrode) as the power source has been accepted as a promising approach. The carbonaceous materials which are used as negatrode of supercapacitor mostly suffer from low capacitance. Although the development of negative electrode materials is relatively slow, recently few transition metal oxides and hydroxides such as α-$MnO_2$, $Mn_3O_4$, $Ce(OH)_2$ have shown significant performance as negative electrodes for supercapacitor. Y. Chen et al. reported α-$MnO_2$ nanospheres prepared by chemical precipitation followed by annealing process exhibited maximum specific capacitance of 736.3 F/g at a specific current of 1 A/g accompanied by excellent cycling stability [137]. Due to the oxygen vacancies resulting from annealing and high SSA, the α-$MnO_2$ nanospheres exhibited high electrochemical performances as negatrode. J.-X. Feng et al. fabricated negative electrode based on amorphous porous $Mn_3O_4$/NGP (Ni/graphite/paper) via electrodeposition [138]. The material achieved a maximum specific capacitance of 432 F/g at scan rate of 5 mV/s. The multi-valences of Mn (+2

and +3) and stable negative potential window (-0.8 to 0 V) made the composite suitable as negatrode of supercapacitor. X. Liang et al. reported $Ce(OH)_2$ as negative electrode prepared *in-situ* by electrochemical method [139]. The electrode was able to achieve high specific capacitance of 187 F/g at a specific current of 1 A/g.

Recently, the coordination complexes like metal hexacyanoferrates have gained attention due to their semiconducting nature with narrow band gap, high SSA and the redox ability i.e., high charge conductive nature. Hence these compounds show promising applications in energy storage and conversion, photocatalysis, ion sensing etc. H. Pang et al. have reported manganese hexacyanoferrate hydrate nanocubes prepared by simple precipitation method [140]. It exhibited excellent electrochemical performance due to its nanocubic structure with micro- and mesopores which facilitates efficient charge transfer and mass transport. It achieved maximum specific capacitance of 690 F/g at 1.3 A/g specific current using 1 M $K_2SO_4$ electrolyte. J. Chen et al. prepared $Ni_3[Fe(CN)_6]_2 \cdot H_2O$ by simple precipitation method [141]. The electrode material showed maximum specific capacitance of 574.7 F/g at specific current of 0.2 A/g in 1 M $KNO_3$ electrolyte accompanied with good capacitance retention of 87.46% over 1000 cycles. J.-G. Wang et al. reported cobalt hexacyanoferrate (CoHCF) submicroboxes prepared by traditional precipitation method [142]. The nanosized CoHCF having hierarchically mesoporous structure facilitates the charge storage property due to shorten diffusion path and increased number of redox active sites. The as-prepared material exhibited high specific capacitance of 288 F/g at 0.5 A/g with excellent rate capability. A hybrid capacitor (CoHCF||AC) was prepared providing a high specific energy of 42.5 Wh/kg at specific power of 990 W/kg accompanied by excellent cycling performance. Q. Zhou et al. synthesized a composite of nickel hexacyanoferrate (NiHCF) and surface

modified reduced graphene oxide (rGO) by co-precipitation method [143]. The NiHCF nanoparticles were uniformly anchored on the modified rGO and shown the synergistic effect on electrochemical performance. The composite material exhibited maximum specific capacitance of 270 F/g at specific current of 0.5 A/g. The fabricated asymmetric supercapacitor using NiHCF-modified rGO as positive and sandwiched graphene carbon (SGC) as negative electrode achieved high specific energy 25.4 Wh/kg with power delivery rate 600 W/kg accompanied with 93% capacity retention after 2000 cycles.

## I.5 Scope and objectives

Although plenty of research works have been reported using different combination of materials as electrode materials for supercapacitor application, the detailed literature survey revealed that different type of manganese based materials can be developed for the further improvement of their electrochemical performance. The day-to-day discovery of new portable electronics creates high demand of supercapacitors which should be capable of giving high specific power with high specific energy. The electrochemical performance of a supercapacitor not only depends on the electrode materials, but it also depends on the electrolyte, electrode designs etc. Hence there is huge opportunity to choose the proper electrode materials, the synthetic route and the electrolyte to get the maximum performance.

### I.5.1 Choice of electrode materials

The active materials of the electrode play the vital role in determining the performance of a supercapacitor. There is a huge scope to investigate the different types of Mn-based compounds. Being a second row transition element Mn can

implement some properties like electron mobility, good conductivity, excellent charging-discharging profile and high cycle life. Instead of that manganese-based nanomaterials are promising in the area of energy research because of the following reasons: (i) manganese shows variable oxidation states from +2 to +7. Thus it is exceptionally redox active. (ii) Mn is highly abundant element in comparison to the other transition metals. (iii) Manganese oxides show very high theoretical capacitance along with a wide positive potential window in comparison with other transition metal oxides. (iv) Manganese compounds can easily form composites with hierarchical nanostructures by simple and facile conventional methods like hydrothermal, precipitation and electrodeposition method. The manganese oxide and its composites with carbon material or other transition metal oxides need thorough investigation with respect to their different architecture, charge storage mechanism, enhancement of specific energy in asymmetric supercapacitor designed from them. There is a possibility for investigation of the electrochemical performance of the Mn-based bimetallic hydroxides or sulfides. Metal hexacyanoferrates are the new class of energy materials comparable to others. Hence, there is a lot of possibility to enhance their electrochemical properties.

## I.5.2 Choice of the synthetic route

As the porosity and morphology of an electrode material greatly depend on the synthetic route, the choice of a simple, cost effective, and environment friendly method is important for this purpose. The best common, simple and green strategy is the precipitation method. Except the need of expensive autoclave, the hydrothermal method is extremely useful to synthesize porous material with hierarchical architecture. The electrochemical deposition is a simple, low cost, highly effective

and convenient method to fabricate uniformly extended nanostructure with large-area coverage in aqueous electrolyte. Furthermore, the fast nucleation and growth on a large variety of conducting substrates facilitates its use in energy storage devices directly as binder free electrode.

### I.5.3 Choice of electrolyte

A suitable electrolyte also enhances the performance of the electrolyte. Except the limitation of the potential window, aqueous electrolyte is beneficial for supercapacitor due to their high ionic mobility and low equivalent series resistance and easy handling. To improve the conductivity of conventional aqueous electrolytes and charge storage, foreign redox system like $K_3[Fe(CN)_6]$/ $K_4[Fe(CN)_6]$ can be added to it.

### I.5.3 Objective of the present work

The objectives of the present research works deal with the synthesis of manganese-based materials such as oxides/sulfides/hydroxides and their composites with carbon material or other pseudocapacitive transition metal oxide as electrode materials for supercapacitor application by some simple techniques such as hydrothermal, precipitation and electrodeposition method. To increase the specific energy, asymmetric supercapacitor can be fabricated. The effect of redox system aided aqueous electrolyte can also be analyzed on the performance of supercapacitor.

## I.6 Organization of the Thesis

A total of six chapters are included in the present thesis.

**Chapter I** discusses the basic introduction of the present research topic. Different synthetic routes of the materials and various characterization techniques have been depicted. Finally, the existing literature related to the research topic has been discussed in detail along with the scope and objectives of the present work.

**Chapter II** deals with the synthesis and fabrication of a hybrid-type asymmetric supercapacitor (ASC) by combining $Mn_3O_4$ nanoparticle-supported multi-wall carbon nanotube ($Mn_3O_4$@MWCNT) composite as positive and reduced graphene oxide (rGO) as negative electrodes. A controlled hydrothermal synthesis of $Mn_3O_4$ in the presence of MWCNT resulted in well-distributed $Mn_3O_4$ nanoparticles on the MWCNT backbone in the $Mn_3O_4$@MWCNT composite. The structure, morphology and SSA of the as-prepared materials have been investigated by XRD, FT-IR, XPS FESEM, TEM, and BET analysis. The electrochemical characterizations were carried out in terms of CV, GCD and EIS analysis.

**Chapter III** deals with a simple and cost-effective precipitation approach which was carried out to fabricate CuO nano-needle, and its electrochemical performance was evaluated in a redox-mediated electrolyte (2 MKOH and 0.3 M $K_3Fe(CN)_6$). The CuO nanoparticles were further modified with $MnO_2$ by a hydrothermal method, and the electrochemical behavior of the resulting CuO–$MnO_2$ ($CMO_6$) was thoroughly examined. The as-synthesized electrode materials were structurally and morphologically characterized using XRD, FTIR, XPS, SEM, and TEM. The electrochemical performances of the CuO and $MnO_2$–CuO composites have been examined in detail.

**Chapter IV** deals with a simple electrodeposition technique which were used to synthesis of 3D interconnected binary metallic manganese-cobalt sulfide (Mn-Co-

S) nanosheets on nickel foam. The morphology and elemental composition of the as-synthesized binder free electrodes were investigated with the FESEM and XPS technique, respectively.

**Chapter V** deals with a negative electrode based on $MnSn(OH)_6$ nanocubes prepared by a simple precipitation method at room temperature for supercapacitor application. The as-prepared material was structurally and morphologically characterized with the help of XRD, FT-IR, FESEM, and HRTEM analyses. The electrochemical performance is investigated through a three-electrode cell system in a negative potential window (-1.0 to 0.0 V).

**Chapter VI** deals with the synthesis of four different metal hexacyanoferrates, MHCF (M = Mn, Ni, Cu and Zn) via a simple, cost effective precipitation method. The as-synthesized MHCF were characterized using XRD analysis and FESEM images were recorded for the analysis of morphology. The photocatalytic activity of the four compounds was examined with respect to the photoreduction of Cr(VI) to Cr(III).

**Chapter VII** summarizes the whole work. The novelty and main findings of the research work has also been depicted with the full scope of the future work.

# References

[1] Aneke, M.; Wang, M. Energy storage technologies and real life applications–A state of the art review. Appl. Energy **2016**,*179*, 350-377.

[2] York, R. Do alternative energy sources displace fossil fuels?. Nat. Clim. Change **2012**, *2*, 441-443.

[3] Gong, J.; Li, C.; Wasielewski, M.R. Advances in solar energy conversion. *Chem. Soc. Rev.* **2019**, *48*, 1862-1864.

[4] Milan, P.; Wächter, M.; Peinke, J. Turbulent character of wind energy. *Phys. Rev. Lett.* **2013**, *110*, 138701.

[5] Lin, Y.; Zhao, H.; Yu, F.; Yang, J. Design of an extended experiment with electrical double layer capacitors: Electrochemical energy storage devices in green chemistry. *Sustainability* **2018**, *10*, 3630.

[6] Chaturvedi, B.K.; Nautiyal, A.; Kandpal, T.C.; Yaqoot, M. Projected transition to electric vehicles in India and its impact on stakeholders. *Energy Sustainable Dev*. **2022**, *66*, 189-200.

[7] Aijaz, I.; Ahmad, A. Electric Vehicles for Environmental Sustainability. in '*Smart Technologies for Energy and Environmental Sustainability*' **2022**, 131-145, Springer, Cham.

[8] Zubi, G.; Dufo-López, R.; Carvalho, M.; Pasaoglu, G. The lithium-ion battery: State of the art and future perspectives. *Renew. Sustain. Energy Rev.* **2018**, *89*, 292-308.

[9] Sarjeant, W.J.; Zirnheld, J.; MacDougall, F.W.; Bowers, J.S.; Clark, N.; Clelland, I.W.; Price, R.A.; Hudis, M.; Kohlberg, I.; McDuff, G.; McNab, I. Capacitors—past, present, and future. in '*Handbook of Low and High Dielectric Constant Materials and Their Applications*' **1999**. 423-491, Academic Press.

[10] Simon, P.; Gogotsi, Y. Materials for electrochemical capacitors. *Nat. Mater.* **2008**, *7*, 845-854.

[11] Wang, Y.; Xia, Y. Recent progress in supercapacitors: from materials design to system construction. *Adv Mater.* **2013**, *25*, 5336-5342.

[12] Divyashree, A.; Hegde, G. Activated carbon nanospheres derived from bio-waste materials for supercapacitor applications–a review. *RSC Adv.* **2015**, *5*, 88339-88352.

[13] Lim, E.; Jo, C.; Lee, J. A mini review of designed mesoporous materials for energy-storage applications: from electric double-layer capacitors to hybrid supercapacitors. *Nanoscale* **2016**, *8*, 7827-7833.

[14] Ji, H.; Zhao, X.; Qiao, Z.; Jung, J.; Zhu, Y.; Lu, Y.; Zhang, L.L.; MacDonald, A.H.; Ruoff, R.S. Capacitance of carbon-based electrical double-layer capacitors. *Nat. Commun*. **2014**, *5*, 1-7.

[15] Simon, P.; Gogotsi, Y. Charge storage mechanism in nanoporous carbons and its consequence for electrical double layer capacitors. Philos. Trans. R. Soc. A: Mathematical, Physical and Engineering Sciences, **2010**, *368*, 3457-3467.

[16] Schütter, C.; Pohlmann, S.; Balducci, A. Industrial requirements of materials for electrical double layer capacitors: impact on current and future applications. *Adv. Energy Mater.* **2019**, *9*, 1900334.

[17] Wang, Y.; Song, Y.; Xia, Y. Electrochemical capacitors: mechanism, materials, systems, characterization and applications. *Chem. Soc. Rev.* **2016**, *45*, 5925-5950.

[18] Jost, K.; Dion, G.; Gogotsi, Y. Textile energy storage in perspective. *J. Mater. Chem. A* **2014**, *2*, 10776-10787.

[19] Lu, Q.; Chen, J.G.; Xiao, J.Q. Nanostructured electrodes for high-performance pseudocapacitors. *Angew. Chem. Int. Ed. 2013, 52*, 1882-1889.

[20] Muzaffar, A.; Ahamed, M.B.; Deshmukh, K.; Thirumalai, J. A review on recent advances in hybrid supercapacitors: Design, fabrication and applications. *Renew. Sustain. Energy Rev.* **2019**, *101*, 123-145.

[21] Chodankar, N.R.; Pham, H.D.; Nanjundan, A.K.; Fernando, J.F.; Jayaramulu, K.; Golberg, D.; Han, Y.K.; Dubal, D.P. True meaning of pseudocapacitors and their performance metrics: asymmetric versus hybrid supercapacitors. *Small* **2020**, *16*, 2002806.

[22] Chatterjee, D.P.; Nandi, A.K. A review on the recent advances in hybrid supercapacitors. *J. Mater. Chem. A* **2021**, *9*, 15880-15918.

[23] Zhou, Y.; Lachman, N.; Ghaffari, M.; Xu, H.; Bhattacharya, D.; Fattahi, P.; Abidian, M.R.; Wu, S.; Gleason, K.K.; Wardle, B.L.; Zhang, Q.M. A high performance hybrid asymmetric supercapacitor via nano-scale morphology control of graphene, conducting polymer, and carbon nanotube electrodes. *J. Mater. Chem. A* **2014**, *2*, 9964-9969.

[24] Choudhary, N., Li, C., Moore, J., Nagaiah, N., Zhai, L., Jung, Y.; Thomas, J. Asymmetric supercapacitor electrodes and devices. *Adv Mater.* **2017**, *29*, 1605336.

[25] Zhang, F.; Zhang, T.; Yang, X.; Zhang, L.; Leng, K.; Huang, Y.; Chen, Y., A high-performance supercapacitor-battery hybrid energy storage device based on graphene-enhanced electrode materials with ultrahigh energy density. *Energy Environ. Sci.* **2013**, *6*, 1623-1632.

[26] Zuo, W.; Li, R.; Zhou, C.; Li, Y.; Xia, J.; Liu, J. Battery-supercapacitor hybrid devices: recent progress and future prospects. *Adv. Sci.* **2017**, *4*, 1600539.

[27] Vlad, A.; Singh, N.; Rolland, J.; Melinte, S.; Ajayan, P.M.; Gohy, J.F. Hybrid supercapacitor-battery materials for fast electrochemical charge storage. *Sci. Rep.* **2014**, *4*, 1-7.

[28] Miao, L.; Song, Z.; Zhu, D.; Li, L,; Gan, L.; Liu, M. Recent advances in carbon-based supercapacitors. *Mater. Adv.* **2020**, *1*, 945-966.

[29] Shao, H.; Wu, Y.C.; Lin, Z.; Taberna, P.L.; Simon, P. Nanoporous carbon for electrochemical capacitive energy storage. *Chem. Soc. Rev.* **2020**, *49*, 3005-3039.

[30] Feng, H.P.; Tang, L.; Zeng, G.M.; Tang, J.; Deng, Y.C.; Yan, M.; Liu, Y.N.; Zhou, Y.Y.; Ren, X.Y.; Chen, S. Carbon-based core–shell nanostructured materials for electrochemical energy storage. *J. Mater. Chem. A* 2018, 6, 7310-7337.

[31] Simon, P.; Gogotsi, Y. Capacitive energy storage in nanostructured carbon–electrolyte systems. *Acc. Chem. Res.* 2013, 46, 1094-1103.

[32] Gogotsi, Y. Not just graphene: The wonderful world of carbon and related nanomaterials. *MRS Bull.* **2015**, *40*, 1110-1121.

[33] Gamby, J.; Taberna, P.L.; Simon, P.; Fauvarque, J.F.; Chesneau, M. Studies and characterisations of various activated carbons used for carbon/carbon supercapacitors. *J. Power Sources* **2001**, *101*, 109-116.

[34] Alslaibi, T.M.; Abustan, I.; Ahmad, M.A.; Foul, A.A. A review: production of activated carbon from agricultural byproducts via conventional and microwave heating. *J. Chem. Technol. Biotechnol.* **2013**, *88*, 1183-1190.

[35] Yin, J.; Zhang, W.; Alhebshi, N.A.; Salah, N.; Alshareef, H.N. Synthesis strategies of porous carbon for supercapacitor applications. *Small Methods* **2020**, *4*, 1900853.

[36] Obreja, V.V. On the performance of supercapacitors with electrodes based on carbon nanotubes and carbon activated material—a review. *Physica E Low Dimens. Syst. Nanostruct.* **2008,** *40*, 2596-2605.

[37] Allen, M.J.; Tung, V.C.; Kaner, R.B. Honeycomb carbon: a review of graphene. *Chem. Rev.* **2010**, *110*, 132-145.

[38] Xu, M.; Liang, T.; Shi, M.; Chen, H. Graphene-like two-dimensional materials. *Chem. Rev.* **2013**, *113*, 3766–3798.

[39] Kim, H.; Abdala, A.A.; Macosko, C.W. Graphene/polymer nanocomposites. *Macromolecules* **2010**, *43*, 6515–6530.

[40] Ghosh, D.; Giri, S.; Mandal, M.; Das, C.K. High performance supercapacitor electrode material based on vertically aligned PANI grown on reduced graphene oxide/$Ni(OH)_2$ hybrid composite. *RSC Adv.* **2014**, *4*, 26094–26101.

[41] Yoo, E.; Kim, J.; Hosono, E.; Zhou, H.S.; Kudo, T.; Honma, I. Large reversible Li storage of graphene nanosheet families for use in rechargeable lithium ion batteries. *Nano Lett*. **2008**, 8, 2277–2282.

[42] Sahoo, N.G.;; Pan, Y.; Li, L.; Chan, S.H. Graphene-based materials for energy conversion. *Adv. Mater.* **2012**, *24*, 4203–4210.

[43] Fowler, J.D.; Allen, M.J.; Tung, V.C.; Yang, Y.; Kaner, R.B.; Weiller, B.H. Practical chemical sensors from chemically derived graphene. *ACS Nano* **2009**, *3*, 301–306.

[44] Liu, M.; Yin, X.; Ulin-Avila, E.; Geng, B.; Zentgraf, T.; Ju, L.; Wang, F.; Zhang, X. A graphene-based broadband optical modulator. *Nature* **2011**, *474*, 64–67.

[45] Singh, V.; Joung, D.; Zhai, L.; Das, S.; Khondaker, S.I.; Seal, S. Graphene based materials: past, present and future. *Prog. Mater. Sci.* **2011**, *56*, 1178–1271.

[46] Novoselov, K.S.; Geim, A.K.; Morozov, S.V.; Jiang, D.E.; Zhang, Y.; Dubonos, S.V.; Grigorieva, I.V.; Firsov, A.A. Electric field effect in atomically thin carbon films. *Science* **2004**, *306*, 666–669.

[47] Stoller, M.D.; Park, S.; Zhu, Y.; An, J.; Ruoff, R.S. Graphene-based ultracapacitors. *Nano Lett.* **2008**, *8*, 3498-3502.

[48] Ai, W.; Cao, X.; Sun, Z.; Jiang, J.; Du, Z., Xie, L.; Wang, Y.; Wang, X.; Zhang, H.; Huang, W.; Yu, T. Redox-crosslinked graphene networks with enhanced electrochemical capacitance. *J. Mater. Chem. A* **2014**, *2*, 12924-12930.

[49] Peigney, A.; Laurent, C.; Flahaut, E.; Bacsa, R.R.; Rousset, A. Specific surface area of carbon nanotubes and bundles of carbon nanotubes. *Carbon* **2001**, *39*, 507-514.

[50] Hiraoka, T.; Izadi-Najafabadi, A.; Yamada, T.; Futaba, D.N.; Yasuda, S.; Tanaike, O.; Hatori, H.; Yumura, M.; Iijima, S.; Hata, K. Compact and light supercapacitor electrodes from a surface-only solid by opened carbon nanotubes with 2200 $m^2 g^{-1}$ surface area. *Adv. Funct. Mater.* **2010**, *20*, 422-428.

[51] Pan, H.; Li, J.; Feng, Y. Carbon nanotubes for supercapacitor. *Nanoscale Res. Lett.* **2010**, *5*, 654-668.

[52] Jiang, Y.; Liu, J. Definitions of pseudocapacitive materials: a brief review. *Energy Environ. Mater.* **2019**, *2*, 30-37.

[53] Choi, C.; Ashby, D.S.; Butts, D.M.; DeBlock, R.H.; Wei, Q.; Lau, J.; Dunn, B. Achieving high energy density and high power density with pseudocapacitive materials. *Nat. Rev. Mater.* **2020**, *5*, 5-19.

[54] Augustyn, V.; Simon, P.; Dunn, B. Pseudocapacitive oxide materials for high-rate electrochemical energy storage. *Energy Environ. Sci.* **2014**, *7*, 1597-1614.

[55] Shi, F.; Li, L.; Wang, X.L.; Gu, C.D.; Tu, J.P. Metal oxide/hydroxide-based materials for supercapacitors. *RSC Adv.* **2014**, *4*, 41910-41921.

[56] Faraji, S.; Ani, F.N. Microwave-assisted synthesis of metal oxide/hydroxide composite electrodes for high power supercapacitors–a review. *J. Power Sources* **2014**, *263*, 338-360.

[57] Abdah, M.A.A.M.; Azman, N.H.N.; Kulandaivalu, S.; Sulaiman, Y. Review of the use of transition-metal-oxide and conducting polymer-based fibres for high-performance supercapacitors. *Mater. Des.* **2020**, *186*, 108199.

[58] Brousse, T.; Bélanger, D.; Long, J.W. To be or not to be pseudocapacitive?. *J. Electrochem. Soc.* **2015**, *162*, A5185.

[59] Zheng, J.P.; Cygan, P.J.; Jow, T.R. Hydrous ruthenium oxide as an electrode material for electrochemical capacitors. *J. Electrochem. Soc.* **1995**, *142*, 2699.

[60] Huang, M.; Li, F.; Dong, F.; Zhang, Y.X.; Zhang, L.L. MnO 2-based nanostructures for high-performance supercapacitors. *J. Mater. Chem. A* **2015**, *3*, 21380-21423.

[61] Dubal, D.P.; Dhawale, D.S.; Salunkhe, R.R.; Pawar, S.M.; Lokhande, C.D. A novel chemical synthesis and characterization of $Mn_3O_4$ thin films for supercapacitor application. *Appl. Surf. Sci.* **2010**, *256*, 4411-4416.

[62] Kim, S.I.; Lee, J.S.; Ahn, H.J.; Song, H.K.; Jang, J.H. Facile route to an efficient NiO supercapacitor with a three-dimensional nanonetwork morphology. *ACS Appl. Mater. Interfaces* **2013**, *5*, 1596-1603.

[63] Xia, X. H.; Tu, J. P.; Mai, Y. J.; Wang, X. L.; Gu, C. D.; Zhao, X. B. Self-supported hydrothermal synthesized hollow $Co_3O_4$ nanowire arrays with high supercapacitor capacitance. *J. Mater. Chem.* **2011**, *21*, 9319-9325.

[64] Khalid, S.; Khan, Y.; Ahmed, E.; Nawaz, S.; Khalid, N.R.; Ahmed, W. Transition metal sulfides for supercapacitors. in '*Emerging Nanotechnologies for Renewable Energy*' **2021**, 407-445, Elsevier.

[65] Barik, R.; Ingole, P.P. Challenges and prospects of metal sulfide materials for supercapacitors. *Curr. Opin. Electrochem.* **2020**, *21*, 327-334.

[66] Naveenkumar, P.; Kalaignan, G.P. Electrodeposited MnS on graphene wrapped Ni-Foam for enhanced supercapacitor applications. *Electrochim. Acta* **2018**, *289*, 437-447.

[67] Kumbhar, V.S.; Lee, Y.R.; Ra, C.S.; Tuma, D.; Min, B.K.; Shim, J.J. Modified chemical synthesis of MnS nanoclusters on nickel foam for high performance all-solid-state asymmetric supercapacitors. *RSC Adv.* **2017**, *7*, 16348-16359.

[68] Chen, T.; Tang, Y.; Qiao, Y.; Liu, Z.; Guo, W.; Song, J.; Mu, S.; Yu, S.; Zhao, Y.; Gao, F. All-solid-state high performance asymmetric supercapacitors based on novel MnS nanocrystal and activated carbon materials. *Sci. Rep.* **2016**, 6, 23289.

[69] Shi, J.; Li, X.; He, G.; Zhang, L.; Li, M. Electrodeposition of high-capacitance 3D CoS/graphene nanosheets on nickel foam for high-performance aqueous asymmetric supercapacitors. *J. Mater. Chem. A* **2015**, *3*, 20619-20626.

[70] Lin, J.Y.; Chou, S.W. Cathodic deposition of interlaced nanosheet-like cobalt sulfide films for high-performance supercapacitors. *RSC Adv.* **2013**, *3*, 2043-2048.

[71] Sahoo, S.; Shim, J.J. Room-temperature synthesis of NiS hollow spheres on nickel foam for high-performance supercapacitor electrodes. *Mater. Lett.* **2018**, *210*, 105-108.

[72] Yu, L.; Yang, B.; Liu, Q.; Liu, J.; Wang, X.; Song, D.; Wang, J.; Jing, X. Interconnected NiS nanosheets supported by nickel foam: soaking fabrication and supercapacitors application. *J. Electroanal. Chem.* **2015**, *739*, 156-163.

[73] Ahmed, N.; Ali, B.A.; Ramadan, M.; Allam, N.K. Three-Dimensional Interconnected Binder-Free Mn–Ni–S Nanosheets for High Performance Asymmetric Supercapacitor Devices with Exceptional Cyclic Stability. *ACS Appl. Energy Mater.* **2019**, *2*, 3717-3725.

[74] Khalafallah, D.; Wu, Z.; Zhi, M.; Hong, Z. Rational Design of Porous Structured Nickel Manganese Sulfides Hexagonal Sheets-in-Cage Structures as an Advanced Electrode Material for High-Performance Electrochemical Capacitors. *Chem. Euro. J.* **2020**, *26*, 2251-2262.

[75] Cheng, C.; Kong, D.; Wei, C.; Du, W.; Zhao, J.; Feng, Y.; Duan, Q. Self-template synthesis of hollow ellipsoid Ni−Mn sulfides for supercapacitors, electrocatalytic oxidation of glucose and water treatment. *Dalton Trans.* **2017**, *46*, 5406-5413.

[76] Meng, Y.; Sun, P.; He, W.; Teng, B.; Xu, X. Uniform P doped Co–Ni–S nanostructures for asymmetric supercapacitors with ultra-high energy densities. *Nanoscale* **2019**, *11*, 688-697.

[77] Meng, Y.; Sun, P.; He, W.; Teng, B.; Xu, X. Construction of hierarchical Co-Ni-S nanosheets as free-standing electrode for superior-performance asymmetric supercapacitors. *Appl. Surf. Sci.* **2019**, *470*, 792-799.

[78] Yang, J.; Yu, C.; Fan, X.; Liang, S.; Li, S.; Huang, H.; Ling, Z.; Hao, C.; Qiu, J. Electroactive edge site-enriched nickel–cobalt sulfide into graphene frameworks for high-performance asymmetric supercapacitors. *Energy Environ. Sci.* **2016**, *9*, 1299-1307.

[79] Chen, W.; Xia, C.; Alshareef, H.N. One-step electrodeposited nickel cobalt sulfide nanosheet arrays for high-performance asymmetric supercapacitors. *ACS Nano* **2014**, *8*, 9531-9541.

[80] Wang, F.; Zhou, K.; Zheng, J.; Ma, J. Rapid synthesis of porous manganese cobalt sulfide grown on Ni foam by microwave method for high performance supercapacitors. *Synth. Met.* **2019**, *256*, 116113.

[81] Li, G.; Chang, Z.; Li, T.; Ma, L.; Wang, K. Hierarchical Mn-Co sulfide nanosheets on nickel foam by electrochemical co-deposition for high-performance pseudocapacitors. *Ionics* **2019**, *25*, 3885-3895.

[82] Zhao, Y.; Shi, Z.; Li, H.; Wang, C.A. Designing pinecone-like and hierarchical manganese cobalt sulfides for advanced supercapacitor electrodes. *J. Mater. Chem. A* **2018**, *6*, 12782-12793.

[83] Liu, S.; Jun, S.C. Hierarchical manganese cobalt sulfide core–shell nanostructures for high-performance asymmetric supercapacitors. *J. Power Sources* **2017**, *342*, 629-637.

[84] Theerthagiri, J.;, Karuppasamy, K.; Durai, G.; Rana, A.U.H.S.; Arunachalam, P.; Sangeetha, K.; Kuppusami, P.; Kim, H.S. Recent advances in metal chalcogenides (MX; X= S, Se) nanostructures for electrochemical supercapacitor applications: a brief review. *Nanomaterials* **2018**, *8*, 256.

[85] Shi, Y.; Peng, L.; Ding, Y.; Zhao, Y.; Yu, G. Nanostructured conductive polymers for advanced energy storage. *Chem. Soc. Rev.* **2015**, *44*, 6684-6696.

[86] Snook, G.A.; Kao, P.; Best, A.S. Conducting-polymer-based supercapacitor devices and electrodes. *J Power Sources* **2011**, *196*, 1-12.

[87] Borenstein, A.; Hanna, O.; Attias, R.; Luski, S.; Brousse, T.; Aurbach, D. Carbon-based composite materials for supercapacitor electrodes: a review. *J. Mater. Chem. A*, **2017**, *5*, 12653-12672.

[88] He, Y.; Chen, W.; Li, X.; Zhang, Z.; Fu, J.; Zhao, C.; Xie, E., Freestanding three-dimensional graphene/$MnO_2$ composite networks as ultralight and flexible supercapacitor electrodes. *ACS Nano* **2013**, *7*, 174-182.

[89] Jin, Y.; Chen, H.; Chen, M.; Liu, N.; Li, Q. Graphene-patched CNT/$MnO_2$ nanocomposite papers for the electrode of high-performance flexible asymmetric supercapacitors. *ACS Appl. Mater. Interfaces* **2013**, *5*, 3408-3416.

[90] Wang, L.; Ouyang, Y.; Jiao, X.; Xia, X.; Lei, W.; Hao, Q. Polyaniline-assisted growth of $MnO_2$ ultrathin nanosheets on graphene and porous graphene for asymmetric supercapacitor with enhanced energy density. *Chem. Eng. J.* **2018**, *334*, 1-9.

[91] Xia, L.; Yu, L.; Hu, D.; Chen, G.Z., Electrolytes for electrochemical energy storage. *Mater. Chem. Front.* **2017**, *1*, 584-618.

[92] Zhong, C.; Deng, Y.; Hu, W.; Qiao, J.; Zhang, L.; Zhang, J. A review of electrolyte materials and compositions for electrochemical supercapacitors. *Chem. Soc. Rev.* **2015**, *44*, 7484-7539.

[93] Aldama, I.; Barranco, V.; Kunowsky, M.; Ibañez, J.; Rojo, J.M. Contribution of cations and anions of aqueous electrolytes to the charge stored at the electric electrolyte/electrode interface of carbon-based supercapacitors. *J. Phys. Chem. C* **2017**, *121*, 12053-12062.

[94] Qin, W.; Zhou, N.; Wu, C.; Xie, M.; Sun, H.; Guo, Y.; Pan, L. Mini-review on the redox additives in aqueous electrolyte for high performance supercapacitors. *ACS Omega* **2020**, *5*, 3801-3808.

[95] Krummacher, J.; Schütter, C.; Hess, L.H.; Balducci, A. Non-aqueous electrolytes for electrochemical capacitors. *Curr. Opin. Electrochem.* **2018**, *9*, 64-69.

[96] Verma, K.D.; Sinha, P.; Banerjee, S.; Kar, K.K.; Ghorai, M.K. Characteristics of separator materials for supercapacitors. in '*Handbook of Nanocomposite Supercapacitor Materials I*' **2020**, 315-326, Springer, Cham.

[97] Zhang, Y.Z.; Wang, Y.; Cheng, T.; Yao, L.Q.; Li, X.; Lai, W.Y.; Huang, W. Printed supercapacitors: materials, printing and applications. Chem. Soc. Rev. 2019, 48, 3229-3264.

[98] Nigam R.; Verma K.D.; Pal T.; Kar K.K. Applications of Supercapacitors. in '*Handbook of Nanocomposite Supercapacitor Materials II*' **2020**, *302*, Springer, Cham.

[99] Gan, Y.X.; Jayatissa, A.H.; Yu, Z.; Chen, X.; Li, M. Hydrothermal synthesis of nanomaterials. *J. Nanomater.* **2020**, *2020*.

[100] Cartwright, P.F.S.; Newman, E.J.; Wilson, D.W. Precipitation from homogeneous solution. A review. *Analyst* **1967**, *92*, 663-679.

[101] Guo, J.K.; Li, J.; Kou, H.M. Advanced ceramic materials. in *Modern Inorganic Synthetic Chemistry*' **2017**, 463-492, Elsevier.

[102] Park, S.H.; Son, J.G.; Lee, T.G.; Park, H.M.; ong Song, J. One-step large-scale synthesis of micrometer-sized silver nanosheets by a template-free electrochemical method. *Nanoscale Res. Lett.* **2013**, *8*, 248.

[103] Wang, N.; Sun, B.; Zhao, P.; Yao, M.; Hu, W.; Komarneni, S. Electrodeposition preparation of $NiCo_2O_4$ mesoporous film on ultrafine nickel wire for flexible asymmetric supercapacitors. *Chem. Eng. J.* **2018**, *345*, 31-38.

[104] Wu, S.; Guo, H.; San Hui, K.; Hui, K.N. Rational design of integrated $CuO@Co_xNi_{1-x}(OH)_2$ nanowire arrays on copper foam for high-rate and long-life supercapacitors. *Electrochim. Acta* **2019**, *295*, 759-768.

[105] Asen, P.; Shahrokhian, S. One step electrodeposition of $V_2O_5$/polypyrrole/graphene oxide ternary nanocomposite for preparation of a high performance supercapacitor. *Int. J. Hydrogen Energy* **2017**, *42*, 21073-21085.

[106] Sahoo, S.; Naik, K.K.; Rout, C.S. Electrodeposition of spinel $MnCo_2O_4$ nanosheets for supercapacitor applications. *Nanotechnology* **2015**, *26*, 455401.

[107] Zhao, N.; Fan, H.; Zhang, M.; Ma, J.; Du, Z.; Yan, B.; Li, H.; Jiang, X. Simple electrodeposition of $MoO_3$ film on carbon cloth for high-performance aqueous symmetric supercapacitors. *Chem. Eng. J.* **2020**, *390*, 124477.

[108] Ye, Z.; Li, T.; Ma, G.; Peng, X.; Zhao, J. Morphology controlled $MnO_2$ electrodeposited on carbon fiber paper for high-performance supercapacitors. *J. Power Sources* **2017**, *351*, 51-57.

[109] Conway, B.E. Electrochemical supercapacitors: scientific fundamentals and technological applications. *Springer Science & Business Media* **2013**.

[110] Sakita, A.M.; Della Noce, R.; Lavall, R.L. Potential-dependent electrochemical impedance spectroscopy as a powerful tool for evaluating supercapacitor electrode performance. *J. Electrochem. Soc.* **2021**. *168*, 080525.

[111] Epp, J. X-ray diffraction (XRD) techniques for materials characterization. in '*Materials characterization using nondestructive evaluation (NDE) methods*' 2016, 81-124, Woodhead Publishing.

[112] Dutta, A. Fourier transform infrared spectroscopy. in '*Spectroscopic methods for nanomaterials characterization*' **2017**, 73-93, Elsevier.

[113] Kumar, C.S. ed. Raman spectroscopy for nanomaterials characterization. *Springer Science & Business Media* **2012**.

[114] Shard, A.G. X-ray photoelectron spectroscopy. in '*Characterization of Nanoparticles*' **2020**, 349-371, Elsevier.

[115] Wang, J.G.; Kang, F.; Wei, B. Engineering of $MnO_2$-based nanocomposites for high-performance supercapacitors. *Prog. Mater Sci.* **2015**, *74*, 51-124.

[116] Hu, Y.; Zhang, Y.; Yuan, D.; Li, X.; Cai, Y.; Wang, J. Controllable structure transitions of $Mn_3O_4$ nanomaterials and their effects on electrochemical properties. *Nanoscale Horiz.* **2017**, *2*, 326-332.

[117] Raj, B.G.S.; Asiri, A.M.; Wu, J.J.; Anandan, S. Synthesis of $Mn_3O_4$ nanoparticles via chemical precipitation approach for supercapacitor application. *J Alloys Compd*, **2015**, *636*, 234-240.

[118] Luo, Y.; Yang, T.; Li, Z.; Xiao, B.; Zhang, M. High performance of $Mn_3O_4$ cubes for supercapacitor applications. *Mater. Lett.* **2016**, *178*, 171-174.

[119] Li, B.; Zhang, X.; Dou, J.; Hu, C. Facile synthesis of pseudocapacitive $Mn_3O_4$ nanoparticles for high-performance supercapacitor. *Ceram. Int.* **2019**, *45*, 16297-16304.

[120] Qi, Z.; Younis, A.; Chu, D.; Li, S. A facile and template-free one-pot synthesis of $Mn_3O_4$ nanostructures as electrochemical supercapacitors. *Nano-Micro Lett.* **2016**, *8*, 165-173.

[121] Wei, W.; Cui, X.; Chen, W.; Ivey, D.G. Manganese oxide-based materials as electrochemical supercapacitor electrodes. *Chem. Soc. Rev*. **2011**, *40*, 1697-1721.

[122] Cui, X.; Hu, F.; Wei, W.; Chen, W. Dense and long carbon nanotube arrays decorated with $Mn_3O_4$ nanoparticles for electrodes of electrochemical supercapacitors. *Carbon* **2011**, *49*, 1225-1234.

[123] Poon, R.; Zhitomirsky, I. High areal capacitance of $Mn_3O_4$-carbon nanotube electrodes. *Mater. Lett.* **2018**, *215*, 4-7.

[124] Hiremath, V.; Cho, M.; Seo, J.G. Self-assembled $Mn_3O_4$ nano-clusters over carbon nanotube threads with enhanced supercapacitor performance. *New J. Chem.* **2018**, *42*, 19608-19614.

[125] Hu, Y.; Guan, C.; Feng, G.; Ke, Q.; Huang, X.; Wang, J. Flexible asymmetric supercapacitor based on structure-optimized $Mn_3O_4$/reduced graphene oxide nanohybrid paper with high energy and power density. *Adv. Funct. Mater.* **2015**, *25*, 7291-7299.

[126] Xiao, Y.; Cao, Y.; Gong, Y.; Zhang, A.; Zhao, J.; Fang, S.; Jia, D.; Li, F. Electrolyte and composition effects on the performances of asymmetric

supercapacitors constructed with $Mn_3O_4$ nanoparticles–graphene nanocomposites. *J. Power Sources* **2014**, *246*, 926-933.

[127] Toupin, M.; Brousse, T.; Bélanger, D. Charge storage mechanism of $MnO_2$ electrode used in aqueous electrochemical capacitor. *Chem. Mater.* **2004**, *16*, 3184-3190.

[128] Wu, C.; Zhu, Y.; Ding, M.; Jia, C.; Zhang, K. Fabrication of plate-like $MnO_2$ with excellent cycle stability for supercapacitor electrodes. *Electrochim Acta,* **2018**, *291*, 249-255.

[129] Xia, A.; Yu, W.; Yi, J.; Tan, G.; Ren, H.; Liu, C. Synthesis of porous δ-$MnO_2$ nanosheets and their supercapacitor performance. *J. Electroanal. Chem.* **2019**, *839*, 25-31.

[130] Ye, J.; Li, Z.; Dai, Z.; Zhang, Z.; Guo, M.; Wang, X. Facile synthesis of hierarchical CuO nanoflower for supercapacitor electrodes. *J. Electronic Mater.* **2016**, *45*, 4237-4245.

[131] Shinde, S.K.; Yadav, H.M.; Ghodake, G.S.; Kadam, A.A.; Kumbhar, V.S.; Yang, J.; Hwang, K.; Jagadale, A.D.; Kumar, S.; Kim, D.Y. Using chemical bath deposition to create nanosheet-like CuO electrodes for supercapacitor applications. *Colloids Surf. B: Biointerfaces* **2019**, *181*, 1004-1011.

[132] Zhang, Y.X.; Li, F.; Huang, M. One-step hydrothermal synthesis of hierarchical $MnO_2$-coated CuO flower-like nanostructures with enhanced electrochemical properties for supercapacitor. *Mater. Lett.* **2013**, *112*, 203-206.

[133] Huang, M.; Zhang, Y.; Li, F.; Zhang, L.; Ruoff, R.S.; Wen, Z.; Liu, Q. Self-assembly of mesoporous nanotubes assembled from interwoven ultrathin birnessite-type $MnO_2$ nanosheets for asymmetric supercapacitors. *Sci. Rep.* **2014**, *4*, 1-8.

[134] Zhang, Z.; Ma, C.; Huang, M.; Li, F.; Zhu, S.; Hua, C.; Yu, L.; Zheng, H.; Hu, X.; Zhang, Y. Birnessite $MnO_2$-decorated hollow dandelion-like CuO architectures for supercapacitor electrodes. *J. Mater. Sci.: Mater. Electron.* **2015**, 26, 4212-4220.

[135] Li, Y.; Cao, L.; Qiao, L.; Zhou, M.; Yang, Y.; Xiao, P.; Zhang, Y. Ni–Co sulfide nanowires on nickel foam with ultrahigh capacitance for asymmetric supercapacitors. *J.Mater. Chem. A* **2014**, *2*, 6540-6548.

[136] Rani, B.J.; Yuvakkumar, R.; Ravi, G.; Kumar, P.; Babu, E.S.; Saravanakumar, B.; Velauthapillai, D. High performance $MnSn(OH)_6$ electrodes for energy conversion application. *Mater. Lett.* **2021**, *282*, 128888.

[137] Chen, Y.; Zhou, C.; Liu, G.; Kang, C.; Ma, L.; Liu, Q. Hydroxide ion dependent α-$MnO_2$ enhanced via oxygen vacancies as the negative electrode for high-performance supercapacitors. *J. Mater. Chem. A* **2021**, *9*, 2872-2887.

[138] Feng, J.X.; Ye, S.H.; Lu, X.F.; Tong, Y.X.; Li, G.R. Asymmetric paper supercapacitor based on amorphous porous $Mn_3O_4$ negative electrode and $Ni(OH)_2$ positive electrode: a novel and high-performance flexible electrochemical energy storage device. *ACS Appl. Mater. Interfaces* **2015**, *7*, 11444-11451.

[139] Liang, X.; Xue, D. $Ce(OH)_3$ as a novel negative electrode material for supercapacitors. *Nanotechnology* **2020**, *31*, 374003.

[140] Pang, H.; Zhang, Y.; Cheng, T.; Lai, W.Y.; Huang, W. Uniform manganese hexacyanoferrate hydrate nanocubes featuring superior performance for low-cost

supercapacitors and nonenzymatic electrochemical sensors. *Nanoscale* **2015**, *7*, 16012-16019.

[141] Chen, J.; Huang, K.; Liu, S.; Hu, X. Electrochemical supercapacitor behavior of $Ni_3(Fe(CN)_6)_2.(H_2O)$ nanoparticles. *J. Power Sources* **2009**, *186*, 565-569.

[142] Wang, J.G.; Zhang, Z.; Zhang, X.; Yin, X.; Li, X.; Liu, X.; Kang, F.; Wei, B. Cation exchange formation of prussian blue analogue submicroboxes for high-performance Na-ion hybrid supercapacitors. *Nano Energy* **2017**, *39*, 647-653.

[143] Zhou, Q.; Wei, T.; Liu, Z.; Zhang, L.; Yuan, B.; Fan, Z. Nickel hexacyanoferrate on graphene sheets for high-performance asymmetric supercapacitors in neutral aqueous electrolyte. *Electrochim. Acta* **2019**, *303*, 40-48.

# Chapter II

*Asymmetric supercapacitor based on $Mn_3O_4$-MWCNT composite and rGO Electrode*

## II.1 Introduction

A sustainable and renewable energy resource is required as an alternative to fit the worlds expanding energy need without causing any environmental detriment [1, 2]. Electrochemical capacitors also known as supercapacitors (SC) have drawn tremendous attention with great potential application in energy storage systems for portable electronic devices and hybrid electric vehicles due to its unique properties of high power density, long cycle life, low maintenance cost and green environmental protection [3, 4]. Although, SC delivers very high power density (~10 to $10^4$ $W{\cdot}kg^{-1}$), it suffers from lower energy density (~0.2 to 10 $Wh{\cdot}kg^{-1}$) compared to the conventional batteries (~10 to 200 $Wh{\cdot}kg^{-1}$) [5]. The energy density (E) is related with the operating voltage (V) and capacitance according to the following equation: $E = 0.5CV^2$.

To achieve high energy density along with high power density and long cycle life, a great effort has been devoted to develop asymmetric supercapacitors (ASCs) by combining a battery like Faradaic electrode (as energy source) and a capacitive electrode (as power source) [6]. So far, various redox active metal oxides or hydroxides such as $Mn_3O_4$, $Fe_3O_4$, $Co_3O_4$, $Co(OH)_2$, $Ni(OH)_2$ and their composites with carbonaceous materials like graphene or/and carbon nanotubes have been well investigated as supercapacitor active material [7-12].

The manganese based material like $Mn_3O_4$ can be considered as one of the most promising electrode materials because of its low cost and environmental compatibility accompanied with high pseudocapacitance [13]. However, the

poor electrical conductivity often results in low rate capability in these metal oxides. In this context an increase in electrical conductivity of the pseudocapacitive metal oxides can be obtained by formation of nanocomposites with various carbonaceous materials which are highly conductive in nature.

Recently, activated carbon (AC) is extensively used for the capacitive electrode of ASCs due to its high specific surface area and moderate cost. However, it suffers from small pore diameter (0.5 nm), which is not accessible to hydrate ions (0.6-0.76 nm) resulting in a poor capacitive performance [14, 15]. In order to minimize above mentioned problem reduced graphene oxide (rGO) nanosheets was employed instead of AC. Nowadays, rGO has attracted extensive attention in the energy research due to its unique properties such as flexible porous structure with its mesopores and microspores, high surface area, high conductivity, high energy density, and good electrochemical stability [6, 11, 16].

Here, we report a simple hydrothermal method for the synthesis of $Mn_3O_4$@multi-wall carbon nanotube ($Mn_3O_4$@MWCNT) composite as supercapacitor electrode material with improved rate capability. To obtain an improved cell voltage in aqueous electrolyte an aqueous asymmetric supercapacitor was constructed by combining $Mn_3O_4$@MWCNT and rGO as positive and negative electrode, respectively, which was able to give high cell voltage of 1.6 V resulting in high energy density of 26.8 Wh/kg.

## II.2 Experimental Section

### *II.2.1 Materials*

All materials were used during experiment without further purification. $MnCl_2.4H_2O$, graphite powder, $H_2O_2$ were obtained from Loba chemie, Mumbai. MWCNT was obtained from Iljin Nano Technology, Korea, (95% purity and 15–35 nm diameter). $H_2SO_4$, ortho phosphoric acid, Ethanolamine, ethanol and acetone were bought from E. Merck Ltd. India.

### *II.2.2 Preparation of pure $Mn_3O_4$ and $Mn_3O_4$@MWCNT composite*

A simple and cost effective hydrothermal method was carried out by using $MnCl_2.4H_2O$ as metal precursor and ethanolamine (EA) as hydrolysing agent for the synthesis of $Mn_3O_4$. For the synthesis of $Mn_3O_4$@MWCNT composite, the hydrothermal reaction was carried out in presence of dispersed MWCNTs. Briefly, 30 mg MWCNTs were taken in 20 mL water and ultrasonicated for 45 min. Then the dispersed MWCNTs were poured in 20 mL 0.1 M aqueous solution of $MnCl_2.4H_2O$ and the whole mixture were again ultrasonicated for 15 min. Then ethanolamine (0.4 mL) was slowly added dropwise into the solution mixture under vigorous stirring condition. The whole solution mixture was transferred into a 50 mL autoclave and kept in muffle furnace for 6 h at 180 °C. The greenish black precipitate was washed with water and ethanol mixture for 4-5 times and dried at 70 °C. The pure $Mn_3O_4$ was prepared by following the same procedure without the addition of MWCNT.

### *II.2.3 Preparation of rGO*

Reduced graphene oxide was prepared by the hydrothermal reduction of graphene oxide in presence of ascorbic acid. Graphene oxide was prepared by modified Hummers' method [17]. Briefly, 1 g of commercially available fine graphite powder was dispersed in a mixture of conc. $H_2SO_4$ (120 mL) and ortho phosphoric acid (13.3 mL). Then 6 g $KMnO_4$ was added pinch by pinch to avoid excess heating. After 12 h stirring, the whole mixture was poured slowly in a mixture of 30% $H_2O_2$ (1.5 mL) in ice water. The GO powder was collected after washing the solid material in succession with 10% HCl, water and ethanol. Reduced graphene oxide (rGO) was prepared by the reduction of as prepared GO with ascorbic acid. 50 mg GO with 50 mg L-ascorbic acid was ultrasonicated in 40 mL $H_2O$ for 30 min. Then the mixture solution was transferred into a 50 mL Teflon autoclave and was kept in muffle furnace at 180 °C for 6 h. The product was washed with water and ethanol mixture and dried at 60 °C.

## II.3 Results and Discussion

Ethanolamine, an organic solvent have been extensively used for the synthesis of a variety type nanostructured metal oxides such as $Mn_3O_4$, $Fe_3O_4$, $Co_3O_4$, SnO etc. as a hydrolyzing agent [8, 18-20]. The schematic presentation of the formation of $Mn_3O_4$@MWCNT composite is shown in Scheme II.1. The $Mn_3O_4$ nanoparticles were formed via a Mn-EA complex formation (Scheme II.1b) [21]. Similarly, the composite with MWCNT followed the same mechanism where the MWCNT served as a template.

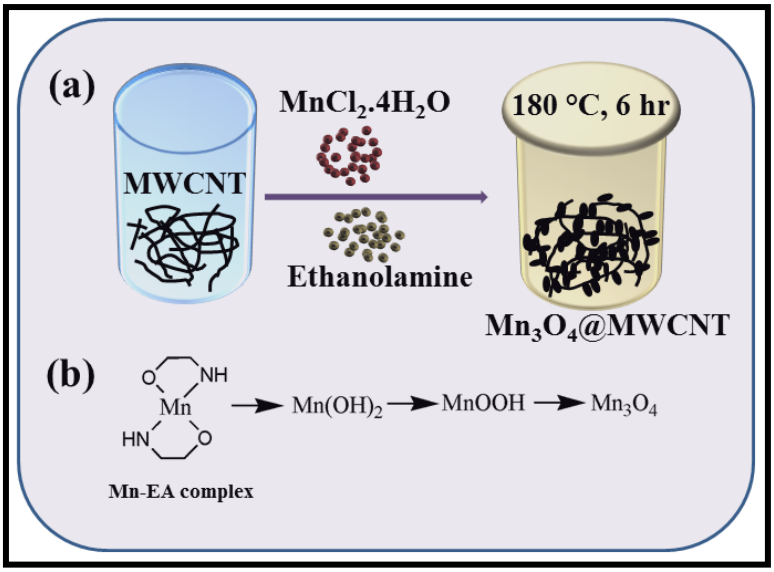


**Scheme II.1** (a) The schematic diagram of the synthesis of composite; (b) The mechanism of the formation of $Mn_3O_4$ nanoparticles.

The as prepared materials were characterized by X-Ray Diffraction (XRD) analysis, Fourier Transform Infrared (FTIR) spectroscopy, Raman Spectroscopy study, X-Ray Photoelectron Spectroscopy (XPS), Field-Emission Scanning Electron Microscope (FESEM) and Transmission Electron Microscope (TEM) for structural, chemical composition and morphological determination. The surface area of the material was determined by $N_2$ adsorption-desorption isotherm. The electrochemical behavior was analyzed in terms of cyclic voltammetry (CV), galvanostatic charge-discharge (GCD) curve and electrochemical impedance spectra (EIS).

### *II.3.1 XRD analysis*

The X-ray diffraction analysis was carried out using the Rigaku ULTIMA-III X-ray diffractometer with Cu Kα radiation (λ = 1.548 Å). The XRD pattern of $Mn_3O_4$ and $Mn_3O_4$@MWCNT composite is shown in Figure II.1a. The diffraction pattern of $Mn_3O_4$ is well matched with the JCPDS card no. 04-007-1841. The peaks at 2θ =

18.01, 28.91, 30.99, 32.38, 36.08, 38.09, 44.40, 49.89, 53.86, 56.02, 59.9 and 64.61 degree are corresponding to the plane of (101), (112), (200), (103), (211), (004), (220), (204), (312), (303), (224) and (314), respectively. All the peaks are also present in $Mn_3O_4$@MWCNT composite with an extra peak at 2θ = 26 which attributes for the characteristic (002) plane of MWCNT [22]. Figure II.2a shows the XRD pattern of GO and rGO. For GO, the characteristics peak of (002) plane of GO arises at 2θ = 10.2° which is missing in rGO indicating the successful reduction of GO.

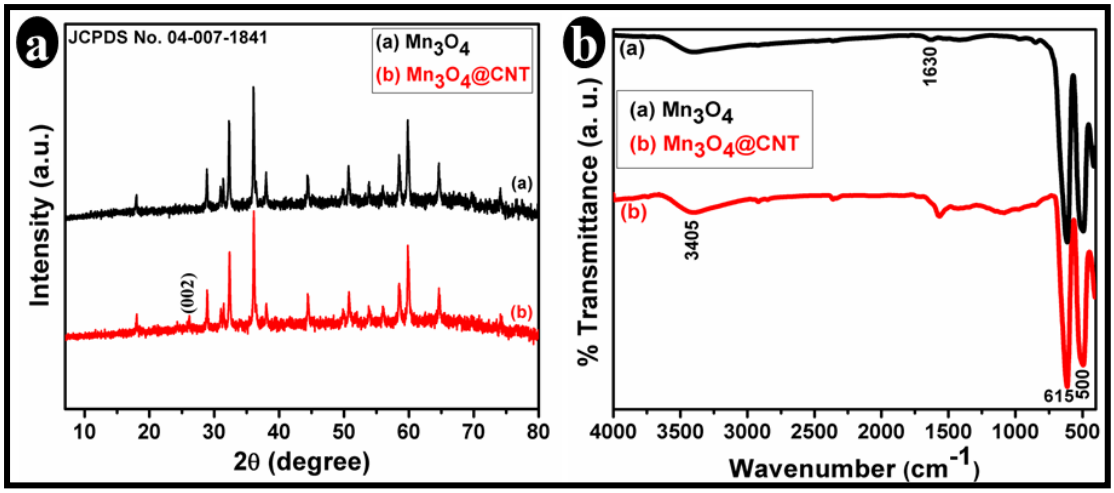


**Figure II.1** (a) XRD pattern, and (b) FTIR spectra of pure $Mn_3O_4$ and $Mn_3O_4$@MWCNT composite.

### *II.3.2 FTIR analysis*

The chemical compositions of as prepared materials were also confirmed by FTIR analyses, which are shown in Figure II.1b. For this characterization dish-shaped pellet was prepared first from as-prepared powder samples and then the analysis was done using NEXUS 870 FTIR (Thermo Nicolet) instrument. The stretching frequency at 615 and 500 $cm^{-1}$ indicate the stretching modes of tetrahedral and octahedral sites of $Mn_3O_4$ [23, 24]. The peak at 3405 $cm^{-1}$ attributes the presence of physisorbed water

molecule in the materials. The -C=C- stretching frequency of MWCNT arises at 1564 $cm^{-1}$ in composite spectrum along with other peaks of $Mn_3O_4$ [25]. Figure II.2b shows the FTIR spectra of GO and rGO. The obtained peaks for GO is well-matched with the literature. The peaks at 1726, 1623, 1400, 1232 and 1049 $cm^{-1}$ are attributed for C=O (carboxyl/carbonyl), C=C (aromatic), C-O (carboxy), C-O (epoxy) and C-O (alkoxy), respectively [26, 28]. In case of rGO almost all peaks were diminished indicating successful reduction with large extent.

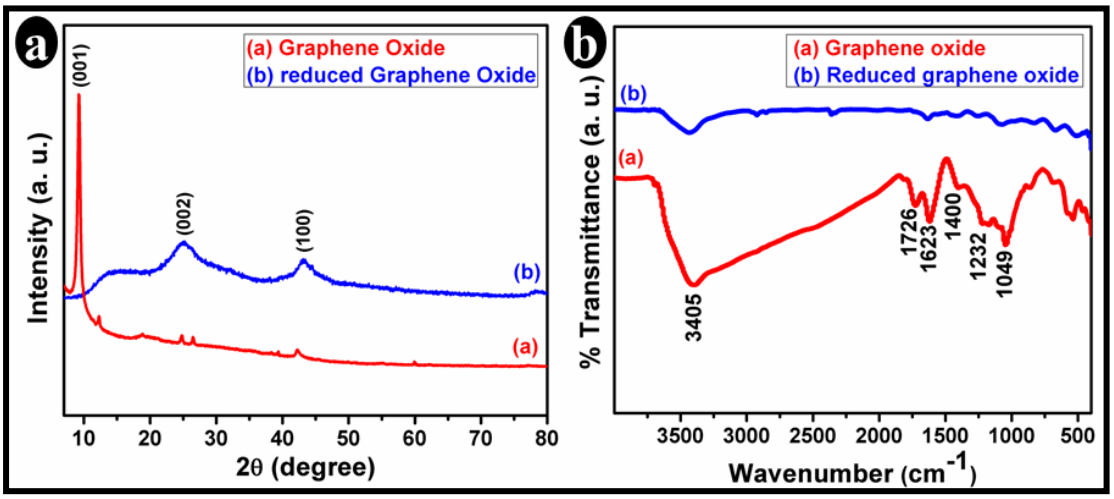


**Figure II.2** (a) XRD pattern, and (a) FTIR spectra of GO and rGO.

### *II.3.3 Raman study*

The Raman spectroscopy also confirms the successful formation of the $Mn_3O_4$@MWCNT composite which was carried out at an excitation wave length of 488 nm. All the peaks (Figure II.3a) observed at 289, 316, 372, 478, and 657 $cm^{-1}$ confirms the crystalline $Mn_3O_4$ nanoparticles in the composite [29, 30]. The most intense peak at 657 $cm^{-1}$, is considered as the characteristic peak for spinel $Mn_3O_4$ having $A_g$ symmetry, which appears due to the interior movement of oxygen in the octahedral unit $MnO_6$. The peaks at 1334 and 1599 $cm^{-1}$ can be attributed to the D

and G band of MWCNT [31-32]. The D band is mainly originated from the structural defects on surface of MWCNT and G band stands for the $E_{2g}$ graphite mode.

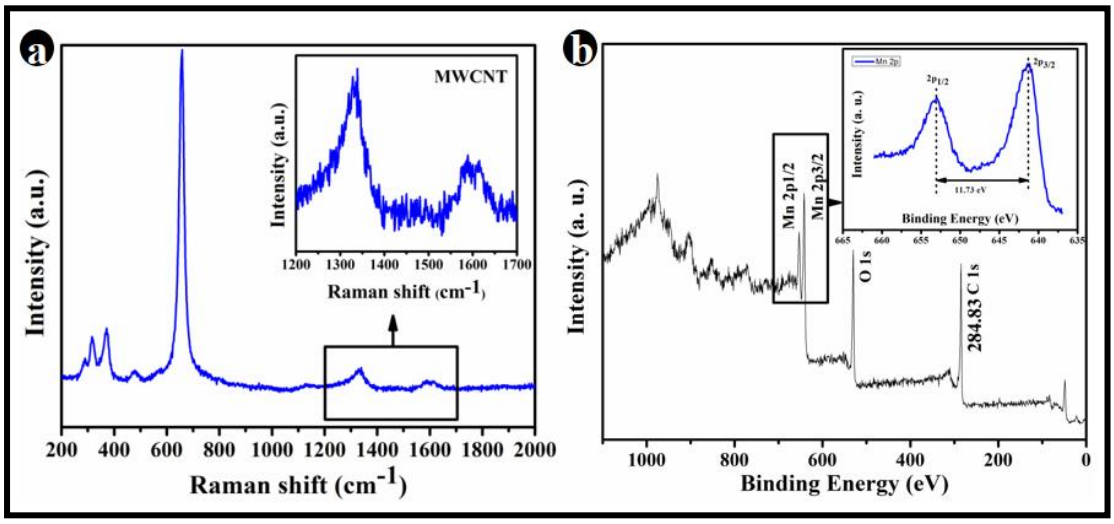


**Figure II.3** (a) Raman spectrum of as prepared $Mn_3O_4$-MWCNT composite. The enlarged peaks for MWCNT (inset); (b) XPS spectrum (survey scan) of $Mn_3O_4$-MWCNT composite. Magnified view of Mn 2p level (inset).

### *II.3.4 XPS Study*

For the chemical analysis of the composite, X-ray Photoelectron Spectroscopy (XPS) was carried out using PHI 5000 Versa Probe II XPS analyzer with monochromatic Al Kα X-Ray source (hυ = 1486.71 eV). Figure II.3b shows the total survey scan of XPS spectra for $Mn_3O_4$@MWCNT composites where all the peaks of C, Mn and O can be seen. The C 1s peak at binding energy of 284.83 eV indicates the presence of MWCNTs in the composite [33]. The Mn2p level spectrum is shown inset of Figure II.3b. For Mn 2p, the two peaks at 653.0 and 641.27 eV are attributed to the Mn2p1/2 and Mn2p3/2, respectively with spin energy difference of 73 eV, confirming the $Mn_3O_4$ formation [34].

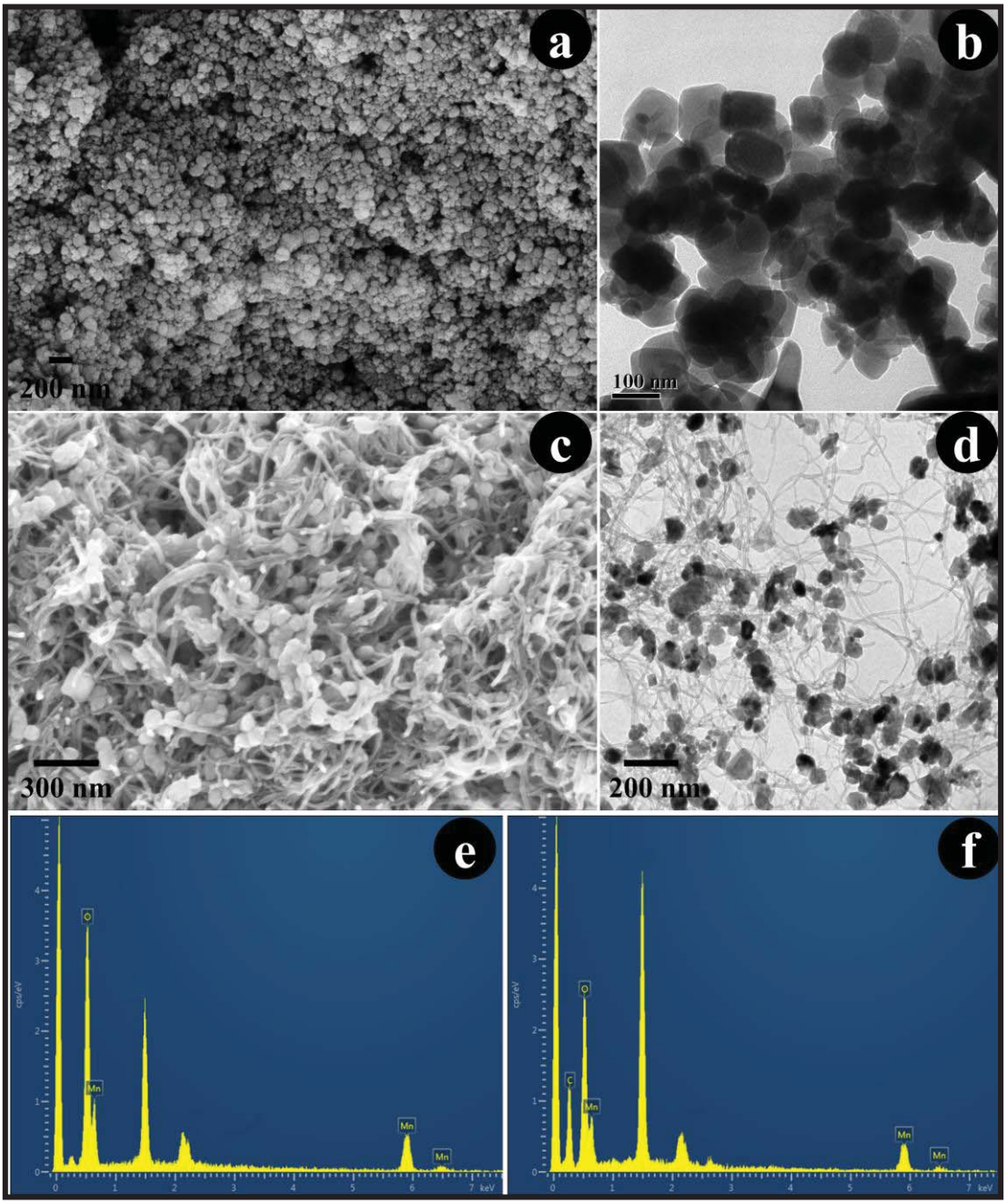


**Figure II.4** FESEM images of as prepared (a) $Mn_3O_4$, and (c) $Mn_3O_4$@MWCNT composite; TEM images of (b) $Mn_3O_4$, and (d) $Mn_3O_4$@MWCNT composite; EDAX spectra of (e) $Mn_3O_4$, and (f) $Mn_3O_4$@MWCNT composite.

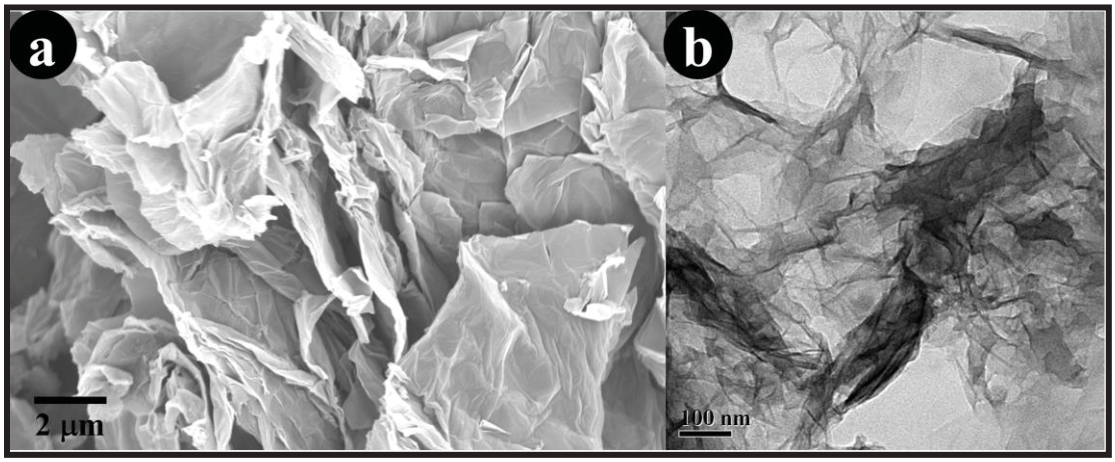


**Figure II.5** FESEM images of as prepared (a) GO, and (b) rGO.

### *II.3.5 Morphological analysis*

The morphological analysis of the as prepared $Mn_3O_4$, $Mn_3O_4$@MWCNT and rGO were carried out in terms of field-emission scanning electron microscope (FESEM) and transmission electron microscope (TEM) analyses using Carl Zeiss-SUPRA 40 and TECNAI G2-20S-TWIN, respectively. Figure II.4a shows the FESEM image of $Mn_3O_4$ nanoparticles with the avarage dimension of tens of nanometer. The coressponding TEM image of the pure $Mn_3O_4$ nanoparticles are represented in Figure II.4b, supporting the FESEM observance. In case of the $Mn_3O_4$@MWCNT composite, the MWCNTs backbone served as the template to grow the $Mn_3O_4$ nanoparticle (Figure II.4c). This is also confirmed from the TEM analysis (Figure II.4d), where apart from only a few aggolomerated nanoparticles, $Mn_3O_4$ nanoparticles were nicely distributed. Here MWCNT acted both as a template for the growth of $Mn_3O_4$ nanoparticle as well it connected individual nanoparticles and thereby a conductive network was formed inside the composite. The energy dispersive X-ray spectroscopy (EDX) analysis of $Mn_3O_4$ and $Mn_3O_4$@MWCNT are shown in Figure II.4e and II.4f. Figure II.5a illustrates the as prepared reduced graphene oxide merely formed

network like morphology which is clearly seen from the corresponding TEM images (Figure II.5b).

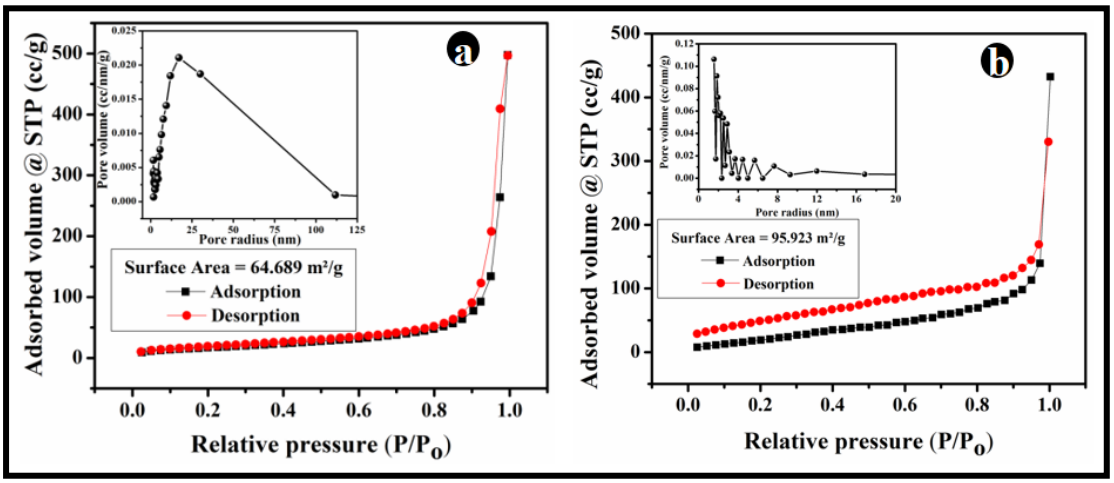


**Figure II.6** $N_2$ adsorption-desorption isotherms and BJH pore size distribution profile (inset) of (a) $Mn_3O_4$@MWCNT composite and (b) rGO.

### *II. 3.6 Brunauer–Emmett–Teller (BET) analysis*

The effective BET surface area of the composite was calculated using a Quantachrome ChemBET analyzer as surface area of an electrode material plays a crucial role in determining the performance. The composites show high surface area and porosity obtained from $N_2$ adsorption-desorption isotherm and Barrett-Joyner-Halenda (BJH) methods and the plots are shown in Figure II.6a. According to the international union of pure and applied chemistry (IUPAC), the BET isotherm exhibit type-4 isotherm with H3 hysteresis loop. The BET surface area of the composite was obtained as 64.68 $m^2/g$. BJH pore size distribution profile (inset) shows perfectly monomodal distribution with the maxima of 17.1 nm for the composites. The surface area of the rGO was determined to be 95.92 $m^2/g$ (Figure II.6b).

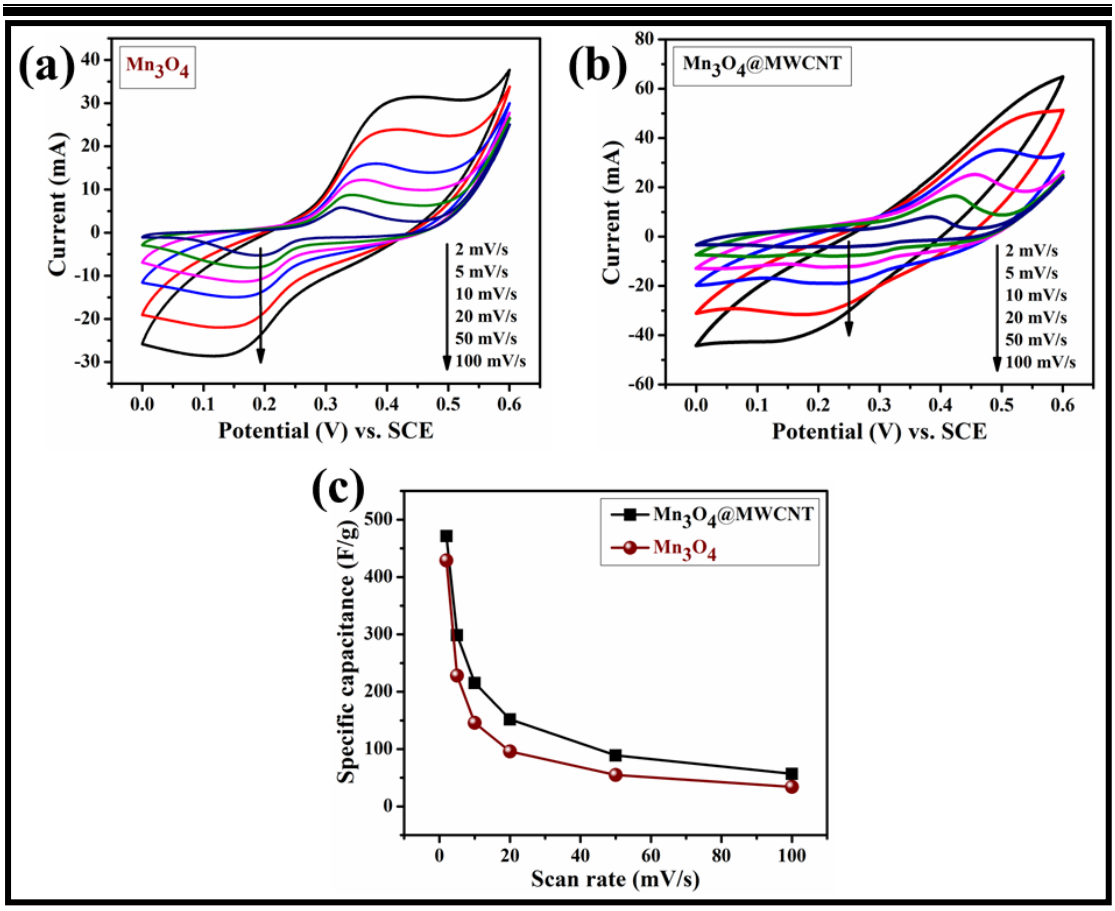


**Figure II.7** CV curves of (a) $Mn_3O_4$, and (b) $Mn_3O_4$@MWCNT at different scan rates of 2, 5, 10 20, 50 and 100 mV/s; (c) Variation of specific capacitance of $Mn_3O_4$ and $Mn_3O_4$@MWCNT at various scan rates.

### *II.3.7 Electrochemical characterizations*

The electrochemical properties the $Mn_3O_4$, $Mn_3O_4$@MWCNT, and rGO were studied in three electrode cell system where the active materials coated Ni foam, Pt foil and saturated calomel electrode (SCE) were used as working electrode, counter electrode and reference electrode, respectively in 1 M KOH electrolyte using Biologic SP-150 instrument. For the preparation of working electrode, cleaned Ni foam (1 cm × 1 cm) was taken as current collector on which active materials paste was casted. The Ni foam was cleaned via ultrasonication for 30 min in 30% HCl to remove the NiO layer on the surface. The active material paste was prepared by mixing it with carbon black

(to increase the conductivity) and polyvinylidene fluoride (PVDF, as binder) with 8:1:1 weight ratio in N-methyl-2-pyrrolidone (NMP) solvent. The as prepared paste was casted onto the cleaned Ni foam and dried under air.

Electrochemical characterization techniques in terms of cyclic voltammetry (CV), galvanostatic charge-discharge (GCD) and electrochemical impedance spectra (EIS) were employed for the as prepared electrode materials. The CV plots of the $Mn_3O_4$, $Mn_3O_4$@MWCNT at different scan rates of 2, 5, 10 20, 50 and 100 mV/s are shown in Figure 6a and Figure 6b, respectively with a potential window of 0-0.6 V (vs SCE). A pair of redox peaks appeared for both the electrode materials indicating the occurrence of faradaic redox reaction during the CV cycle in KOH electrolyte. The redox peak position in the CV plot clearly indicates the reversible redox reaction of Mn(III)/Mn(II), Mn(IV)/Mn(III) and Mn(VI)/Mn(IV) of $Mn_3O_4$ [35]. The associated redox phenomenon of $Mn_3O_4$ in an aqueous electrolyte can be expressed as follows [36]:

$$MnO_x(OH)_y + \delta H_2O + \delta e^- \leftrightarrow MnO_{x-\delta}(OH)_{y+\delta} + \delta OH^- \quad (1)$$

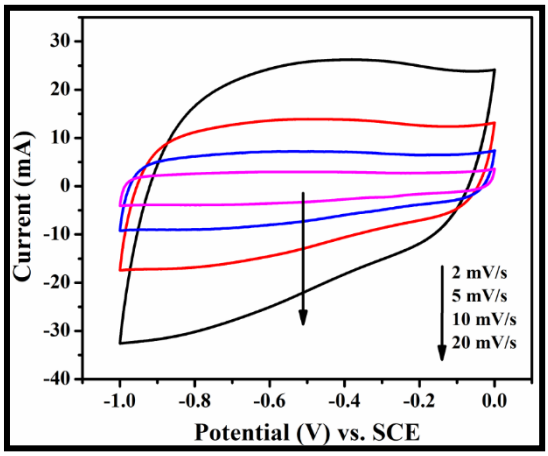


**Figure II.8** Cyclic voltammetry curves of rGO at different scan rates of 2, 5, 10 20, 50 and 100 mV/s.

The two oxymanganese species $MnO_x(OH)_y$ and $MnO_{x-\delta}(OH)_{y+\delta}$ in the equation are at higher and lower oxidation states, respectively. However, certain resistive phenomenon was observed as indicated by the positive and negative shifting of the respective anodic and cathodic peaks in the CV plot with the increasing scan rate. The non-rectangular nature of the CV plots also suggests the pseudocapacitive behavior of the active material.

However, the CV plots of rGO (Figure II.8) showed close to rectangular shape indicating its double layer capacitive behavior; the soft deviation from perfect rectangular nature may be due to the residual surface functional group, which in fact contribute some pseudocapacitance to the total capacitance. The specific capacitance from the CV plot was calculated using the following equation:

$$\text{Specific capacitance, } \mathbf{C_S} = \frac{\int_{V1}^{V2} i(V)dV}{(V2-V1)\nu m} \qquad (1)$$

where, $\int_{V1}^{V2} i(V)dV$ is the area of CV curve, $(V2 - V1)$ is the potential window (V), $\nu$ is the scan rate (mV/s) and $m$ is the mass (g) of the active materials. The highest specific capacitance of 428.9 and 471.3 F/g were achieved for $Mn_3O_4$ and $Mn_3O_4$@MWCNT, respectively at a scan rate of 2 mV/s. For reduced graphene oxide the obtained maximum specific capacitance was 291 F/g at a scan rate of 2 mV/s with potential range of 0 to -1.0 V (vs SCE). The specific capacitance of pure $Mn_3O_4$ and $Mn_3O_4$@MWCNT composites at various scan rates is shown in Figure II.7c.

With the increasing scan rate the fast voltage alternation results in low diffusion of electrolyte ions inside the active material, which affect the capacitance. However, the specific capacitance of the composite is always higher than the pure

$Mn_3O_4$ at each scan rate. This is mainly because of the synergistic effect between the high surface area and highly conductive MWCNT and redox active $Mn_3O_4$.

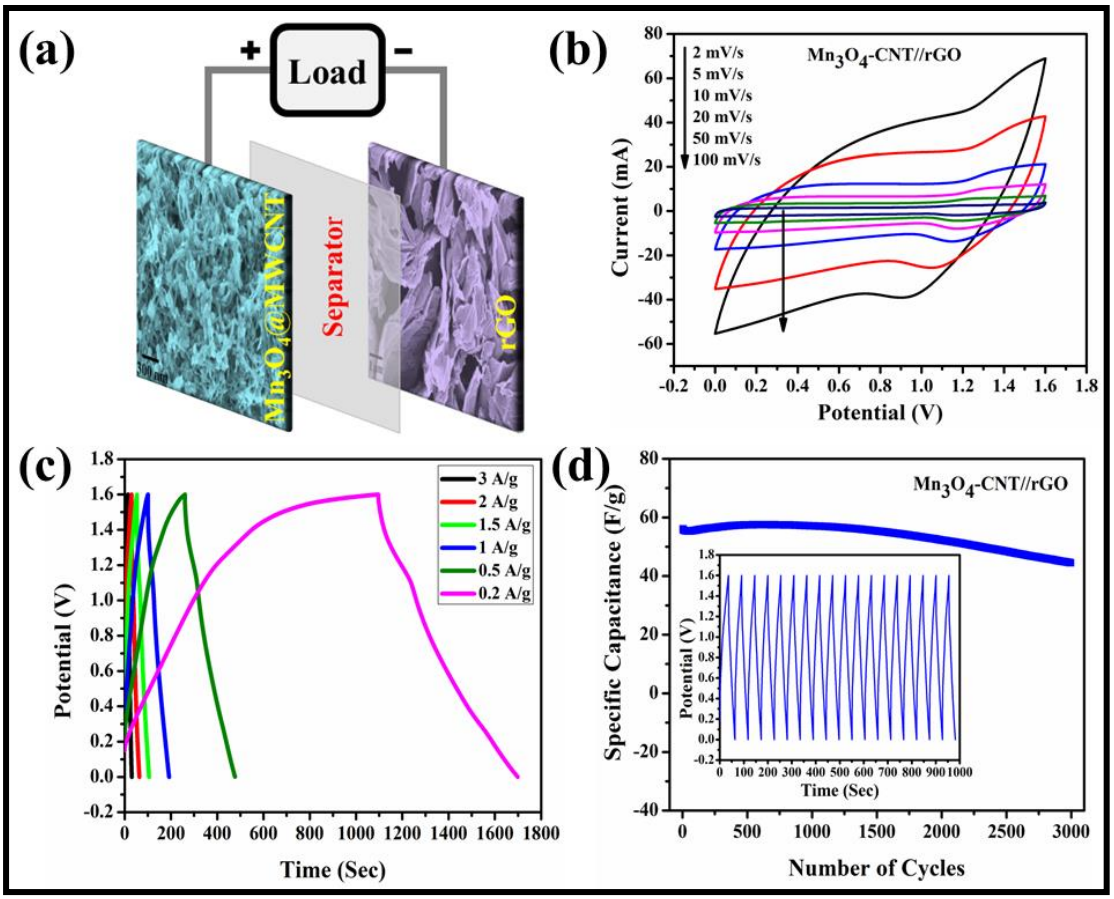


**Figure II.9** (a) Schematic illustration of as constructed asymmetric supercapacitor by combining $Mn_3O_4$@MWCNT and rGO as positive and negative electrode, respectively; (b) CV curves of $Mn_3O_4$@MWCNT//rGO at different scan rates of 2, 5, 10 20, 50 and 100 mV/s; (c) GCD curves of $Mn_3O_4$@MWCNT//rGO with a cell voltage of 1.6 V at current varying from 0.2 to 3 A/g; (d) Cycling performance of $Mn_3O_4$@MWCNT//rGO at a current of 1 A/g.

An asymmetric supercapacitor was constructed by combining the $Mn_3O_4$@MWCNT nanocomposites and rGO nanosheets as positive and negative

electrodes, respectively. The schematic illustration of as constructed asymmetric supercapacitor is shown in Figure II.9a.

In order to get the maximum performance in ASCs, there should be a charge balance between the positive and negative electrode following the equation below:

$$C_+ * V_+ * m_+ = C_-*V_-*m_-$$

where C is specific capacitance, V is potential window, m is the mass of corresponding electrode. From the above equation, the optimum mass ratio of the positive and negative electrode was found to be unity. Considering the effective working potential of the individual electrodes, measured in three electrode systems, the initial working potential was chosen as 0-1.6 V for the asymmetric supercapacitor. Figure II.9b indicates the typical CV curves of $Mn_3O_4$@MWCNT//rGO at different scan rates of 2 to 100 mV/s in 1 M KOH electrolyte within the potential range of 0-1.6 V. The various specific capacitances obtained at different scan rates are shown in Table 1. The maximum specific capacitance obtained for the asymmetric supercapacitor was 173.4 F/g was achieved at a scan rate of 2 mV/s. On increasing the scan rates the specific capacitance decreased, still high capacitance retention of 71.5 F/g at high scan rate of 100 mV/s indicates excellent rate capability of the as fabricated supercapacitor.

**Table 1** Calculated Specific capacitance (F/g) of $Mn_3O_4$@MWCNT//rGO at different scan rates

| **Scan rate (mV/s)** | **2** | **5** | **10** | **20** | **50** | **100** |
|---|---|---|---|---|---|---|
| **Sp. capacitance (F/g)** | **173.4** | **154** | **139.2** | **122.3** | **95.1** | **71.5** |

The galvanostatic charge-discharge curves of $Mn_3O_4$@MWCNT//rGO at different current from 0.2 to 3 A/g in 1 M KOH aqueous electrolyte are shown in Figure II.9c. The nature of the GCD curves indicates the involvement of pseudocapacitance in total capacitance. The specific capacitance from GCD curves was calculated from the following equation:

$$\text{Specific capacitance, } \mathbf{C_S} = \frac{\boldsymbol{i} \times \Delta \boldsymbol{t}}{\boldsymbol{m} \times \Delta \boldsymbol{v}} \qquad (2)$$

where, $\boldsymbol{i}$ is applied current, $\Delta \boldsymbol{t}$ is the discharge time, $\boldsymbol{m}$ is the mass of active material, and $\Delta \boldsymbol{v}$ is potential window. The calculated specific capacitances of the constructed ASC are 75.4, 67.5, 57, 49, 42.7 and 31.3 F/g at the current of 0.2, 0.5, 1, 1.5, 2 and 3 A/g, respectively. The achieved specific capacitance is higher than $Mn_3O_4$@GR//AC asymmetric supercapacitor which shows 38 F/g and 62 F/g at 0.5 A/g in 6M KOH and 1M $Na_2SO_4$ electrolyte, respectively [8]. It is seen that the capacitance gradually decreases with the increase of current. This is mainly due to limiting diffusion of electrolytes ion at higher current, hence only the outer surface is used for effective charge storage. Although the performance of the as fabricated asymmetric supercapacitor is appraisable, there remains a performance layback regarding the low coloumbic efficiency. In order to increase the coloumbic efficiency, the electrochemical tests were repeated within the potential range of 0-1.4V (Figure II.10).

Figure II.10a shows the cyclic voltammetry curves of $Mn_3O_4$@MWCNT//rGO at different scan rates of 2 to 100 mV/s in 1 M KOH electrolyte within the potential range of 0-1.4 V. The highest specific capacitance achieved for the asymmetric capacitor was 218.16 F/g at 2 mV/s scan rate.

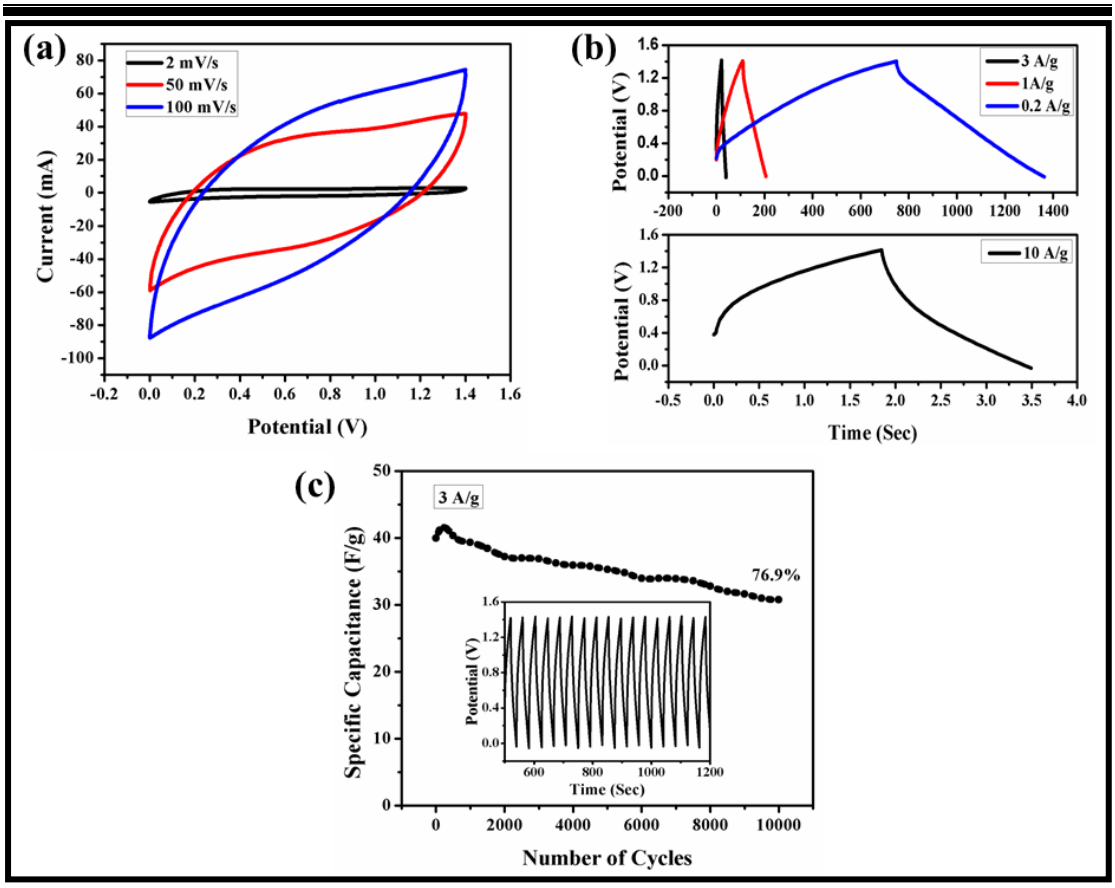


**Figure II.10** (a) CV curves of $Mn_3O_4$@MWCNT//rGO at different scan rates of 2, 50 and 100 mV/s; (b) GCD curves of $Mn_3O_4$@MWCNT//rGO with a cell voltage of 1.4 V at current varying from 0.2 to 10 A/g; (c) Cycling performance of $Mn_3O_4$@MWCNT//rGO at a specific current of 3 A/g.

Figure II.10b depicts the galvanostatic charge-discharge curves for the fabricated asymmetric capacitor at different current density from 0.2 to 10 A/g. The different specific capacitances obtained were 88, 68.6, 40, and 11.75 F/g at the current of 0.2, 1, 3 and 10 A/g, respectively. The ASC achieved specific energy of 23.95, 18.67, 10.9 and 3.2 Wh/kg at the corresponding power delivery rate of 140, 700, 2100 and 7200 W/kg, respectively. The as fabricated asymmetric supercapacitor within the potential range of 0-1.4 V showed an excellent cycle stability by retaining 76.9% specific capacitance at the end of 10000 GCD cycles.

Figure II.9d shows standard cyclic stability with 79.3% specific capacitance retention over 3000 consecutive GCD cycles at 1 A/g current within the potential range 0-1.6 V. Interestingly, within the potential range of 0-1.4 V, the asymmetric supercapacitor showed high capacitance retention of 76% after 10000 consecutive GCD cycles at 3 times higher current density (Figure II.10c). This may be due to some sort of irreversible reaction beyond that potential range, that cause a larger extent of capacitance decay.

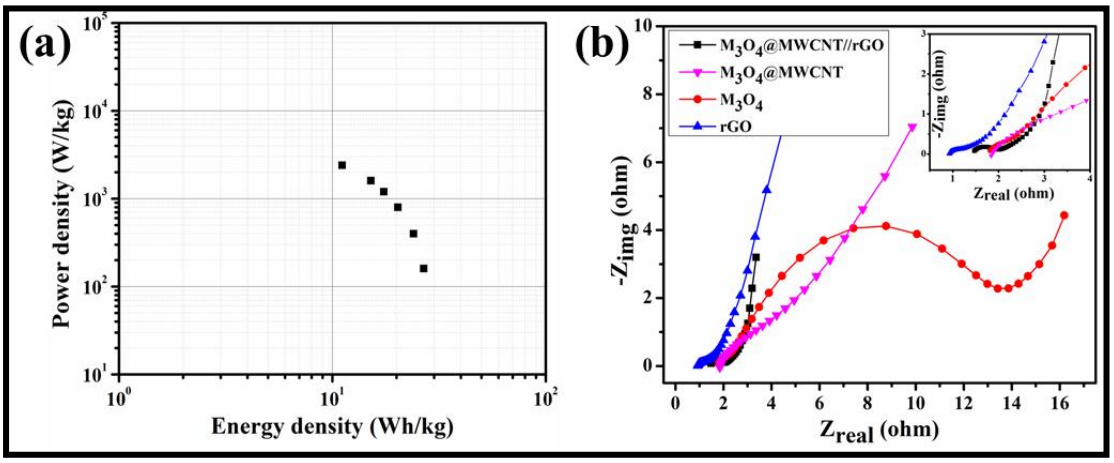


**Figure II.10** (a) Ragone plot of $Mn_3O_4$@MWCNT//rGO in terms of power density vs energy density; (b) Nyquist plots of $Mn_3O_4$, $Mn_3O_4$@MWCNT, rGO, and $Mn_3O_4$@MWCNT//rGO.

The energy and power density are the main two parameters that play the key role in determining the performance of supercapacitor. The energy density and power density was measured by the following equations:

$$\text{Energy density, } \mathbf{E} = \frac{1}{2\ X\ 3.6}\ C_S(\Delta V)^2$$

$$\text{Power density, } \mathbf{P} = \frac{E}{T}\ X\ 3600$$

where, $C_S$ is the specific capacitance, $\Delta V$ is the potential window and $T$ is the discharging time. The maximum energy density of 26.816 Wh/kg was obtained at a power density of 160 W/kg which is comparable or higher than some symmetric and asymmetric supercapacitor such as micro- and meso-porous carbon (<6 Wh/kg) [37], graphene//graphene (~9.1 Wh/kg) [38], CNT//CNT (6 Wh/kg) [39], GH//$MnO_2$-NF (23.2 Wh/kg) [40] activated carbon//mesoporous $MnO_2$ (10.4 Wh/kg) [41]. Generally, in supercapacitor energy and power density has inverse relationship. However, the as fabricated supercapacitor still showed high energy density of 11.128 Wh/kg at a power density of 2400 W/kg. The highest energy density and power density achieved for the fabricated ASC are 23.95 Wh/kg and 7200 W/kg, when the potential range used as 0-1.4V. The various energy and power densities are shown in terms of Ragone plot in Figure II.11a.

**Table II.3** $R_s$ and $R_{ct}$ values obtained from the fitted plot

| **Values are in Ohm** | **$Mn_3O_4$** | **$Mn_3O_4$@MWCNT** | **rGO** | **$Mn_3O_4$@MWCNT//rGO** |
|---|---|---|---|---|
| **$R_s$** | 1.924 | 1.832 | 0.914 | 1.402 |
| **$R_{ct}$** | 12.7 | 2.278 | 0.322 | 1.211 |

In order to understand the various resistive parameters involved with the electrochemical phenomenon occurring within the supercapacitor electrode EIS analysis was carried out of all three electrode material along with the fabricated asymmetric supercapacitor within the frequency range of 50 mHz to 50 kHz. The EIS analysis has been presented in terms of Nyquist plot, shown in Figure II.11b. All the Nyquist plots show a starting semicircle followed by a straight line characteristics of

the charge transfer resistance and Warburg behavior, respectively. The calculated solution resistance ($R_s$) and the charge transfer resistance ($R_{ct}$) values of all the as prepared electrode materials are tabulated in Table II.3.

## II.4 Conclusions

Herein we have systematically demonstrated the improved energy density and power density of $Mn_3O_4$@MWCNT//rGO over the Mn3O4@MWCNT electrode with proper justification. A synergistic interaction between highly electrical conductive MWCNT and pseudocapacitive $Mn_3O_4$ resulted in higher specific capacitance for the $Mn_3O_4$@MWCNT//rGO composite compared to that of virgin $Mn_3O_4$. An aqueous asymmetric supercapacitor was constructed which was able to show high cell voltage of 1.6 V in 1 M KOH electrolyte. The high cell voltage combining high capacitance of positive electrode and high rate capability of negative electrode resulted in high energy and power density of 26.8 Wh/kg and 2400 W/kg, respectively for the $Mn_3O_4$@MWCNT//rGO. The high energy and power density accompanied by standard cycle life strongly demonstrate the high efficiency of the as fabricated supercapacitor for practical purpose.

## References

[1] Hadjipaschalis, I.; Poullikkas, A.; Efthimiou, V. Overview of current and future energy storage technologies for electric power applications. Renew. Sust. Energ. Rev. 2009, 13, 1513-1512.

[2] Liu, C.; Li, F.; Ma, L.P.; Cheng, H.M. Advanced materials for energy storage. Adv. Mater. 2010, 22, E28-E62.

[3] Simon, P.; Gogotsi, Y. Materials for electrochemical capacitors. *Nat. Mater.* **2008**, *7*, 845-854.

[4] Kötz, R.; Carlen, M. Principles and applications of electrochemical capacitors. *Electrochim. Acta* **2000**, *45*, 2483-2498.

[5] Long, J.W.; Bélanger, D.; Brousse, T. Sugimoto, W.; Sassin, M.B.; Crosnier, O. Asymmetric electrochemical capacitors—Stretching the limits of aqueous electrolytes. *MRS Bull.* **2011**, *36*, 513-522.

[6] Wu, Z.-S.; Ren, W.; Wang, D.-W.; Li, F.; Liu, B.; Cheng, H.-M. High-energy $MnO_2$ nanowire/graphene and graphene asymmetric electrochemical capacitors. *ACS Nano* **2010**, *4*, 5835-5842.

[7] Lee, J.W.; Hall, A.S.; Kim, J.D.; Mallouk, T.E. A facile and template-free hydrothermal synthesis of $Mn_3O_4$ nanorods on graphene sheets for supercapacitor electrodes with long cycle stability. *Chem. Mater.* **2012**, *24*, 1158-1164.

[8] Xiao, Y.; Cao, Y.; Gong, Y.; Zhang, A.; Zhao, J.; Fang, S.; Jia, D.; Li, F. Electrolyte and composition effects on the performances of asymmetric

supercapacitors constructed with $Mn_3O_4$ nanoparticles–graphene nanocomposites. *J. Power Sources* **2014**, *246*, 926-933.

[9] Du, X.; Wang, C.; Chen, M.; Jiao, Y.; Wang, J. Electrochemical performances of nanoparticle $Fe_3O_4$/activated carbon supercapacitor using KOH electrolyte solution. *J. Phys. Chem. C* **2009**, *113*, 2643-2646.

[10] Ghosh, D.; Giri, S.; Das, C.K. Hydrothermal synthesis of platelet β $Co(OH)_2$ and $Co_3O_4$: Smart electrode material for energy storage application. *Environ. Prog. Sustain. Energy* 2014, *33*, 1059-1064.

[11] Yan, J.; Fan, Z.; Sun, W.; Ning, G.; Wei, T.; Zhang, Q.; Zhang, R.; Zhi, L.; Wei, F. Advanced asymmetric supercapacitors based on $Ni(OH)_2$/graphene and porous graphene electrodes with high energy density. *Adv. Funct. Mater*. **2012**, *22*, 2632-2641.

[12] Ghosh, D.; Mandal, M.; Das, C.K. Solid state flexible asymmetric supercapacitor based on carbon fiber supported hierarchical $Co(OH)_xCO_3$ and $Ni(OH)_2$. *Langmuir* **2015**, *31*, 7835-7843.

[13] Wei, W.; Cui, X.; Chen, W.; Ivey, D.G. Manganese oxide-based materials as electrochemical supercapacitor electrodes. *Chem. Soc. Rev.* **2011**, *40*, 1697-1721.

[14] Qu, D. Studies of the activated carbons used in double-layer supercapacitors. *J. Power Sources* **2002**, *109*, 403-411.

[15] Largeot, C.; Portet, C.; Chmiola, J.; Taberna, P.L.; Gogotsi, Y.; Simon, P. Relation between the ion size and pore size for an electric double-layer capacitor., *J. Am. Chem. Soc.* **2008**, *130*, 2730-2731.

[16] Mandal, M.; Maitra, A.; Das, T.; Das, C.K. Graphene and related two-dimensional materials, in Graphene materials: fundamentals and emerging applications (Eds. A. Tiwari and M. Syväjärvi), John Wiley & Sons, Inc. USA **2015**, 3-23.

[17] Marcano, D.C.; Kosynkin, D.V.; Berlin, J.M.; Sinitskii, A.; Sun, Z.; Slesarev, A.; Alemany, L.B.; Lu, W.; Tour, J.M. Improved synthesis of graphene oxide. *ACS Nano* **2010**, *4*, 4806.

[18] Wang, L.; Ji, H.; Wang, S.; Kong, L.; Jiang, X.; Yang, G. Preparation of $Fe_3O_4$ with high specific surface area and improved capacitance as a supercapacitor. *Nanoscale* **2013**, *5*, 3793-3799.

[19] Xiong, S.; Yuan, C.; Zhang, X.; Xi, B.; Qian, Y. Controllable synthesis of mesoporous $Co_3O_4$ nanostructures with tunable morphology for application in supercapacitors., *Chem. Euro. J.* **2009**, *15*, 5320-5326.

[20] Wang, L.; Ji, H.; Zhu, F.; Chen, Z.; Yang, Y.; Jiang, X.; Pinto, J.; Yang, G. Large-scale preparation of shape controlled SnO and improved capacitance for supercapacitors: from nanoclusters to square microplates, *Nanoscale* **2013**, *5*, 7613-7621.

[21] Wang, L.; Li, Y.; Han, Z.; Chen, L.; Qian, B.; Jiang, X.; Pinto, J.; Yang, G. Composite structure and properties of $Mn_3O_4$/graphene oxide and $Mn_3O_4$/graphene, *J. Mater. Chem. A* **2013**, *1*, 8385-8397.

[22] Bindumadhavan, K.; Srivastava, S.K.; Mahanty, S. $MoS_2$–MWCNT hybrids as a superior anode in lithium-ion batteries. *Chem. Commun.* **2013**, *49*, 1823-1825.

[23] Tian, Z.Y.; Mountapmbeme Kouotou, P.; Bahlawane, N.; Tchoua Ngamou, P.H. Synthesis of the catalytically active $Mn_3O_4$ spinel and its thermal properties., *J. Phys. Chem. C* **2013**, *117*, 6218-6224.

[24] Wang, W.Z.; Xu, C.K.; Wang, G.H.; Liu, Y.K.; Zheng, C.L. Preparation of smooth single-crystal $Mn_3O_4$ nanowires. *Adv. Mater.* **2002**, *14*, 837-840.

[25] Mali, S.S.; Betty, C.A.; Bhosale, P.N.; Patil, P.S. Synthesis, characterization of hydrothermally grown MWCNT–$TiO_2$ photoelectrodes and their visible light absorption properties. *ECS J. Solid State Sc.* **2012**, *1*, M15.

[26] Zhang, H.; Hines, D.; Akins, D.L. Synthesis of a nanocomposite composed of reduced graphene oxide and gold nanoparticles. *Dalton Trans.* **2014**, *43*, 2670-2675.

[27] Yang, T.; Liu, L.H.; Liu, J.W.; Chen, M.L.; Wang, J.H. Cyanobacterium metallothionein decorated graphene oxide nanosheets for highly selective adsorption of ultra-trace cadmium. *J. Mater. Chem.* **2012**, *22*, 21909-21916.

[28] Wu, N.; She, X.; Yang, D.; Wu, X.; Su, F.; Chen, Y. Synthesis of network reduced graphene oxide in polystyrene matrix by a two-step reduction method for superior conductivity of the composite, *J. Mater. Chem.* **2012**, 22, 17254-17261.

[29] Malavasi, L.; Galinetto, P.; Mozzati, M.C.; Azzoni, C.B.; Flor, G. Raman spectroscopy of $AMn_2O_4$ (A= Mn, Mg and Zn) spinels, *Phys. Chem. Chem. Phys.* **2002**, *4*, 3876-3880.

[30] Li, L.; Guo, Z.; Du, A.; Liu, H. Rapid microwave-assisted synthesis of $Mn_3O_4$–graphene nanocomposite and its lithium storage properties, *J. Mater. Chem.* **2012**, *22*, 3600-3605.

[31] Chen, J.J.; Zhang, Q.; Shi, Y.N.; Qin, L.L.; Cao, Y.; Zheng, M.S.; Dong, Q.F. A hierarchical architecture S/MWCNT nanomicrosphere with large pores for lithium sulfur batteries. *Phys. Chem. Chem. Phys.* **2012**, *14*, 5376-5382.

[32] Chouit, F.; Guellati, O.; Boukhezar, S.; Harat, A.; Guerioune, M.; Badi, N. Synthesis and characterization of HDPE/N-MWNT nanocomposite films. *Nanoscale Res. Lett.* 2014, 9, 1-6.

[33] Estrade-Szwarckopf, H. XPS photoemission in carbonaceous materials: A "defect" peak beside the graphitic asymmetric peak. *Carbon* **2004**, *42*, 1713-1721.

[34] Dubal, D.P.; Holze, R. A successive ionic layer adsorption and reaction (SILAR) method to induce $Mn_3O_4$ nanospots on CNTs for supercapacitors. *New J. Chem.* 2013, 37, 403-408.

[35] Hu, C.C.; Tsou, T.W. Ideal capacitive behavior of hydrous manganese oxide prepared by anodic deposition. *Electrochem.Commun.* **2002**, *4*, 105-109.

[36] Zhou, T.; Mo, S.; Zhou, S.; Zou, W.; Liu, Y.; Yuan, D. $Mn_3O_4$/worm-like mesoporous carbon synthesized via a microwave method for supercapacitors. *J. Mater. Sci.* **2011**, *46*, 3337-3342.

[37] Zheng, C.; Qi, L.; Yoshio, M.; Wang, H. Cooperation of micro-and meso-porous carbon electrode materials in electric double-layer capacitors. *J. Power Sources* **2010**, *195*, 4406-4409.

[38] Wang, H.; Liang, Y.; Mirfakhrai, T.; Chen, Z.; Casalongue, H.S.; Dai, H. Advanced asymmetrical supercapacitors based on graphene hybrid materials. *Nano Res.* 2011, 4, 729-736.

[39] Kaempgen, M.; Chan, C.K.; Ma, J.; Cui, Y.; Gruner, G. Printable thin film supercapacitors using single-walled carbon nanotubes. *Nano Lett.* **2009**, *9*, 1872-1876.

[40] Gao, H.; Xiao, F.; Ching, C.B.; Duan, H. High-performance asymmetric supercapacitor based on graphene hydrogel and nanostructured $MnO_2$, *ACS Appl. Mater. Interfaces* **2012**, *4*, 2801-2810.

[41] Wang, Y.T.; Lu, A.H.; Zhang, H.L.; Li, W.C. Synthesis of nanostructured mesoporous manganese oxides with three-dimensional frameworks and their application in supercapacitors. *J. Phys. Chem. C* **2011**, *115*, 5413-5421.

# Chapter III

*Synthesis of CuO-$MnO_2$ composite and electrochemical performance in redox mediated electrolyte*

## III.1 Introduction

This chapter can be considered as an extended work of the chapter II, where a composite based on a pseudocapacitive material like manganese oxide and a capacitive material like carbon nanotubes was studied for supercapacitor application. In this chapter we have investigated the electrochemical performance of the manganese oxide with another transition metal oxide such as CuO. To enhance the efficiency of the electrode materials, the idea of incorporating combinatorial transition metal oxides with multiple electroactive redox sites, has been developing. Not only the choice of electrode materials but also the surface architectures of the material, electrolyte, separator, etc. can alter the efficiency of the supercapacitor. Recently, in terms of modification of electrolyte, addition of a foreign redox system into the mother electrolyte solution as an additional source of pseudocapacitance is being taken into consideration. CuO-$MnO_2$ is a well-known composite which is previously reported for various applications like supercapacitors [1-7], Li-ion batteries [8, 9], heterogeneous catalysts [10-14], sensors [15, 16], etc. However, to the best of our knowledge this work is the first report on supercapacitor application of CuO-$MnO_2$ composite using redox mediated electrolyte.

Herein, pristine CuO and $MnO_2$ nanosheet-wrapped CuO nano-needles were synthesized by the precipitation method followed by a simple and facile hydrothermal technique and the electrochemical properties were studied in terms of cyclic voltammetry (CV), galvanostatic charge–discharge (GCD) curve and electrochemical impedance spectra (EIS) in redox couple, $[Fe(CN)_6]^{3-}/[Fe(CN)_6]^{4-}$ mediated aqueous electrolyte.

## III.2 Experimental Section

### *III.2.1 Materials and reagents*

Copper(II) nitrate trihydrate, potassium hexacyanoferrate(III), sodium hydroxide, potassium permanganate were bought from Merck, India. All the chemicals were used for the experiment without doing any purification.

### *III.2.2 Synthesis of CuO*

The CuO with various morphologies have been synthesized by a large number of synthetic routes [1-6]. A simple and cost effective precipitation method was carried out for CuO synthesis [17]. In brief, 30 mL 0.1 M aqueous solution of $Cu(NO_3)_2 \cdot 3H_2O$ was added drop wise to 20 mL 0.1 M aqueous solution of $K_3[Fe(CN)_6]$ with continuous stirring. The solid tawny brown colored precipitation of $Cu_3[Fe(CN)_6]_2$ was formed immediately. The solution was continuously stirred for another 1 h and then it was kept in undisturbed condition for 12 h. After that 1 M NaOH solution was poured dropwise to the mixture with continuous stirring. The prompt color change from tawny brown to deep brown was observed. The solid product was gently washed with water for 5-6 times and dried it in hot air oven at 60 °C.

### *III.2.3 Synthesis of CuO-$MnO_2$ composites*

For the preparation of CuO-$MnO_2$ composites, 35 mg of as-prepared CuO was dispersed in 35 mL 0.025 M aqueous solution of $KMnO_4$. Then the solution was poured in to 50 mL stainless steel autoclave and was kept in the furnace at 180 °C for 3 h. After cooling at room temperature, the obtained solid brown product was washed in succession with water and absolute alcohol for several times and dried at 60 °C for

12 h. This was labelled as CMO3. The CMO6 composite was prepared following the same procedure except the time given for hydrothermal synthesis was 6 h. The pure $MnO_2$ was synthesized with same procedure without addition of pure CuO.

## III.3 Results and Discussion

The chemical and structural analysis of the as-prepared electrode materials were carried out by X-ray diffraction (XRD, Rigaku ULTIMA-III X-ray diffractometer with Cu Kα radiation (λ= 1.548 Å) analysis, Fourier transform infrared (FTIR, NEXUS 870 Thermo-Nicolet) spectroscopy, and X-ray photoelectron spectroscopy (XPS, using a PHI 5000 Versa Probe II XPS analyzer with a monochromatic Al Kα x-ray source ($h\upsilon$ = 1486.71 eV)). From the field emission scanning electron microscopy (FESEM, Carl Zeiss-SUPRA 40) and tunneling electron microscopy (TEM, TECNAI G2-20S-TWIN) images, the surface morphology of the electrode materials was investigated. The surface area of the material was determined by the $N_2$ adsorption–desorption isotherm.

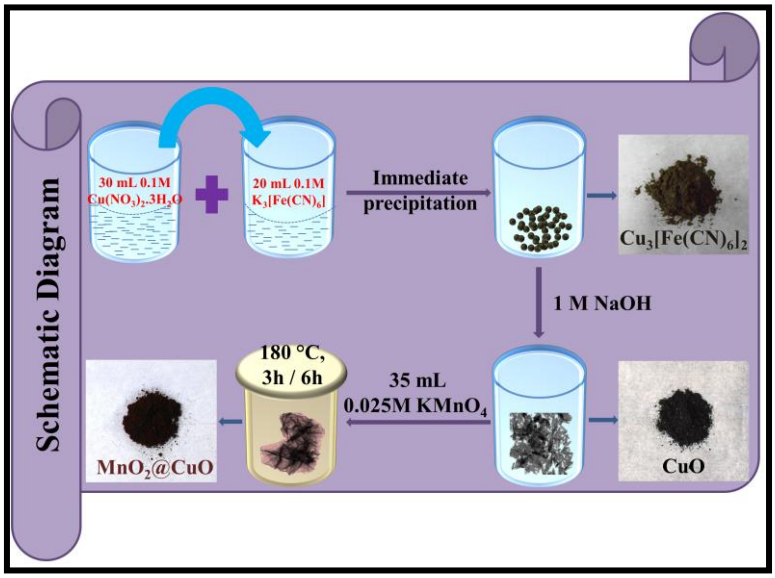


**Scheme III.1** Synthetic procedure of CuO-$MnO_2$ composites.

The synthesis procedure involves two step chemical reactions: first a quick precipitation of copper hexacyanoferrate [CuHCFe] (Co-precipitation method) and then the decomposition of CuHCFe complex in alkaline medium [18, 19]. The chemical reactions associated with the synthesis procedure are as follows:

$$3Cu(NO_3)_2 + 2K_3[Fe(CN)_6] = Cu_3[Fe(CN)_6]_2 + 6KNO_3 \quad (1)$$

$$Cu_3[Fe(CN)_6]_2 + 6NaOH = 3Cu(OH)_2 + 2Na_3[Fe(CN)_6]_2 \quad (2)$$

$$Cu(OH)_2 = CuO + H_2O \ (3)$$

The $MnO_2$ nanosheets are formed from self-decomposition of $KMnO_4$ during hydrothermal reaction [20]. The total synthesis procedure is schematically represented in Scheme III.1.

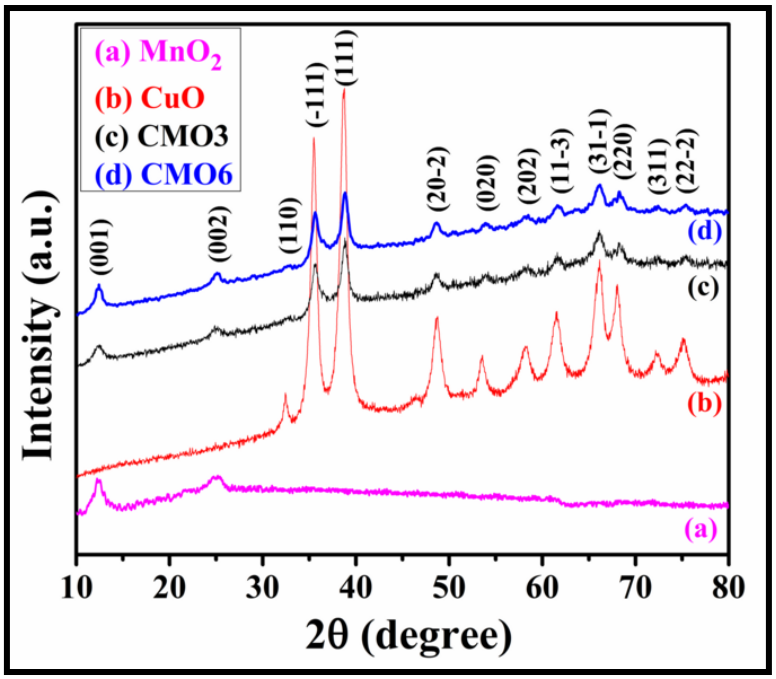


**Figure III.1** XRD patterns of as prepared of pure (a) $MnO_2$, (b) CuO, (c) CMO3, and (d) CMO6 composites.

### *III.3.1 XRD analysis*

The XRD patterns were taken to determine the phase composition of pure $MnO_2$, CuO and CMO composites as shown in Figure 1. For pure CuO, the peaks at 2θ (˚) of 32.4, 35.5, 38.7, 48.7, 53.5, 58.3, 61.5, 66, 68, 72.3, and 75.1 correspond to (110), (-111), (111), (20-2), (020), (202), (11-3), (31-1), (220), (311), and (22-2) planes of face centered cubic crystal. All the peaks are well matched with JCPDS Card No: 05-0661 (Tenorite, Syn). The precursor of the CuO is copper hexacyanoferrate which is confirmed by the XRD pattern as shown in Figure III.2. For the composites, all the peaks of CuO are present along with the two basal reflections of (001) and (002) at 12.5 and 24.7 peaks for $MnO_2$ which are also present in case of pure $MnO_2$ (Figure III.1a). The peaks of the composites are less intense than the pure CuO as the $MnO_2$ nanosheets wrap around the CuO nano-needles. Furthermore, the characteristic peaks of $MnO_2$ were more prominent in CMO6.

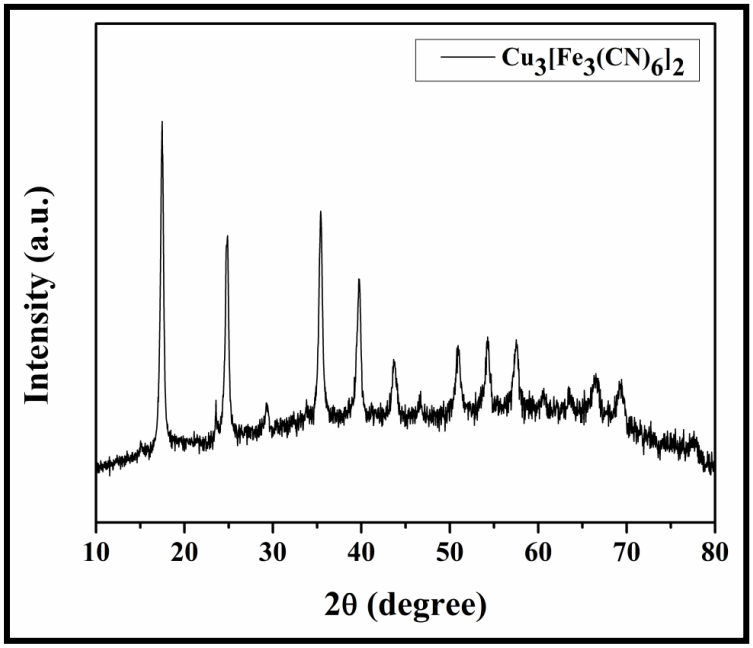


**Figure III.2** XRD pattern of $Cu_3[Fe_3(CN)_6]_2$.

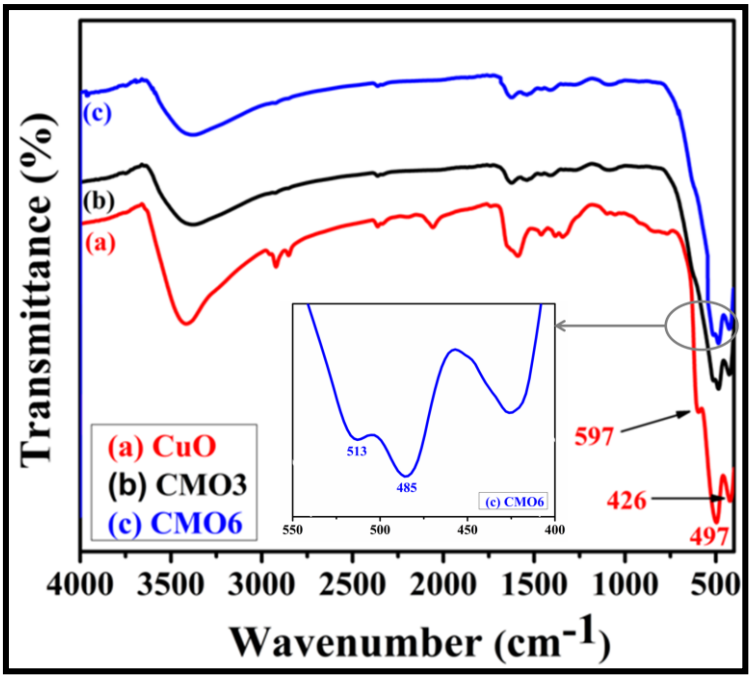


**Figure III.3** FT-IR spectra of as prepared pure (a) CuO, (b) CMO3, and (c) CMO6 composites.

### *III.3.2 FTIR analysis*

To investigate the chemical and structural property FTIR analysis was carried out and the results are shown in Figure III.3. Pressed KBr pellets of CuO and the composites (CMO3 and CMO6) were used to execute FTIR analysis by NEXUS 870 FTIR (Thermo Nicolet) instrument. The three main characteristic peaks of CuO were observed at 597, 497 and 426 $cm^{-1}$ for $A_u$, $B_u$ and $B_u$ mode, respectively which confirms the formation of CuO nano-needles. The Cu-O stretching values along (-101) and (101) directions demonstrate the absorption peaks at 597 and 497 $cm^{-1}$, respectively [21-24]. The broad absorption peaks between 1300 to 4000 $cm^{-1}$ are ascribed as chemisorbed and/ or physisorbed $H_2O$ and $CO_2$ molecules [24, 25]. Moreover, there is no peak in between 610 $cm^{-1}$ and 660 $cm^{-1}$ indicating the absence of any other phases like $Cu_2O$ which appears at 615 $cm^{-1}$ [26]. In both the composite,

the two main characteristic peaks are observed at 513 and 485 $cm^{-1}$ corresponding to Mn-O stretching modes in octahedral environment [27]. The peak at 1385 $cm^{-1}$ appears due to the coordination of Mn by O-H [27].

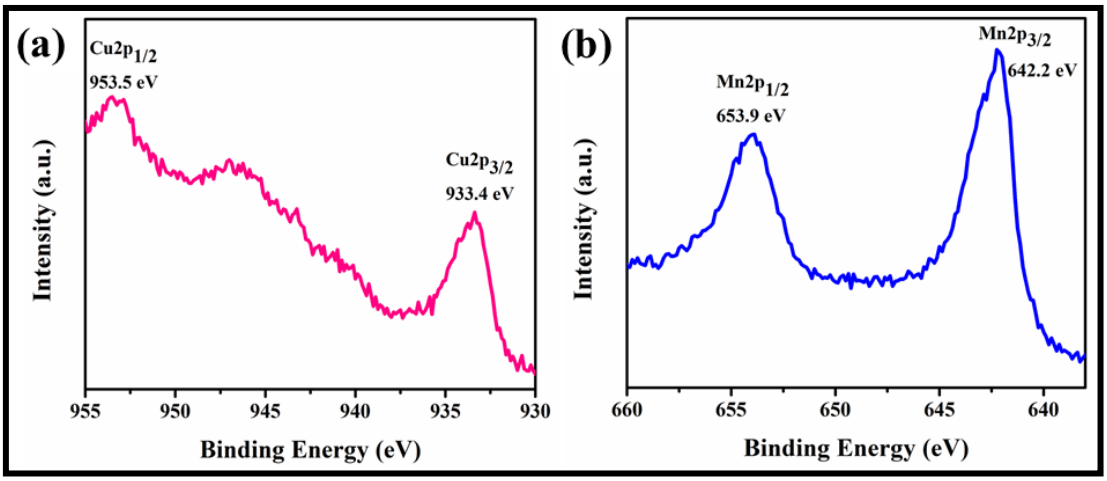


**Figure III.4** XPS spectra of CMO6 composite: (a) Cu 2p spectrum, and (b) Mn 2p spectrum.

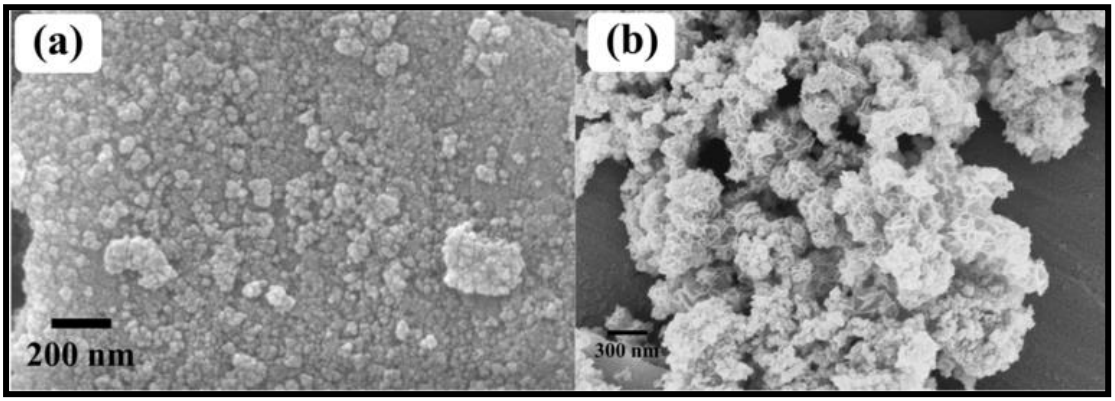


**Figure III.5** FESEM image of (a) $Cu_3[Fe_3(CN)_6]_2$, and (b) CMO3 composite.

### *III.3.3 XPS study*

For the chemical analysis of the composite, XPS was carried out which is shown in Figure III.4. The XPS spectra were accomplished by taking the reference peaks of C1s at 284.2 eV. For the Cu2p in CuO, the two major peaks of Cu2p1/2 and Cu2p3/2

are found at 953.5 and 933.5 eV, respectively, indicating the presence of CuO in composite [11]. Figure 3b shows XPS spectrum for Mn2p, the two peaks at 653.9 and 642.2 eV are attributed to the Mn2p1/2 and Mn2p3/2, respectively, with spin energy difference of 11.7 eV [28].

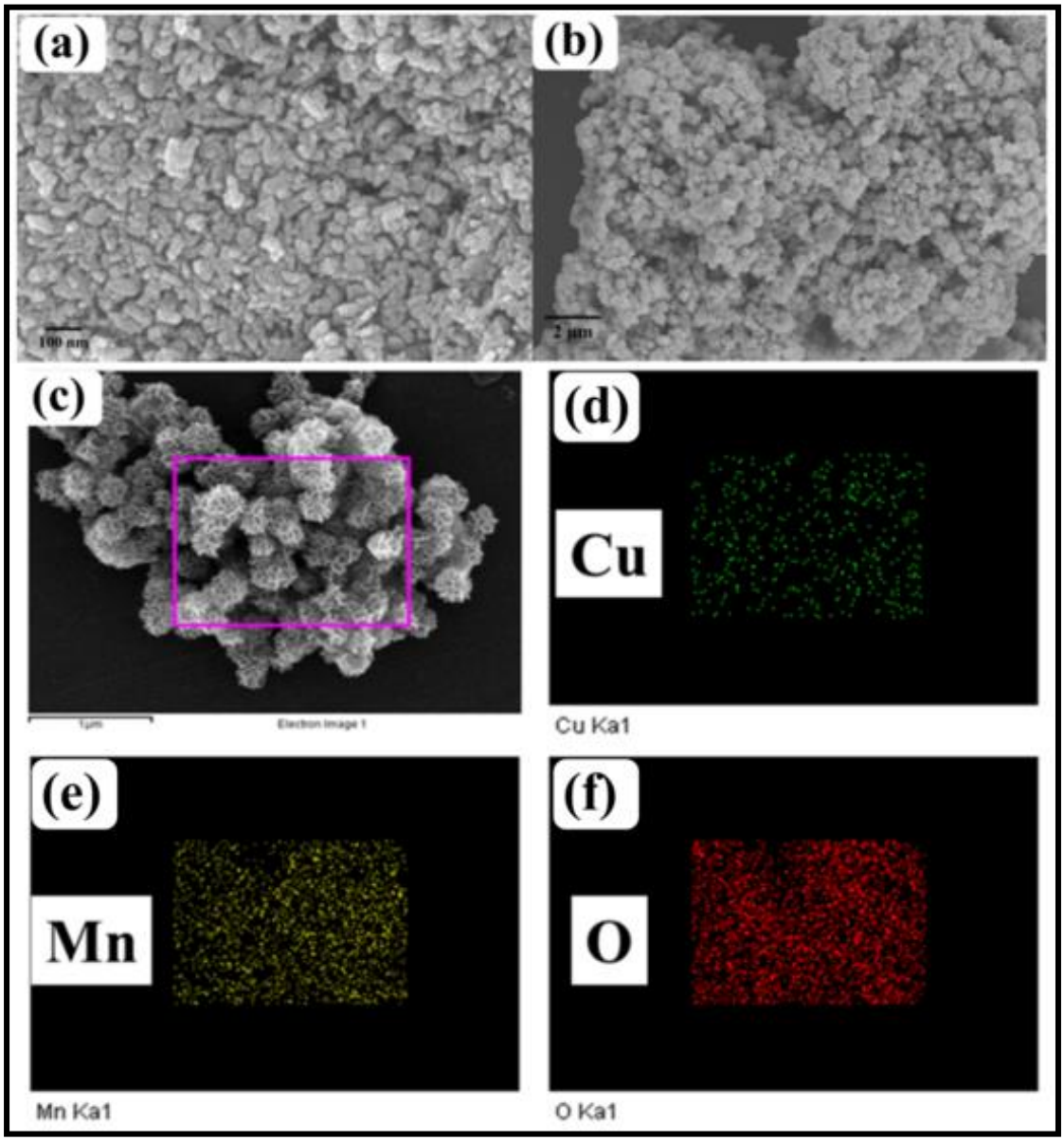


**Figure III.6** FESEM images of as prepared (a) pure CuO and (b) CMO6 composites; (c-f) Mapping images of CMO6 composite.

### *III.3.4 Morphological analysis*

Figure III.5 presents the corresponding FESEM images of as synthesized CuO and CMO6 composites. It can be seen that the CuO particles are having nano-needle like structure of length 80-100 nm. Copper hexacyanoferrate, the precursor of CuO nano-needle, consists of small nanoparticles as shown in Figure III.5a. The FESEM image of CMO3 is shown in Figure III.5b, which indicates the CuO nano-needles are covered up with $MnO_2$ nanosheets. However, for CMO6 composite, the CuO nanorods are fully wrapped by $MnO_2$ nanosheets (Figure III.6c), possibly due to longer time of growth. The element mapping images (Figure III.6d-f) confirm the presence of Cu, Mn and O implying the formation of CuO-$MnO_2$ composite.

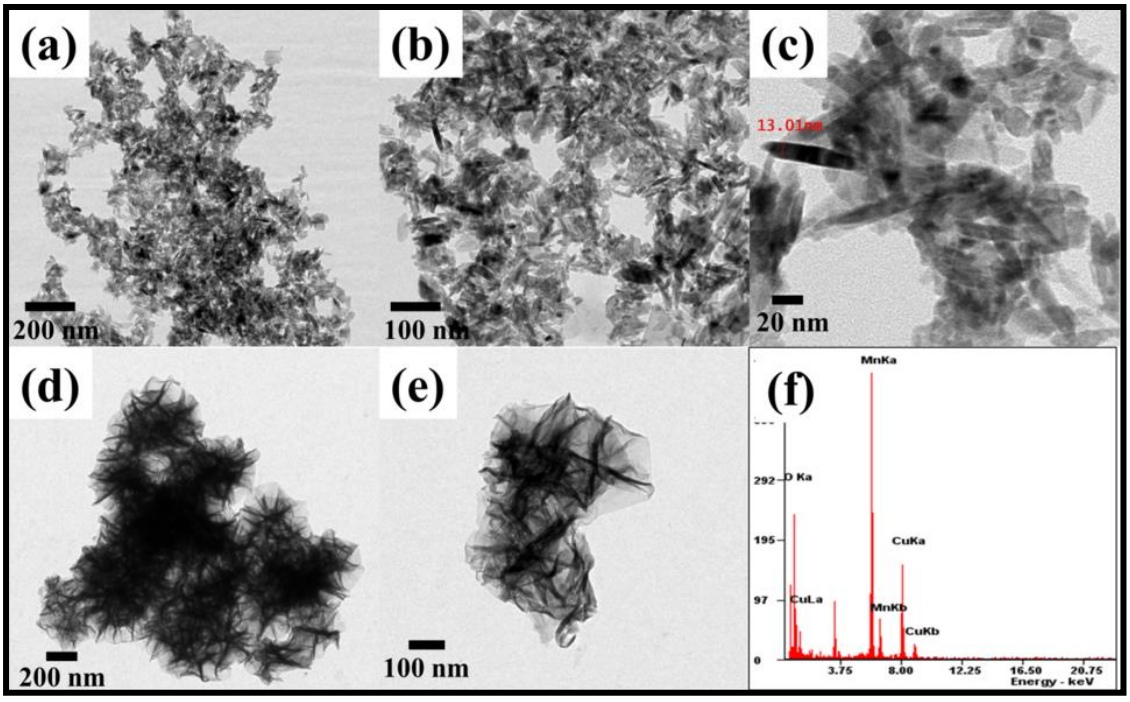


**Figure III.7** TEM images of as- prepared (a, b, c) pure CuO, and (d, e) CMO6 composite with different magnification. (f) EDAX spectrum of the CMO6 composite.

The TEM images of CuO and CMO6 composite are shown in Figure III.7. The nano-needle structures of CuO were again supported by the TEM images shown in

Figure III.7a-c. The length and width of each CuO nano-needle is of 80-100 nm and 10-15 nm, respectively. The TEM images of the CMO6 composite are shown in Figure III.7d-e having different magnifications. Figure III.7d-e denote that the CuO nano-needles were entirely wrapped by $MnO_2$ nanosheets in CMO6. The energy dispersive X-ray (EDAX) analysis spectrum (Figure III.7f) also confirms the presence of CuO in the composite.

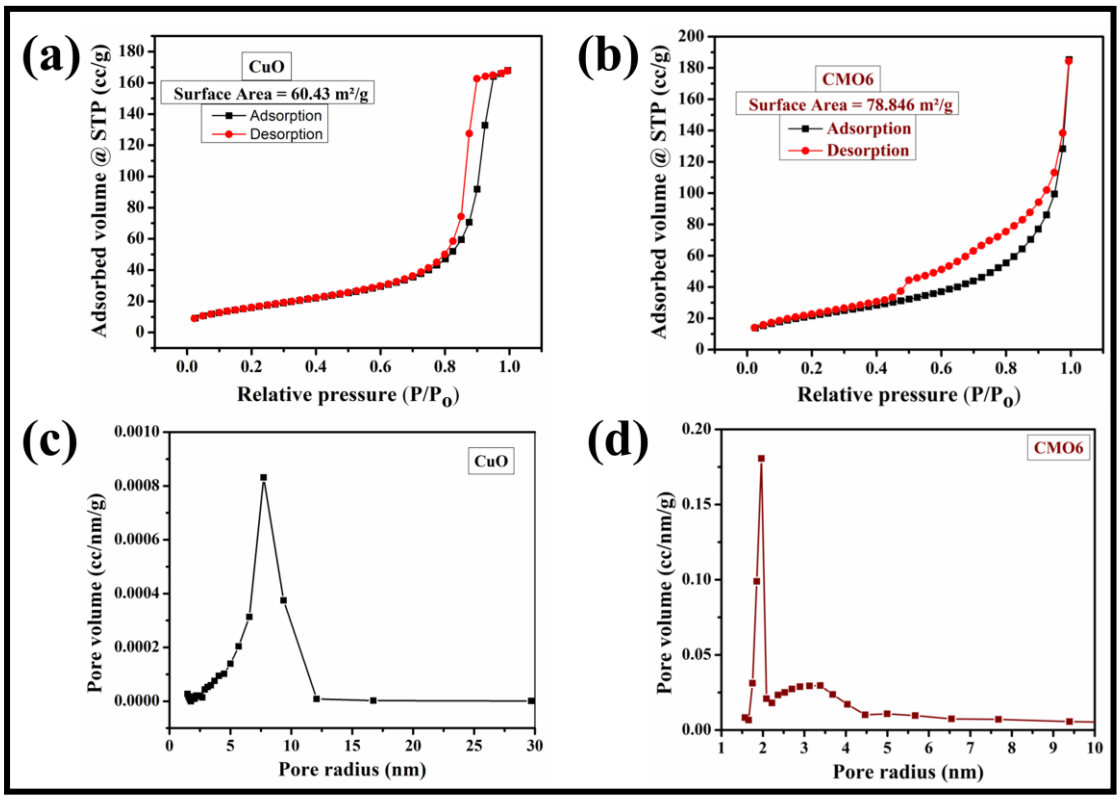


**Figure III.8** $N_2$ adsorption-desorption isotherms of (a) CuO and (b) CMO6 composite; BJH pore size distribution profile of (c) CuO and (d) CMO6 composite.

### *III.3.5 BET analysis*

The surface area plays crucial role in determining the efficiency of a material as an adsorbent or electrode material. The $N_2$ adsorption-desorption isotherms and Barrett-Joyner-Halenda (BJH) profiles confirm higher surface area and enhanced porosity in

the composites in comparison with the pure CuO nano-needles. The surface area of the pure CuO, CMO3 and CMO6 composites were obtained to be 60.43 $m^2/g$, 66.984 $m^2/g$ and 78.846 $m^2/g$, respectively, as measured by Brunauer-Emmett-Teller (BET) method. The BJH pore size distribution profile (Figure III.8b, III.9b and III.8d) shows perfectly monomodal distribution with the maxima of 7.73 nm, 1.79 nm and 1.96 nm for CuO nano-needle, CMO3 and CMO6 composite, respectively. According to the international union of pure and applied chemistry (IUPAC), all the BET isotherms show type-4 isotherm with H3 hystorysis loop. The highly porous nature of the composites appears due to the presence of highly mesoporous and ultrafine $MnO_2$ nanosheets which results in high electrochemical capacity of the nanocomposite (*vide infra*).

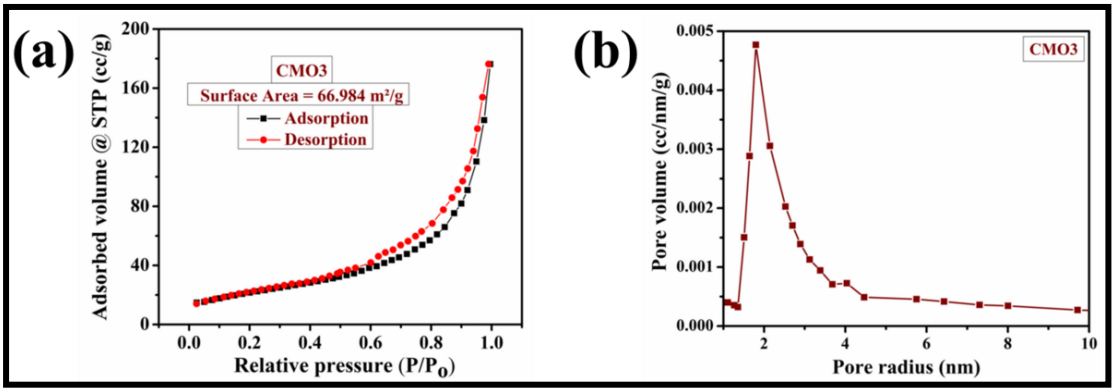


**Figure III.9** $N_2$ adsorption-desorption isotherms (a) and BJH pore size distribution profile (b) of CMO3 composite.

### *III.3.6 Electrochemical characterizations*

Electrochemical measurements were carried out using a computer-controlled electrochemical working station (Biologic SP 150 and Autolab potentiostat) with a conventional three-electrode electrochemical cell in 2 M KOH aqueous solution containing 0.3 M $K_3[Fe(CN)_6]$. The working electrode was prepared on Ni foam. A

platinum plate and a saturated calomel electrode (SCE) were used as counter electrode and reference electrode, respectively. The electrochemical behavior was analyzed in terms of cyclic voltammetry (CV), galvanostatic charge–discharge (GCD) curve and electrochemical impedance spectra (EIS). The specific capacitance of the electrode materials were calculated from CV and GCD measurements using eq 1 and 2, respectively.

$$C_s = \frac{\int_{V1}^{V2} i(V)dV}{2(V2-V1)vm} \quad \text{..... (1)}$$

$$C_s = \frac{i \times \Delta t}{m \times \Delta V} \quad \text{..... (2),}$$

where, $\int_{V1}^{V2} i(V)dV$ is the area of the CV curve, $\Delta V = (V2 - V1)$ is the potential window (V), $v$ is the scan rate (mV/s) and m is the mass (g) of the active materials, $i$ is the applied current (A), and $\Delta t$ is the discharge time (s).

After fabrication of the working electrode, the electrochemical characterizations were carried out in terms of cyclic voltammetry (CV), galvanostatic charge-discharge (GCD) and electrochemical impedance spectroscopy (EIS). The CV curves of CuO and CMO6 composites at various scan rates in 2 M KOH electrolyte solution containing 0.3 M $K_3[Fe(CN)_6]$ are shown in Figure III.10a and 10b, respectively. Both the CV curves show very high value of current, indicating the high activity of the redox electrolyte. The comparison of CV curves of all the as-synthesized materials at 10 mV/s is shown in Figure III.10c. The high area of the CV curve of CMO6 indicates higher capacitance of the composite than pure CuO and CMO3 composite. The redox active electrolyte surpluses electron density in conventional electrolyte, improving the ionic conductivity of the electrolyte and enhances the charge storage properties. Furthermore, shift of the oxidation and

reduction potential peaks with increasing scan rate indicates the quasi-reversible nature of the pseudocapacitive electrode materials in presence of the redox active electrolyte. The oxidation peak among the pair of redox peaks in the CV curves appears due to the charging process, involving the conversion of $K_4[Fe(CN)_6]$ to $K_3[Fe(CN)_6]$, whereas the reduction peak involves the reverse reaction. The specific capacitance of 7521, 1839, 1051, 872, 745 and 615 F/g were calculated for CMO6 electrode at the scan rate of 1, 10, 20, 50, 100, and 200 mV/s, respectively. But the pristine CuO achieved the capacitance of 7363, 1239, 757, 381, 219 and 125 F/g at the scan rate of 1, 10, 20, 50, 100, and, 200 mV/s, respectively. Furthermore, the CMO3 composite shows the specific capacitance of 5354, 1021.5, 686, 391, 244.8 and 152 F/g at the scan rate of 1, 10, 20, 50, 100 and 200 mV/s, respectively. One interesting point is that the pristine CuO exhibited better electrochemical performance at low scan rate than at high scan rate. This may be due to lower rate capability of CuO electrode. The CMO6 composite having high rate capability, shows better performance throughout the whole range of scan rate. At higher scan rate, the electrolyte ions do not get enough time to completely diffuse inside the electrode pores; hence the capacitance comes mainly from the outer surface of the materials. Whereas at lower scan rate, not only the outer surface Faradaic redox reactions, but also the diffusion processes within the pores contribute to the total capacitance. Therefore, the porosity of the materials may affect the ion diffusion kinetics depending on the pore size which influences the rate capability performance. The BET analysis (Figure III.8a, and 8b) exhibited that the CMO6 composite has higher surface area as well as high pore volume than the pure CuO. Hence the CMO6 exposes more number of redox active site to the electrolyte ions and shows remarkable performance. Although CMO3 composite has high surface area and pore

volume as compared to pure CuO, probably the small pore size of CMO3 makes it barely accessible for the electrolytes ions leading to lower diffusional capacitance of the composite at low scan rate than that in pure CuO.

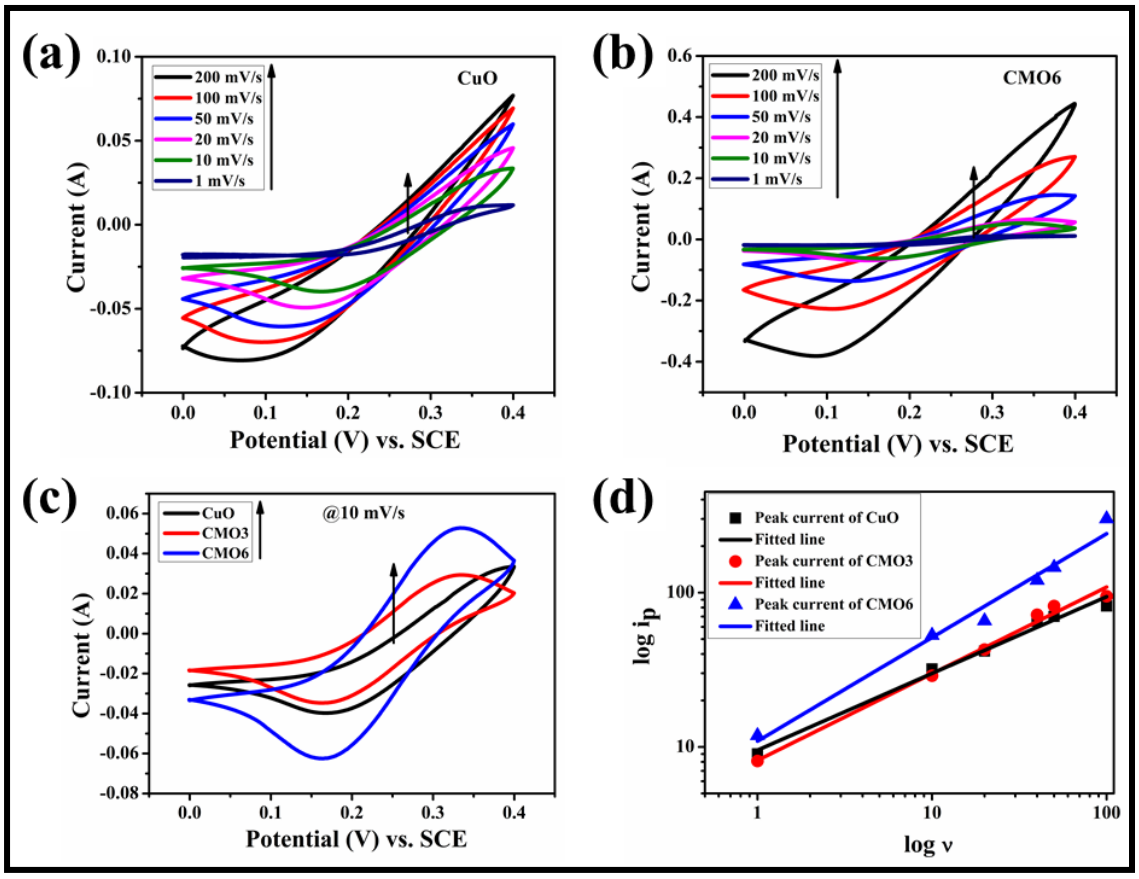


**Figure III.10** CV plot of (a) pure CuO and (b) CMO6 composite in 2 M KOH containing 0.3 M $K_3[Fe(CN)_6]$ at different scan rate. (c) CV curves of all the materials at a scan rate of 10 mV/s. (d) Log $i_p$ *vs* log ν plot of as-synthesized CuO and CuO-$MnO_2$ composites.

The total current generated in CV is the combination of diffusion controlled Faradaic redox current and non-diffusion controlled capacitive current. These different types of current contribution can be calculated quantitatively using Power law: $i_p = a\ \upsilon^b$ where, $i_p$ is the anodic peak current, υ is the scan rate (mV/s), a and b are the adjustable parameters [29]. The value of b gives the idea about the extent of

diffusion controlled Faradaic redox current and non-diffusion controlled capacitive current. A 0.5 value of b signifies the ideal diffusion controlled Faradaic redox process, whereas the non-diffusion controlled capacitive current is expressed by a unit value of b. The value of b is easily calculated from the slope of the log ($i_p$) vs log (υ) linear curve. From the Figure 7d, the value of b is calculated to be 0.51, 0.56 and 0.67 for CuO, CMO3 and CMO6, respectively, indicating that the capacitances of the electrodes are mainly contributed by diffusion controlled Faradaic redox charge transfer process.

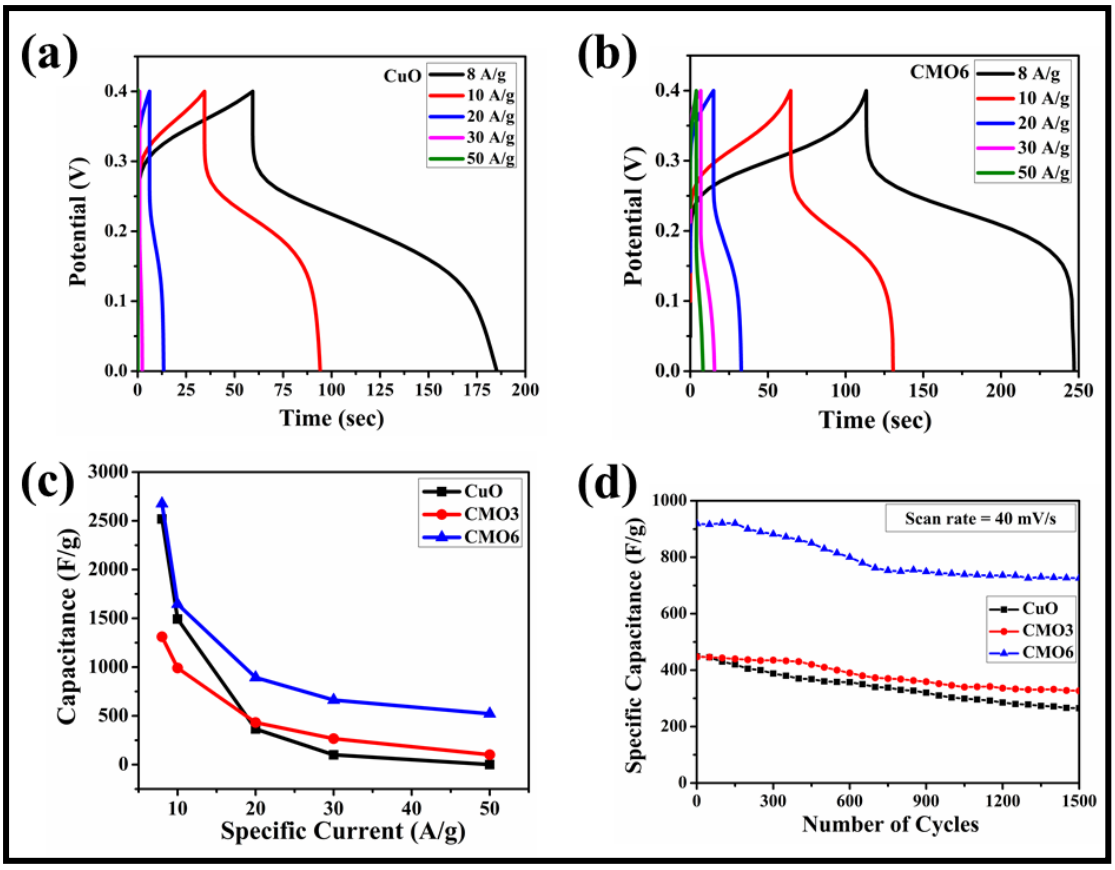


**Figure III.11** GCD curves of (a) pure CuO, and (b) CMO6 composite in 2 M KOH containing 0.3 M $K_3[Fe(CN)_6]$ at different current density. (c) Capacitance vs specific current plot and (d) % change in the specific capacitance vs number of CV cycles of as-synthesized CuO, CMO3 and CMO6 composite.

The galvanostatic charge-discharge (GCD) curves of CuO and CMO6 at various specific current with a potential window of 0.0 – 0.4 V in mixed 2 M KOH and 0.3 M $K_3[FeCN_6]$ are shown in Figure III.11a and 11b. The non-linear behavior of the discharge curves indicates the Faradaic redox reactions of pseudocapacitive electrodes and the redox active electrolyte. Furthermore, it is seen that the discharge times are always larger than the charging time at all specific current, implies the high columbic efficiency of the electrode which is really promising. The specific capacitance of 2690, 1641, 889, 668 and 539 F/g were calculated at specific current of 8, 10, 20, 30 and 50 A/g, respectively, for the CMO6 composite electrode. While the bare CuO achieved the specific capacitance of 2519, 1492.7, 365, 100 and 1 F/g at specific current of 8, 10, 20, 30 and 50 A/g, respectively. The CMO6 composite shows very high electrochemical performance in redox mediated electrolyte which is very high compared to previously reported literature (Table III.1).

With increasing the specific current, specific capacitance of both the electrode decreases as the electrons and ions gets lower time to diffuse into the electrode at high current density. Furthermore, with the increase in current density from 8 A/g to 50 A/g, the capacitance of CuO, CMO3 and CMO6 composite retained 0.04%, 7.7% and 20%, respectively (Figure III.11c). So, the CMO6 composite shows better rate capability performance in comparison with the bare CuO and CMO3 composite. Even at high current density of 50 A/g, it provides high capacitance of 539 F/g, indicating higher stability and better electrochemical performance of the CMO6 electrode. The cycle stability of the as-synthesized materials was studied at a scan rate of 40 mV/s in the same electrolyte which shows the 59%, 73% and 79% capacitance retention after 1500 CV cycles of pure CuO, CMO3 and CMO6 (Figure III.11d), respectively.

**Table III.1:** Specific capacitance of CuO-$MnO_2$ composite reported earlier.

| Materials | Capacitance | Specific Current | Electrolyte | Reference |
|---|---|---|---|---|
| Diatom@CuO@$MnO_2$ | 240 F/g | 0.5 A/g | 1 M $Na_2SO_4$ | 7 |
| Cu/CuO@$MnO_2$ | 177 mF cm-2 | 0.5 $mA/cm^2$ | 1 M KOH | 6 |
| CuO@$MnO_2$ | 252.6 F g1 | 0.1 A/g | 1 M $Na_2SO_4$ | 5 |
| CuO/$MnO_2$ | 228 F/g | 0.25 A/g | 1 M $Na_2SO_4$ | 4 |
| CuO@$MnO_2$ | 276 F/g | 0.6 A/g | 1 M $Na_2SO_4$ | 2 |
| CuO-$MnO_2$ | 2690 F/g | 8 A/g | 2 M KOH + 0.3 M $K_3[Fe(CN)_6]$ | This Work |

The electrochemical impedance spectra were recorded in the frequency range of 200 kHz-0.2 Hz, with sinus amplitude of 10 mV, and expressed in terms of Nyquist plot (Figure III.12) which depicts real and imaginary part of the complex impedance. The bare CuO nano-needle shows very high magnitude of x-axis ($Z_{Re}$) intercept, indicating high equivalent series resistance ($R_s$) than the composite. Further, in high frequency region, the smaller diameter of the semi-circle of the composite implies that it has lower charge transfer resistance ($R_{ct}$) compared to the bare CuO. The $R_s$ and $R_{ct}$ values of CMO6 composite are lower than the pristine CuO and CMO3 composite [Table III.2], suggesting the high electrochemical performance of the CMO6 composite for supercapacitor application.

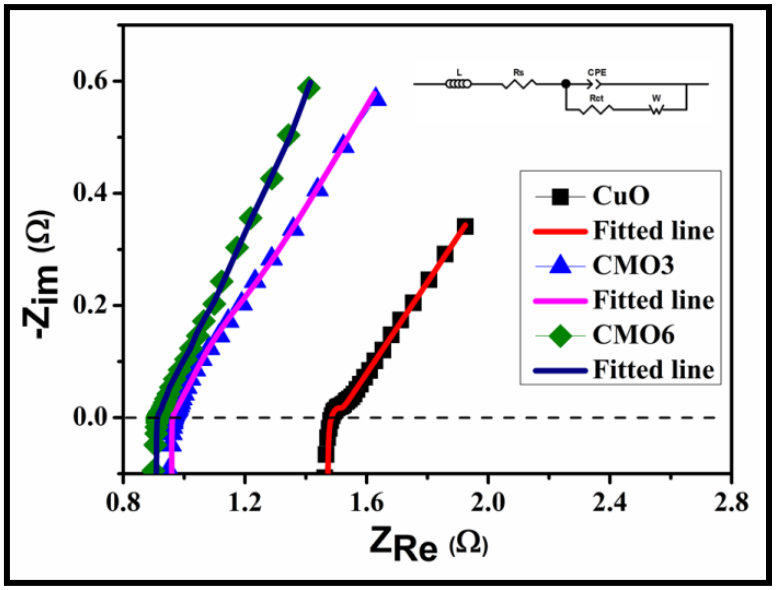


**Figure III.12** (a) Nyquist plots for CuO and $MnO_2$-CuO composite (inset: the corresponding equivalent circuit.

**Table III.2:** Values of different parameters calculated from equivalent circuit model of pure CuO, CMO3 and CMO6 composite

| Electrode | Inductor (H) | $R_s$ (Ω) | $R_{ct}$ (Ω) | W ( Ω $s^{-1}$) |
|---|---|---|---|---|
| CuO | 1.06 X $10^{-6}$ | 1.47 | 0.036 | 0.715 |
| CMO3 | 0.15 X $10^{-6}$ | 0.96 | 0.012 | 1.048 |
| CMO6 | 0.14 X $10^{-6}$ | 0.91 | 0.010 | 1.251 |

## III.4 Conclusions

A simple and cost effective precipitation approach in combination with conventional hydrothermal method was adopted for fabrication of $MnO_2$-CuO nanocomposites (CMO3 and CMO6). In the composites the CuO nano-needles are uniformly covered with $MnO_2$ nano-sheets. The synthesized materials were characterized using different microscopic and spectroscopic tools. The work beautifully describes a comparative

study of the electrochemical behavior of the composites in a redox mediated electrolyte (0.3 M $K_3[Fe(CN)_6]$ in 2 M KOH). The as-synthesized CMO6 composite with highest surface area and porosity displays the highest value of capacitance when compared to CuO and CMO3. The CMO6 composite achieved high specific capacitance of 2690 F/g at current density of 8 A/g with better rate capability. The results of the electrochemical studies imply that the composite CMO6 could be a promising electrode material for supercapacitor application.

## References

[1] Zhang, Y.X.; Li, F.; Huang, M. One-step hydrothermal synthesis of hierarchical $MnO_2$-coated CuO flower-like nanostructures with enhanced electrochemical properties for supercapacitor. *Mater. Lett.* **2013**, *112*, 203-206.

[2] Huang, M.; Zhang, Y.; Li, F.; Wang, Z.; Hu, N.; Wen, Z.; Liu, Q. Merging of Kirkendall growth and Ostwald ripening: CuO@$MnO_2$ core-shell architectures for asymmetric supercapacitors. *Sci. Rep.* **2014**, *4*, 4518.

[3] Dubey, R.; Guruviah, V. Review of carbon-based electrode materials for supercapacitor energy storage. *Ionics* **2019**, *25*, 1419-1445.

[4] Zhang, Z.; Ma, C.; Huang, M.; Li, F.; Zhu, S.; Hua, C.; Yu, L.; Zheng, H.; Hu, X.; Zhang, Y. Birnessite $MnO_2$-decorated hollow dandelion-like CuO architectures for supercapacitor electrodes. *J. Mater. Sci.: Mater. Electron.* **2015**, *26*, 4212-4220.

[5] Guo, X.L.; Li, G.; Kuang, M.; Yu, L.; Zhang, Y.X. Tailoring kirkendall effect of the $KCu_7S_4$ microwires towards CuO@$MnO_2$ core-shell nanostructures for supercapacitors. *Electrochim. Acta* **2015**, *174*, 87-92.

[6] Wang, X.; Chen, C.; Chen, K.; Chen, H.; Jun Yuan, S. $MnO_2$ nanosheets-decorated CuO nanoneedles arrays@ Cu foils for supercapacitors. *Int. J. Electrochem. Sci.* **2016**, *11*, 3425-3435.

[7] Zhang, Y.; Guo, W.W.; Zheng, T.X.; Zhang, Y.X.; Fan, X. Engineering hierarchical Diatom@ CuO@$MnO_2$ hybrid for high performance supercapacitor. *Appl. Surf. Sci.* **2018**, *427*, 1158-1165.

[8] Chen, Q.; Heng, B.; Wang, H.; Sun, D.; Wang, B.; Sun, M.; Guan, S.; Fu, R.; Tang, Y. Controlled facile synthesis of hierarchical CuO@$MnO_2$ core–shell nanosheet arrays for high-performance lithium-ion battery. *J. Alloys Compd.* **2015**, *641*, 80-86.

[9] Zeng, C., Gao, C., Yuan, L., Liang, T., Yang, R., Zhang, W. and Nie, S. Water evaporation-induced self-assembly of hierarchical CuO/$MnO_2$ composite nanospheres and their applications in Lithium-ion batteries. *Nano* **2017**, *12*, 1750022.

[10] Yang, Z.; Yang, Y.; Zhu, X.; Chen, G.; Zhang, W. An outward coating route to CuO/$MnO_2$ nanorod array films and their efficient catalytic oxidation of acid fuchsin dye. *Ind. Eng. Chem. Res.* **2014**, *53*, 9608-9615.

[11] Pal, J.; Mondal, C.; Sasmal, A.K.; Ganguly, M.; Negishi, Y.; Pal, T. Account of nitroarene reduction with size-and facet-controlled CuO–$MnO_2$ nanocomposites. *ACS Appl Mater Interfaces* **2014**, *6*, 9173-9184.

[12] Luo, X.; Liang, H.; Qu, F.; Ding, A.; Cheng, X.; Tang, C.Y.; Li, G. Free-standing hierarchical α-$MnO_2$@CuO membrane for catalytic filtration degradation of organic pollutants. *Chemosphere* **2018**, *200*, 237-247.

[13] Norsic, C.; Tatibouët, J.M.; Batiot-Dupeyrat, C.; Fourré, E. Methanol oxidation in dry and humid air by dielectric barrier discharge plasma combined with $MnO_2$–CuO based catalysts. *Chem. Eng. J.* **2018**, *347*, 944-952.

[14] Qian, K.; Qian, Z.; Hua, Q.; Jiang, Z.; Huang, W. Structure–activity relationship of CuO/$MnO_2$ catalysts in CO oxidation. *Appl. Surf. Sci.* **2013**, *273*, 357-363.

[15] Prathap, M.A.; Sun, S.; Wei, C.; Xu, Z.J. A novel non-enzymatic lindane sensor based on CuO–$MnO_2$ hierarchical nano-microstructures for enhanced sensitivity. *Chem. Commun.* **2015**, *51*, 4376-4379.

[16] Bhuvaneshwari, S.; Papachan, S.; Gopalakrishnan, N. Free standing CuO-$MnO_2$ nanocomposite for room temperature ammonia sensing. *AIP Conf. Proc.* **2017**, *1832*, 050126.

[17] Wessells, C.D.; Huggins, R.A.; Cui, Y. Copper hexacyanoferrate battery electrodes with long cycle life and high power. *Nat. Commun.* **2011**, *2*, 1-5.

[18] Kaipannan, S.; Marappan, S. Fabrication of 9.6 V high-performance asymmetric supercapacitors stack based on nickel hexacyanoferrate-derived $Ni(OH)_2$ nanosheets and bio-derived activated carbon. *Sci. Rep.* **2019**, *9*, 1-14.

[19] Subramani, K.; Jeyakumar, D.; Sathish, M. Manganese hexacyanoferrate derived $Mn_3O_4$ nanocubes–reduced graphene oxide nanocomposites and their charge storage characteristics in supercapacitors. *Phys. Chem. Chem. Phys.* **2014**, *16*, 4952-4961.

[20] Huang, M.; Zhang, Y.; Li, F.; Zhang, L.; Wen, Z.; Liu, Q. Facile synthesis of hierarchical $Co_3O_4$@ $MnO_2$ core–shell arrays on Ni foam for asymmetric supercapacitors. *J. Power Sources* **2014**, *252*, 98-106.

[21] Kliche, G.; Popovic, Z.V. Far-infrared spectroscopic investigations on CuO. *Phys. Rev. B* **1990**, *42*, 10060.

[22] Ethiraj, A.S.; Kang, D.J. Synthesis and characterization of CuO nanowires by a simple wet chemical method. *Nanoscale Res. Lett.* **2012**, *7*, 70.

[23] Chen, L.; Li, L.; Li, G. Synthesis of CuO nanorods and their catalytic activity in the thermal decomposition of ammonium perchlorate. *J. Alloys Compd.* **2008**, *464* 532-536.

[24] Zhao, B.; Liu, P.; Zhuang, H.; Jiao, Z.; Fang, T.; Xu, W.; Lu, B.; Jiang, Y. Hierarchical self-assembly of microscale leaf-like CuO on graphene sheets for high-performance electrochemical capacitors. *J. Mater. Chem. A* **2013**, *1*, 367-373.

[25] Khan, R.; Vaseem, M.; Jang, L.W.; Yun, J.H.; Hahn, Y.B.; Lee, I.H. Low temperature preparation of CuO nanospheres and urchin-shaped structures via hydrothermal route. *J. Alloys Compd.* **2014**, *609*, 211-214.

[26] Zheng, L.; Liu, X. Solution-phase synthesis of CuO hierarchical nanosheets at near-neutral pH and near-room temperature. *Mater. Lett.* **2007**, *61*, 2222-2226.

[27] Huang, M.; Zhang, Y.; Li, F.; Zhang, L.; Ruoff, R.S.; Wen, Z.; Liu, Q. Self-assembly of mesoporous nanotubes assembled from interwoven ultrathin birnessite-type $MnO_2$ nanosheets for asymmetric supercapacitors. *Sci. Rep.* **2014**, *4*, 3878.

[28] Tang, B.; Wang, G.; Zhuo, L.; Ge, J. Novel dandelion-like beta-manganese dioxide microstructures and their magnetic properties. *Nanotechnology* **2006**, *17*, 947.

[29] Ray, A.; Roy, A.; Saha, S.; Ghosh, M.; Roy Chowdhury, S.; Maiyalagan, T.; Bhattacharya, S.K.; Das, S. Electrochemical energy storage properties of Ni-Mn-oxide electrodes for advance asymmetric supercapacitor application. *Langmuir* **2019**, *35*, 8257-8267.

# Chapter IV

*Aqueous asymmetric supercapacitor based on electro-synthesized Mn−Co−S nanosheets and rGO electrode*

## IV.1 Introduction

Supercapacitor or electrochemical capacitor, with some unique properties such as high power density, moderate energy density, low charging time, high cyclic stability and environmental friendliness, can be developed as an alternative energy storage device which can bridge between battery and conventional capacitors [1, 2]. For this reason, supercapacitors find promising application in various electronic gadgets like, smartphones, smartwatches, etc. However, the main disadvantage which creates the barrier for its practical usage is the lack of high specific energy. To overcome this issue, scientists are keen to find proper combination of active electrode materials, electrolytes, and separators which have important role in supercapacitor's overall performances [3, 4].

The previous chapter described the electrochemical performance of manganese based combinatorial transition metal oxides. However, electrochemical performances of the various transition metal sulfides, an important class of inorganics, such as MnS [5-7], CoS [8, 9] and NiS [10, 11] have been thoroughly investigated and reported as high performance supercapacitive electrode materials. Recently, binary metal sulfides such as Mn-Ni-S [12-14], Co-Ni-S [15-18], and Mn-Co-S [19-22] have attracted enormous attention due to their large number of redox active sites, high thermal stability and electrical conductivity compared to that of their corresponding unitary metal sulphides [23]. Cheng et al. achieved high specific capacitance of 1636.8 F/g at 2 A/g specific current with great cyclic stability for Ni-Mn sulfide hollow ellipsoids [14]. Also, the electrodeposited Mn-Ni-S attributes exceptionally high specific capacitance of 2849 F/g at 1 A/g specific current with an excellent rate capability, as reported by Ahmed et al. [12]. Wang et al. successfully developed vertically cross-

linked Mn-Co-S on Ni foam which showed high specific capacitance 2084 F/g at a specific current of 1 A/g [19]. In another work, Li et al. electrochemically co-deposited three-dimensional hierarchical porous Mn-Co-S nanosheets on Ni foam. The binder free electrode exhibited areal capacitance of 1.724 $F/cm^2$ at 1 $mA/cm^2$ [20]. Therefore by tuning the composition of the mixed-metal sulfides, required electrochemical performances can be achieved.

However, the most important point to be taken care of for the supercapacitor devices is the specific energy lack. With increasing potential window of the devices, the specific energy increases. The capacitive-type negative electrode has significant role to improve the specific energy of supercapacitor by offering the wider potential window in combination with the pseudocapacitor-type positive electrode. So, choosing a proper negative electrode is essential. The more commonly used negative electrode is activated carbon [24, 25]. However, graphene [26] or reduced graphene oxide [27-29], carbon nanotube [30], have been investigated recently as negative electrode due to their excellent characteristics such as large surface area, high electrical conductivity and outstanding electrochemical stability. The reduced graphene oxide (rGO) was used as negative electrode for this work.

Unlike some other methods which involve multistep and complicated process, electrochemical deposition is a simple, low cost, highly effective and convenient method to fabricate a uniformly extended nanostructure with large-area coverage in aqueous electrolyte [31]. Furthermore, it does not need any harsh conditions, even the morphology and thickness can be tuned easily by controlling the deposition parameters, such as, concentration of electrolytic solution, potential in potentiostatic electrodeposition, scan rate in potentiodynamic, current density in galvanostatic deposition, and time. The fast nucleation and growth on a large variety of conducting

substrates like Ni foam [8, 12] or wire [32], Cu foam [33, 34], stainless steel [35, 36], ITO coated glass [37, 38], carbon cloth [18, 39] or fiber [40, 41] facilitates its use in energy storage devices directly as binder free electrode.

Herein, we report a simple, single-step electrosythesis method for the construction of three dimensionally interconnected manganese-cobalt sulphide nanosheets on nickel foam (MnCoS@NF). The MnCoS@NF achieved high specific capacitance of 1952.8 F/g at 2 A/g scan rate with high performance rate. Thereafter, an aqueous asymmetric supercapacitor (AAS) was fabricated using Mn-Co-S nanosheets and reduced graphene oxide (rGO) nanosheets as positive and negative electrodes, respectively, which delivered the high specific capacitance of 360 F/g at 10 A/g with excellent rate capability.

## IV.2 Experimental Section

### *IV.2.1 Materials*

The chemicals were purchased from various commercial sources and used in this project without any prior treatment. Ni foam, cobalt chloride ($CoCl_2$), manganese acetate ($Mn(CH_3CO_2)_2$), thiourea ($CS(NH_2)_2$), $H_2SO_4$, ortho phosphoric acid, ethanol and acetone were purchased from Merck, India. Fine graphite powder, $H_2O_2$ were obtained from Loba chemie, Mumbai.

### *IV.2.2 Electrosynthesis of Mn-Co-S nanosheets on nickel foam (MnCoS@NF)*

The three dimensional (3D) interconnected Mn-Co-S nanosheets were synthesized via electrochemical deposition method using Autolab potentiostat (Scheme IV.1). A three-electrode cell system, containing Ni foam, Pt foil and Ag/AgCl electrode as working, counter and reference electrode, respectively, was constructed for the

deposition. The electrolyte was prepared by mixing of 10 mM $CoCl_2$, 10 mM $Mn(CH_3CO_2)_2$, and 100 mM thiourea in 50 mL millipore $H_2O$. Firstly, the Ni foam (1 cm X 1.5 cm) was immersed in 3 M HCl and ultrasonicated for 15 min to remove the nickel oxide layer. After that the Ni foam was washed with water and ethanol for 4-5 times and dried, which was directly used as working electrode. For the deposition, six cycles of the cyclic voltamogram was run with the potential window of -1.2 V and 0.2 V at the scan rate of 5 mV/s. The electrodeposited Ni foam was washed with plenty of DI water and dried at room temperature. The amount of mass loading on the Ni foam was calculated to be about 0.7 mg.

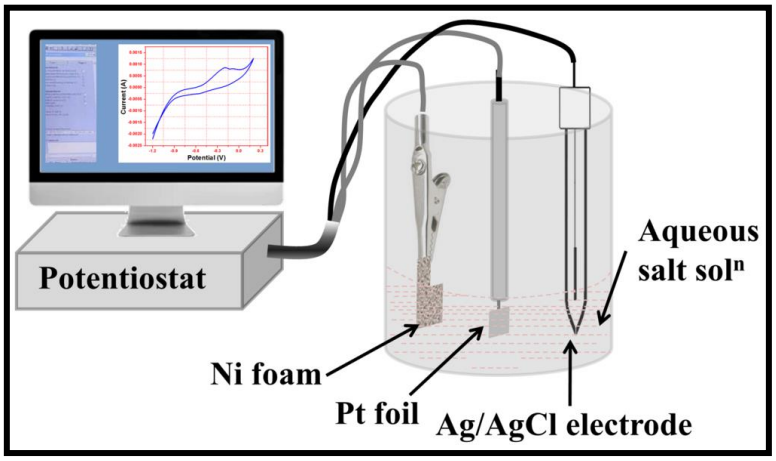


**Scheme IV.1** Electrosynthesis of Mn-Co-S nanosheets on nickel foam.

### *IV.2.3 Synthesis of reduced graphene oxide (rGO) nanosheets*

Reduced graphene oxide (rGO) was synthesized by the chemical reduction of graphene oxide using hydrazine solution. Firstly, graphene oxide (GO) was prepared by following modified Hummers' method [42]. Briefly, 1 g of commercially available fine graphite powder was dispersed in a mixture of concentrated $H_2SO_4$ and ortho-phosphoric acid with a ratio of 9:1. Then, 6 g of solid $KMnO_4$ powder was added pinch wise to avoid excess heating. After 12 h continuous stirring, required volume of

30% $H_2O_2$ was added to the whole mixture. Here a gradual color change from grenish to golden yellow to grey was observed. Finally, the GO powder was obtained after washing the solid material successively with 10% HCl, DI water and ethanol.

Reduced graphene oxide (rGO) was prepared by the reduction of the as-prepared GO using hydrazine hydrate [29]. Briefly, 50 mg GO powder was ultrasonicated in 30 mL of $H_2O$ for 30 min and then the mixture solution was heated at 95 ˚C. Two mL of hydrazine hydrate was added to it and the mixture was kept in stirring condition for a overnight at the same temperature. The solid product was collected, washed with water-ethanol mixture and subsequently dried at 60 ˚C.

### *IV.2.4 Construction of aqueous* **MnCoS@NF||rGO@NF** *asymmetric supercapacitor*

An aqueous asymmetric supercapacitor (AAS) was assembled using MnCoS@NF and rGO@NF as positive and negative electrode, respectively, with Whatman filter paper grade no. 42 (pore diameter of 2.5 μm) separator. This separator and both the electrodes were soaked in 2 M KOH aqueous electrolyte for 1 h and then these were finally assembled together to make the device. All electrochemical studies of the device were performed using the two-electrode cell setup.

## IV.3 Results and Discussion

The chemical composition of the as-prepared electrode materials were investigated by X-ray photoelectron spectroscopy instrument (ESCA+ Omicron Nanotechnology (Oxford Instruments). Using field emission scanning electron microscopy (FESEM, Carl Zeiss-SUPRA 40) the surface morphology of the electrode materials was

investigated. The electrochemical characterizations were performed using Autolab potentiostat and CorrTest electrochemical analyser.

The 3D interconnected Mn-Co-S nanosheets were grown on cleaned nickel foam by using cyclic voltammetry. For the uniform deposition of the nanosheets the CV were performed at slow scan rate. A silvery to yellow colour change was observed after deposition.

### *IV.3.1 Morphological analysis*

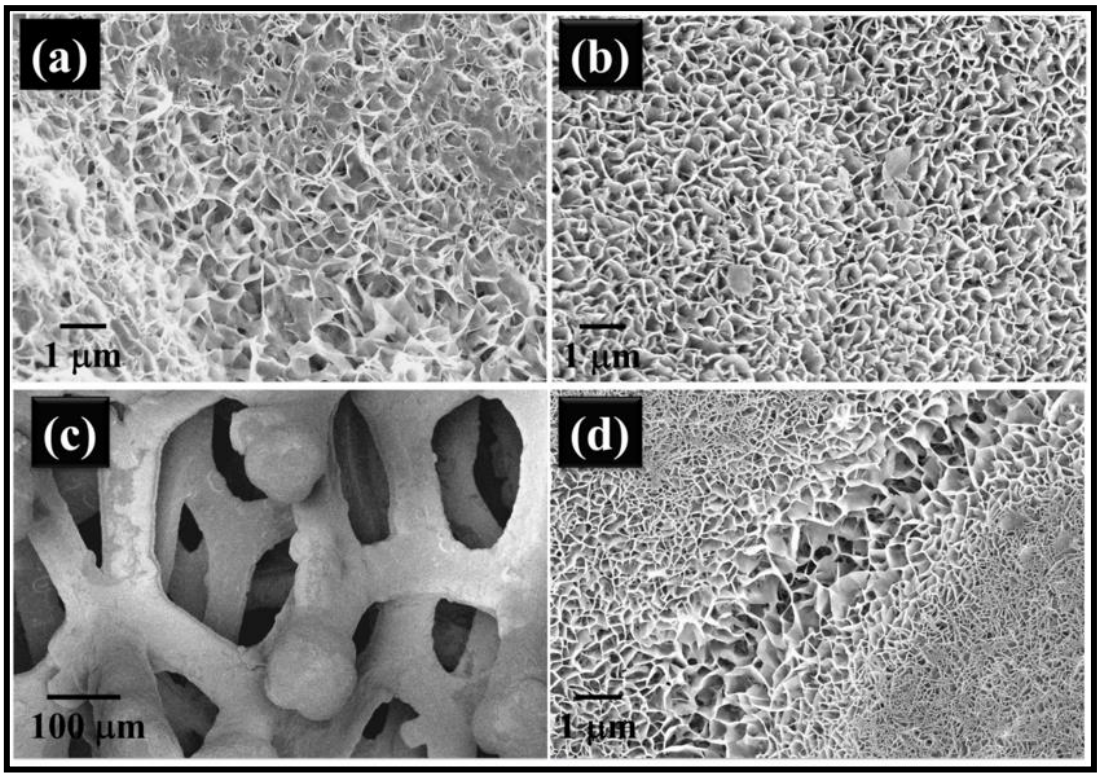


**Figure IV.1** FESEM images of the electrosynthesized (a) MnS, (b) CoS, (c) Mn-Co-S (in low magnification), and (d) Mn-Co-S (in high magnification) nanosheets grown on nickel foam.

The morphology of the as-prepared electrodeposited materials was investigated with FESEM and shown in Figure IV.1. The highly porous MnS, CoS and Mn-Co-S

nanosheets were grown on Ni foam to form 3D hierarchically interconnected nanosheets-like structures. This architecture of the as-synthesized materials facilitates the easy insertion/de-insertion of the electrolyte ions and improves the electrochemical performances.

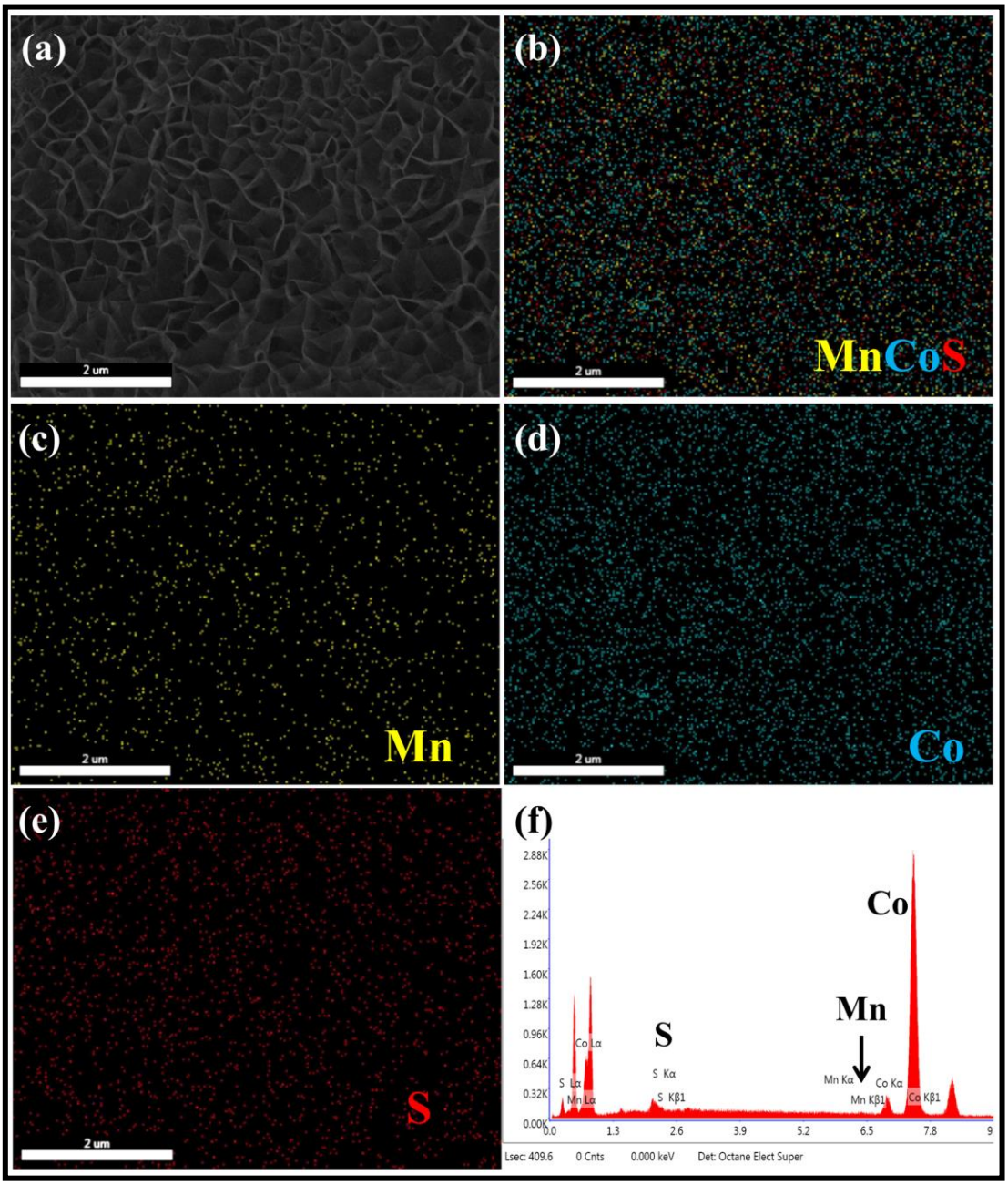


**Figure IV.2 (a-e)** Elemental mapping analysis including Mn, Co and S; (f) EDS spectrum of Mn-Co-S nanosheets.

The energy dispersive spectroscopy (EDS) element mapping images and EDS spectrum (Figure IV.2) of electrosynthesized Mn-Co-S nanosheets confirm the presence of Mn, Co and S. This can be clearly seen from the mapping images where the elements Mn, Co and S were seen to be uniformly distributed over the nickel foam. The nanosheet-like structure of rGO was observed from the FESEM and TEM images (Figure IV.3).

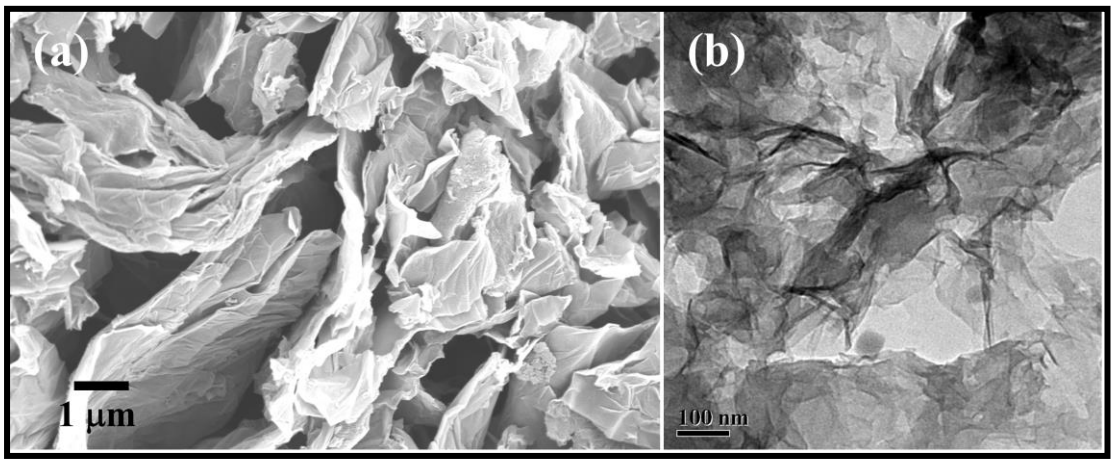


**Figure IV.3** (a) FESEM and (b) TEM images of rGO.

***IV.3.2 XPS study***

To examine the surface element with their oxidation state the XPS measurement was carried out. The nickel-foam supported Mn-Co-S nanosheets were directly used for XPS analysis. The survey spectrum (Figure IV.4a) of the Mn-Co-S clearly exhibited the peak for Co, Mn, S and O. The O may come from surface oxygen-containing functional groups [43, 44]. The peak for Ni from nickel foam was also observed from the uncovered places. The high magnified XPS spectra of Co, Mn and S are shown in Figure IV.4(b-d). The Mn 2p photoelectron spectrum consists of two doublet peaks of Mn $2p_{1/2}$ and Mn $2p_{3/2}$. The Mn $2p_{3/2}$ spectrum fits with two peaks at 645.8 eV and 642.9 eV corresponding for $Mn^{2+}$ and $Mn^{3+}$, respectively [43]. For Co 2p, two spin-

orbit doublets with two satellite peaks (787.5 eV and 802.5 eV) were identified in the spectrum. The peaks at 782.25 eV and 797.9 eV are attributed to $Co^{2+}$ whereas the peaks at 776.17 eV and 796.6 eV correspond for $Co^{3+}$ [44]. The two main peaks of in Figure IV.4d at 162.8 eV and 159.6 eV are consistent with S $2p_{1/2}$ and S $2p_{3/2}$, respectively, of metal-sulfur bonds. Therefore, XPS result suggests a composition of $Mn^{2+}$, $Mn^{3+}$, $Co^{2+}$, $Co^{3+}$, and $S^{2-}$ at the surface of MnCoS@NF.

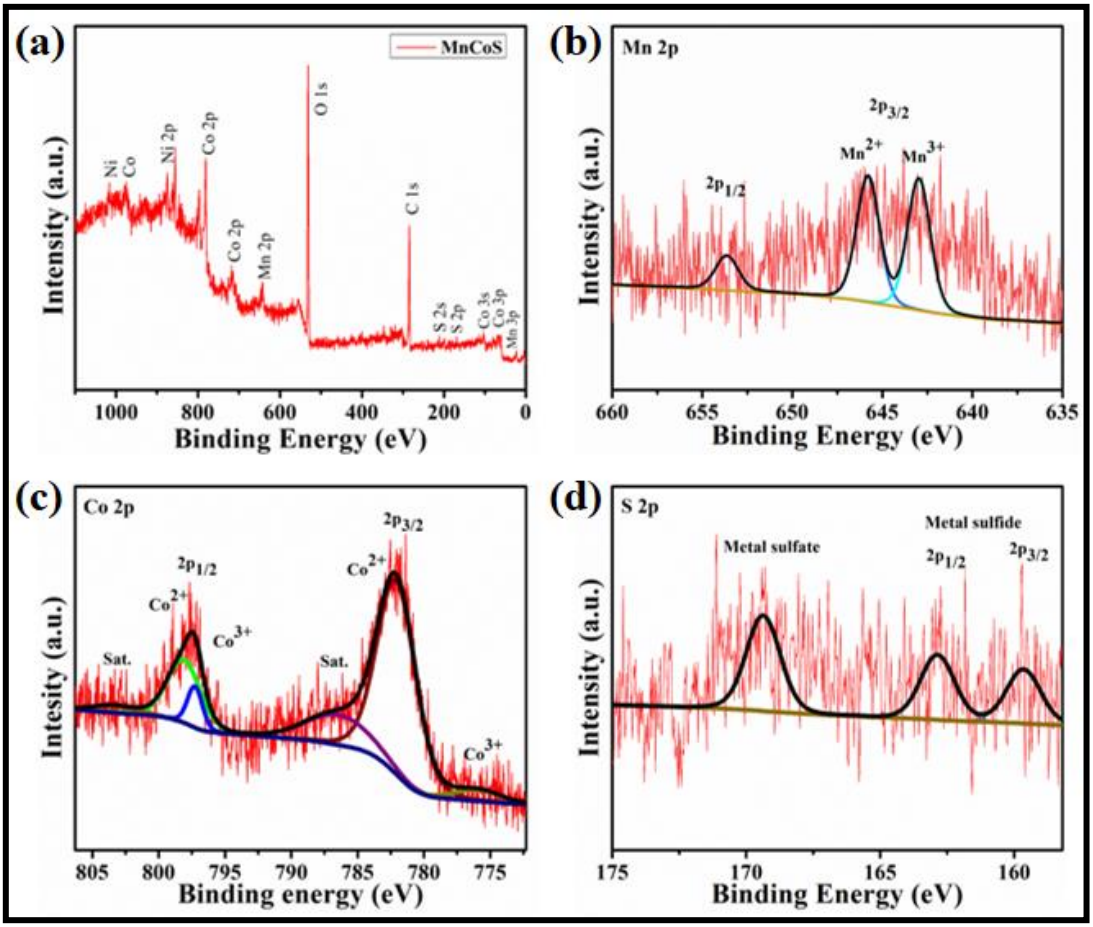


**Figure IV.4** (a) XPS spectrum (survey scan) of the Mn-Co-S nanosheets; Magnified view of (b) Mn 2p, (c) Co 2p and (d) S 2p level.

### *IV.3.3 XRD analysis*

The X-ray diffraction (XRD) analysis was performed using the Rigaku ULTIMA-III X-ray diffractometer with Cu Kα radiation (λ = 1.548 Å). The XRD patterns of GO

and rGO are shown in Figure IV.5. For GO, the characteristic peak of (001) plane of GO arises at 2θ = 10.2° which is missing in rGO indicating the successful reduction of GO. The corresponding peaks of (002) and (100) plane of rGO are located at 24.8° and 43°, respectively [45].

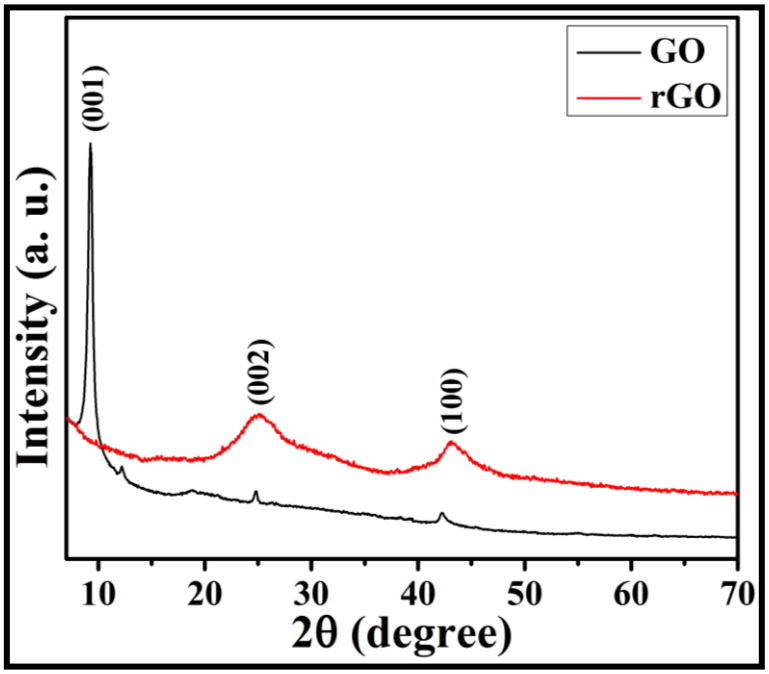


**Figure IV.5** XRD pattern of GO and rGO.

### *IV.3.4* Electrochemical characterizations

The electrochemical characterizations, i.e., cyclic voltammetry (CV), galvanostatic charge-discharge (GCD) and electrochemical impedance spectra (EIS) of the as-prepared materials were recorded in 2 M KOH electrolyte. Firstly, the electrochemical performance of the individual electrode was investigated using three-electrode cell setup using electrodeposited Ni foil, Pt foil and silver/silver chloride (Ag/AgCl) as working, counter and reference electrode, respectively. The working potential window of 0.0 – 0.45 V was chosen for MnCoS@NF electrode, whereas for rGO@NF it was -

1.0 – 0.0 V. The specific capacitance from the CV curve was calculated using the following equation:

$$\text{Specific capacitance, } \mathbf{C_S} = \frac{\int_{V1}^{V2} i(V)dV}{(V2-V1)\nu m} \qquad (1)$$

where, $\int_{V1}^{V2} i(V)dV$ is the area of CV curve, $(V2 - V1)$ is the potential window (V), $\nu$ is the scan rate (mV/s) and $m$ is the mass (g) of the active materials.

An aqueous asymmetric supercapacitor (AAS) was fabricated by assembling the Mn-Co-S@Ni foam and rGO@Ni foam as positive and negative electrodes, respectively. The negative electrode was prepared by casting the rGO paste on cleaned nickel foam. The rGO paste was prepared by mixing 95 wt% rGO and 5 wt% polyvinylidene fluoride (PVDF) in N-methyl-2-pyrrolidone (NMP) solvent. Then both the electrodes were sandwiched using a non-conducting Whatman filter paper as separator in between them. The electrodes and separator were soaked in 2 M KOH aqueous electrolyte for 1 h before assembling the device. In order to get the maximum performance in AAS, the charge balance theory ($Q_+ = Q_-$) was applied to calculate the mass ratio of the positive and negative electrodes following the equation below:

$$Q_+ = Q_- \qquad (2)$$

$$\Rightarrow C_+ * V_+ * m_+ = C_-*V_-*m_- \qquad (3)$$

where, C is specific capacitance (F/g), V is potential window (V), m is the mass of corresponding electrode (g).

The specific capacitance from GCD curves was calculated from the following equation:

$$\text{Specific capacitance, } \mathbf{C_S} = \frac{\boldsymbol{i} \times \Delta \boldsymbol{t}}{\boldsymbol{m} \times \Delta \boldsymbol{v}} \qquad (4)$$

where, $\boldsymbol{i}$ is applied current (A), $\Delta \boldsymbol{t}$ is the discharge time (s), $\boldsymbol{m}$ is the mass of active material (g), and $\Delta \boldsymbol{v}$ is potential window (V).

The specific energy (Wh/kg) and specific power (W/kg) were calculated using the following equations:

$$\text{Specific energy, } \mathbf{E} = \frac{\mathbf{1}}{\mathbf{2\ X\ 3.6}}\ \boldsymbol{C_S(\Delta V)^2} \qquad (5)$$

$$\text{Specific power, } \mathbf{P} = \frac{\boldsymbol{E}}{\Delta \boldsymbol{t}}\ \boldsymbol{X}\ \mathbf{3600} \qquad (6)$$

where, $\boldsymbol{C_S}$ is the specific capacitance (F/g), $\boldsymbol{\Delta V}$ is the potential window (V) and $\Delta \boldsymbol{t}$ is the discharging time (s).

### *IV.3.4.1 Electrochemical Performance of the as-prepared materials.*

The electrochemical performances of the as-prepared materials were carried out in terms of CV, GCD, and EIS using three-electrode system in 2 M KOH as electrolyte. The comparison of the electrochemical performances of MnS, CoS and Mn-Co-S nanosheets are shown in Figure IV.6. All the cyclic voltammetry curves show a couple of redox peaks, indicating pseudocapacitive nature of the materials. The bimetallic sulfide shows more intense specific current than the other two unimetallic sulfides, signifying high activity and specific capacitance. The redox peaks due to the redox reactions between $M^{2+}$ and $M^{3+}$ (M ≡ Mn and Co) can be expressed as following equations [46, 8]:

$$MS + OH^- \leftrightarrow M(OH)S + e^- \qquad (7)$$

$$M(OH)S + OH^- \leftrightarrow MOS + H_2O + e^- \qquad (8)$$

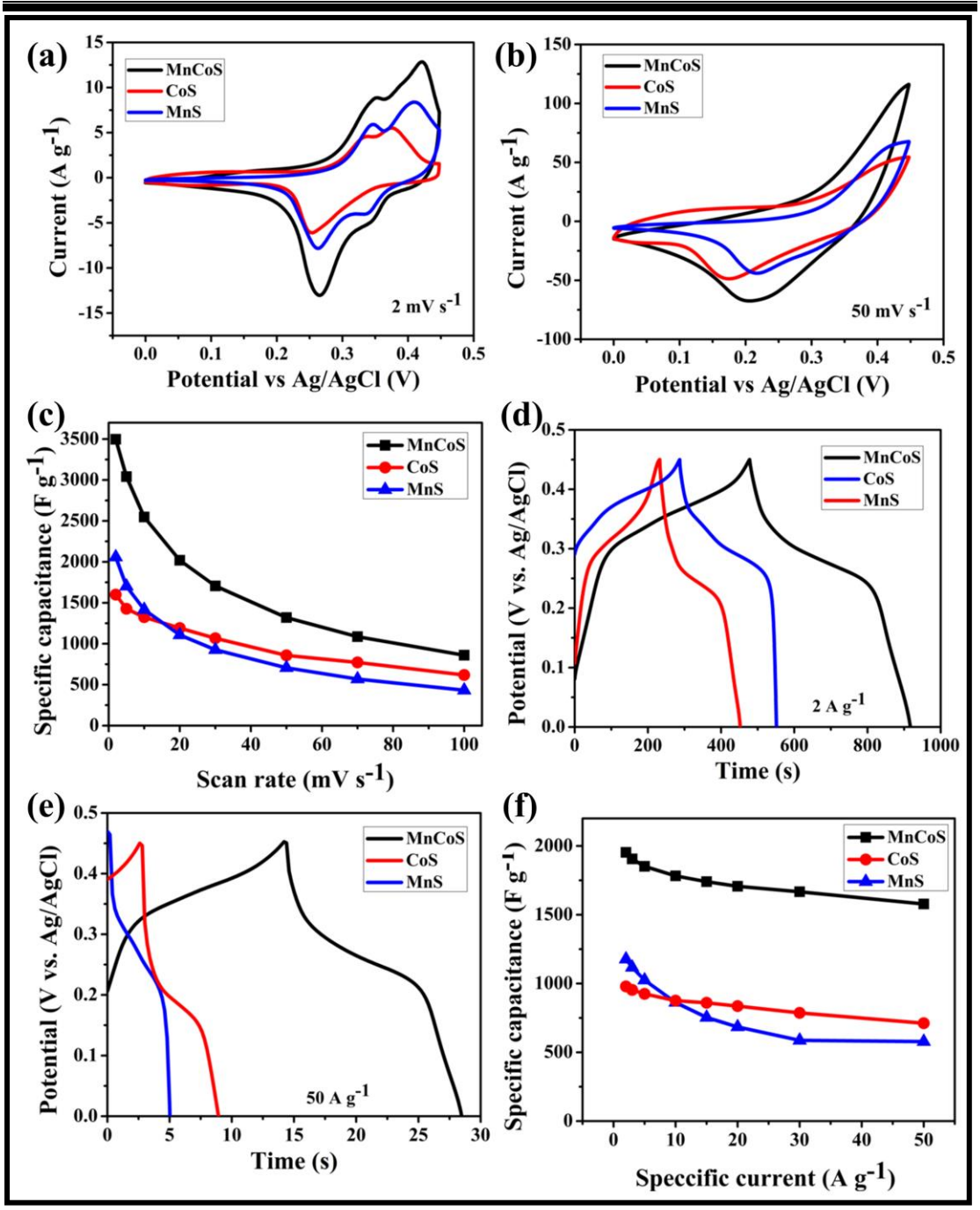


**Figure IV.6** Cyclic voltammograms of as prepared MnS, CoS, and MnCoS at (a) 2 mV/s and, (b) 50 mV/s; (c) variation of the specific capacitance with the scan rate; Galvanostatic charge-discharge curves of as prepared sulfides at (d) 2 A/g and, (e) 50 A/g; (f) Variation of the specific capacitance with the specific current.

The specific capacitance of the as-prepared materials were calculated at different scan rate and depicted in Figure IV.6c. The highest capacitance of 1599.6 F/g, 2058 F/g, and 3496 F/g were calculated for CoS, MnS, and Mn-Co-S, respectively, at the scan rate of 2 mV/s. The synergism between two metal sulphides having high capacitance causes the exceptionally high capacitance of the binary metal sulfide. Furthermore, at high scan rate of 50 mV/s, the Mn-Co−S sustained very high specific capacitance of 860 F/g. To investigate the charge storage and delivery capacity of as-prepared electrodes, GCD measurements were carried out at different specific current. Figure IV.6d represents the comparative charge-discharges curves of the as-prepared electrodes at 2 A/g. From very low specific current of 2 A/g to very high specific current of 50 A/g, the symmetric nature of the GCD curves indicating characteristics of battery-like performance. The specific capacitance of Mn-Co-S calculated from the GCD curves also exhibited exceptional specific capacitance showing synergism effect between MnS and CoS. The comparison between the specific capacitance of the as-prepared sulfides at different specific current is drawn in Figure IV.6f.

The CV curves of Mn-Co-S at different scan rates are shown in Figure IV.7a. The redox peaks were shifted with varying the scan rate due to the different diffusion rate of electrolyte ions. It can be seen that the cathodic peak current is approximately linear with the square roots of the scan rate shown in Figure IV.7c, indicating diffusion control charge storage process. This can also be calculated quantitatively using Power law: $i_p = a\ \upsilon^b$ where, $i_p$ is the cathodic peak current, $\upsilon$ is the scan rate (mV/s), a and b are the adjustable parameters [12, 47]. The value of b gives the idea about the charge storage phenomena. The value of b is easily evaluated by plotting log ($i_p$) vs log ($\upsilon$) which gives a linear relationship. The value of slope b = 0.5

signifies the ideal diffusion controlled Faradaic redox process, whereas b = 1 indicates non-diffusion controlled capacitive process. From the Figure IV.7d, the value of b is calculated to be 0.56 for Mn-Co-S, which indicates that charge is stored mainly by diffusion controlled Faradaic redox process. The specific capacitance were calculated of 3496, 3040.6, 2547.8, 2019, 1706, 1319.6, and 860 F/g at 2, 5, 10, 20, 30, 50 and 100 mV/s, respectively. The GCD curves of Mn-Co-S at different specific currents are depicted in Figure IV.7b, indicating battery like supercapacitive characteristics. The maximum (1952.9 F/g) and minimum (1577.7 F/g) specific capacitance achieved by Mn-Co-S were much higher than those of MnS and CoS.

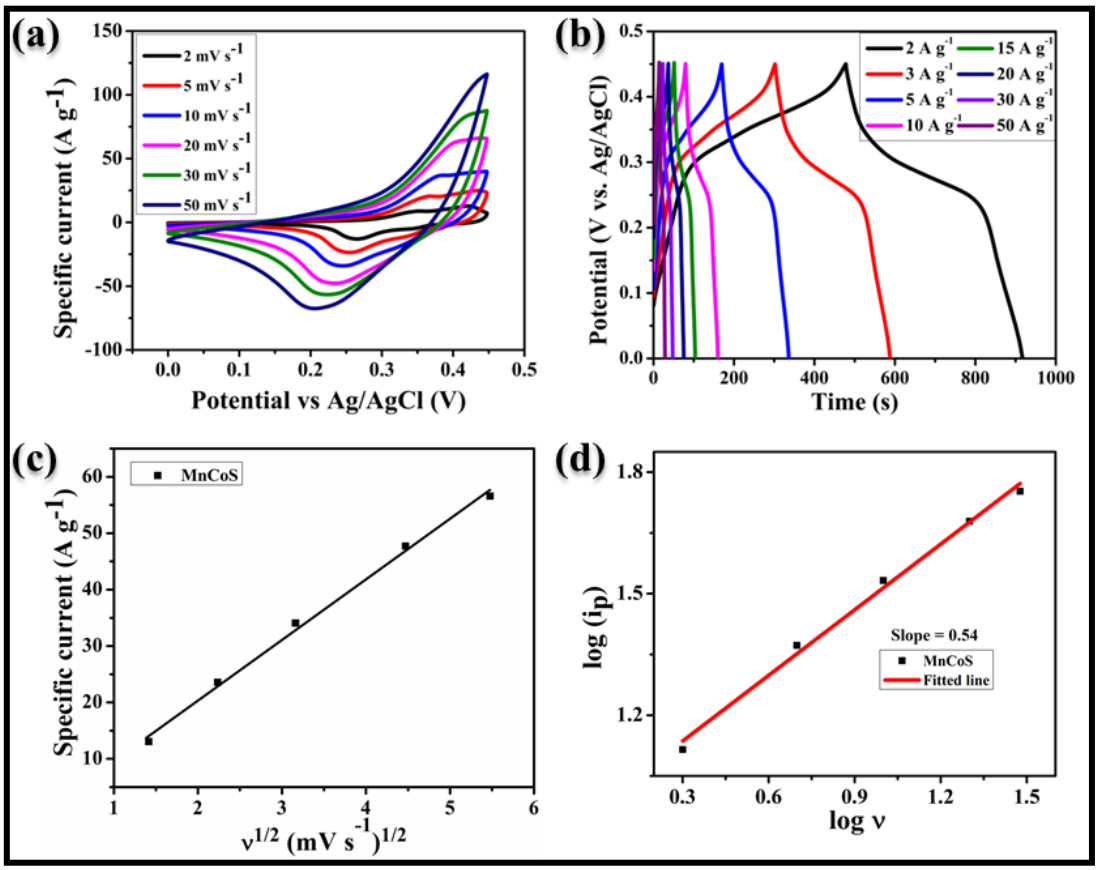


**Figure IV.7** (a) Cyclic voltammograms of Mn-Co-S at different scan rates; (b) Galvanostatic charge-discharge curves of of Mn-Co-S at different specific current; (c) The cathodic peak current vs square root of various scan rates plot of Mn-Co-S electrode, (d) log ($i_p$) vs log ν plot of as-synthesized Mn-Co-S nanosheets.

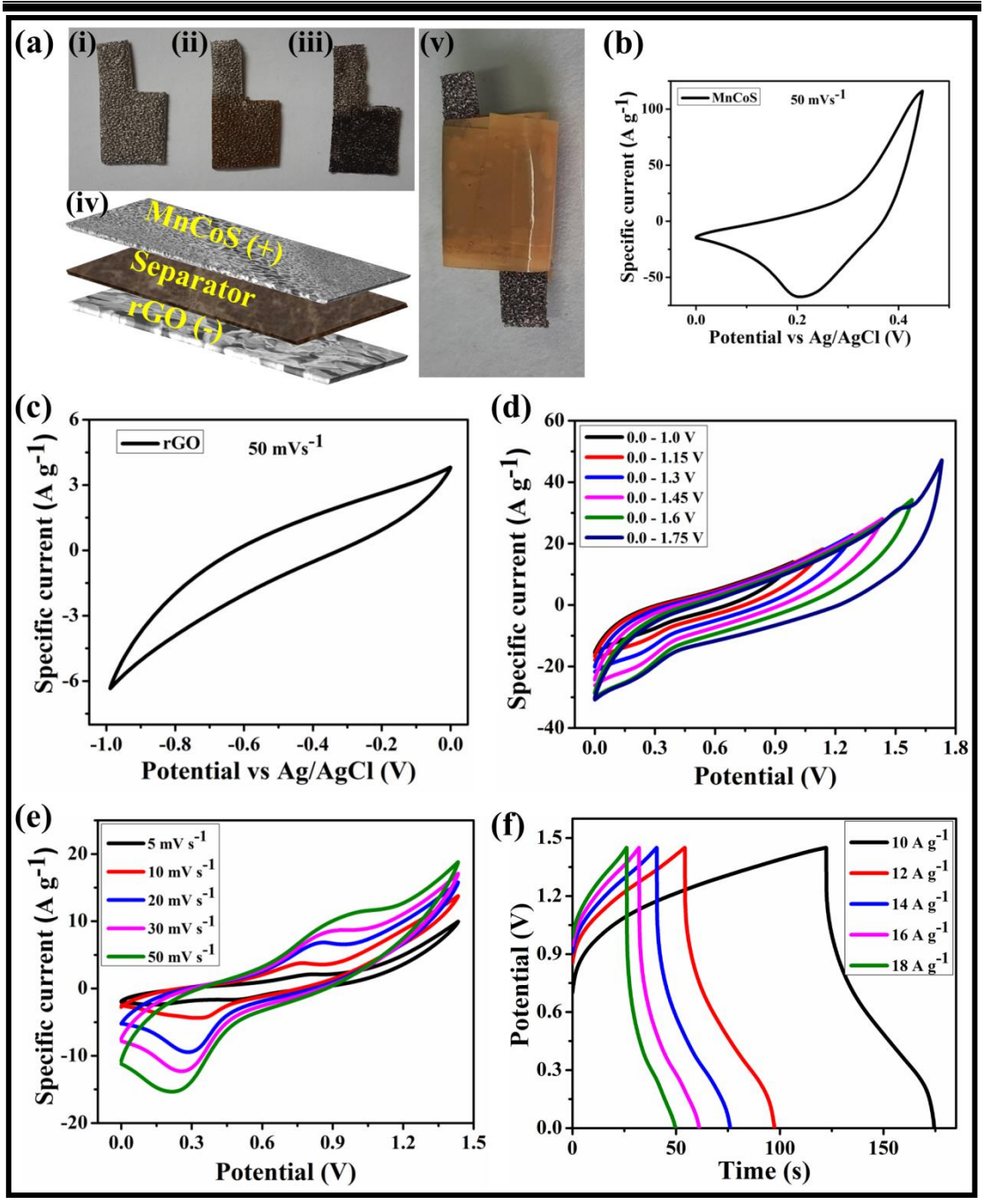


**Figure IV.8** (a) Digital photographs of Ni foam (i) bare, (ii) after growth of Mn-Co-S nanosheets, (iii) after pasting with rGO, (iv) schematic illustration of the asymmetric supercapacitor and (v) digital photograph of the fabricated device; CV curves of (b) Mn-Co-S and (c) rGO at scan rate of 50 mV $s^{-1}$; (d) CV curves at different potential windows of ASC device; (e) CV curves at different scan rates; (b) GCD curves at different specific current.

To further explore the Mn-Co-S electrode for practical application, an aqueous asymmetric supercapacitor (AAS) was fabricated using MnCoS@NF and rGO@NF as positive and negative electrode, respectively, with filter paper separator. Digital photographs of a bare Ni foam, MnCoS@NF and rGO@NF are shown in Figure IV.6a(i-iii). A schematic illustration and digital photograph of the fabricated AAS are given in Figure IV.6a(iv-v). For the asymmetric supercapacitor, the cyclic voltammetry curves were first taken using different potential window (0.0 to 1.75 V) in 2 M KOH electrolyte to find out the stable potential window of AAS (Figure IV.6d). The more suitable potential window can be accomplished from both the electrodes. Figure IV.6e shows the CV curves of the AAS device at different scan rates (5 to 50 mV $s^{-1}$). The CV curves show redox peaks indicating Faradaic behaviour of the AAS. The GCD curves of AAS at different specific current (10 to 18 A $g^{-1}$) are depicted in Figure IV.6f. The maximum specific capacitance achieved by the AAS is 360 F $g^{-1}$ at 10 A $g^{-1}$ specific current. The fabricated AAS showed high rate capability as it sustained the high specific capacitance of 292.9 F $g^{-1}$ at a high specific current of 18 A $g^{-1}$. The specific capacitances at different specific current are shown in Figure IV.9a. The 3D interconnected architecture of the positive Mn-Co-S electrode facilitates the easy insertion/de-insertion of electrolyte ions. The synergistic effect of the Mn-Co-S architecture and the highly electrochemically active negative rGO electrode aid the exceptional rate capability to the AAS.

The fabricated AAS showed excellent electrochemical stability with a very high Coulombic efficiency (Figure IV.b, inset). The specific capacitance was retained about 93.9% after consecutive 3000 GCD cycles. Figure IV.c presents the Nyquist plot of the AAS in the frequency range of 0.01 Hz to 100 kHz. The AAS exhibited comparatively low charge transfer resistance of (~3 Ω) in high frequency regime,

facilitating faradaic process. Furthermore, almost zero intercept in X-axis indicates very low internal resistance which means high conductivity providing high electrochemical activity of the AAS. The specific energy and specific power were calculated to test the efficiency of the device for real applications.

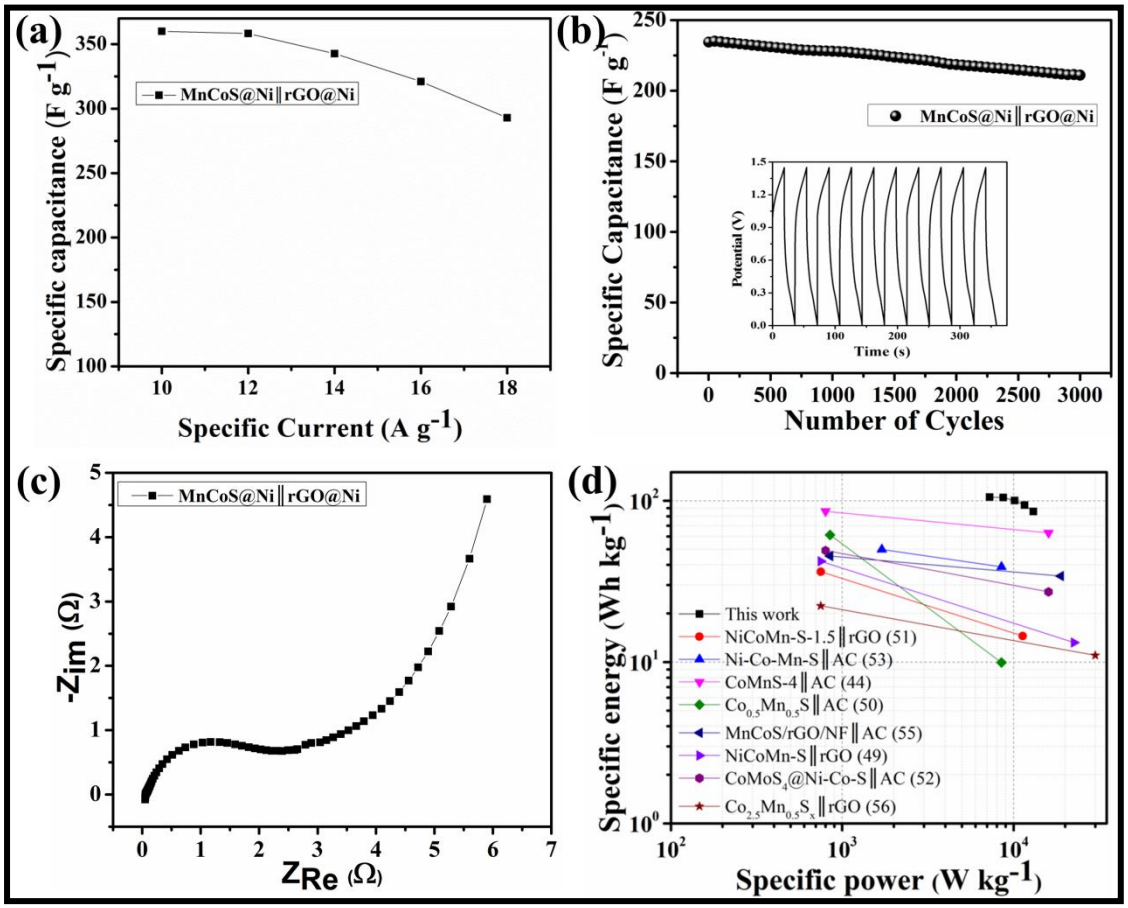


**Figure IV.9** Electrochemical performance of MnCoS@NF‖rGO@NF AAS: (a) Calculated specific capacitance at different specific current; (b) Cycling performance at a current of 20 A/g. First 10 GCD cycles (inset); (c) Nyquist plot; (d) Comparison of the electrochemical performance with other reported device in terms of Ragone plot.

Figure IV.9d represents the Ragone plot in terms of their specific energy vs specific power. The AAS exhibited high specific energy of 105.1 Wh/kg at a power delivery rate of 7.25 kW/kg. Even at high specific power of 13.05 kW/kg, the fabricated device was able to supply a high specific energy of 85.55 Wh/kg. The obtained value of the specific energy and specific power of the present device was higher than recently reported similar kind of asymmetric supercapacitor devices (Table IV.1) such as NiCoMn-S‖AC exhibited a maximum specific energy of 50 Wh/kg with a specific power of 0.85 kW/kg [48], NiCoMn-S‖rGO achieved a maximum specific energy of 42.1 Wh/kg at a power delivery rate of 0.75 kW/kg [49], CoMnS-4‖AC showed highest specific energy of 85.91Wh/kg at a specific power of 0.8 kW/kg [44], $Co_{0.5}Mn_{0.5}S$‖AC exhibited a maximum specific energy of 61.34 Wh/kg at a specific power of 0.85 kW/kg [50].

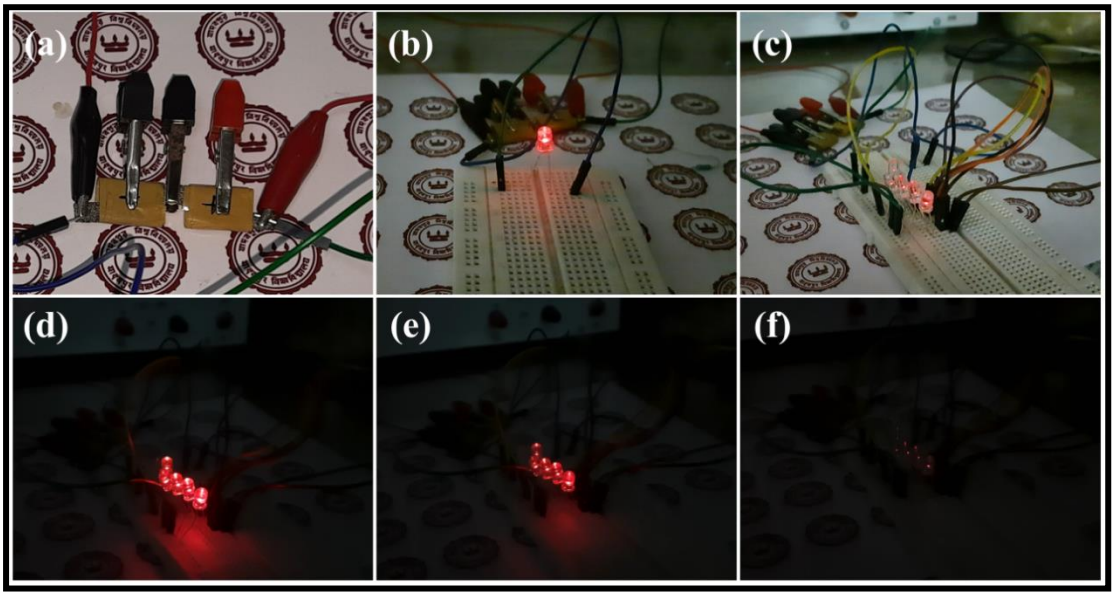


**Figure IV.10** LED lighting: (a) Two series-connected AAS; (b) One red LED lighting for 900 s; (c) Five parallel-connected red LED lighting for 180 s, (d) at 30 s, (e) at 150 s and (f) at 180 s.

**Table IV.1** Comparison of the electrochemical performances between our present work and the similar reported supercapacitors

| **Devices** | **$C_{sp}$ (F/g)** | **$I_{sp}$ (A/g)** | **$E_{sp}$ (Wh/kg)** | **$P_{sp}$ (W/kg)** | **Demon-strated practical apps** | **Ref.** |
|---|---|---|---|---|---|---|
| MnCoS@NF‖rGO@NF | 360 | 10 | 105.1 | 7250 | Yes | This work |
| NiCoMn-S‖AC | 124.5 | 1 | 50 | 850 | Yes | 48 |
| NiCoMn-S‖rGO | 134.7 | 1 | 42.1 | 750 | Yes | 49 |
| $Co_{0.5}Mn_{0.5}S$‖AC | 152.9 | 1 | 61.34 | 850 | No | 50 |
| NiCoMn-S-1.5‖rGO | 111.6 | 1 | 36.3 | 750 | No | 51 |
| CoMnS-4‖AC | 241.6 | 1 | 85.91 | 800 | No | 44 |
| $CoMoS_4$@Ni-Co-S‖AC | 138.2 | 1 | 49.1 | 800 | Yes | 52 |
| Ni–Co–Mn-S‖AC | 124.2 | 2 | 49.8 | 1700 | No | 53 |
| CoMnS‖AC | 51.9 | 0.5 | 48.5 | 524.5 | No | 54 |
| MnCoS/rGO/NF‖AC | 112.9 | 1 | 45.4 | 850.2 | No | 55 |
| $Co_{2.5}Mn_{0.5}S_x$‖rGO | 71.3 | 1 | 22.3 | 750 | Yes | 56 |
| $MnCo_2S_4$‖rGO | 88 | 1 | 31.3 | 800 | No | 22 |

[$C_{sp}$ = Specific Capacitance; $I_{sp}$ = Specific Current; $E_{sp}$ = Specific Energy; $P_{sp}$ = Specific Power; Apps = Application]

The fabricated AAS was finally demonstrated in real field applications. Two similar single devices were connected in series to increase the voltage. After charging the device for 15 s, it was able to light up a red LED for 540 s (Figure IV.10). Five parallel connected red LEDs can be lit up for 180 s with the same devices.

## IV.4 Conclusions

In conclusion, 3D interconnected Mn-Co-S nanosheets were grown on nickel foam using a simple, single-step electrosythesis method. The MnCoS@NF achieved high specific capacitance of 1952.8 F/g at scan rate of 2 A/g with high rate performance. Thereafter, a fabricated MnCoS@NF‖rGO@NF AAS delivered high specific capacitance of 360 F/g at 10 A/g with excellent rate capability. The AAS delivered high specific energy (105.1 Wh/kg) at a high specific power (7.25 kW/kg) along with high electrochemical stability (93.9 % specific capacitance retained after 3000 consecutive GCD cycle). A series-connected device was able to lit up five parallel-connected red LEDs for 180 s.

## References

[1] Conway, B. E. Eletrochemical Supercapacitors; Springer US: Boston, MA, 1999.

[2] Miller, J. R.; Simon, P. Fundamentals of electrochemical capacitor design and operation. *Electrochem. Soc. Interface* **2008**, *17*, 31−32.

[3] Wang, F.; Wu, X.; Yuan, X.; Liu, Z.; Zhang, Y.; Fu, L.; Zhu, Y.; Zhou, Q.; Wu, Y.; Huang, W. Latest advances in supercapacitors: from new electrode materials to novel device designs. *Chem. Soc. Rev.* **2017**, *46*, 6816-6854.

[4] Zhong, C.; Deng, Y.; Hu, W.; Qiao, J.; Zhang, L.; Zhang, J. A review of electrolyte materials and compositions for electrochemical supercapacitors. *Chem. Soc. Rev.* **2015**, *44*, 7484-7539.

[5] Naveenkumar, P.; Kalaignan, G.P. Electrodeposited MnS on graphene wrapped Ni-Foam for enhanced supercapacitor applications. *Electrochim. Acta* **2018**, *289*, 437-447.

[6] Kumbhar, V.S.; Lee, Y.R.; Ra, C.S.; Tuma, D.; Min, B.K.; Shim, J.J. Modified chemical synthesis of MnS nanoclusters on nickel foam for high performance all-solid-state asymmetric supercapacitors. *RSC Adv.* **2017**, *7*, 16348-16359.

[7] Chen, T.; Tang, Y.; Qiao, Y.; Liu, Z.; Guo, W.; Song, J.; Mu, S.; Yu, S.; Zhao, Y.; Gao, F. All-solid-state high performance asymmetric supercapacitors based on novel MnS nanocrystal and activated carbon materials. *Sci. Rep.* **2016**, *6*, 23289.

[8] Shi, J.; Li, X.; He, G.; Zhang, L.; Li, M. Electrodeposition of high-capacitance 3D CoS/graphene nanosheets on nickel foam for high-performance aqueous asymmetric supercapacitors. *J. Mater. Chem. A* **2015**, *3*, 20619-20626.

[9] Lin, J.Y.; Chou, S.W. Cathodic deposition of interlaced nanosheet-like cobalt sulfide films for high-performance supercapacitors. *RSC Adv.* **2013**, *3*, 2043-2048.

[10] Sahoo, S.; Shim, J.J. Room-temperature synthesis of NiS hollow spheres on nickel foam for high-performance supercapacitor electrodes. *Mater. Lett.* **2018**, *210*, 105-108.

[11] Yu, L.; Yang, B.; Liu, Q.; Liu, J.; Wang, X.; Song, D.; Wang, J.; Jing, X. Interconnected NiS nanosheets supported by nickel foam: soaking fabrication and supercapacitors application. *J. Electroanal. Chem.* **2015**, *739*, 156-163.

[12] Ahmed, N.; Ali, B.A.; Ramadan, M.; Allam, N.K. Three-Dimensional Interconnected Binder-Free Mn–Ni–S Nanosheets for High Performance Asymmetric Supercapacitor Devices with Exceptional Cyclic Stability. *ACS Appl. Energy Mater.* **2019**, *2*, 3717-3725.

[13] Khalafallah, D.; Wu, Z.; Zhi, M.; Hong, Z. Rational Design of Porous Structured Nickel Manganese Sulfides Hexagonal Sheets-in-Cage Structures as an Advanced Electrode Material for High-Performance Electrochemical Capacitors. *Chem. Euro. J.* **2020**, *26*, 2251-2262.

[14] Cheng, C.; Kong, D.; Wei, C.; Du, W.; Zhao, J.; Feng, Y.; Duan, Q. Self-template synthesis of hollow ellipsoid Ni−Mn sulfides for supercapacitors, electrocatalytic oxidation of glucose and water treatment. *Dalton Trans.* **2017**, *46*, 5406-5413.

[15] Meng, Y.; Sun, P.; He, W.; Teng, B.; Xu, X. Uniform P doped Co–Ni–S nanostructures for asymmetric supercapacitors with ultra-high energy densities. *Nanoscale* **2019**, *11*, 688-697.

[16] Meng, Y.; Sun, P.; He, W.; Teng, B.; Xu, X. Construction of hierarchical Co-Ni-S nanosheets as free-standing electrode for superior-performance asymmetric supercapacitors. *Appl. Surf. Sci.* **2019**, *470*, 792-799.

[17] Yang, J.; Yu, C.; Fan, X.; Liang, S.; Li, S.; Huang, H.; Ling, Z.; Hao, C.; Qiu, J. Electroactive edge site-enriched nickel–cobalt sulfide into graphene frameworks for high-performance asymmetric supercapacitors. *Energy Environ. Sci.* **2016**, *9*, 1299-1307.

[18] Chen, W.; Xia, C.; Alshareef, H.N. One-step electrodeposited nickel cobalt sulfide nanosheet arrays for high-performance asymmetric supercapacitors. *ACS Nano* **2014**, *8*, 9531-9541.

[19] Wang, F.; Zhou, K.; Zheng, J.; Ma, J. Rapid synthesis of porous manganese cobalt sulfide grown on Ni foam by microwave method for high performance supercapacitors. *Synth. Met.* **2019**, *256*, 116113.

[20] Li, G.; Chang, Z.; Li, T.; Ma, L.; Wang, K. Hierarchical Mn-Co sulfide nanosheets on nickel foam by electrochemical co-deposition for high-performance pseudocapacitors. *Ionics* **2019**, *25*, 3885-3895.

[21] Zhao, Y.; Shi, Z.; Li, H.; Wang, C.A. Designing pinecone-like and hierarchical manganese cobalt sulfides for advanced supercapacitor electrodes. *J. Mater. Chem. A* **2018**, *6*, 12782-12793.

[22] Liu, S.; Jun, S.C. Hierarchical manganese cobalt sulfide core–shell nanostructures for high-performance asymmetric supercapacitors. *J. Power Sources* **2017**, *342*, 629-637.

[23] Theerthagiri, J.;, Karuppasamy, K.; Durai, G.; Rana, A.U.H.S.; Arunachalam, P.; Sangeetha, K.; Kuppusami, P.; Kim, H.S. Recent advances in metal chalcogenides (MX; X= S, Se) nanostructures for electrochemical supercapacitor applications: a brief review. *Nanomaterials* **2018**, *8*, 256.

[24] Tarimo, D.J.; Oyedotun, K.O.; Mirghni, A.A.; Sylla, N.F.; Manyala, N. High energy and excellent stability asymmetric supercapacitor derived from sulphur-reduced graphene oxide/manganese dioxide composite and activated carbon from peanut shell. *Electrochim. Acta* **2020**, *353*, 136498.

[25] Neeraj, N.S.; Mordina, B.; Srivastava, A.K.; Mukhopadhyay, K.; Prasad, N.E. Impact of process conditions on the electrochemical performances of $NiMoO_4$ nanorods and activated carbon based asymmetric supercapacitor. *Appl. Surf. Sci.* **2019**, *473*, 807-819.

[26] Xia, C.; Jiang, Q.; Zhao, C.; Beaujuge, P.M.; Alshareef, H.N. Asymmetric supercapacitors with metal-like ternary selenides and porous graphene electrodes. *Nano Energy* **2016**, *24*, 78-86.

[27] Mandal, M.; Ghosh, D.; Chattopadhyay, K.; Das, C.K. A Novel asymmetric supercapacitor designed with $Mn_3O_4$@multi-wall carbon nanotube nanocomposite and reduced graphene oxide electrodes. *J. Electron. Mater.* **2016**, *45*, 3491-3500.

[28] Younes, H.; Zou, L. Asymmetric configuration of pseudocapacitive composite and rGO electrodes for enhanced capacitive deionization. *Environ. Sci. Water Res. Technol.* **2020**, *6*, 392-403.

[29] Ashraf, M.; Shah, S.S.; Khan, I.; Aziz, M.A.; Ullah, N.; Khan, M.; Adil, S.F.; Liaqat, Z.; Usman, M.; Tremel, W.; Tahir, M.N. A high-performance asymmetric supercapacitor based on tungsten oxide nanoplates and highly reduced graphene oxide electrodes. *Chem. Eur. J.* **2021**, *27*, 6973-6984.

[30] Jiang, H.; Li, C.; Sun, T.; Ma, J. A green and high energy density asymmetric supercapacitor based on ultrathin $MnO_2$ nanostructures and functional mesoporous carbon nanotube electrodes. *Nanoscale* **2012**, *4*, 807-812.

[31] Park, S.H.; Son, J.G.; Lee, T.G.; Park, H.M.; ong Song, J. One-step large-scale synthesis of micrometer-sized silver nanosheets by a template-free electrochemical method. *Nanoscale Res. Lett.* **2013**, *8*, 248.

[32] Wang, N.; Sun, B.; Zhao, P.; Yao, M.; Hu, W.; Komarneni, S. Electrodeposition preparation of $NiCo_2O_4$ mesoporous film on ultrafine nickel wire for flexible asymmetric supercapacitors. *Chem. Eng. J.* **2018**, *345*, 31-38.

[33] Wu, S.; Guo, H.; San Hui, K.; Hui, K.N. Rational design of integrated CuO@ $Co_xNi_{1-x}(OH)_2$ nanowire arrays on copper foam for high-rate and long-life supercapacitors. *Electrochim. Acta* **2019**, *295*, 759-768.

[34] Sivasakthi, P.; Bapu, G.R.; Murugavel, K.; Mohan, S. Facile method of pulse electrodeposited NiO-$CeO_2$Sm doped nanocomposite electrode on copper foam for supercapacitor application. *J. Alloys Compd.* **2017**, *709*, 240-247.

[35] Vardhan, P.V.; Idris, M.B.; Ramanathan, V.; Devaraj, S. Electrodeposited $MnCO_3$ as a high performance electrode material for supercapacitor. *ChemistrySelect* **2018**, *3*, 6775-6778.

[36] Asen, P.; Shahrokhian, S. One step electrodeposition of $V_2O_5$/polypyrrole/graphene oxide ternary nanocomposite for preparation of a high performance supercapacitor. *Int. J. Hydrogen Energy* **2017**, *42*, 21073-21085.

[37] Ye, G.; Zhu, D.; Zhou, Q.; Li, D.; Zuo, Y.; Duan, X.; Zhou, W.; Xu, J. One-step electrodeposition method to prepare robust flexible PEDOT-based films for ultra-stable supercapacitors. *ChemElectroChem* **2018**, *5*, 1130-1136.

[38] Sahoo, S.; Naik, K.K.; Rout, C.S. Electrodeposition of spinel $MnCo_2O_4$ nanosheets for supercapacitor applications. *Nanotechnology* **2015**, *26*, 455401.

[39] Zhao, N.; Fan, H.; Zhang, M.; Ma, J.; Du, Z.; Yan, B.; Li, H.; Jiang, X. Simple electrodeposition of $MoO_3$ film on carbon cloth for high-performance aqueous symmetric supercapacitors. *Chem. Eng. J.* **2020**, *390*, 124477.

[40] Serrapede, M.; Rafique, A.; Fontana, M.; Zine, A.; Rivolo, P.; Bianco, S.; Chetibi, L.; Tresso, E.; Lamberti, A. Fiber-shaped asymmetric supercapacitor exploiting rGO/$Fe_2O_3$ aerogel and electrodeposited MnOx nanosheets on carbon fibers. *Carbon* **2019**, *144*, 91-100.

[41] Ye, Z.; Li, T.; Ma, G.; Peng, X.; Zhao, J. Morphology controlled $MnO_2$ electrodeposited on carbon fiber paper for high-performance supercapacitors. *J. Power Sources* **2017**, *351*, 51-57.

[42] Marcano, D.C.; Kosynkin, D.V.; Berlin, J.M.; Sinitskii, A.; Sun, Z.; Slesarev, A.S.; Alemany, L.B.; Lu, W.; Tour, J.M. Correction to improved synthesis of graphene oxide. *ACS Nano* **2018**, *12*, 2078-2078.

[43] Zhu, Y.; Chen, H.; Chen, S.; Li, C.; Fan, M.; Shu, K. Sea urchin-like architectures and nanowire arrays of cobalt–manganese sulfides for superior electrochemical energy storage performance. *J. Mater. Sci.* **2018**, *53*, 6157-6169.

[44] Hu, X.; Liu, S.; Chen, Y.; Jiang, J.; Cong, H.; Tang, J.; Sun, Y.; Han, S.; ; Lin, H. Rational design of flower-like cobalt–manganese-sulfide nanosheets for high performance supercapacitor electrode materials. *New J. Chem.* **2020**, *44*, 11786-11795.

[45] Gupta, B.; Kumar, N.; Panda, K.; Kanan, V.; Joshi, S.; Visoly-Fisher, I. Role of oxygen functional groups in reduced graphene oxide for lubrication. *Sci.Rep.* **2017**, *7*, 1-14.

[46] Tang, Y.; Chen, T.; Yu, S.; Qiao, Y.; Mu, S.; Hu, J.; Gao, F. Synthesis of graphene oxide anchored porous manganese sulfide nanocrystals via the nanoscale Kirkendall effect for supercapacitors. *J. Mater. Chem. A* **2015**, *3*, 12913-12919.

[47] Mandal, M.; Nagaraj, R.; Chattopadhyay, K.; Chakraborty, M.; Chatterjee, S.; Ghosh, D.; Bhattacharya, S.K. A high-performance pseudocapacitive electrode based on CuO–$MnO_2$ composite in redox-mediated electrolyte. *J. Mater. Sci.* **2021**, *56*, 3325-3335.

[48] Kang, C.; Ma, L.; Chen, Y.; Fu, L.; Hu, Q.; Zhou, C.; Liu, Q. Metal-organic framework derived hollow rod-like NiCoMn ternary metal sulfide for high-performance asymmetric supercapacitors. *Chem. Eng. J.* **2022**, *427*, 131003.

[49] Cao, J.; Hu, Y.; Zhu, Y.; Cao, H.; Fan, M.; Huang, C.; Shu, K.; He, M.; Chen, H.C. Synthesis of mesoporous nickel-cobalt-manganese sulfides as electroactive materials for hybrid supercapacitors. *Chem. Eng. J.* **2021**, ***405***, 126928.

[50] Iqbal, M.Z.; Khan, J. Optimization of cobalt-manganese binary sulfide for high performance supercapattery devices. *Electrochim. Acta* **2021**, *368*, 137529.

[51] Zhang, J.; Li, C.; Fan, M.; Ma, T.; Chen, H.; Wang, H. Two-dimensional nanosheets constituted trimetal Ni-Co-Mn sulfide nanoflower-like structure for high-performance hybrid supercapacitors. *Appl. Surf. Sci.* **2021**, *565*, 150482.

[52] Ma, F.; Dai, X.; Jin, J.; Tie, N.; Dai, Y. Hierarchical core-shell hollow $CoMoS_4$@Ni–Co–S nanotubes hybrid arrays as advanced electrode material for supercapacitors. *Electrochim. Acta* **2020**, *331*, 135459.

[53] Wei, C.; Chen, Q.; Cheng, C.; Liu, R.; Zhang, Q.; Zhang, L. Mesoporous nickel cobalt manganese sulfide yolk–shell hollow spheres for high-performance electrochemical energy storage. *Inorg. Chem. Front.* **2019**, *6*, 1851-1860.

[54] Peng, H.; Wei, G.; Sun, K.; Ma, G.; Feng, E.; Yang, X.; Lei, Z. Integrated and heterostructured cobalt manganese sulfide nanoneedle arrays as advanced electrodes for high-performance supercapacitors. *New J. Chem.* **2018**, *42*, 18328-18334.

[55] Han, X.; Xuan, H.; Gao, J.; Liang, T.; Yang, J.; Xu, Y.; Han, P.; Du, Y. Construction of manganese-cobalt-sulfide anchored onto rGO/Ni foam with a high capacity for hybrid supercapacitors. *Electrochim. Acta* **2018**, *288*, 31-41.

[56] Chen, S.; Chen, H.; Li, C.; Fan, M.; Lv, C.; Tian, G.; Shu, K. Tuning the electrochemical behavior of $Co_xMn_{3-x}$ sulfides by varying different Co/Mn ratios in supercapacitor. *J. Mater. Sci.* **2017**, *52*, 6687-6696.

# Chapter V

*Room temperature synthesis of $MnSn(OH)_6$ nanocubes: An excellent negative electrode for supercapacitor*

## V.1 Introduction

A supercapacitor device mainly consists of two electrodes i.e. positive and negative electrodes soaked in an aqueous or non-aqueous electrolyte. A porous separator is placed in between the electrodes to prevent short-circuit allowing only electrolyte ion permeation [1]. Although the performance of a supercapacitor device depends on various components or factors such as electrolyte, separator, current collectors, and device assembling technology, choice of the electrode materials plays the key role [2, 3].

According to the charge storage mechanism, electrode materials are classified into two categories. The materials such as transition metal oxide/hydroxides/sulfides, conducting polymers which give the capacitance as a result of first Faradaic redox reactions are called as pseudocapacitive materials. Such materials have been well investigated as positive electrode materials for the supercapacitor [4-6]. On the other hand, carbonaceous materials like graphene, carbon nanotubes, and activated carbons give the capacitance by charge accumulation at the electrode/electrolyte interface and have been extensively studied as the negative electrode [7]. But the lower capacitance of these carbon-based materials triggers the researchers for searching a new class of negative electrode materials. Although the development of negative electrode materials is relatively slow, recently few transition metal oxides such as $V_2O_5$ [8], $Fe_3O_4$ [9], α-$MnO_2$ [10], $Mn_3O_4$ [11] have shown significant performance as negative electrodes for supercapacitor. Feng et al. fabricated negative electrode based on amorphous porous $Mn_3O_4$/NGP via electrodeposition achieved a maximum specific capacitance of 432 F/g at scan rate of 5 mV/s [11]. Carbon coated $SnO_2$ was considered as negative electrode which provided specific capacitance of 150 F/g at 2

A/g [12]. Besides that, hydroxide based material such as $Ce(OH)_2$ was also used as negative electrode which was able to achieve high specific capacitance of 187 F/g at a specific current of 1 A/g [13].

Although various bimetallic hydroxides based on cobalt, manganese, nickel [14-16] are extensively studied and proved to be promising electrode for supercapacitor, manganese tin hydroxide is scarcely explored. Recently, Rani et al. investigated the electrochemical performance of $MnSn(OH)_6$ electrodes in the positive potential window of 0.2 to 0.6 V [17]. However, the oxygen vacancy of the material also makes it possible for the material to act as a negative electrode for supercapacitor.

Herein, we report a manganese based bimetallic hydroxide, $MnSn(OH)_6$ nanocubes, as a promising negative electrode in 2 M KOH electrolyte. The as-synthesized material was able to achieve the maximum specific capacitance of 330 F/g at a scan rate of 5 mV/s.

## V.2 Experimental Section

### *V.2.1 Materials*

Manganese(II) chloride tetrahydrate, Tin(IV) chloride pentahydrate, Ethanolamine, Ethanol were taken from Merck, India. All the as-received chemicals were used for the experiment.

### *V.2.2 Synthesis of $MnSn(OH)_6$ nanocubes*

A facile single-pot cost-effective precipitation method was adopted at room temperature (25 ˚C) for the synthesis of $MnSn(OH)_6$ nanocubes. Firstly, 20 mL of 0.05 M aqueous solution of $MnCl_2$ was taken in a beaker. Then 245 μL ethanolamine

(EA) was added dropwise under stirring condition at 300 rpm. After 10 minutes, 20 mL of 0.05 M ethanolic solution of $SnCl_4$ was added dropwise. The obtained browny precipitate was washed with water for several times and dried at 60 ˚C for 12 h.

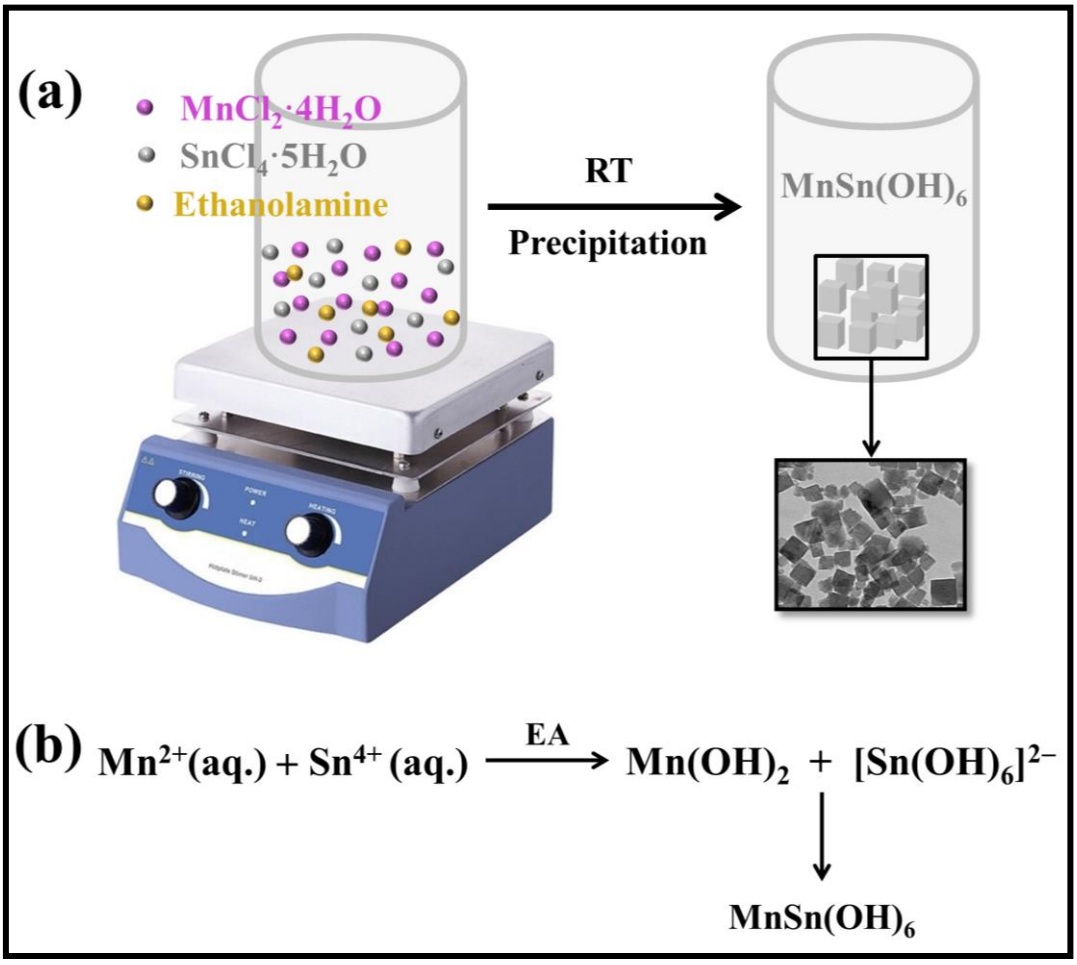


**Scheme V.1** (a) Schematic depicting the synthetic procedure of $MnSn(OH)_6$; (b) The mechanism of the formation of $MnSn(OH)_6$ nanocubes.

## V.3 Results and Discussion

The manganese tin hydroxide nanocubes were prepared using a simple chemical precipitation method (Scheme V.1a). Here, ethanolamine (EA) acts as hydrolyzing agent forming $Mn(OH)_2$. The aqueous solution of $SnCl_4$ produces hexaaquatin(IV), $[Sn(OH)_6]^{2-}$ which ultimately combines with the pre-formed $Mn(OH)_2$ to give

$MnSn(OH)_6$ nanocubes via phase transformation depending up on the Ostwald ripening process (Scheme V.1b) [17-19].

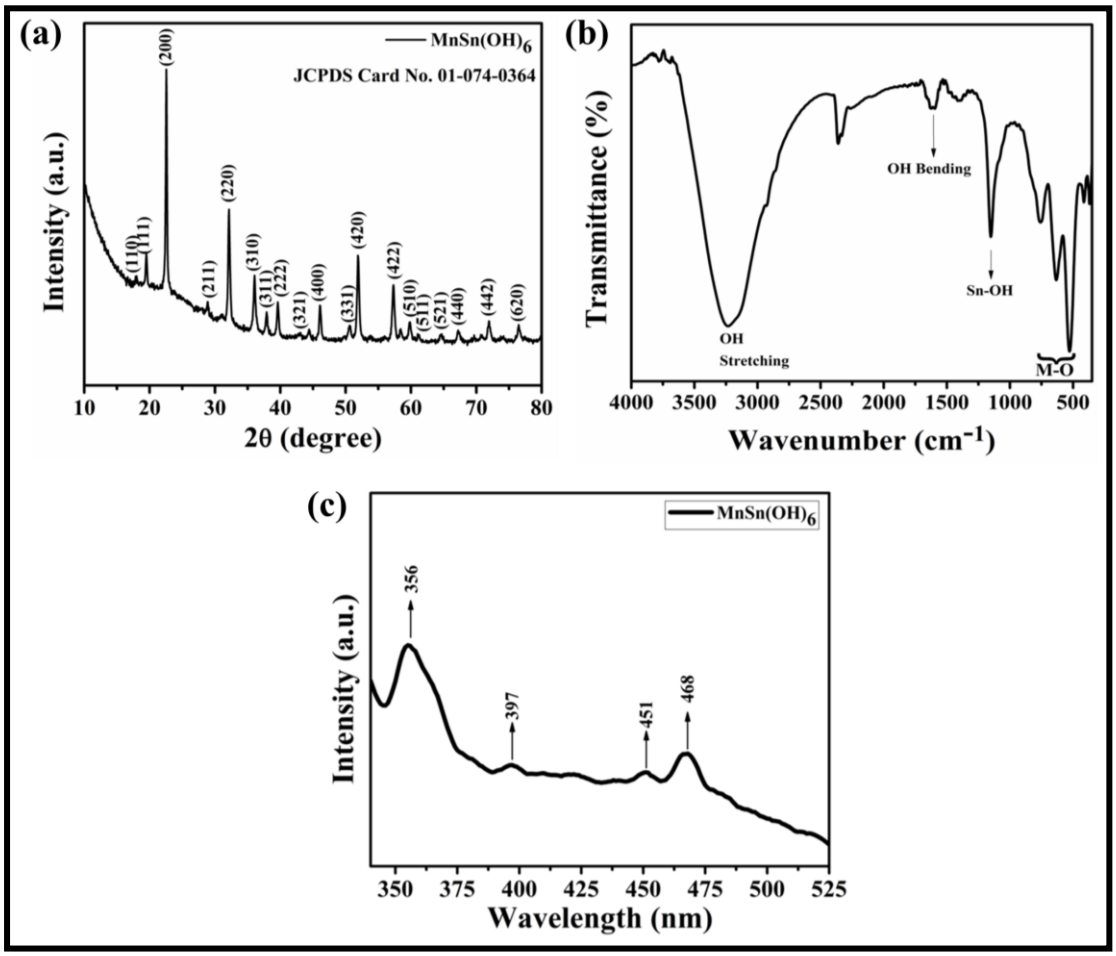


**Figure V.1** (a) XRD pattern, (b) FTIR, and (c) PL spectrum of as-synthesized $MnSn(OH)_6$ nanocubes.

### *V.3.1 XRD analysis*

The crystalline nature of the as-synthesized electrode material can investigated by X-ray diffraction (XRD, Rigaku ULTIMA-III X-ray diffractometer with Cu Kα, λ = 1.548 Å) study. Figure V.1a shows the XRD pattern of $MnSn(OH)_6$ nanocubes which revealed the cubic polycrystalline structure with Pn3m space group. The peaks obtained for the material was perfectly matched with the JCPDS card no. 01-074-0364. The major diffraction peaks at 2θ of 15.9˚, 19.5˚, 22.5˚, 28.8˚, 32.1˚, 36.0˚,

37.9˚, 39.6˚, 42.9˚, 46.0˚, 50.5˚, 51.9˚, 57.3˚, 59.8˚, 61.1˚, 64.5˚, 67.2˚, 71.9˚ and 76.4˚ correspond to the plane of (110), (111), (200), (211), (220), (310), (311), (222), (321), (400), (331), (420), (422), (510), (511), (521), (440), (442) and (620), respectively.

### *V.3.2 FTIR analysis*

The chemical composition of the as-synthesized material was investigated by Fourier-transform infrared (FTIR) Spectrometer (Thermo Nicolet NEXUS 870 FT-IR) between 400 and 4000 $cm^{-1}$. Figure V.1b shows strong absorption band at 528 and 632 $cm^{-1}$, which is attributed to the Sn-O vibration of $MnSn(OH)_6$ nanocubes. The characteristic Mn-O coupling and the Sn-OH vibrations are located at 752 and 1151 $cm^{-1}$, respectively [20, 21]. The ν(OH) stretching vibrations with its corresponding δ(OH) deformations of $MnSn(OH)_6$ could be ascribed at 3234 and 1551 $cm^{-1}$, respectively [22]. The photoluminescence (PL) study was performed to investigate any intrinsic point defects like oxygen vacancies present in the material.

### *V.3.3 Photoluminescence spectra*

Photoluminescence (PL) spectra were recorded using a spectrofluorometer (RF- 5301, Shimadzu, Japan). The PL peaks (Figure V.1c) at 356 and 397 nm are attributed to near band edge emission and the oxygen vacancies are represented by the peak at 451 and 468 nm [20].

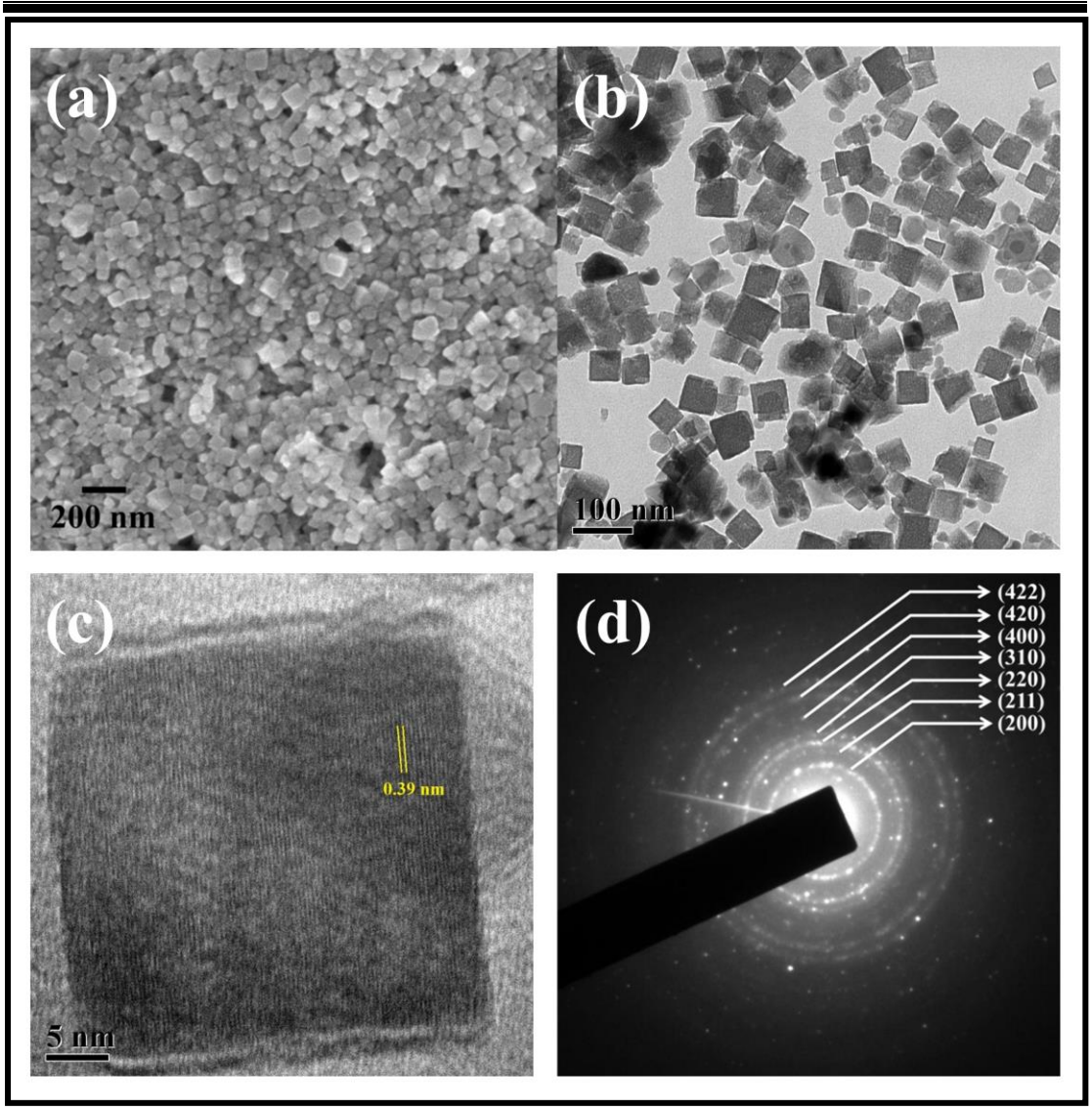


**Figure V.2** (a) FESEM image, (b, c) HRTEM images with different magnification and (d) SAED pattern of as-synthesized $MnSn(OH)_6$ nanocubes.

### *V.3.4 Morphological analysis*

The morphology was investigated using field emission scanning electron microscope (FESEM, Carl Zeiss-SUPRA 40) and transmission electron microscopy (TEM, TECNAI G2-20STWIN). Figure V.2a shows the FESEM image of the as-synthesized $MnSn(OH)_6$, which suggests the uniform cubic structure having the average arm length of 75-100 nm. The uniform structure and fine edge morphology having high

conductivity promises to exhibit the high electrochemical performance. The HRTEM images (Figure V.2b) also supports the cubic structure. A single nanocube is shown in Figure V.2c which shows the lattice fringes with the interfringe distance of 0.39 nm which is close to the interplanar distance of 200 plane. The selected area electron diffraction (SAED) pattern of $MnSn(OH)_6$ nanocubes shows the polycrystalline nature with diffraction rings of (200), (211), (220), (310), (400), (420) and (422), shown in Figure V.2d.

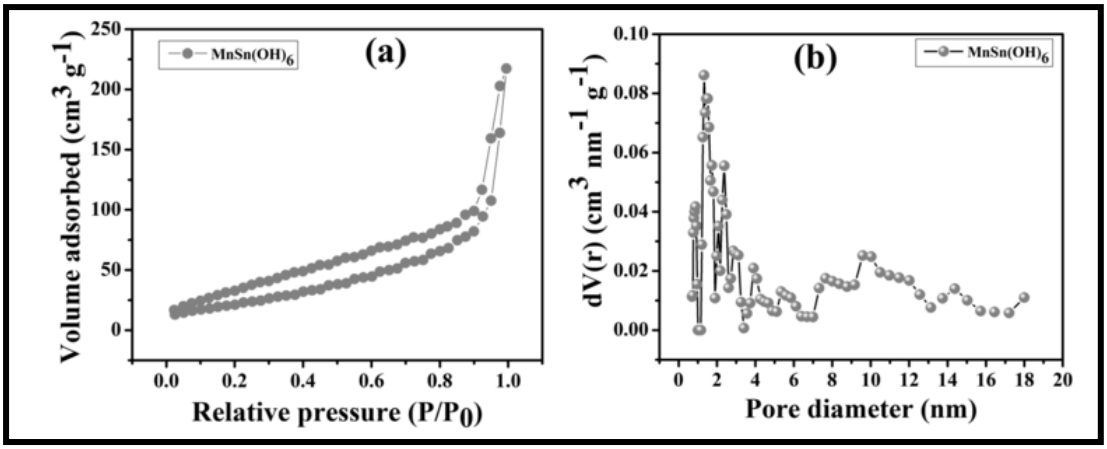


**Figure V.3** (a) Nitrogen adsorption–desorption isotherm, and (b) pore size distribution curve of $MnSn(OH)_6$ nanocubes.

### *V.3.5 BET analysis*

As the electrochemical performance of an electrode material depends also its surface area and pore size distribution, the BET analysis was carried out for the as-synthesized material. Figure V.3a and 3b represents the nitrogen adsorption-desorption isotherm and pore size distribution curve, respectively. The nature of the isotherms falls in the type IV category with a H3 type hysteresis loop indicating the mesoporous nature of the sample. The pore distribution curve also supports the mesoporous nature of $MnSn(OH)_6$ nanocubes. The calculated BET surface area and

pore volume were 83.52 $m^2$/g and 0.27 $cm^3$/g, respectively. The high surface area and pore volume of the as-synthesized material enhances the wettability of the electrolyte and therefore improves the charge storage property of the material.

### *V.3.5* Electrochemical characterizations

For the fabrication of working electrode, nickel foam (1 x 1) $cm^2$ was used as current collector. Prior use, the nickel foam was gently washed with 3 M HCl to remove the oxide layer from the surface. Then a paste of the active material, $MnSn(OH)_6$, carbon black (CB) and polyvinylidone fluoride (PVDF) with ratio 8:1:1 in N-methyl pyrrolidone (NMP) was pasted uniformly on the nickel foam and dried it at 60 ˚C for overnight. The CB and PVDF are used to increase conductivity and as binder, respectively. The electrochemical performances were tested by performing cyclic voltammetry (CV), galvanostatic charge–discharge (GCD) and electrochemical impedance spectra (EIS) using Biologic SP 150 and Autolab potentiostat. The specific capacitance was calculated from CV and GCD using Equation 1 and 2, respectively.

$$\boldsymbol{C_s = \frac{\int_{V1}^{V2} i(V)dV}{2(V2-V1)vm}} \quad \text{..... (1)}$$

$$\boldsymbol{C_s = \frac{i \times \Delta t}{m \times \Delta V}} \quad \text{..... (2),}$$

where, $\int_{V1}^{V2} i(V)dV$ = area of the CV curve, $\Delta V = (V2 - V1)$ = potential window (V), $v$ = scan rate (V/s), m = mass (g) of the active materials, $i$ = applied current (A), and $\Delta t$ = discharge time (s).

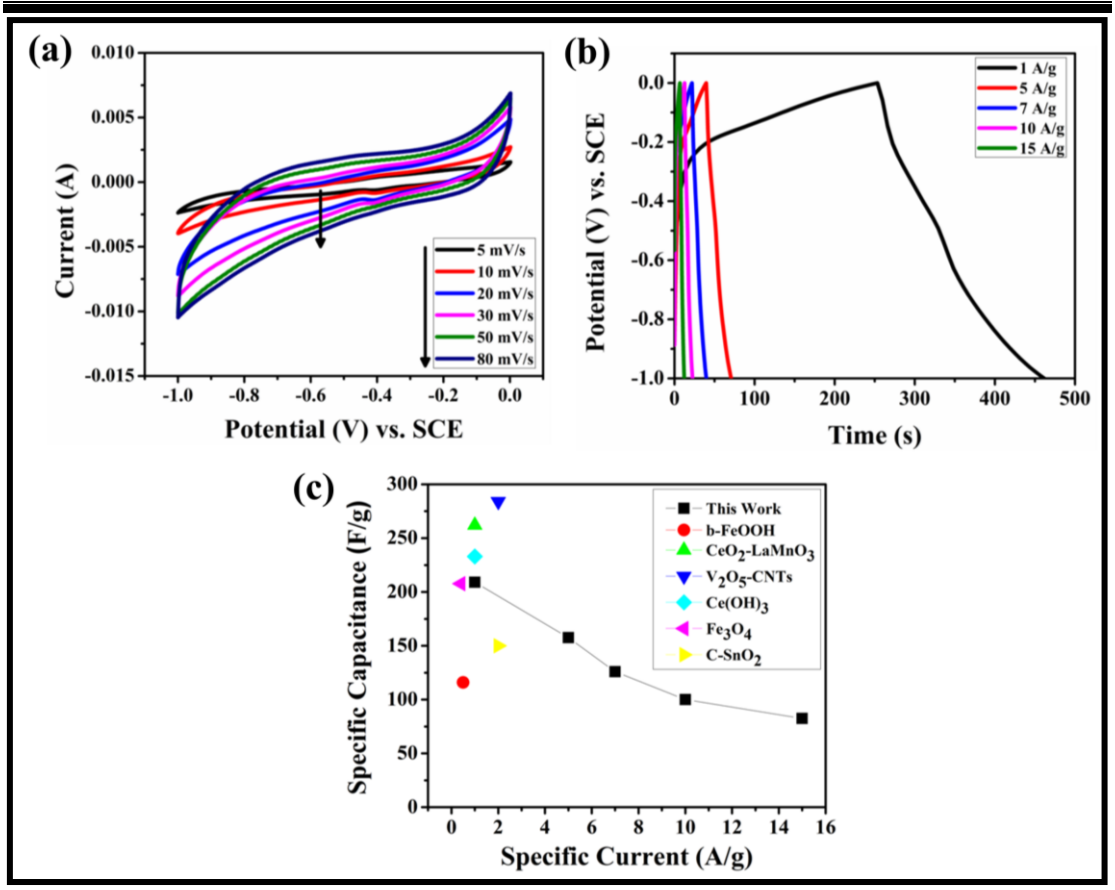


**Figure V.4** Electrochemical behaviors of $MnSn(OH)_6$ nanocubes: (a) CV curves at scan rate of 5, 10, 20, 30, 50 and 80 mV/s; (b) GCD curves at specific current of 1, 5, 7, 10 and 15 A/g; (c) Comparison of specific capacitance of as-prepared materials with the literature.

After preparation of working electrode the electrochemical characterizations in terms of cyclic voltammetry (CV) and galvanostatic charge-discharge (GCD) were performed to check the electrochemical performance. The CV measurement was performed using three-electrode cell system within the potential range of -1.0 to 0.0 V varying the scan rate from 5 to 80 mV/s in 2 M KOH electrolyte (Figure V.4a). The nickel foam having active material, saturated calomel electrode and Pt foil were used as working, reference and counter electrode, respectively. The as-synthesized $MnSn(OH)_6$ nanocubes showed excellent performance in negative potential window. The highest specific capacitance of 330 F/g was achieved at scan rate of 5 mV/s. The

uniform structure and fine edge morphology with high conductivity due to oxygen vacancies promote the redox reaction which results in high pseudocapacitance [20]. Furthermore, oxygen vacancies not only improve the conductivity but also decrease the diffusion energy and synergistically enhance the capacitive signature consequently.

To check the energy storage capacity of the as-synthesized $MnSn(OH)_6$ nanocubes the typical galvanostatic charge-discharge (GCD) study was carried out at various specific current. Figure V.4b shows the GCD profile in the negative potential window (-1.0 to 0.0 V) indicating the pseudocapacitive nature of the material. The maximum specific capacitance of 209 F/g was achieved at specific current of 1 A/g. The specific capacitance versus specific current curve for the as-prepared materials is depicted in Figure V.4c along with maximum capacitance achieved by some other negative electrode materials (Table 1) [8, 9, 12, 13, 23, 24]. The $MnSn(OH)_6$ nanocubes achieved the comparable specific capacitance.

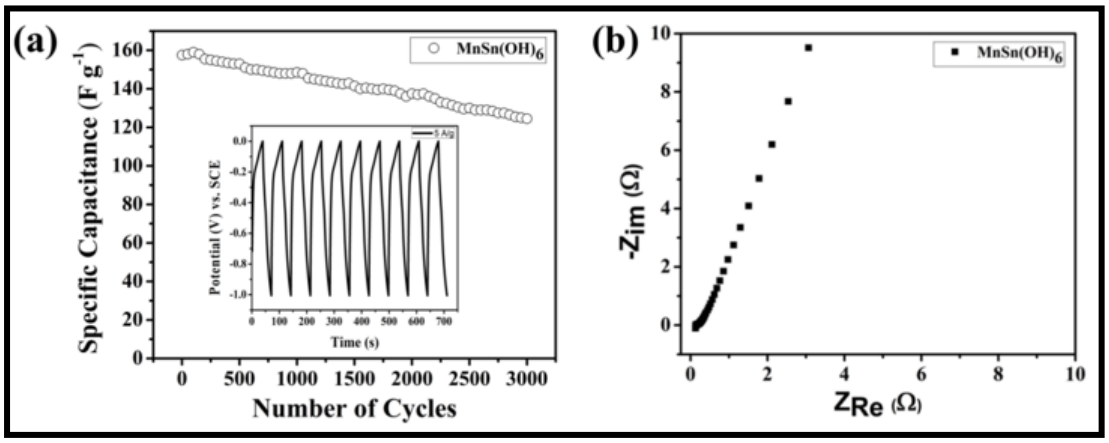


**Figure V.5** (a) GCD life cycle at 5 A/g (inset: First 10 GCD cycle); (b) Nyquist plot.

The electrochemical stability was examined by performing the consecutive 3000 GCD cycles at a specific current of 5 A/g (Figure V.5a), indicating the good stability with 79% retention of the specific capacitance. The small diameter of the semicircle at

high-frequency region of the EIS spectrum (Figure V.5b) indicates very low charge-transfer resistance which facilitates the high electrochemical performance.

## V.4 Conclusion

In summary, a negative electrode based on $MnSn(OH)_6$ nanocubes is successfully synthesized by a simple precipitation method at room temperature for supercapacitor application. The as-prepared materials exhibited highest specific capacitance of 209 F/g at a specific current of 1 A/g in 2 M KOH electrolyte with excellent cycling stability (79% specific capacitance retention after 3000 consecutive GCD cycles). The uniform structure and fine edge morphology having high conductivity due to oxygen vacancies promotes the electrochemical performance.

## References

[1] Simon, P.; Gogotsi, Y. Materials for electrochemical capacitors. *Nat. Mater.* **2008** *7*, 845-854.

[2] Majumdar, D.; Mandal, M.; Bhattacharya, S.K. $V_2O_5$ and its carbon-based nanocomposites for supercapacitor applications. *ChemElectroChem* **2019**, *6*, 1623-1648.

[3] Wang, G.; Zhang, L.; Zhang, J. A review of electrode materials for electrochemical supercapacitors. *Chem. Soc. Rev.* **2012**, *41*, 797-828.

[4] Muzaffar, A.; Ahamed, M.B.; Deshmukh, K.; Thirumalai, J. A review on recent advances in hybrid supercapacitors: Design, fabrication and applications. *Renew. Sustain. Energy Rev.* **2019**, *101*, 123-145.

[5] Ghosh, D.; Mandal, M.; Das, C.K. Solid state flexible asymmetric supercapacitor based on carbon fiber supported hierarchical $Co(OH)_xCO_3$ and $Ni(OH)_2$. *Langmuir* **2015**, *31*, 7835-7843.

[6] Sun, J.; Wu, C.; Sun, X.; Hu, H.; Zhi, C.; Hou, L.; Yuan, C. Recent progresses in high-energy-density all pseudocapacitive-electrode-materials-based asymmetric supercapacitors. *J. Mater. Chem. A* **2017**, *5*, 9443-9464.

[7] Balaji, T.E.; Tanaya Das, H.; Maiyalagan, T. Recent trends in bimetallic oxides and their composites as electrode materials for supercapacitor applications. *ChemElectroChem* **2021**, *8*, 1723-1746.

[8] Wang, F.; Xiao, S.; Hou, Y.; Hu, C.; Liu, L.; Wu, Y. Electrode materials for aqueous asymmetric supercapacitors. *RSC Adv.* **2013**, *3*, 13059-13084.

[9] Sun, G.; Ren, H.; Shi, Z.; Zhang, L.; Wang, Z.; Zhan, K.; Yan, Y.; Yang, J.; Zhao, B. $V_2O_5$/vertically-aligned carbon nanotubes as negative electrode for asymmetric supercapacitor in neutral aqueous electrolyte. *J. Colloid Interface Sci.* **2021**, *588*, 847-856.

[10] Wang, L.; Ji, H.; Wang, S.; Kong, L.; Jiang, X.; Yang, G. Preparation of $Fe_3O_4$ with high specific surface area and improved capacitance as a supercapacitor. *Nanoscale* **2013**, *5*, 3793-3799.

[11] Chen, Y.; Zhou, C.; Liu, G.; Kang, C.; Ma, L.; Liu, Q. Hydroxide ion dependent α-$MnO_2$ enhanced via oxygen vacancies as the negative electrode for high-performance supercapacitors. *J. Mater. Chem. A* **2021**, *9*, 2872-2887.

[12] Feng, J.X.; Ye, S.H.; Lu, X.F.; Tong, Y.X.; Li, G.R. Asymmetric paper supercapacitor based on amorphous porous $Mn_3O_4$ negative electrode and $Ni(OH)_2$ positive electrode: a novel and high-performance flexible electrochemical energy storage device. *ACS Appl. Mater. Interfaces* **2015**, *7*, 11444-11451.

[13] Naresh, V.; Martha, S.K. Carbon coated $SnO_2$ as a negative electrode additive for high performance lead acid batteries and supercapacitors. *J. Electrochem. Soc.* **2019**, *166*, A551.

[14] Liang, X.; Xue, D. $Ce(OH)_3$ as a novel negative electrode material for supercapacitors. *Nanotechnology* **2020**, *31*, 374003.

[15] Vidhya, M.S.; Ravi, G.; Yuvakkumar, R.; Velauthapillai, D.; Thambidurai, M.; Dang, C.; Saravanakumar, B. Nickel–cobalt hydroxide: a positive electrode for supercapacitor applications. *RSC Adv.* **2020**, *10*, 19410-19418.

[16] Liu, H.; Liang, Z.; Liu, S.; Zhang, L.; Xia, H.; Xie, W. Nickel manganese hydroxides with thin-layer nanosheets and multivalences for high-performance supercapacitor. *Results Phys.* **2020**, *16*, 102831.

[17] Nanwani, A.; Deshmukh, K.A.; Sivaraman, P.; Peshwe, D.R.; Sharma, I.; Dhoble, S.J.; Swart, H.C.; Deshmukh, A.D.; Gupta, B.K. Two-dimensional layered magnesium–cobalt hydroxide crochet structure for high rate and long stable supercapacitor application. *npj 2D Mater. Appl.* **2019**, I, 1-7.

[18] Mandal, M.; Ghosh, D.; Chattopadhyay, K.; Das, C.K. A novel asymmetric supercapacitor designed with $Mn_3O_4$@ multi-wall carbon nanotube nanocomposite and reduced graphene oxide electrodes. *J. Electron. Mater.* **2016**, *45*, 3491-3500.

[19] Meng, X.; Li, P.; Du, M.; Ji, P. Polydopamine-mediated formation of $MnSn(OH)_6$ on cryptomelane-type manganese oxide for catalyzing glucose isomerization to fructose. *Ind. Eng. Chem. Res.* **2017**, *56*, 8428-8436.

[20] Raj, B.G.S.; Kim, H.Y.; Kim, B.S. Ultrasound assisted formation of $Mn_2SnO_4$ nanocube as electrodes for high performance symmetrical hybrid supercapacitors. *Electrochim. Acta* **2018**, *278*, 93-105.

[21] Rani, B.J.; Yuvakkumar, R.; Ravi, G.; Kumar, P.; Babu, E.S.; Saravanakumar, B.; Velauthapillai, High performance $MnSn(OH)_6$ electrodes for energy conversion application. *Mater. Lett.* **2021**, *282*, 128888.

[22] Subbarayan, S.; Natesan, M.; Chen, S.M. Simple synthesis of $CoSn(OH)_6$ nanocubes for the rapid electrochemical determination of rutin in the presence of quercetin and acetaminophen. *New J. Chem.* **2020**, *44*, 11271-11281.

[23] Harrison, P.G.; Bailey, C.; Bowering, N. Evolution of microstructure during the thermal processing of manganese-promoted tin (IV) oxide catalysts. *Chem. Mater.* **2003**, *15*, 979-987.

[24] Nagamuthu, S.; Vijayakumar, S.; Ryu, K.S. Cerium oxide mixed $LaMnO_3$ nanoparticles as the negative electrode for aqueous asymmetric supercapacitor devices. *Mater. Chem. Phys.* **2017**, *199*, 543–551.

[25] Jin, W.H.; Cao, G.T.; Sun, J.Y. Hybrid supercapacitor based on $MnO_2$ and columned FeOOH using $Li_2SO4$ electrolyte solution. *J. Power Sources* **2008**, *175*, 686–691.

# Chapter VI

*Electrochemical performance and photocatalytic activity of some metal hexacyanoferrates (MHCF, M = Mn, Ni, Cu and Zn)*

## VI.1 Introduction

The transition metal complex like metal hexacyanoferrate (MHCFs, M ≡ metal ion) has recently got attention from scientific community, as the hexacyanoferrate compound shows some unique solid state chemistry and promising applications in the field of photocatalysis [1], electrocatalysis [2], ion-sensing [3] etc. This coordination polymer frameworks also known as Prussian blue analogues, have been extensively studied as promising electrode material for electrochemical capacitor due to their 3D network structure with high porosity, large electroactive sites, stable reversible redox properties, facile preparation and low cost [4-9].

Now-a-day's excessive and indiscriminate uses of organic–mineral complexes in electronic gadgets as well as usage of inorganic compound in the wood preservation industry have progressively become the most serious matter of environmental concern [10]. Mixing of the acid wastewater from mine drainage and heavy metal like chromium from preservation industry to the ground water is very dangerous towards aquatic life and mutagenic to human [11, 12]. The waste water without treatment is hazardous for ecosystem, as most of the synthetic dyes are toxic, mutagenic, carcinogenic and enhance the chemical oxygen demand (COD) of the water body. Generally, chromium (Cr) is present in compounds in two common oxidation states such as Cr(III) and Cr(VI) [13]. Amongst these, Cr(VI) is immensely toxic, carcinogenic, whereas Cr(III) is less toxic and more easily soluble in water as $Cr(OH)_3$. Cr (VI) is used in several industrial fields like textile production, electroplating, metal finishing, leather tanning, dyeing, etc. [14]. As a result, higher degrees of contamination due to discharges of Cr (VI) in waste water, makes the aquatic life severely harmful. Presence of Cr (VI) in drinking water causes kidney,

liver, bladder, and skin cancer [15]. So, there is an urgent demand for effective methods for efficient reduction of Cr (VI) to Cr (III) in industrial waste water. Different methods including ion exchange, precipitation, reverse osmosis, photocatalysis and adsorption are developed [16-18]. However, each method has its own advantages along with numerous drawbacks. The photo-catalytic process is highly efficient and cost effective as compared to the other methods.

In this work, a set of MHCF (M ≡ Ni, Zn, Mn and Cu) was prepared using a simple precipitation method. Electrochemical performances of the as-prepared materials were investigated in terms of CV, GCD and EIS analysis. The photocatalytic activity on the reduction of highly toxic Cr(VI) using sunlight was also performed.

## VI.2 Experimental Section

### *VI.2.1 Materials*

Manganese nitrate tetrahydrate ($Mn(NO_3)_2 \cdot 4H_2O$), Nickel nitrate hexahydrate ($Ni(NO_3)_2 \cdot 6H_2O$), Copper nitrate trihydrate ($Cu(NO_3)_2 \cdot 3H_2O$), Zinc nitrate hexahydrate ($Zn(NO_3)_2 \cdot 6H_2O$), potassium hexacyanoferrate ($K_3[Fe(CN)_6]$), potassium hydroxide (KOH), potassium dichromate ($K_2Cr_2O_7$) were purchased from Merck, India. All reagents were directly used for the experiment without further purification.

### *VI.2.2 Synthesis of metal hexacyanoferrate (MHCF; M = Mn,Ni, Cu, Zn)*

For the synthesis of metal hexacyanoferrate (MHCF), simple precipitation method was followed. Briefly, 20 mL 0.1 M aqueous solution of $M(NO_3)_2$ [M= Ni, Cu, Zn, and Mn] was taken in a 100 mL beaker. Then 20 mL 0.1 M aqueous solution of $K_3Fe(CN)_6$ was slowly added to it under vigorous stirring condition. The solution was

magnetically stirred for 1 hour. Then the solution was kept for 12 h in undisturbed condition at room temperature. After that the solid precipitate was filtered, washed with distilled water and ethanol for 4-5 times. Finally, the desired solid product (MHCF) was dried in air oven at 70°C for 6 h.

## VI.3 Results and Discussion

### *VI.3.1 Formation of the MHCF*

The synthetic procedure involves the precipitation method where a quick precipitation of metal hexacyanoferrate (MHCF, M = Mn, Ni, Cu and Zn) was achieved. The chemical reaction involved in this synthetic process can be written as follows:

$$M(NO_3)_2 + K_3[Fe(CN)_6] \rightarrow M_x[Fe(CN)_6]_y + KNO_3$$

### *VI.3.2 X-Ray diffraction (XRD) analysis*

X-ray diffraction (XRD) analysis was performed by Rigaku ULTIMA-III X-ray diffractometer with Cu $K_\alpha$ radiation (λ = 1.5418 °A). The XRD patterns of the as-prepared MHCF (M = Mn, Ni, Cu and Zn) are shown in Figure 1. The observed XRD peaks of the MHCF (M = Mn, Ni, Cu and Zn) are well-matched with those in the JCPDS card number 01-074-7327, 01-082-2283, 01-086-0513 and 00-038-0688, respectively. The peaks at 16.8, 23.9, 34.1, 38.3, 42.1, 48.9, 52.2, 55.2, 63.8, and 66.5 corresponding to the planes (002), (022), (004), (024), (224), (135), (244), (335), (246), and (137) respectively, indicate the formation of polycrystalline $Mn_4[Fe(CN)_6]_{2.667}\cdot 15.84H_2O$. The peaks at 17.3, 24.4, 35.1, 39.4, 50.4, 53.7, and 56.7 corresponding to the planes (200), (220), (400), (420), (440), (600), and (620) respectively, indicate the formation of polycrystalline $Ni_3[Fe(CN)_6]_2\cdot H_2O$ with cubic crystal systems. The peaks at 17.5, 24.9, 35.4, 39.7, 43.7, 50.9, 54.3, and 57.6

corresponding to the planes (200), (220), (400), (420), (422), (440), (442) and (620) respectively, indicate the formation of $Cu[Fe(CN)_6]_{0.667}$. The peaks at 9.7, 13.4, 14.0, 16.2, 19.5, 21.4, 24.4, 28.1, and 32.7 corresponding to the planes (012), (104), (110), (113), (024), (116), (300), (119), and (226) respectively, indicate the formation of polycrystalline $Zn_3(Fe(CN)_6)_2$ with rhombohedral crystal system.

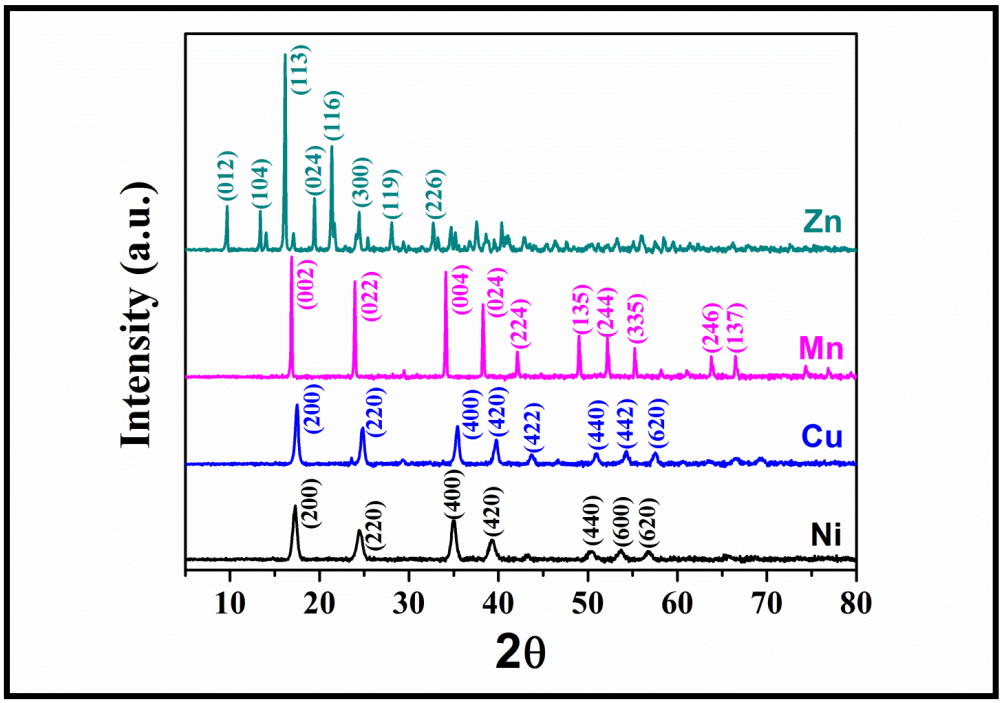


**Figure VI.1** XRD pattern of as-prepared MHCF (M = Mn, Ni, Cu and Zn).

### *VI.3.3 FTIR analysis*

To determine the structure, the FTIR spectra were recorded of the as-synthesized metal hexacyanoferrates (Figure VI.2). The sharp absorption peak at 2148.9 $cm^{-1}$ is assigned to the CN ligand in $Fe^{III}$-C≡N-$Mn^{II}$ [19]. The absorption peaks at 3381 $cm^{-1}$ and 1610 $cm^{-1}$ can be assigned to the O-H stretching mode and H-O-H bending mode of $H_2O$, respectively, owing to the existence of interstitial water in structure [20]. For NiHCF, the absorption peaks at 2098 $cm^{-1}$ and 2163 $cm^{-1}$ are ascribed to the characteristic peaks of Prussian blue analogs and the C≡N ligand ($Fe^{III}$-C≡N-$Ni^{II}$),

respectively [21]. For CuHCF, the strong absorption peak at 2092 $cm^{-1}$ attributes to the C≡N ligands stretching [22]. The absorption peaks at 3400 $cm^{-1}$ and 1620 $cm^{-1}$ can be assigned to the O-H stretching mode and H-O-H bending mode of $H_2O$, respectively, owing to the existence of interstitial water in structure [20]. For ZnHCF, the peak at 2094 $cm^{-1}$ and 494 $cm^{-1}$ correspond the C≡N ligands and –N─Zn, respectively [1]. The Fe-C stretching was detected at 602 $cm^{-1}$. For –O─H moiety of $H_2O$, a broad peak was observed at 3637 $cm^{-1}$ and the H-O-H bending peak was identified at 1607 $cm^{-1}$.

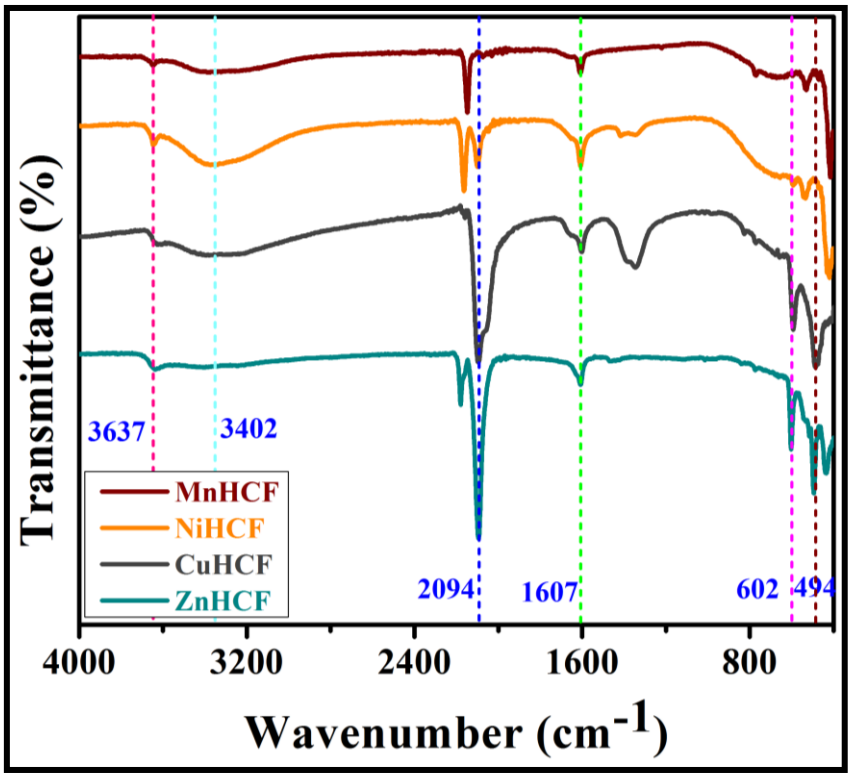


**Figure VI.2** FT-IR pattern of as-prepared MHCF (M = Mn, Ni, Cu and Zn).

### *VI.3.4 Morphological analysis*

To investigate the surface morphology of the as-synthesized metal hexacyanoferrate (M = Mn, Ni, Cu and Zn) photo-catalysts, the field emission scanning electron microscopy (FESEM,Carl Zeiss-SUPRA 40) images were captured (Figure VI.3).

From the FESEM of MnHCF, it can be seen that this is of cubic structure with an average length of about 1 μm (Figure VI.3a). The NiHCF and CuHCF are nano-sized particles (Figure VI.3b and c). The FESEM image of ZnHCF suggests the rhombohedral structure with an average length of 200 - 500 nm (Figure VI.3d).

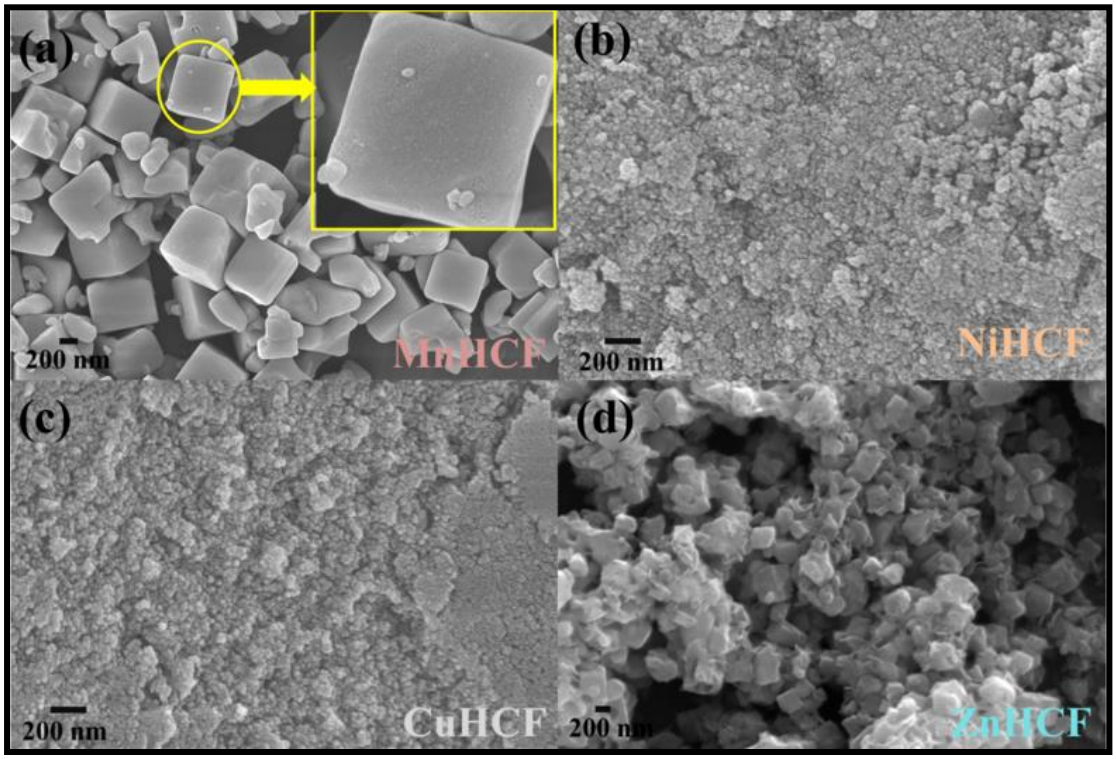


**Figure VI.3** FESEM images of as-prepared metal hexacyanoferrate: MnHCF (a), NiHCF (b), CuHCF (c) and ZnHCF (d).

### *VI.3.5 BET analysis*

The textural properties of the as-prepared MHCF were investigated by nitrogen-adsorption desorption measurements. The $N_2$ adsorption-desorption isotherm and their corresponding pore size distribution curves are shown in Figure VI.4 and the measured BET surface area, pore volume and the pore sizes are tabulated in Table VI.1. All the adsorption-desorption isotherms of MHCF exhibited type III isotherm with weak H3 hysteresis loop [23]. The pore-size distribution curves reveal the

mesoporous nature of the all materials. The increasing order of the BET surface area is MnHCF>ZnHCF>CuHCF>NiHCF. Amongst them the MnHCF was achieved high specific surface area of 664.33 $m^2/g$ with high pore volume of 0.51174 which is beneficial for the electrochemical performance.

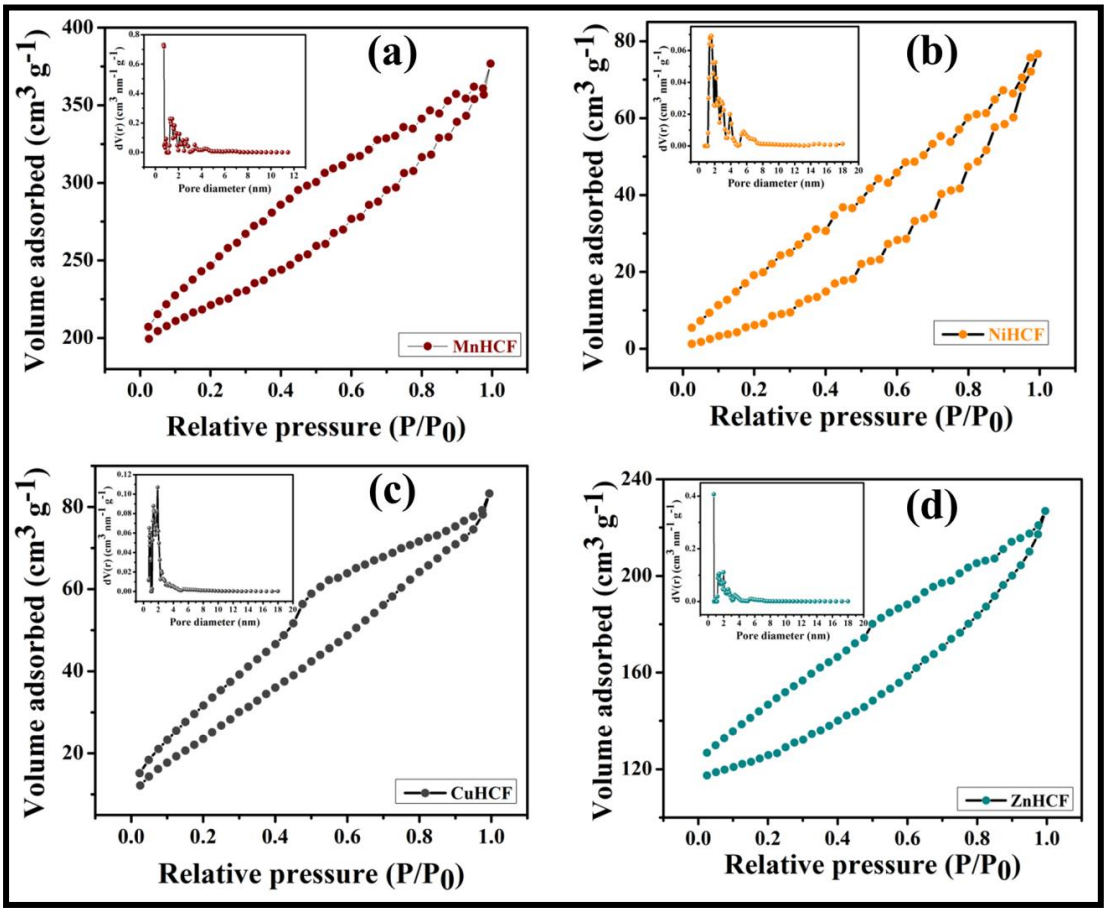


**Figure VI.4** Nitrogen adsorption-desorption isotherm and their corresponding pore size distribution curve (in inset) of as-prepared metal hexacyanoferrate: (a) MnHCF, (b) NiHCF, (c) CuHCF, and (d) ZnHCF.

**Table VI.1** Texture properties of as-prepared MHCF samples

| Samples | BET surface area ($m^2$/g) | Pore volume (cc/g) | Pore size (nm) |
|---|---|---|---|
| MnHCF | 664.33 | 0.51174 | 0.7049 |
| NiHCF | 56.50 | 0.1078 | 1.5149 |
| CuHCF | 98.81 | 0.1140 | 1.8972 |
| ZnHCF | 379 | 0.3108 | 0.7374 |

### *VI.3.6 UV–vis spectra analysis*

The optical properties of the as-synthesized MHCF were investigated by UV-vis spectroscopy. The band gap was calculated from Tauc plot using the equation below:

$$\alpha h\nu = A\,(h\nu - E_g)^{1/2}$$

where, $\alpha$ = absorption coefficient, $A$ = dimensional constant and $E_g$ = bandgap energy.

The UV-vis spectra of as-synthesized MHCF are depicted in Figure VI.4a. The three characteristic peaks of $[Fe(CN)_6]^{2-}$ were appeared at 261, 302 and 422 nm due to ligand-to-metal charge transfer transitions [24-27] The d-d transition of the metals was observed within the range of 400-425 nm. The plot of $(\alpha h\nu)^2$ versus $h\nu$ gives the bang gap value by extrapolating value of $h\nu$ at α = 0. The calculated band gap was 2.8, 3.05, 3.1 and 1.9 eV of MnHCF, NiHCF, CuHCF and ZnHCF, respectively. The lower band gap of the ZnHCF suggests its efficiency of showing visible light driven photocatalytic activity [1].

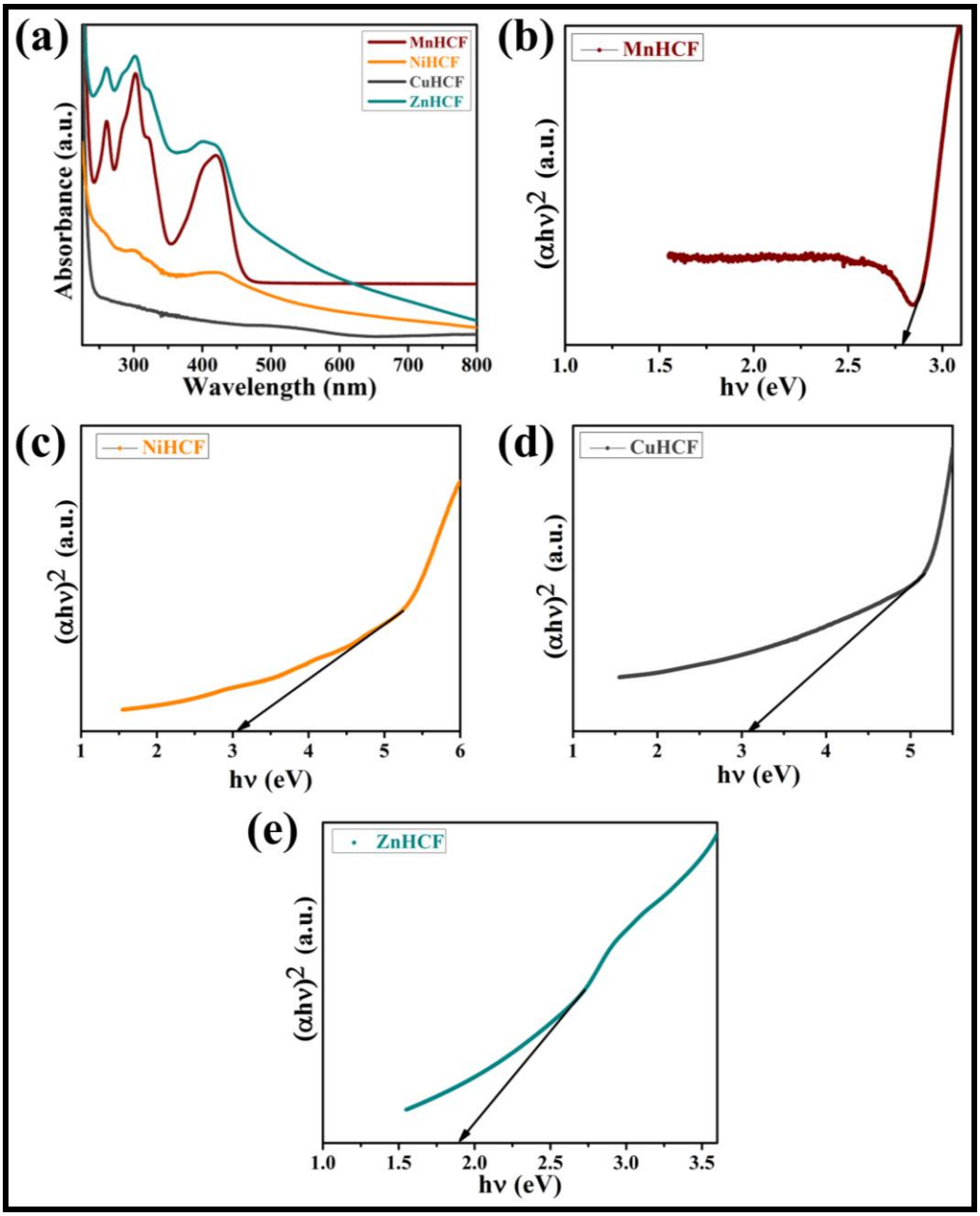


**Figure VI.5** (a) UV-vis spectra of all MHCF and Tauc plots of (b) MnHCF, (c) NiHCF, (d) CuHCF and (e) ZnHCF.

### *VI.3.7 Electrochemical Experiments*

Electrochemical performances were explored using a computer-controlled electrochemical working station (Autolab potentiostat and CS313, CorrTest, China) with a conventional three-electrode electrochemical cell in 1 M $Na_2SO_4$ aqueous

electrolyte. The working electrode was prepared by drop casting of ethanolic solution of MHCF on teflon-coated graphite rod and dried for 6 h. Then, 5 μL of 0.5 (w/v) % nafion (as binder) was dropped on it and then dried overnight. A platinum plate and a saturated calomel electrode (SCE) were taken as counter electrode and reference electrode, respectively. The specific capacitance of the electrode materials were calculated from CV and GCD measurements using eq 1 and 2, respectively.

$$\boldsymbol{C_s = \frac{\int_{V2}^{V1} i(V)dV}{(V2-V1)vm}} \quad \textbf{..... (1)}$$

$$\boldsymbol{C_s = \frac{i \times \Delta t}{m \times \Delta V}} \quad \textbf{..... (2)}$$

where, $\int_{V2}^{V1} i(V)dV$ is the area of the CV curve, $\Delta V = (V2 - V1)$ is the potential window (V), $v$ is the scan rate (mV/s) and m is the mass (g) of the active materials, $i$ is the applied current (A), and $\Delta t$ is the discharge time (s).

The CV curves of the as-synthesized MHCF in 1 M $Na_2SO_4$ were shown in Figure VI.6. The neutral electrolyte was chosen as metal hexacyanoferrates are fairly stable in acidic or basic condition. All the MHCF materials show redox peaks indicating pseudocapacitive behavior. These redox peaks can be ascribed to the reversible faradaic redox reaction of $Fe^{II}/Fe^{III}$ in the MHCF which are accompanying with the reversible intercalation/de-intercalation of $Na^+$ ion for sustaining local charge neutrality. The corresponding redox reactions are as follows [28]:

$$M^{II}[Fe^{III}(CN)_6] + Na^+ + e^- \leftrightarrow NaM^{II}[Fe^{II}(CN)_6]$$

$$M^{II}[Fe^{III}(CN)_6] + Na^+ + e^- \leftrightarrow NaM^{III}[Fe^{III}(CN)_6]$$

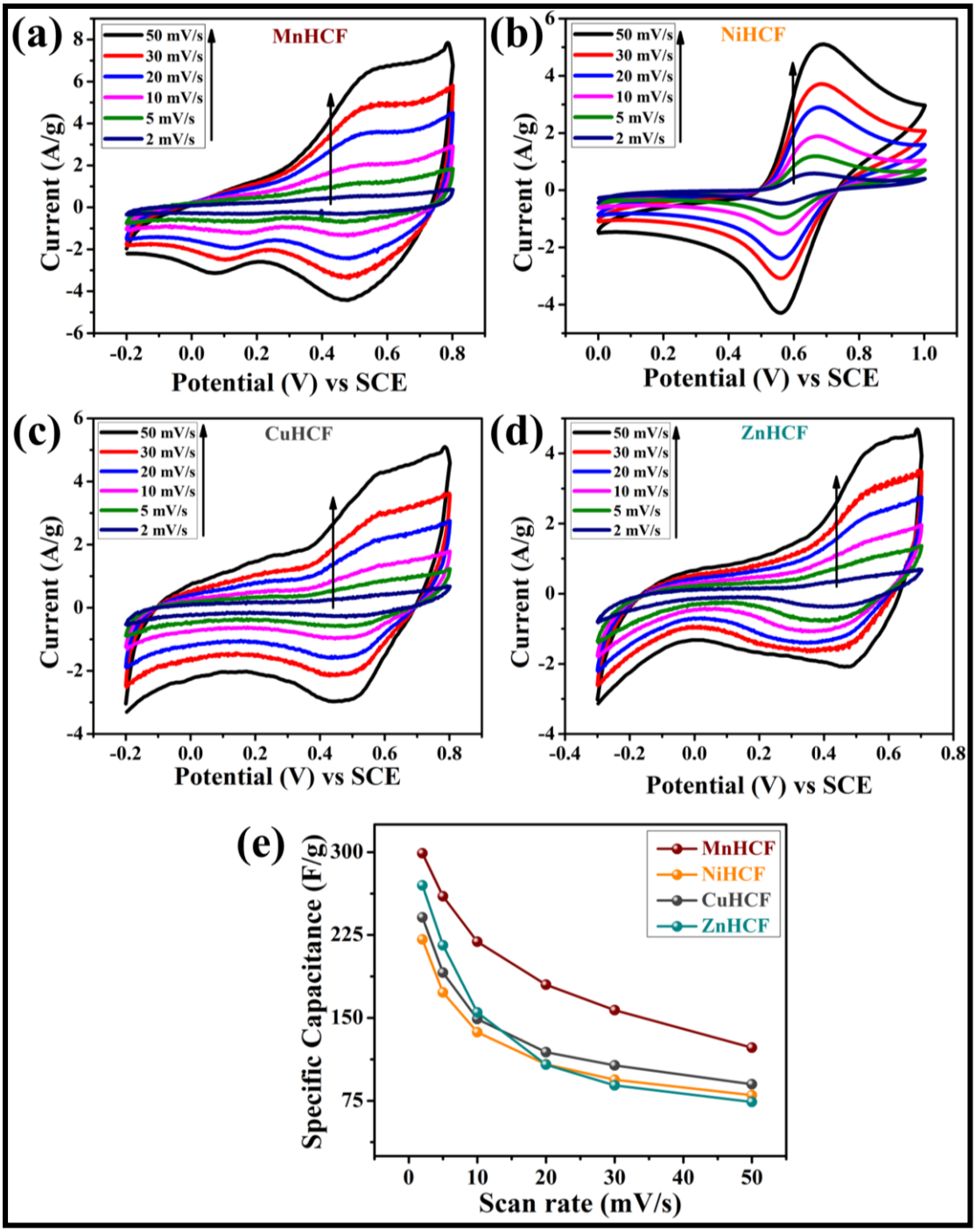


**Figure VI.6** CV curves of (a) MnHCF, (b) NiHCF, (c) CuHCF, and (d) ZnHCF at different scan rate of 2 to 50 mV/s; (e) Specific capacitance of as-synthesized MHCF at various scan rates.

The specific capacitances were calculated from the CV curve. The maximum specific capacitances of 299 F/g, 221 F/g, 241 F/g and 270 F/g at scan rate of 2 mV/s

were achieved by MnHCF, NiHCF, CuHCF and ZnHCF respectively. Due to high specific surface area with high pore volume of MnHCF, it exhibited high specific capacitance. The specific capacitance decreases with increasing scan rate. At lower scan rate, the electrode achieved maximum capacitance due to the complete redox process due to the highest diffusion of electrolyte ions into the inner active site. However, it cannot get enough time at high scan rate and produces lower capacitance [7].

The rate performance of the as-prepared electrodes was investigated through the galvanostatic charge-discharge measurement at different specific capacitance. The GCD curves are shown in Figure VI.7. The non-linear behavior of GCD curves indicates the pseudocapacitive behavior of the materials which were well-matched with the CV experiments. The specific capacitance decreases with increasing the specific current. The maximum specific capacitance of 208, 149, 163 and 187 F/g at specific capacitance of 1 A/g were achieved by the MnHCF, NiHCF, CuHCF and ZnHCF, respectively. MnHCF achieved high specific capacitance probably due to the high active surface area. It showed 40% capacitance retention at specific capacitance of 5 A/g, indicating high rate performance amongst the MHCF whereas ZnHCF showed the lowest rate performance.

The electrochemical stability of the electrodes was explored by consecutive GCD in 1 M $Na_2SO_4$ electrolyte at a specific current of 5 A/g. The cycling performance of MHCF is shown in Figure VI.7f. The retention of specific capacitance of the MnHCF, NiHCF, CuHCF and ZnHCF, was 84%, 76%, 72% and 61%, respectively after 1500 cycles.

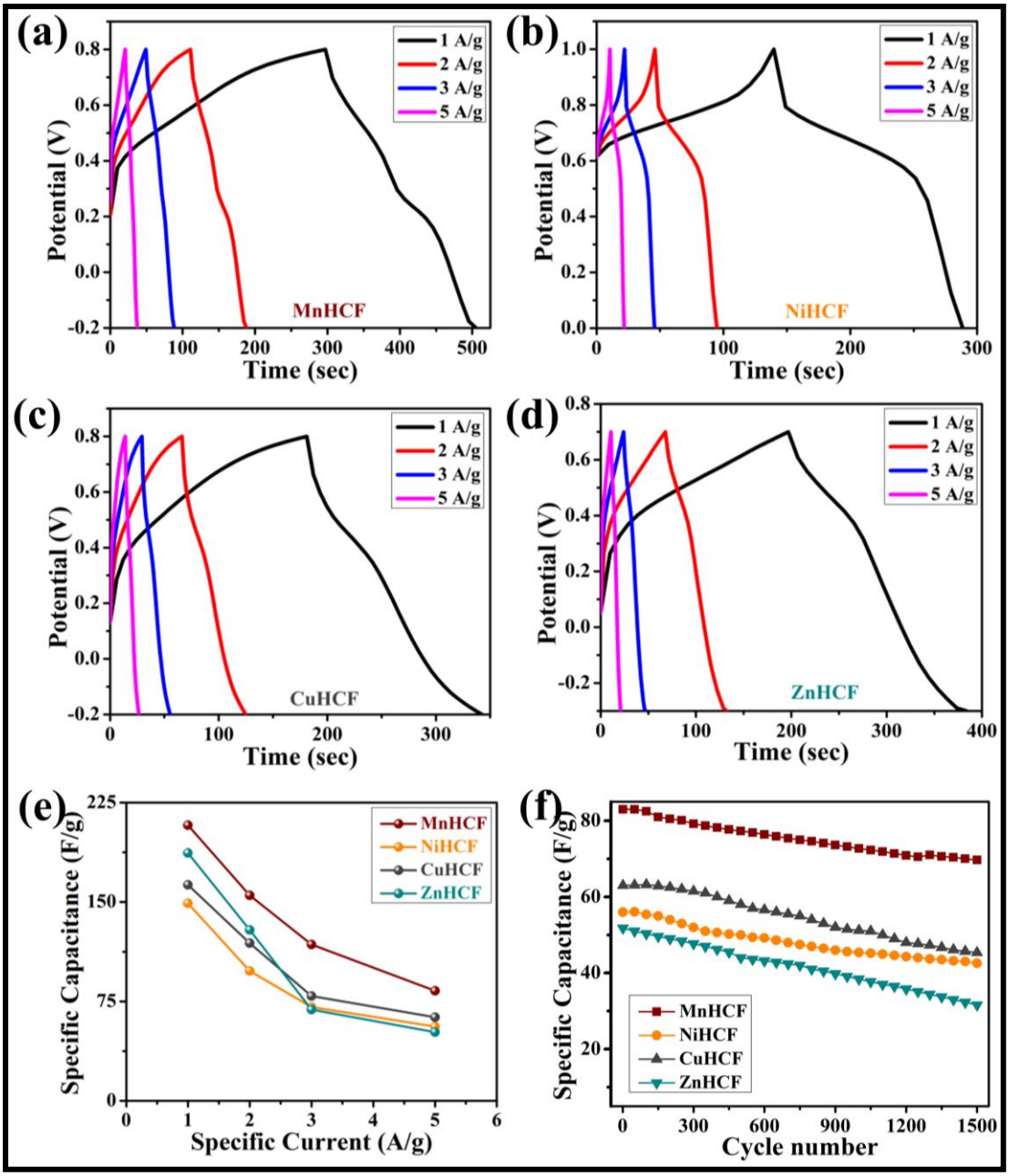


**Figure VI.7** GCD curves of (a) MnHCF, (b) NiHCF, (c) CuHCF, and (d) ZnHCF at different specific current of 1 to 5 A/g; (e) Specific capacitance of as-synthesized MHCF at various scan rates; (f) Cycling performance of MHCF at a specific current of 5 A/g for 1500 cycles.

### *VI.3.6 Photocatalytic Reduction of Cr(VI)*

The photocatalytic reduction of Cr(VI) was performed by taking the aqueous dichromate solution containing the different as-synthesized catalyst (MHCF) under sunlight. A set of four beakers containing 25 mL $2\times10^{-4}$ M aqueous solution of $K_2Cr_2O_7$ with 25 mg of different MHCF (M = Mn, Ni, Cu and Zn) was taken and stirred for 1 h in dark condition to reach the adsorption−desorption equilibrium. One blank test was also performed without catalyst. After that all the beakers were put under sunlight for 2 h with occasional shaking. The solutions were centrifuged separately time to time and the UV-vis spectra were recorded.

Figure VI.8 shows the photocatalytic reduction of aqueous Cr(VI) under sunlight in the presence of the as-synthesized metal hexacyanoferrate, MHCF (M = Mn, Ni, Cu and Zn). The diversity in the efficiency of different metal hexacyanoferrate may be a result of several factors, such as composition, particle size, morphology, crystallinity, crystal defects, specific surface area, band gap, state of dispersion, adsorption capacity for Cr(VI), etc. [15]. These factors are strongly coupled with each other and hence it is hard to identify the specific function and influence of a single parameter in the photocatalytic activity of different metal hexacyanoferrates. From the Figure VI.8, it can be seen that as-synthesized zinc hexacyanoferrate nanocubes reveal superior photocatalytic activity when compared to other catalysts. With increasing exposure time, the main absorption band of Cr(VI) cantered at 363 nm notably decreases due to decreasing the concentration of Cr(VI). It is calculated that the as-prepared zinc hexacyanoferrate nanocubes exhibit excellent photochemical reducing capability. The photo-catalytic activity i.e., reducing capability of the material is calculated (Equation 3) by monitoring the decrease in the absorption intensity which is directly proportional to the Cr(IV) concentration. A

decrease in absorption intensity from 1.02 to 0.33 at 365 nm implies 68% reducing capability of the as prepared ZnHCF within 2 h. However, the MnHCF, NiHCF and CuHCF showed the reducing activity of 7%, 17%, and 23%, respectively

$$\textbf{Catalytic activity}\ (\%) = \frac{|(\textit{Final absorption intensity} - \textit{Initial absorption intensity})|}{\textit{Initial absorption intensity}} \times 100\% \quad \textbf{...(3)}$$

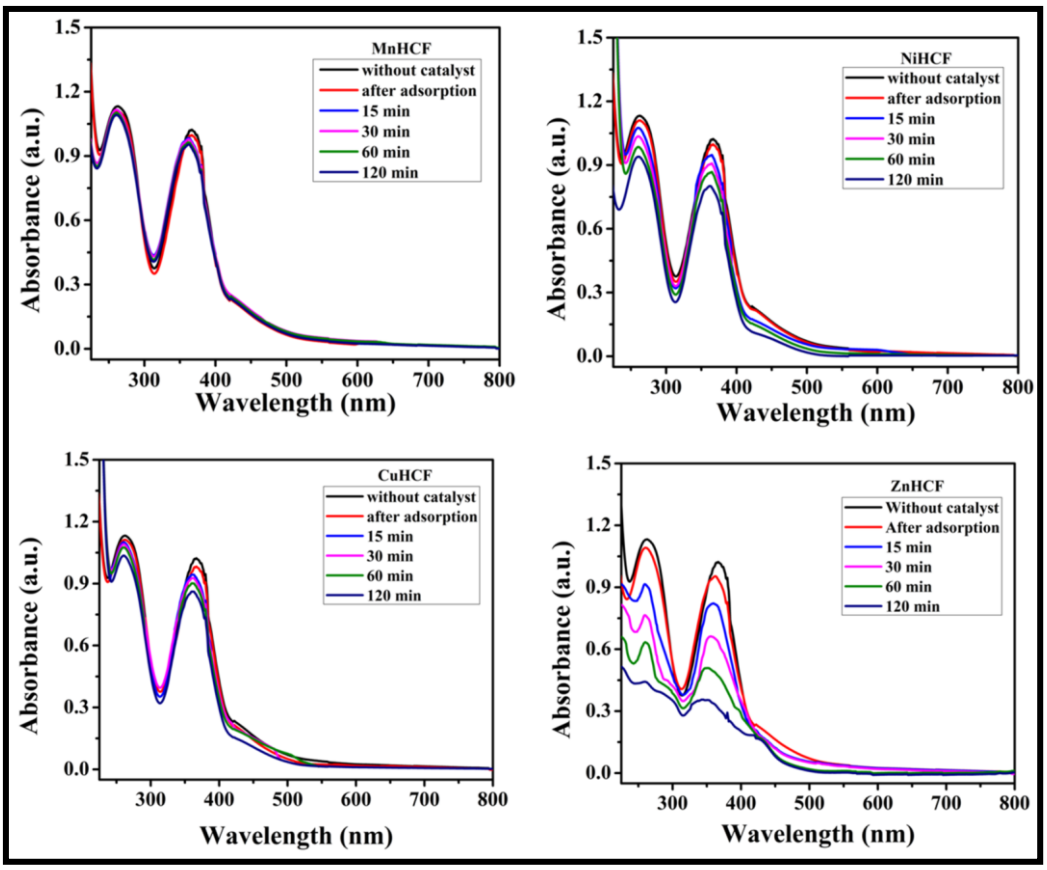


**Figure VI.8** Photocatalytic reduction of 25 mL of $2 \times 10^{-4}$ M aqueous solution of dichromate under sunlight in the presence of different MHCF (M = Mn, Ni, Cu and Zn) (25 g).

The reduction of Cr(VI) to Cr(III) is mainly carried out by the photoexcited electrons and therefore, good electron−hole pair separation is attained in this reduction process. The better photocatalytic activity of the as-prepared ZnHCF catalyst for the reduction of Cr(VI) under sunlight can be explained by taking into consideration of some unique properties of Zn which is responsible for the

exceptional behaviour of ZnHCF. Zinc has a completely filled valance shell *3d* orbitals and a narrow band gap. Due to highly dispersive nature of conduction band, the $d^{10}$ electronic configuration supports photo-generated electron-hole separation. On photo-irradiation with sunlight, MHCF semiconductors absorb light and electrons from valence band are excited to conduction band, generating the holes in the valance band. These photoexcited electrons in conduction bands of the semiconductors reduce Cr(VI) to Cr(III) with a visual color change of the solution from leuco to colorless. The probable reaction pathway for the photocatalytic reduction of Cr(VI) under sunlight over MHCF in aqueous solution is as follows:

$$MHCF + hv \rightarrow MHCF\ (e^- + h^+)$$

$$2H_2O + 4h^+ \rightarrow O_2 + 4H^+$$

$$Cr_2O_7^{2-} + 14H^+ + 6e^- \rightarrow 2Cr^{3+} + 7H_2O$$

## VI.4 Conclusion

In summary, four different metal hexacyanoferrates, MHCF (M = Mn, Ni, Cu and Zn) were synthesized via a simple and cost effective precipitation method. The as-prepared MHCF were structurally characterized using XRD and FTIR analysis and the morphology was captured with FESEM. The band gap was determined from the Tauc plot. The electrochemical performances were investigated using three-cell electrode system in 1 M $Na_2SO_4$ electrolyte. MnHCF showed good electrochemical properties with high specific capacitance of 208 F/g at 1 A/g specific current probably due to high specific area. The ZnHCF semiconductor exhibited more superior catalytic property for visible-light-driven photoreduction of Cr(VI), with excellent photochemical reducing capability of about 68%. Thus the as-synthesized metal

hexacyanoferrates show promising applications in the field of environmental photocatalysis.

**References**

[1] Jassal, V.; Shanker, U.; Kaith, B. S.; Shankar, S. Green synthesis of potassium zinc hexacyanoferrate nanocubes and their potential application in photocatalytic degradation of organic dyes. *RSC Adv.* **2015**, *5*, 26141-26149.

[2] Sitnikova, N. A.; Komkova, M. A.; Khomyakova, I. V.; Karyakina, E. E.; Karyakin, A. A. Transition metal hexacyanoferrates in electrocatalysis of $H_2O_2$ reduction: an exclusive property of Prussian Blue. *Anal. Chem.* **2014**, *86*, 4131-4134.

[3] Jassal, V.; Shanker U.; Shankar, S. Synthesis characterization and applications of nano-structured metal hexacyanoferrates: a review. *J. Environ. Anal. Chem.* **2015**, *2*, 2380-2391.

[4] Chen, J.; Huang, K.; Liu, S. Insoluble metal hexacyanoferrates as supercapacitor electrodes. *Electrochem. Commun.* **2008**, *10*, 1851-1855.

[5] Chen, J.; Huang, K.; Liu, S.; Hu, X. Electrochemical supercapacitor behavior of $Ni_3(Fe(CN)_6)_2(H_2O)$ nanoparticles. *J. Power Sources* **2009**, *186*, 565-569.

[6] Zhao, F.; Wang, Y.; Xu, X.; Liu, Y.; Song, R.; Lu, G.; Li, Y. Cobalt hexacyanoferrate nanoparticles as a high-rate and ultra-stable supercapacitor electrode material. *ACS Appl. Mater. Interfaces* **2014**, *6*, 11007-11012.

[7] Zhang, X.; He, P.; Zhang, X.; Li, C.; Liu, H.; Wang, S.; Dong, F. Manganese hexacyanoferrate/multi-walled carbon nanotubes nanocomposite: facile synthesis, characterization and application to high performance supercapacitors. *Electrochim. Acta* **2018**, *276*, 92-101.

[8] He, Y.; Zhang, P.; Wang, M.; Wang, F.; Tan, D.; Li, Y.; Feng, X. Nano-sandwiched metal hexacyanoferrate/graphene hybrid thin films for in-plane asymmetric micro-supercapacitors with ultrahigh energy density. *Mater. Horiz.* **2019**, *6*, 1041-1049.

[9] Zhou, Q.; Wei, T.; Liu, Z.; Zhang, L.; Yuan, B.; Fan, Z. Nickel hexacyanoferrate on graphene sheets for high-performance asymmetric supercapacitors in neutral aqueous electrolyte. *Electrochim. Acta* **2019**, *303*, 40-48.

[10] Liu, J.; He, X.; Lin, X.; Chen, W.; Zhou, Q.; Shun, W.; Huang, L. Ecological effects of combined pollution associated with e-waste recycling on the composition and diversity of soil microbial communities *Environ. Sci. Technol.* **2015**, *49*, 6438–6447.

[11] Turpeinen, R.; Kairesalo, T.; Häggblom, M.M. Microbial community structure and activity in arsenic-, chromiumand copper-contaminated soils *FEMS Microbiol. Ecol.* **2004**, *47*, 39–50.

[12] Liu, F., Zhang, W., Tao, L., Hao, B. and Zhang, J. Simultaneous photocatalytic redox removal of chromium(VI) and arsenic(III) by hydrothermal carbon-sphere@nano-$Fe_3O_4$ *Environ. Sci. Nano* **2019**, *6*, 937-947.

[13] Hsu, C. L.; Wang, S. L.; Tzou, Y. M. Photocatalytic reduction of Cr(VI) in the presence of $NO_3^-$ and $Cl^-$ electrolytes as influenced by Fe(III) *Environ. Sci. Technol.* **2007**, *41*, 7907−7914.

[14] Bhaumik, M.; Maity, A.; Srinivasu, V.V.; Onyango, M.S. Enhanced removal of Cr(VI) from aqueous solution using polypyrrole/$Fe_3O_4$ magnetic nanocomposite *J. Hazard. Mater.* **2011**, *190*, 381−390.

[15] Testa, J.J.; Grela, M.A.; Litter, M.I. Heterogeneous photocatalytic reduction of chromium(VI) over $TiO_2$ particles in the presence of oxalate: Involvement of Cr(V) species *Environ. Sci. Technol.* **2004**, *38*, 1589−1594.

[16] Joshi, K. M.; Shrivastava, V. S. Photocatalytic degradation of Chromium(VI) from wastewater using nanomaterials like $TiO_2$, ZnO, and CdS *Appl. Nanosci.* **2011**, *1*, 147-155.

[17] Dinda, D.; Gupta, A.; Saha, S. K. Removal of toxic Cr(VI) by UVactive functionalized graphene oxide for water purification. *J. Mater. Chem. A* **2013**, *1*, 11221−11228.

[18] Mondal, C.; Ganguly, M.; Pal, J.; Roy, A.; Jana, J.; Pal, T. Morphology controlled synthesis of $SnS_2$ nanomaterial for promoting photocatalytic reduction of aqueous Cr(VI) under visible light. *Langmuir* **2014**, *30*, 4157-4164.

[19] Pang, H.; Zhang, Y.; Cheng, T.; Lai, W.Y.; Huang, W. Uniform manganese hexacyanoferrate hydrate nanocubes featuring superior performance for low-cost supercapacitors and nonenzymatic electrochemical sensors. *Nanoscale* **2015**, *7*, 16012-16019.

[20] Wang, J.G.; Zhang, Z.; Zhang, X.; Yin, X.; Li, X.; Liu, X.; Kang, F.; Wei, B. Cation exchange formation of prussian blue analogue submicroboxes for high-performance Na-ion hybrid supercapacitors. *Nano Energy* **2017**, *39*, 647-653.

[21] Lu, K.; Song, B.; Zhang, J.; Ma, H. A rechargeable Na-Zn hybrid aqueous battery fabricated with nickel hexacyanoferrate and nanostructured zinc. *J. Power Sources* **2016**, *321*, 257-263.

[22] Ma, X.H.; Jia, W.; Wang, J.; Zhou, J.H.; Wu, Y.D.; Wei, Y.Y.; Zi, Z.F.; Dai, J.M. Synthesis of copper hexacyanoferrate nanoflake as a cathode for sodium-ion batteries. *Ceram. Int.* **2019**, *45*, 740-746.

[23] Chaudhary, K.; Mogha, N.K.; Lalwani, S.; Sharma, R.K.; Masram, D.T. Ruthenium oxide nanoparticles immobilized over Citrus limetta waste derived carbon material for electrochemical detection of hexestrol. J. Mater. Chem. B **2020**, *8*, 7956-7965.

[24] Yang, M.; Yang, Y.; Qu, F.; Lu, Y.; Shen, G.; Yu, R. Attachment of nickel hexacyanoferrates nanoparticles on carbon nanotubes: preparation, characterization and bioapplication. *Anal. Chim. Acta* **2006**, *571*, 211-217.

[25] Babu, R.S.; Prabhu, P.; Narayanan, S.S. Facile immobilization of potassium-copper hexacyanoferrate nanoparticles using a room-temperature ionic liquid as an ionic binder and its application towards BHA determination. *J. Solid State Electrochem.* **2016**, *20*, 1575-1583.

[26] Silva, M.N.; Ardisson, J.D.; Fabris, J.D.; Nossol, E. Zinc hexacyanoferrate/multi-walled carbon nanotubes films for rechargeable aqueous batteries. *J. Braz. Chem. Soc.* **2020**, *31*, 1787-1795.

[27] Kong, Q.; Chen, X.; Yao, J.; Xue, D. Preparation of poly (N-vinyl-2-pyrrolidone)-stabilized transition metal (Fe, Co, Ni and Cu) hexacyanoferrate nanoparticles. *Nanotechnology* **2004**, *16*, 164.

[28] Tang, Z.; Shang, X.; Hu, B.; Nie, P.; Shi, W.; Yang, J.; Liu, J. Fabrication of various metal hexacyanoferrates@CNF through acid-regulation for high-performance supercapacitor with superior stability. *Carbon* **2022**, *187*, 47-55.

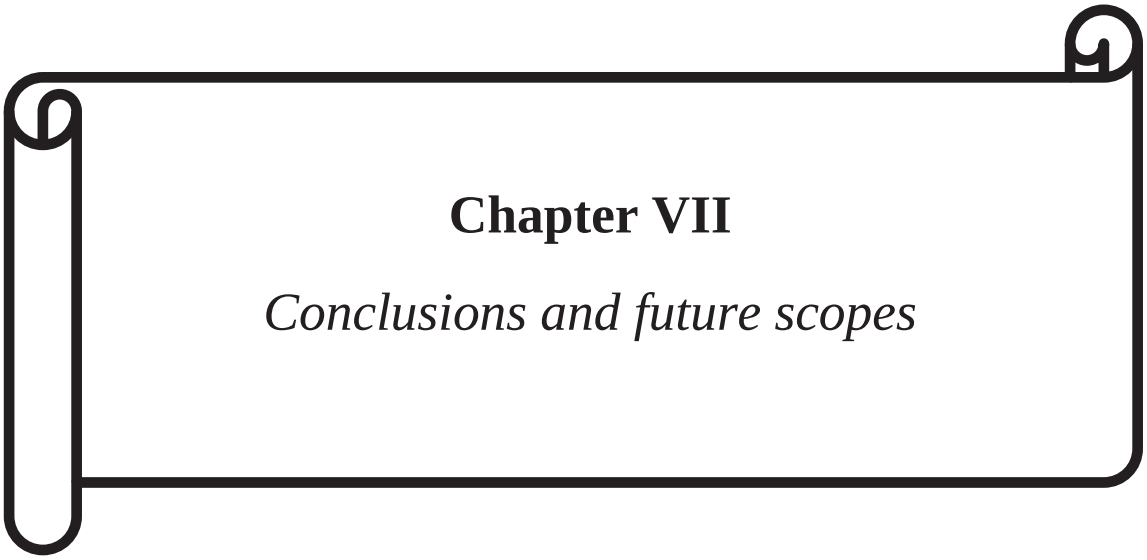

# Chapter VII

*Conclusions and future scopes*

## VII.1 Conslusions

The thesis mainly deals with the synthesis and electrochemical characterization of various types of manganese based nanomaterials for energy storage application. The work described manganese based materials as promising pseudocapacitive electrode for supercapacitor application. The combination of manganese oxide with carbonaceous material or other transition metal oxide greatly improved the electrochemical performance as a synergism effect between both the materials. Incorporation of some other metal in the manganese based hydroxide or sufide help greatly to improve the electrochemical properties. The manganese based oxides ($Mn_3O_4$, $MnO_2$), bimettalic hydroxide ($MnSn(OH)_6$) and sulfide (MnCoS) and coordination complex ($Mn[Fe(CN)_6]$) have been investigated as supercapacitor electrode materials. In case of supercapacitor not only the active material but also its performance is effected by the electrolyte used. By adding redox mediated electrolyte in conventional electrolyte improved enormously the charge storage property. The synthesized materials were structurelly characterized by various techniques like X-ray diffraction (XRD), Fourier transform infrared spectroscopy (FTIR), Raman spectroscopy etc. and morphologically analysed by Field emission scanning electron microscopy (FE-SEM) and Transmission electron microscopy (TEM). The electrochemical performance of the materials were performed in terms of CV, GCD and EIS study.

$Mn_3O_4$ and $Mn_3O_4$@MWCNT composites have been successfully synthesized using a simple hydrothermal method. The as-synthesized materials were characterized using different microscopic and spectroscopic tools. In three-electrode cell system, $Mn_3O_4$ and $Mn_3O_4$@MWCNT exhibited maximum specific capacitances of 428.9 F/g

and 471.3 F/g, respectively, at a scan rate of 2 mV/s. A synergistic interaction between highly electrical conductive MWCNT and pseudocapacitive $Mn_3O_4$ resulted in higher specific capacitance. An aqueous asymmetric supercapacitor was constructed using $Mn_3O_4$@MWCNT and rGO as positive and negative electrode, respectively, which was able to show high cell voltage of 1.6 V in 1 M KOH electrolyte. The high cell voltage combining high capacitance of positive electrode and high rate capability of negative electrode resulted in high energy and power density of 26.8 Wh/kg and 2400 W/kg, respectively for the $Mn_3O_4$@MWCNT//rGO. The high energy and power density accompanied by standard cycle life strongly demonstrate the high efficiency of the as fabricated supercapacitor for practical purpose.

A simple and facile precipitation method in combination with conventional hydrothermal method was adopted for fabrication of $MnO_2$-CuO nanocomposites (CMO3 and CMO6). In the composites the pure CuO nano-needles are uniformly covered with $MnO_2$ nano-sheets. The as-synthesized materials were characterized using different techniques. The electrochemical behavior of the composites were investigated in a redox mediated electrolyte (0.3 M $K_3[Fe(CN)_6]$ in 2 M KOH). The CMO6 composite with highest surface area and porosity displays the highest value of capacitance when compared to the pristine CuO and CMO3 composite. The CMO6 composite achieved high specific capacitance of 2690 F/g at specific current of 8 A/g with better rate performance. The CMO6 exhibited highest cycle stability with 79% capacitance retention after 1500 CV consecutive cycles at a scan rate of 40 mV/s. The results of the electrochemical studies imply that the composite CMO6 could be a promising electrode material for supercapacitor application.

Three-dimensional interconnected MnCoS nanosheets were deposited on nickel foam using a single-step electrosythesis method. The MnCoS@Ni produced high specific capacitance of 1952.8 F/g at 2 A/g scan rate with high rate performance. A MnCoS@Ni‖rGO@Ni AAS was fabricated which delivered high specific capacitance of 360 F/g at 10 A/g. The AAS also delivered high specific energy (105.1 Wh/kg) at a high specific power (7.25 kW/kg) along with high cyclic stability (93.9 % specific capacitance retained after 3000 consecutive GCD cycle). A series-connected device was able to lit up five parallel-connected red LEDs for 180 s.

A negative electrode based on $MnSn(OH)_6$ nanocubes was prepared by a simple precipitation method at room temperature. The as-synthesized material was structurally and morphologically characterized using different techniques. The uniform structure and fine edge morphology having high conductivity due to oxygen vacancies promote the redox reaction which results in high pseudocapacitance. The oxygen vacancies of the as-synthesized were confirmed by photoluminescence spectrum. The electrochemical performance was investigated through a three-electrode cell system in a negative potential window (-1.0 to 0.0 V) and a maximum specific capacitance of 209 F/g was calculated at a specific current of 1 A/g. The electrodes also exhibited excellent cycling stability with 79% specific capacitance retention after 3000 consecutive GCD cycles.

A set of co-ordination complexes such as metal hexacyanoferrates, (MHCF, M = Mn, Ni, Cu and Zn) were synthesized via a facile and cost effective precipitation method. The as-synthesized MHCF were structurally and morphologically characterized. The band gap was determined from the Tauc plot. The electrochemical properties were studied using three-cell electrode cell system in 1 M $Na_2SO_4$ electrolyte. The MnHCF showed good electrochemical performance with high

specific capacitance of 208 F/g at 1 A/g specific current probably due to high specific area. Amongst the MHCF, ZnHCF semiconductor exhibited more superior catalytic property for visible-light-driven photoreduction of Cr(VI), with excellent photochemical reducing capability of about 68%. Thus the as-synthesized metal hexacyanoferrates show promising applications in the field of energy storage and environmental photocatalysis as well.

## VII.2 Scope of future work

Although there are several articles reported on manganese-based pseudocapacitive electrode materials, but intense research is still required to understand the proper charge storage mechanism to make it suitable for practical purpose. Making hybrid supercapacitor with the carboneceous material has shown improved electrochemical performance. So, there is huge scope to find out the best component composition in the composites based on the manganese-based materials and other carboneceous material/ transition metal oxides/ sulfides/ hydroxides and conducting polymers. Redox mediated conventional electrolyte has shown very high capacitance. Therefore, an intesive research can be performed to find out the best suitable electrolyte from various redox active electrolytes.

# Publications

## *P.1 Journal article*

1. **M. Mandal**, R. Nagaraj, K. Chattopadhyay et al., A high-performance pseudocapacitive electrode based on CuO-$MnO_2$ composite in redox-mediated electrolyte, *Journal of Materials Science* **2021**, *56*, 3325-3335.

2. **M. Mandal**, D. Ghosh, K. Chattopadhyay et al., A novel asymmetric supercapacitor designed with $Mn_3O_4$@Multi-wall carbon nanotube nanocomposite and reduced graphene oxide electrodes. *Journal of Electronic Materials* **2016**, *45*, 3491-3500.

3. K. Chattopadhyay, **M Mandal**, D.K. Maiti, Smart MOFs for biotechnological applications: A mini review, *ACS Applied Bio Materials* **2021**, *4*, 8159-8171.

4. D. Majumdar, **M. Mandal**, S.K. Bhattacharya, Journey from supercapacitors to supercapatteries: Recent advancements in electrochemical energy storage systems, *Emergent Materials* **2020**, *3*, 347-367.

5. D. Majumdar, **M. Mandal**, S.K. Bhattacharya, Review on $V_2O_5$ and its' carbon-based nanocomposites for supercapacitor applications. *ChemElectroChem* **2019**, *6*, 1623-1648.

6. M. Chakraborty, K.K. Bera, **M. Mandal**, N. Sepay et al., Visible light assisted photo-electrocatalytic oxidation of methanol using low Pt content NiO-Rutile $TiO_2$ ternary heterojunction. *Applied Surface Science* **2020**, 541.

7. S. Chatterjee, A. Ray, **M. Mandal**, S. Das et al., Synthesis and characterization of CuO-NiO nanocomposites for electrochemical supercapacitors. *Journal of Materials Engineering and Performance* **2020**, *29*, 8036-8048.

8. K.K. Bera, M. Chakraborty, S.K. Bera, **M. Mandal** et al., Synthesis of different Pt-ZnO composites for synergistic photo-electrocatalytic oxidation of methanol in alkali, *ChemistrySelect*, **2021**, *6*, 6586-6596.

9. **M. Mandal**, K. Chattopadhyay, M. Chakraborty et al., Room temperature synthesis of $MnSn(OH)_6$ nanocubes: An excellent negative electrode for supercapacitor, **2022** (*Communicated*).

10. **M. Mandal**, K. Chattopadhyay, M. Chakraborty et al., Electro-synthesized Mn−Co−S nanosheets on Ni Foam for aqueous asymmetric supercapacitor. **2022** (*Communicated*).

## *P.2 Book chapter*

**M. Mandal**, K. Chattopadhyay, A. Jain et al., Porous carbon materials for supercapacitor applications in 'Handbook of Porous Carbon Materials', *Springer Nature Singapore Pte Ltd* **2022** (*Provisionally Accepted*).

## *P.3 Book*

K. Chattopadhyay, **M. Mandal**, *Analytical Chemistry – Skill Enhancement Course, CBS Publishers & Distributors Pvt. Ltd.* **2021** (ISBN: 978-93-90703-90-8)

## *P.4 Conference proceedings paper*

1. **M. Mandal**, K. Chattopadhyay, S.K. Bhattacharya, Sunlight mediated photocatalytic reduction of aqueous Cr(Vl) using metal hexacyanoferrate (M = Mn, Ni, Cu and Zn), *IOP Conference Series: Materials Science and Engineering* **2021**, *1080*, 012047.

2. **M. Mandal**, R. Nagaraj, K. Chattopadhyay et al., Investigation of the electrochemical performance of pristine CuO and $MnO_2$@CuO nanocomposite in redox mediated electrolyte. *Proceedings of ICESD 2020* (ISBN 978-93-83660-56-8), **2020**, 220-223.

3. S. Chatterjee, A. Ray, **M. Mandal** et al., Comparative Study on Electrochemical Energy Storage Properties of Cu-Ni-Oxide Nanocomposites for Supercapacitor Applications. *Proceedings of ICESD 2020* (ISBN 978-93-83660-56-8), **2020**, 216-219.

### *Presented in National Seminar*

1. **M. Mandal,** Pseudocapacitive Electrode based on Poly[Ni(salen)] Prepared by Electrochemical Polymerization. National Seminar on Modern Trends in Chemistry for Sustainable Development, 3rd March 2020, Vijaygarh Jyotish Roy College, Kolkata, India.

2. **M. Mandal,** Fabrication of an asymmetric supercapacitor based on $Mn_3O_4$-multi wall carbon nanotube composite and reduced graphene oxide. National Seminar on Current Development in Chemical Sciences (NSCDCS), 7th March 2018, Jadavpur University, Kolkata, India

## Webinars Attended

### *W.1 International*

1. "International virtual conference on "Advanced nanomaterials applications" organized by Centre for Nanotechnology Research, Vellore Institute of Technology, India during $17^{th}$ - $19^{th}$ Jun, 2020.

2. International e-conference on "Advanced functional materials and optoelectronic devices" organized by Centre for Renewable Energy, VBS Purvanchal University, India during $13^{th}$ – $15^{th}$ Jun, 2020.

### *W.2 National*

3. National level webinar "Metal-organic frameworks (MOFs) for energy and environment related applications" organized by Department of Chemistry, Mahadevananda Mahavidyalaya, India $27^{th}$ Jun, 2020.

4. The webinar on 'Steps towards life: Chemistry!', by Prof. Jean Marie Lehn, organized by the Dept. of Chemistry, Adamas University, India $29^{th}$ May, 2020.

5. National webinar on "Two dimensional materials for diverse applications" organized by Dept. of Basic Sciences, Cambridge Institute of Technology, India, $23^{rd}$ May, 2020.

*J Mater Sci* (2021) 56:3325–3335

Energy materials

# A high-performance pseudocapacitive electrode based on CuO–$MnO_2$ composite in redox-mediated electrolyte

Manas Mandal[1,2], Radha Nagaraj[3], Krishna Chattopadhyay[4], Malay Chakraborty[2], Sujit Chatterjee[2], Debasis Ghosh[3], and Swapan Kumar Bhattacharya[2,*]

[1] *Department of Chemistry, Sree Chaitanya College, Habra, 24 Parganas (N), Habra 743268, West Bengal, India*
[2] *Physical Chemistry Section, Department of Chemistry, Jadavpur University, Kolkata 700032, West Bengal, India*
[3] *Centre for Nano & Material Sciences, Jain Global Campus, JAIN University, Bangalore 562112, India*
[4] *School of Chemical Sciences, Indian Association for the Cultivation of Science, Kolkata 700032, West Bengal, India*

**Received:** 24 July 2020
**Accepted:** 3 October 2020
**Published online:** 19 October 2020



## ABSTRACT

In the present work, a simple and cost-effective precipitation approach was carried out to fabricate CuO nano-needle, and its electrochemical performance was evaluated in a redox-mediated electrolyte (2 M KOH and 0.3 M $K_3Fe(CN)_6$). A high specific capacitance of 2519 F/g was recorded at a specific current of 8 A/g. However, the electrode suffered from poor rate capability as the specific capacitance was rapidly decreased to 100 and 1 F/g when the specific current was increased to 30 and 50 A/g, respectively. The CuO nanoparticles were further modified with $MnO_2$ by a hydrothermal method, and the resulting CuO–$MnO_2$ (CMO6) electrode delivered a high specific capacitance of 539 F/g even at very high specific current of 50 A/g. The as-synthesized electrode materials were structurally and morphologically characterized using X-ray diffraction (XRD) analysis, Fourier transform infrared spectroscopy (FTIR), X-ray photoelectron spectroscopy (XPS), scanning electron microscopy (SEM), and transmission electron microscopy (TEM). The electrochemical performances of the CuO and $MnO_2$–CuO composites have been examined in detail.

Radha Nagaraj and Krishna Chattopadhyay authors have equal contribution to this work.

Handling Editor: Shen Dillon.

Address correspondence to E-mail: skbhatt7@yahoo.co.in

https://doi.org/10.1007/s10853-020-05415-7

## GRAPHIC ABSTRACT

*Synopsis* Modification of pristine CuO nano-needles with $MnO_2$ nanosheets improved the electrochemical performance of the material. The composite was able to deliver a high specific capacitance of 539 F/g even at very high specific current of 50 A/g.

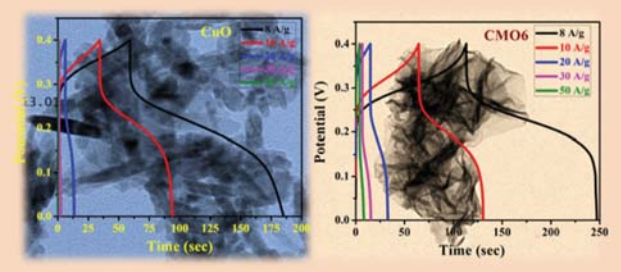


## Introduction

Enormous energy consumption by our electronically biased modern daily life triggers the scientists to search for a sustainable and renewable energy resource for future energy storage. Solar and wind energies have drawn global attention as renewable sources of energy, but their uncertain and discontinuous nature makes them unreliable [1]. Recently, electrochemical capacitors, also known as ultracapacitor or supercapacitors (SCs), have attracted remarkable attention in light of their unique properties of high power density, moderate energy density, long cycle life, fast charging capacity and green environmental protection [2, 3]. Based on the charge storage mechanism, SCs are classified into two pure types besides the hybrid one: (i) electrical double-layer capacitors (EDLCs) and (ii) pseudocapacitors. In EDLCs, the capacitance originates due to charge accumulation at the interfaces between electrode surface and electrolyte. The carbonaceous materials such as graphene and carbon nanotubes (CNTs) show such type of double-layer capacitance [4]. On the other hand, pseudocapacitance comes from the fast Faradaic redox reactions between electrode materials and electrolyte ions. Due to multiple oxidation states of the transition metals, its oxides, hydroxides and sulfides are commonly chosen as the pseudocapacitive electrode materials [5–8]. To enhance the efficiency of the electrode materials, the idea of incorporating combinatorial transition metal oxides with multiple electroactive redox sites has been developing. Not only the choice of electrode materials but also the surface architectures of the material, electrolyte, separator, etc. can alter the efficiency of supercapacitor. Recently, in terms of modification of electrolyte, the addition of a foreign redox system into the mother electrolyte solution as an additional source of pseudocapacitance is being taken into consideration.

CuO–$MnO_2$ is a well-known composite, which is previously reported for various applications like supercapacitors [2, 3, 9–12], Li-ion batteries [13, 14], heterogeneous catalysts [15–19], sensors [20, 21], etc. However, to the best of our knowledge this work is the first report on supercapacitor application of CuO–$MnO_2$ composite using redox-mediated electrolyte. Herein, pristine CuO and $MnO_2$ nanosheet-wrapped CuO nano-needles were synthesized by the precipitation method followed by a simple and facile hydrothermal technique, and the electrochemical properties were studied in terms of cyclic voltammetry (CV), galvanostatic charge–discharge (GCD) curve and electrochemical impedance spectra (EIS) in redox couple, $[Fe(CN)_6]^{3-}/[Fe(CN)_6]^{4-}$-mediated aqueous electrolyte.

## Experimental section

### Materials and reagents

Copper(II) nitrate trihydrate, potassium hexacyanoferrate(III), sodium hydroxide, potassium permanganate were supplied by Merck, India. All the reagents were directly used for the experiment without doing any purification.

### Synthesis of CuO

A large number of synthetic routes have been developed for the preparation of CuO with different morphologies [2, 3, 9–11]. Herein, the co-precipitation method was followed for the synthesis of CuO [22]. Briefly, 30 mL 0.1 M aqueous $Cu(NO_3)_2{\cdot}3H_2O$ solution was added dropwise in 20 mL 0.1 M aqueous $K_3[Fe(CN)_6]$ solution with a continuous stirring. The tawny brown colored precipitate of $Cu_3[Fe(CN)_6]_2$ was formed immediately. After one-hour continuous stirring, the solution was kept for 12 h in undisturbed condition. Then, 1 M NaOH was added dropwise to the mixture with a continuous stirring. The prompt color change from tawny brown to deep brown was recognized. The obtained solid product was washed with water for several times and dried at 60 °C in hot air oven.

### Synthesis of CuO–$MnO_2$ composites

A set of two solutions was prepared, each by dispersing 35 mg of as-prepared CuO in 35 mL 0.025 M aqueous solution of $KMnO_4$. Then, the solutions were transferred in two 50 mL stainless steel autoclaves and were kept in the furnace at 180 °C for 3 and 6 h, respectively. After cooling at room temperature, the solid brown products obtained from the two solutions were carefully washed in succession with water and absolute alcohol for several times. The desired materials were obtained after drying at 60 °C for 12 h, and the two products were labeled as CMO3 and CMO6, respectively. The same procedure without the addition of pure CuO was followed for the preparation of pure $MnO_2$.

## Material characterization

The chemical and structural analyses of the as-prepared electrode materials were carried out by X-ray diffraction (XRD, Rigaku ULTIMA-III X-ray diffractometer with Cu Kα radiation (λ = 1.548 Å) analysis, Fourier transform infrared (FTIR, NEXUS 870 Thermo-Nicolet) spectroscopy, and X-ray photoelectron spectroscopy (XPS, using a PHI 5000 Versa Probe II XPS analyzer with a monochromatic Al Kα X-ray source ($h\upsilon$ = 1486.71 eV)). From the field emission scanning electron microscopy (FESEM, Carl Zeiss-SUPRA 40) and tunneling electron microscopy (TEM, TECNAI G2-20S-TWIN) images, the surface morphology of the electrode materials was investigated. The surface area of the material was determined by the $N_2$ adsorption–desorption isotherm.

Electrochemical measurements were taken using a computer-controlled electrochemical working station (Biologic SP 150 and Autolab potentiostat) with a conventional three-electrode electrochemical cell in 2 M KOH aqueous solution containing 0.3 M $K_3[Fe(CN)_6]$. The working electrode was prepared on Ni foam. A platinum plate and a saturated calomel electrode (SCE) were used as counter electrode and reference electrode, respectively. The electrochemical behavior was analyzed in terms of cyclic voltammetry (CV), galvanostatic charge–discharge (GCD) curve and electrochemical impedance spectra (EIS). The specific capacitance of the electrode materials was calculated from CV and GCD measurements using Eqs. 1 and 2, respectively [23].

$$C_s = \frac{\int_{V2}^{V1} i(V)\mathrm{d}V}{2(V2 - V1)\upsilon m} \tag{1}$$

$$C_s = \frac{i \times \Delta t}{m \times \Delta V}, \tag{2}$$

where $\int_{V2}^{V1} i(V)\mathrm{d}V$ is the area of the CV curve, $\Delta V = (V2 - V1)$ is the potential window ($V$), $\upsilon$ is the scan rate (mV/s) and $m$ is the mass ($g$) of the active materials, $i$ is the applied current (A), and $\Delta t$ is the discharge time (s).

## Results and discussion

The synthesis procedure involves two-step chemical reactions: first a quick precipitation of copper hexacyanoferrate [CuHCFe] (co-precipitation method) and then the decomposition of CuHCFe complex in

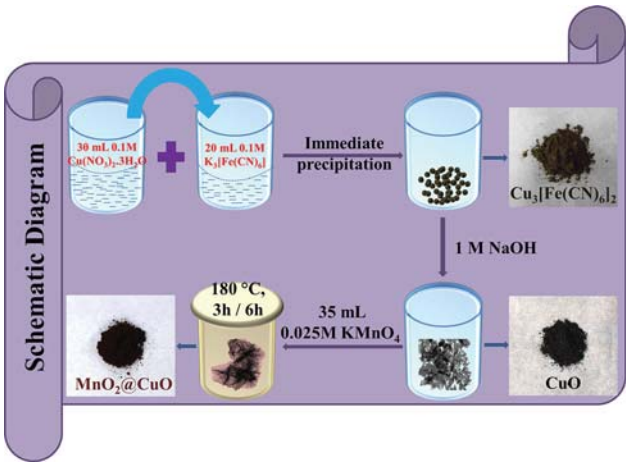


**Scheme 1** Synthetic procedure of CuO–$MnO_2$ composites.

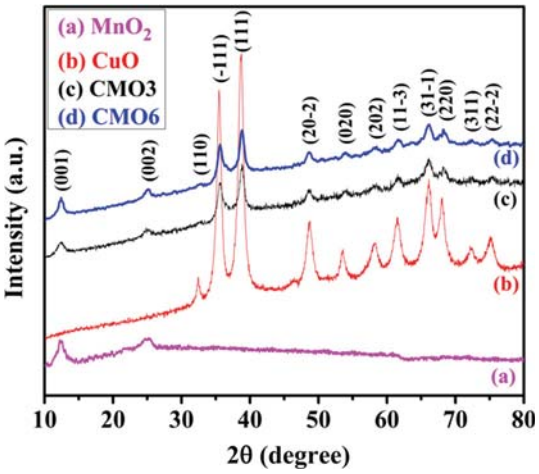


**Figure 1** XRD patterns of as-prepared pure $MnO_2$ (a), CuO (b), CMO3 (c) and CMO6 (d) composites.

alkaline medium [24]. The chemical reactions associated with the synthesis procedure are as follows.

$$3Cu(NO_3)_2+2K_3[Fe(CN)_6] = Cu_3[Fe(CN)_6]_2+6KNO_3 \quad (3)$$

$$Cu_3[Fe(CN)_6]_2+6NaOH = 3Cu(OH)_2+2Na_3[Fe(CN)_6]_2 \quad (4)$$

$$Cu(OH)_2 = CuO + H_2O \quad (5)$$

The $MnO_2$ nanosheets are formed from self-decomposition of $KMnO_4$ during hydrothermal reaction [25]. The total synthesis procedure is schematically represented in Scheme 1.

The XRD patterns were taken to determine the phase composition of pure $MnO_2$, CuO and CMO composites as shown in Fig. 1. For pure CuO, the

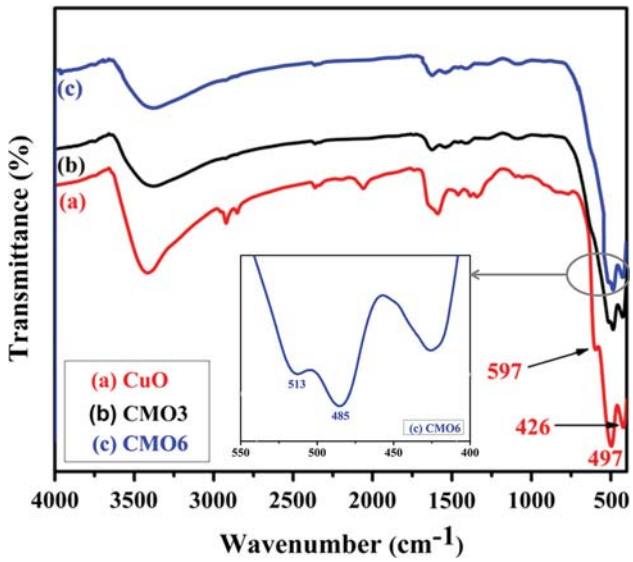


**Figure 2** FTIR spectra of as-prepared pure CuO (a), CMO3 (b) and CMO6 (c) composites.

peaks at 2θ (°) of 32.4, 35.5, 38.7, 48.7, 53.5, 58.3, 61.5, 66, 68, 72.3, and 75.1 correspond to (110), (− 111), (111), (20 − 2), (020), (202), (11 − 3), (31 − 1), (220), (311), and (22 − 2) planes of face-centered cubic crystal. All the peaks are well matched with JCPDS Card No: 05-0661 (Tenorite, Syn). The precursor of the CuO is copper hexacyanoferrate, which is confirmed by the XRD pattern as shown in Figure S1(a). For the composites, all the peaks of CuO are present along with the two basal reflections of (001) and (002) at 12.5 and 24.7 peaks for $MnO_2$, which are also present in case of pure $MnO_2$ (Fig. 1a). The peaks of the composites are less intense than the pure CuO as the $MnO_2$ nanosheets wrap around the CuO nano-needles. Furthermore, the characteristic peaks of $MnO_2$ were more prominent in CMO6.

To investigate the chemical and structural properties, FTIR analysis was carried out and the results are shown in Fig. 2. Pressed KBr pellets of CuO and the composites (CMO3 and CMO6) were used to execute FTIR analysis by NEXUS 870 FTIR (Thermo Nicolet) instrument. The three main characteristic peaks of CuO were observed at 597, 497 and 426 $cm^{-1}$ for $A_u$, $B_u$ and $B_u$ modes, respectively, which confirms the formation of CuO nano-needles. The Cu–O stretching values along (− 101) and (101) directions demonstrate the absorption peaks at 597 and 497 $cm^{-1}$, respectively [26–29]. The broad absorption peaks between 1300 and 4000 $cm^{-1}$ are ascribed as chemisorbed and/or physisorbed $H_2O$ and $CO_2$ molecules

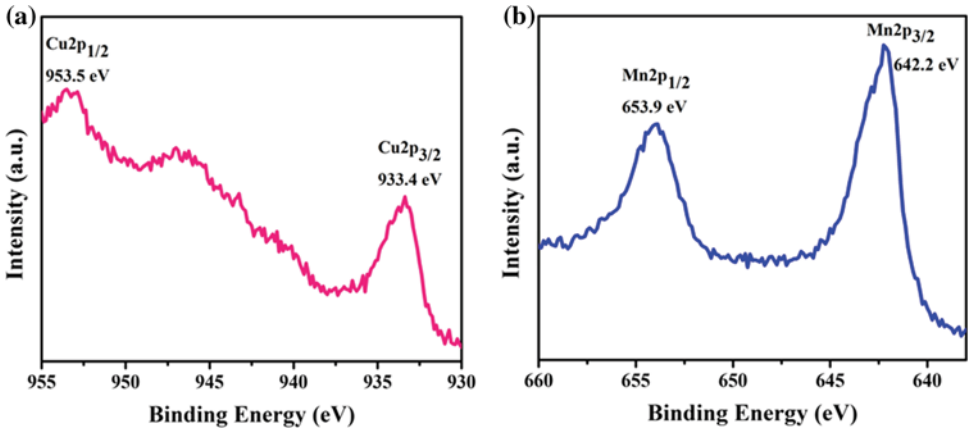


**Figure 3** XPS spectra of CMO6 composite: **a** Cu 2p spectrum and **b** Mn 2p spectrum.

[29, 30]. Moreover, there is no peak in between 610 and 660 $cm^{-1}$ indicating the absence of any other phases like $Cu_2O$, which appears at 615 $cm^{-1}$ [31]. In both the composites, the two main characteristic peaks are observed at 513 and 485 $cm^{-1}$ corresponding to Mn–O stretching modes in octahedral environment [32]. The peak at 1385 $cm^{-1}$ appears due to the coordination of Mn by O–H [32].

For the chemical analysis of the composite, XPS was carried out, which is shown in Fig. 3. The XPS spectra were accomplished by taking the reference peaks of C1s at 284.2 eV. For the Cu2p in CuO, the two major peaks of Cu2p1/2 and Cu2p3/2 are found at 953.5 and 933.5 eV, respectively, indicating the presence of CuO in composite [16]. Figure 3b shows XPS spectrum for Mn2p; the two peaks at 653.9 and 642.2 eV are attributed to the Mn2p1/2 and Mn2p3/2, respectively, with spin energy difference of 11.7 eV [33].

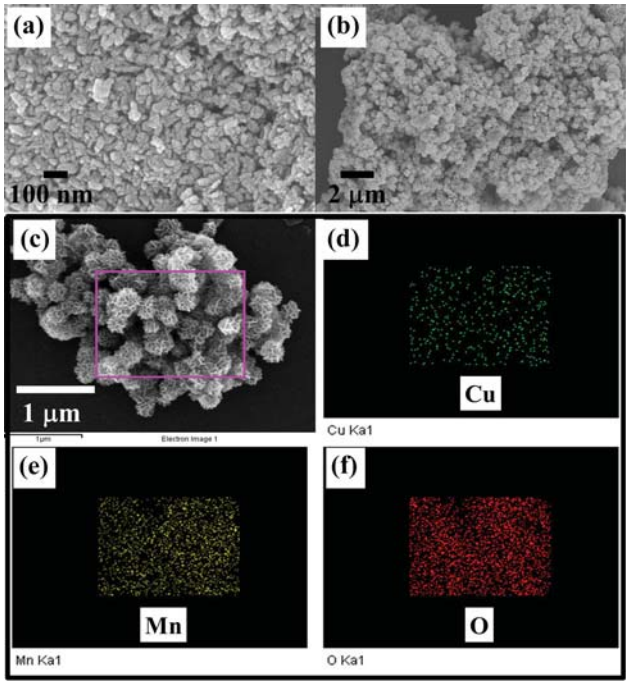


**Figure 4** FESEM images of as-prepared pure CuO (**a**) and CMO6 composites (**b**). Mapping images of CMO6 composite (**c–f**).

Figure 4 presents the corresponding FESEM images of as-synthesized CuO and CMO6 composites. It can be seen that the CuO particles are having nano-needle-like structure of length 80–100 nm. Copper hexacyanoferrate, the precursor of CuO nano-needle, consists of small nanoparticles as shown in Figure S1(b). The FESEM image of CMO3 is shown in Figure S2, which indicates the CuO nano-needles are covered up with $MnO_2$ nanosheets. However, for CMO6 composite, the CuO nanorods are fully wrapped by $MnO_2$ nanosheets (Fig. 4c), possibly due to longer time of growth. The element mapping images (Fig. 4d–f) confirm the presence of Cu, Mn and O implying the formation of CuO–$MnO_2$ composite. The TEM images of CuO and CMO6 composites are shown in Fig. 5. The nano-needle structures of CuO were again supported by the TEM images shown in Fig. 5a–c. The length and width of each CuO nano-needle is of 80–100 nm and 10–15 nm, respectively. The TEM images of the CMO6 composite are shown in Fig. 5d, e having different magnifications. Figure 5d, e denotes that the CuO nano-needles were entirely wrapped by $MnO_2$ nanosheets in CMO6. The energy-dispersive X-ray (EDAX) analysis spectrum (Fig. 5f) also confirms the presence of CuO in the composite.

The surface area plays a crucial role in determining the efficiency of a material as an adsorbent or electrode material. The $N_2$ adsorption–desorption

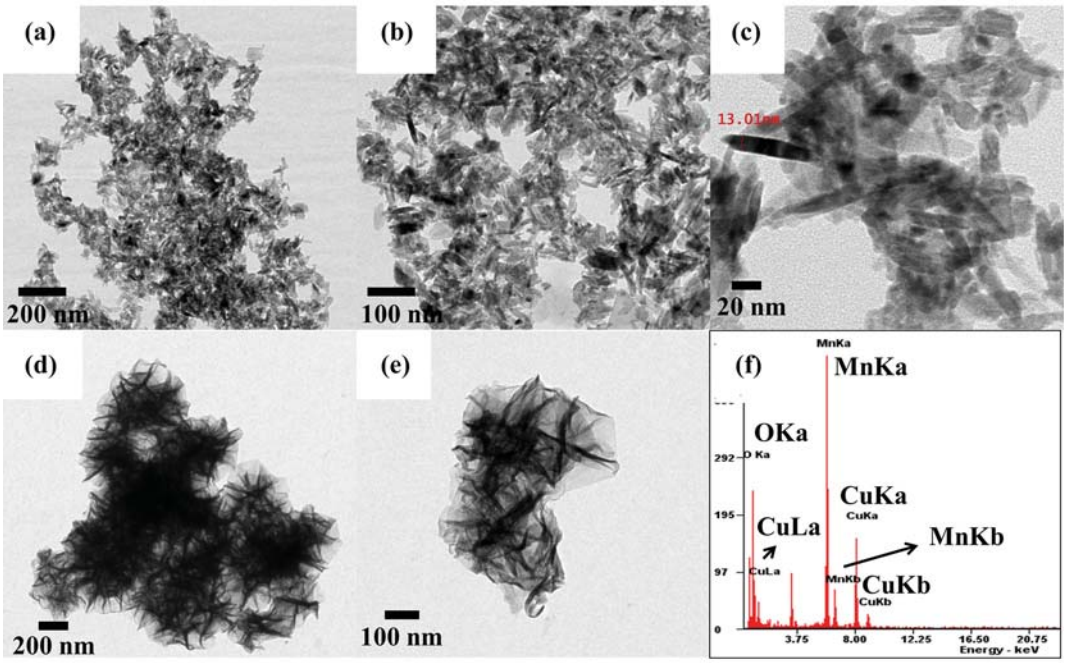


**Figure 5** TEM images of as-prepared pure CuO (**a–c**) and CMO6 composite (**d, e**) with different magnification. EDAX spectrum of the CMO6 composite (**f**).

isotherms and Barrett–Joyner–Halenda (BJH) profiles confirm higher surface area and enhanced porosity in the composites in comparison with the pure CuO nano-needles. The surface area of the pure CuO, CMO3 and CMO6 composites was obtained to be 60.43, 66.984 and 78.846 $m^2/g$, respectively, as measured by the Brunauer–Emmett–Teller (BET) method. The BJH pore size distribution profile (Figs. 6c, d and S3b) shows perfectly monomodal distribution with the maxima of 7.73, 1.96 and 1.79 nm for CuO nano-needle, CMO6 and CMO3 composites, respectively. According to the International Union of Pure and Applied Chemistry (IUPAC), all the BET isotherms show type-4 isotherm with a H3 hysteresis loop. The highly porous nature of the composites appears due to the presence of highly mesoporous and ultrafine $MnO_2$ nanosheets, which results in high electrochemical capacity of the nanocomposite (vide infra).

After fabrication of the working electrode, the electrochemical characterizations were carried out in terms of cyclic voltammetry (CV), galvanostatic charge–discharge (GCD) and electrochemical impedance spectroscopy (EIS). The CV curves of CuO and CMO6 composites at various scan rates in 2 M KOH electrolyte solution containing 0.3 M $K_3[Fe(CN)_6]$ are shown in Fig. 7a, b, respectively. Both the CV curves show very high value of current, indicating the high activity of the redox electrolyte. The comparison of CV curves of all the as-synthesized materials at 10 mV/s is shown in Fig. 7c. The high area of the CV curve of CMO6 indicates higher capacitance of the composite than pure CuO and CMO3 composites. The redox-active electrolyte surpluses electron density in conventional electrolyte, improving the ionic conductivity of the electrolyte and enhances the charge storage properties. Furthermore, the shift of the oxidation and reduction potential peaks with an increasing scan rate indicates the quasi-reversible nature of the pseudocapacitive electrode materials in the presence of the redox-active electrolyte. The oxidation peak among the pair of redox peaks in the CV curves appears due to the charging process, involving the conversion of $K_4[Fe(CN)_6]$ to $K_3[Fe(CN)_6]$, whereas the reduction peak involves the reverse reaction. The specific capacitance of 7521, 1839, 1051, 872, 745 and 615 F/g was calculated for CMO6 electrode at the scan rate of 1, 10, 20, 50, 100 and 200 mV/s, respectively. But the pristine CuO achieved the capacitance of 7363, 1239, 757, 381, 219 and 125 F/g at the scan rate of 1, 10, 20, 50, 100 and 200 mV/s, respectively. Furthermore, the CMO3 composite shows the specific capacitance of 5354, 1021.5, 686, 391, 244.8 and 152 F/g at the scan rate of 1, 10, 20, 50, 100 and 200 mV/s, respectively. One interesting

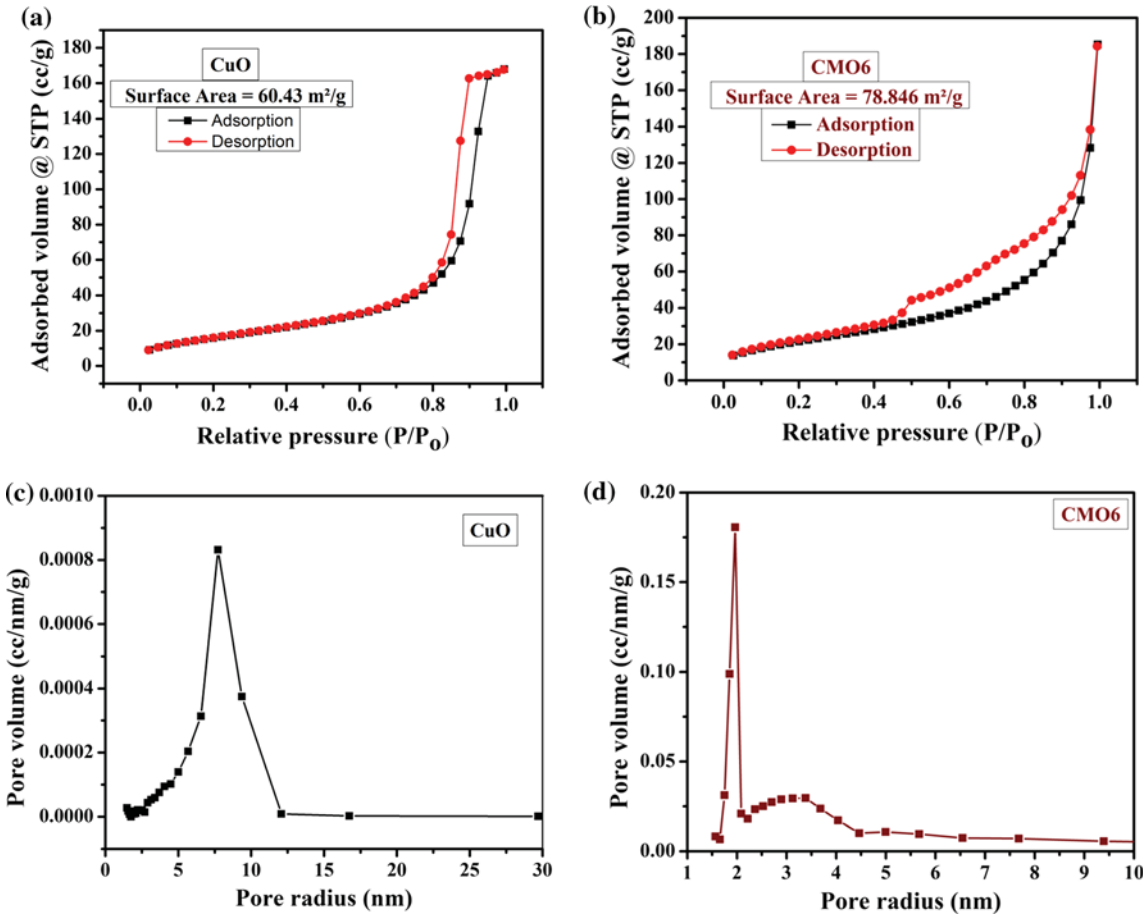


**Figure 6** $N_2$ adsorption–desorption isotherms of CuO (**a**) and CMO6 composite (**b**); BJH pore size distribution profile of CuO (**c**) and CMO6 composite (**d**).

point is that the pristine CuO exhibited better electrochemical performance at a low scan rate than at a high scan rate. This may be due to lower rate capability of CuO electrode. The CMO6 composite having high rate capability shows better performance throughout the whole range of scan rate. At the higher scan rate, the electrolyte ions do not get enough time to completely diffuse inside the electrode pores; hence, the capacitance comes mainly from the outer surface of the materials, whereas at the lower scan rate, not only the outer surface Faradaic redox reactions, but also the diffusion processes within the pores contribute to the total capacitance. Therefore, the porosity of the materials may affect the ion diffusion kinetics depending on the pore size which influences the rate capability performance. The BET analysis (Fig. 6a, b) exhibited that the CMO6 composite has higher surface area as well as high pore volume than the pure CuO. Hence, the CMO6 exposes more number of redox-active site to the electrolyte ions and shows an remarkable performance. Although CMO3 composite has high surface area and pore volume as compared to pure CuO, probably the small pore size of CMO3 makes it barely accessible for the electrolytes ions leading to lower diffusional capacitance of the composite at low scan rate than that in pure CuO.

The total current generated in CV is the combination of diffusion-controlled Faradaic redox current and non-diffusion-controlled capacitive current. These different types of current contribution can be calculated quantitatively using Power law: $i_p = a\ \upsilon^b$ where $i_p$ is the anodic peak current, $\upsilon$ is the scan rate (mV/s), $a$ and $b$ are the adjustable parameters [34]. The value of $b$ gives the idea about the extent of diffusion-controlled Faradaic redox current and non-diffusion-controlled capacitive current. A 0.5 value of $b$ signifies the ideal diffusion-controlled Faradaic redox process, whereas the non-diffusion-controlled capacitive current is expressed by a unit value of

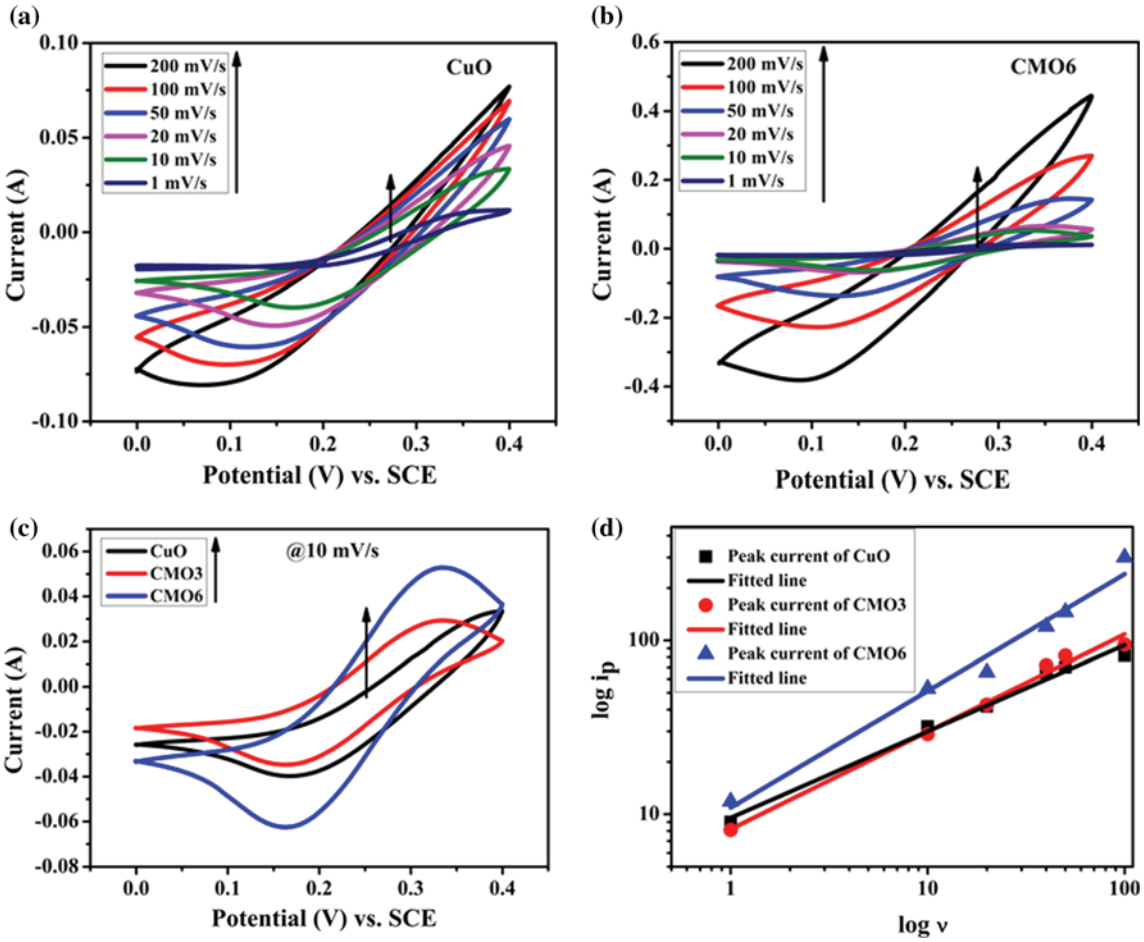


**Figure 7** CV plot of CuO (**a**) and CMO6 (**b**) in 2 M KOH containing 0.3 M $K_3[Fe(CN)_6]$ at different scan rates. CV curves of all the materials at a scan rate of 10 mV/s (**c**). Log $i_p$ versus log $v$ plot (**d**) of as-synthesized CuO and CuO–$MnO_2$ composites.

*b*. The value of *b* is easily calculated from the slope of the log ($i_p$) versus log (υ) linear curve. From Fig. 7d, the value of *b* is calculated to be 0.51, 0.56 and 0.67 for CuO, CMO3 and CMO6, respectively, indicating that the capacitances of the electrodes are mainly contributed by diffusion-controlled Faradaic redox charge transfer process.

The galvanostatic charge–discharge (GCD) curves of CuO and CMO6 at various specific currents with a potential window of 0.0–0.4 V in mixed 2 M KOH and 0.3 M $K_3[FeCN_6]$ are shown in Fig. 8a, b. The nonlinear behavior of the discharge curves indicates the Faradaic redox reactions of pseudocapacitive electrodes and the redox-active electrolyte. Furthermore, it is seen that the discharge times are always larger than the charging time at all specific currents, implying the high columbic efficiency of the electrode, which is really promising. The specific capacitance of 2690, 1641, 889, 668 and 539 F/g was calculated at a specific current of 8, 10, 20, 30 and 50 A/g, respectively, for the CMO6 composite electrode. While the bare CuO achieved the specific capacitance of 2519, 1492.7, 365, 100 and 1 F/g at a specific current of 8, 10, 20, 30 and 50 A/g, respectively. The CMO6 composite shows very high electrochemical performance in redox-mediated electrolyte, which is very high compared to previously reported literature (Table 1).

With increasing the specific current, specific capacitance of both the electrode decreases as the electrons and ions get lower time to diffuse into the electrode at high specific current. Furthermore, with the increase in specific current from 8 to 50 A/g, the capacitance of CuO, CMO3 and CMO6 composites retained 0.04, 7.7 and 20%, respectively (Fig. 8c). So, the CMO6 composite shows better rate capability performance in comparison with the bare CuO and CMO3 composite. Even at high specific current of

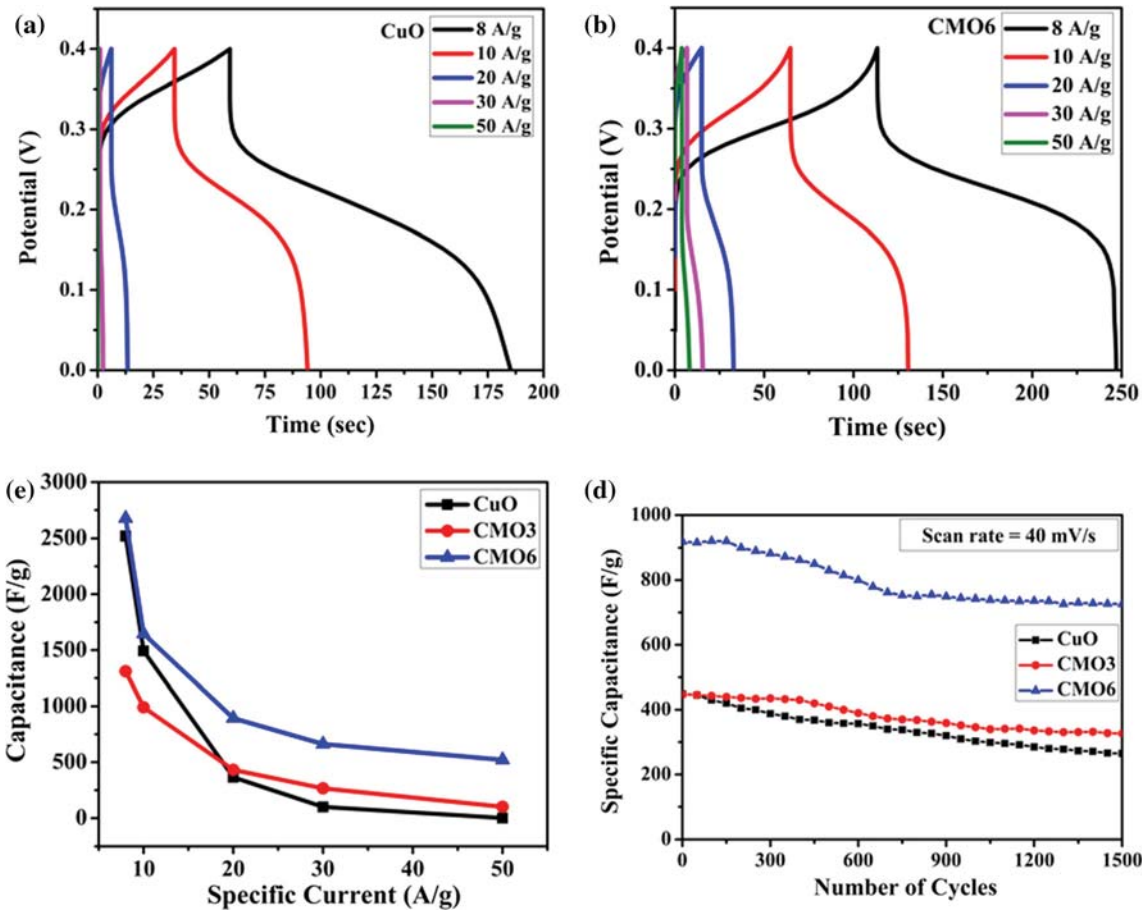


**Figure 8** GCD curves of CuO (**a**) and CMO6 composites (**b**) in 2 M KOH containing 0.3 M $K_3[Fe(CN)_6]$ at different specific currents. Capacitance versus specific current plot (**c**) and % change in the specific capacitance versus number of CV cycles (**d**) of as-synthesized CuO, CMO3 and CMO6 composites.

**Table 1** Specific capacitance of CuO–$MnO_2$ composite reported earlier

| Materials | Capacitance | Specific current | Electrolyte | Reference |
|---|---|---|---|---|
| Diatom@CuO@$MnO_2$ | 240 F/g | 0.5 A/g | 1 M $Na_2SO_4$ | [12] |
| Cu/CuO@$MnO_2$ | 177 mF $cm^{-2}$ | 0.5 mA/$cm^2$ | 1 M KOH | [11] |
| CuO@$MnO_2$ | 252.6 F g1 | 0.1 A/g | 1 M $Na_2SO_4$ | [10] |
| CuO/$MnO_2$ | 228 F/g | 0.25 A/g | 1 M $Na_2SO_4$ | [9] |
| CuO@$MnO_2$ | 276 F/g | 0.6 A/g | 1 M $Na_2SO_4$ | [3] |
| CuO–$MnO_2$ | 2690 F/g | 8 A/g | 2 M KOH + 0.3 M $K_3[Fe(CN)_6]$ | This work |

50 A/g, it provides high capacitance of 539 F/g, indicating higher stability and better electrochemical performance of the CMO6 electrode. The cycle stability of the as-synthesized materials was studied at a scan rate of 40 mV/s in the same electrolyte, which shows the 59, 73 and 79% capacitance retention after 1500 CV cycles of pure CuO, CMO3 and CMO6 (Fig. 8d), respectively.

The electrochemical impedance spectra were recorded in the frequency range of 200 kHz–0.2 Hz, with sinus amplitude of 10 mV, and expressed in terms of Nyquist plot (Fig. 9) which depicts real and imaginary parts of the complex impedance. The bare CuO nano-needle shows very high magnitude of *x*-axis ($Z_{Re}$) intercept, indicating high equivalent series resistance ($R_s$) than the composite. Further, in the

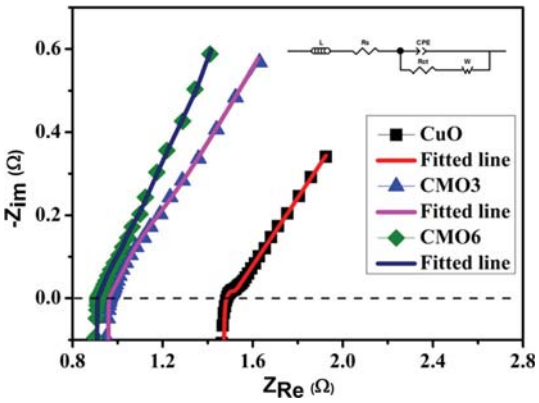


**Figure 9** Nyquist plots for CuO and $MnO_2$–CuO composite (inset: the corresponding equivalent circuit).

high-frequency region, the smaller diameter of the semicircle of the composite implies that it has lower charge transfer resistance ($R_{ct}$) compared to the bare CuO. The $R_s$ and $R_{ct}$ values of CMO6 composite are lower than the pristine CuO and CMO3 composites [Table S1], suggesting the high electrochemical performance of the CMO6 composite for supercapacitor application.

## Conclusions

A simple and cost-effective precipitation approach in combination with conventional hydrothermal method was adopted for fabrication of $MnO_2$–CuO nanocomposites (CMO3 and CMO6). In the composites, the CuO nano-needles are uniformly covered with $MnO_2$ nano-sheets. The synthesized materials were characterized using different microscopic and spectroscopic tools. The work beautifully describes a comparative study of the electrochemical behavior of the composites in a redox-mediated electrolyte (0.3 M $K_3[Fe(CN)_6]$ in 2 M KOH). The as-synthesized CMO6 composite with the highest surface area and porosity displays the highest value of capacitance when compared to CuO and CMO3. The CMO6 composite achieved high specific capacitance of 2690 F/g at specific current of 8 A/g with better rate capability. The results of the electrochemical studies imply that the composite CMO6 could be a promising electrode material for supercapacitor application.

## Acknowledgements

MM thanks to S.C. College, Habra, to give permission to carry out the research. The authors thank to Jadavpur University and Jain University for the instrumental help. DG thanks DST, India (ECR/2018/001039), for the research grant.

## Compliance with ethical standards

**Conflict of interest** The authors declare no conflict of interest.

**Electronic supplementary material:** The online version of this article (https://doi.org/10.1007/s10853-020-05415-7) contains supplementary material, which is available to authorized users.

## References

[1] Khare V, Nema S, Baredar P (2016) Solar–wind hybrid renewable energy system: a review. Renew. Sustain. Energy Rev. 58:23–33

[2] Zhang YX, Li F, Huang M (2013) One-step hydrothermal synthesis of hierarchical $MnO_2$-coated CuO flower-like nanostructures with enhanced electrochemical properties for supercapacitor. Mater. Lett. 112:203–206

[3] Huang M, Zhang Y, Li F et al (2014a) Merging of Kirkendall growth and Ostwald ripening: CuO@$MnO_2$ core-shell architectures for asymmetric supercapacitors. Sci. Rep. 4:4518

[4] Dubey R, Guruviah V (2019) Review of carbon-based electrode materials for supercapacitor energy storage. Ionics 25:1419–1445

[5] Majumdar D, Mandal M, Bhattacharya SK (2019) $V_2O_5$ and its carbon-based nanocomposites for supercapacitor applications. ChemElectroChem 6:1623–1648

[6] Mandal M, Ghosh D, Chattopadhyay K et al (2016) A novel asymmetric supercapacitor designed with $Mn_3O_4$@ multi-wall carbon nanotube nanocomposite and reduced graphene oxide electrodes. J. Electronic. Mater. 45:3491–3500

[7] Ghosh D, Mandal M, Das CK (2015) Solid state flexible asymmetric supercapacitor based on carbon fiber supported hierarchical $Co(OH)_xCO_3$ and $Ni(OH)_2$. Langmuir 31:7835–7843

[8] Mandal M, Ghosh D, Giri S et al (2014) Polyaniline-wrapped 1D $CoMoO_4$·0.75 $H_2O$ nanorods as electrode materials for supercapacitor energy storage applications. RSC Adv. 4:30832–30839

[9] Zhang Z, Ma C, Huang M et al (2015) Birnessite $MnO_2$-decorated hollow dandelion-like CuO architectures for supercapacitor electrodes. J. Mater. Sci. Mater. Electron. 26:4212–4220

[10] Guo XL, Li G, Kuang M, Yu L et al (2015) Tailoring kirkendall effect of the $KCu_7S_4$ microwires towards CuO@$MnO_2$ core-shell nanostructures for supercapacitors. Electrochim. Acta 174:87–92

[11] Wang X, Chen C, Chen K et al (2016) $MnO_2$ nanosheets-decorated CuO nanoneedles arrays@ Cu foils for supercapacitors. Int. J. Electrochem. Sci. 11:3425–3435

[12] Zhang Y, Guo WW, Zheng TX et al (2018) Engineering hierarchical Diatom@ CuO@ $MnO_2$ hybrid for high performance supercapacitor. Appl. Surf. Sci. 427:1158–1165

[13] Chen Q, Heng B, Wang H et al (2015) Controlled facile synthesis of hierarchical CuO@$MnO_2$ core–shell nanosheet arrays for high-performance lithium-ion battery. J. Alloys Compd. 641:80–86

[14] Zeng C, Gao C, Yuan L et al (2017) Water evaporation-induced self-assembly of hierarchical CuO/$MnO_2$ composite nanospheres and their applications in lithium-ion batteries. NANO 12:1750022

[15] Yang Z, Yang Y, Zhu X et al (2014) An outward coating route to CuO/$MnO_2$ nanorod array films and their efficient catalytic oxidation of acid fuchsin dye. Ind. Eng. Chem. Res. 53:9608–9615

[16] Pal J, Mondal C, Sasmal AK et al (2014) Account of nitroarene reduction with size-and facet-controlled CuO–$MnO_2$ nanocomposites. ACS Appl. Mater. Interfaces 6:9173–9184

[17] Luo X, Liang H, Qu F et al (2018) Free-standing hierarchical α-$MnO_2$@CuO membrane for catalytic filtration degradation of organic pollutants. Chemosphere 200:237–247

[18] Norsic C, Tatibouët JM, Batiot-Dupeyrat C et al (2018) Methanol oxidation in dry and humid air by dielectric barrier discharge plasma combined with $MnO_2$–CuO based catalysts. Chem. Eng. J. 347:944–952

[19] Qian K, Qian Z, Hua Q et al (2013) Structure–activity relationship of CuO/$MnO_2$ catalysts in CO oxidation. Appl. Surf. Sci. 273:357–363

[20] Prathap MA, Sun S, Wei C et al (2015) A novel non-enzymatic lindane sensor based on CuO–$MnO_2$ hierarchical nano-microstructures for enhanced sensitivity. Chem. Commun. 51:4376–4379

[21] Bhuvaneshwari S, Papachan S, Gopalakrishnan N (2017) Free standing CuO-$MnO_2$ nanocomposite for room temperature ammonia sensing. AIP Conf. Proc. 1832:050126

[22] Wessells CD, Huggins RA, Cui Y (2011) Copper hexacyanoferrate battery electrodes with long cycle life and high power. Nat. Commun. 2:1–5

[23] Aruchamy K, Nagaraj R, Manohara HM et al (2020) One-step green route synthesis of spinel $ZnMn_2O_4$ nanoparticles decorated on MWCNTs as a novel electrode material for supercapacitor. Mater. Sci. Eng. B 252:114481

[24] Subramani K, Jeyakumar D, Sathish M (2014) Manganese hexacyanoferrate derived $Mn_3O_4$ nanocubes–reduced graphene oxide nanocomposites and their charge storage characteristics in supercapacitors. Phys. Chem. Chem. Phys. 16:4952–4961

[25] Huang M, Zhang Y, Li F et al (2014b) Facile synthesis of hierarchical $Co_3O_4$@ $MnO_2$ core–shell arrays on Ni foam for asymmetric supercapacitors. J. Power Sources 252:98–106

[26] Kliche G, Popovic ZV (1990) Far-infrared spectroscopic investigations on CuO. Phys. Rev. B 42:10060

[27] Ethiraj AS, Kang DJ (2012) Synthesis and characterization of CuO nanowires by a simple wet chemical method. Nanoscale Res. Lett. 7:70

[28] Chen L, Li L, Li G (2008) Synthesis of CuO nanorods and their catalytic activity in the thermal decomposition of ammonium perchlorate. J. Alloys Compd. 464:532–536

[29] Zhao B, Liu P, Zhuang H et al (2013) Hierarchical self-assembly of microscale leaf-like CuO on graphene sheets for high-performance electrochemical capacitors. J. Mater. Chem. A 1:367–373

[30] Khan R, Vaseem M, Jang L et al (2014) Low temperature preparation of CuO nanospheres and urchin-shaped structures via hydrothermal route. J. Alloys Compd. 609:211–214

[31] Zheng L, Liu X (2007) Solution-phase synthesis of CuO hierarchical nanosheets at near-neutral pH and near-room temperature. Mater. Lett. 61:2222–2226

[32] Huang M, Zhang Y, Li F et al (2014c) Self-assembly of mesoporous nanotubes assembled from interwoven ultrathin birnessite-type $MnO_2$ nanosheets for asymmetric supercapacitors. Sci. Rep. 4:3878

[33] Tang B, Wang G, Zhuo L et al (2006) Novel dandelion-like beta-manganese dioxide microstructures and their magnetic properties. Nanotechnology 17:947

[34] Ray A, Roy A, Saha S et al (2019) Electrochemical energy storage properties of Ni-Mn-oxide electrodes for advance asymmetric supercapacitor application. Langmuir 35:8257–8267

# Sunlight mediated photocatalytic reduction of aqueous Cr(Vl) using metal hexacyanoferrate (M = Mn, Ni, Cu and Zn)

**Manas Mandal[1,2], Krishna Chattopadhyay[3], and Swapan Kumar Bhattacharya[1]**

[1] Department of Chemistry, Jadavpur University, Kolkata–700032, India
[2] Department of Chemistry, Sree Chaitanya College, Habra, 24Parganas(N)–743268, India
[3] School of Chemical Sciences, Indian Association for the Cultivation of Science, Kolkata, West Bengal – 700032, India
e-mail: *skbhatt7@yahoo.co.in*

**Abstract**. Four different metal hexacyanoferrates, MHCF (M = Mn, Ni, Cu and Zn) were synthesized via a simple, cost effective precipitation method. The as-synthesized MHCF were characterized using XRD analysis and FESEM images were recorded for the analysis of morphology. Among the four compounds, ZnHCF exhibited most effective catalytic property for visible-light driven photoreduction of Cr(VI) to Cr(III), with excellent photochemical reducing capability of 68% within 2 h.

## 1. Introduction

Now a day's excessive and indiscriminate uses of organic–mineral complexes in electronic gadgets as well as inorganic compound in the wood preservation industry have progressively become the most serious matter of environmental concern [1]. Mixing of the acid wastewater from mine drainage and heavy metal like chromium from preservation industry to the ground water is very dangerous towards aquatic life and mutagenic to human [2-3]. The waste water without treatment is hazardous for ecosystem, as most of the synthetic dyes are toxic, mutagenic and carcinogenic and enhance the chemical oxygen demand (COD) of the water body. Generally, chromium (Cr) is present in compounds in two common oxidation states such as Cr(III) and Cr(VI) [4]. Amongst these, Cr(VI) is enormously toxic, carcinogenic, whereas Cr(III) is less toxic and more easily soluble in water as $Cr(OH)_3$. Cr (VI) is used in several industrial fields like textile production, electroplating, metal finishing, leather tanning, dyeing, etc. [5]. As a result, higher degrees of contamination due to discharges of Cr (VI) in waste water, makes the aquatic life severely harmful. Presence of Cr (VI) in drinking water causes kidney, liver, bladder, and skin cancer [6]. So, the urgent demand for effective methods for efficient reduction of Cr (Vl) to Cr (III) in industrial waste water has been raised. Different methods including ion exchange, precipitation, reverse osmosis, photocatalysis and adsorption are developed [7-9]. However, each method has its own advantages along with numerous drawbacks. The photo-catalytic process is highly efficient and cost effective as compared to the other methods.

The transition metal complex like metal hexacyanoferrate has recently got attention from scientific community, as the hexacyanoferrate compound shows some unique solid state chemistry and promising applications in the field of electrochemical energy storage [10-11], electrocatalysis [12], photocatalysis [13], ion-sensing [14] etc. Jassal et al synthesized potassium zinc hexacyanoferrate nanocubes which were able to degrade Malachite Green up to 94.15% and Eriochrome Black T up to

about 76.13% under optimum condition [13]. Herein, a set of MHCF (M = Ni, Zn, Mn and Cu) was prepared using precipitation method for photocatalytic reduction of Cr (VI) under sunlight.

## 2. Experimental Section

### *2.1. Materials and Method*

Manganese nitrate tetrahydrate, Nickel nitrate hexahydrate, Copper nitrate trihydrate, Zinc nitrate hexahydrate, potassium hexacyanoferrate(III), sodium hydroxide, potassium permanganate, potassium dichromate were purchased from Merck, India. All reagents were directly used for the experiment without further purification.

### *2.2. Synthesis of metal hexacyanoferrate (M = Mn, Ni, Cu, Zn)*

For the synthesis of metal hexacyanoferrate (MHCF), simple precipitation method was followed. Briefly, 20 mL 0.1 M aqueous solution of $M(NO_3)_2$ [M= Ni, Cu, Zn, and Mn] was taken in a 100 mL beaker. Then 20 mL 0.1 M aqueous solution of $K_3Fe(CN)_6$ was slowly added to it under vigorous stirring condition. The solution was magnetically stirred for 1 hour. Then the solution was kept for 12 h in undisturbed condition at room temperature. After that the solid precipitate was filtered, washed with distilled water and ethanol for 4-5 times. Finally, the desired solid product (MHCF) was dried in air oven at 70°C for 6 h.

## 3. Results and Discussions

### *3.1. Formation of the Metal hexacyanoferrate:*

The synthetic procedure involves the precipitation method where a quick precipitation of metal hexacyanoferrate [MHCF], where M = Mn, Ni, Cu and Zn was achieved. The chemical reaction involved in this synthetic process is as follows:

$$M(NO_3)_2 + K_3[Fe(CN)_6] \rightarrow M_x[Fe(CN)_6]_y + KNO_3$$

### *3.2. X-Ray diffraction (XRD) analysis*

X-ray diffraction (XRD) analysis was performed by Rigaku ULTIMA-III X-ray diffractometer with Cu $K_\alpha$ radiation (λ = 1.5418 °A). The XRD patterns of the as-prepared MHCF (M = Mn, Ni, Cu and Zn) are shown in Figure 1. The observed XRD peaks of the MHCF (M = Mn, Ni, Cu and Zn) (Table 1) are well-matched with those in the JCPDS card number 01-074-7327, 01-082-2283, 01-086-0513 and 00-038-0688, respectively.

**Table 1.** List of important powder X-ray diffraction peaks and corresponding (hkl) values of the as prepared MHCF (M = Mn, Ni, Cu and Zn)

| **$Mn_4[Fe(CN)_6]_{2.667}\cdot 15.84H_2O$** JCPDS No. 01-074-7327 | | **$Ni[Fe(CN)_6]_2\cdot H_2O$** JCPDS No. 01-082-2283 | | **$Cu[Fe(CN)_6]_{0.667}$** JCPDS No. 01-086-0513 | | **$Zn_3[Fe(CN)_6]_2$** JCPDS No. 00-038-0688 | |
|---|---|---|---|---|---|---|---|
| 2θ(˚) | (hkl) | 2θ(˚) | (hkl) | 2θ(˚) | (hkl) | 2θ(˚) | (hkl) |
| 16.8 | (002) | 17.3 | (200) | 17.5 | (200) | 9.7 | (012) |
| 23.9 | (022) | 24.4 | (220) | 24.9 | (220) | 13.4 | (104) |
| 34.1 | (004) | 35.1 | (400) | 35.4 | (400) | 14.0 | (110) |
| 38.3 | (024) | 39.4 | (420) | 39.7 | (420) | 16.2 | (113) |
| 42.1 | (224) | 50.4 | (440) | 43.7 | (422) | 19.5 | (024) |
| 48.9 | (135) | 53.7 | (600) | 50.9 | (440) | 21.4 | (116) |
| 52.2 | (244) | 56.7 | (620) | 54.3 | (442) | 24.4 | (300) |
| 55.2 | (335) | | | 57.6 | (620) | 28.1 | (119) |
| 63.8 | (246) | | | | | 32.7 | (226) |
| 66.5 | (137) | | | | | | |

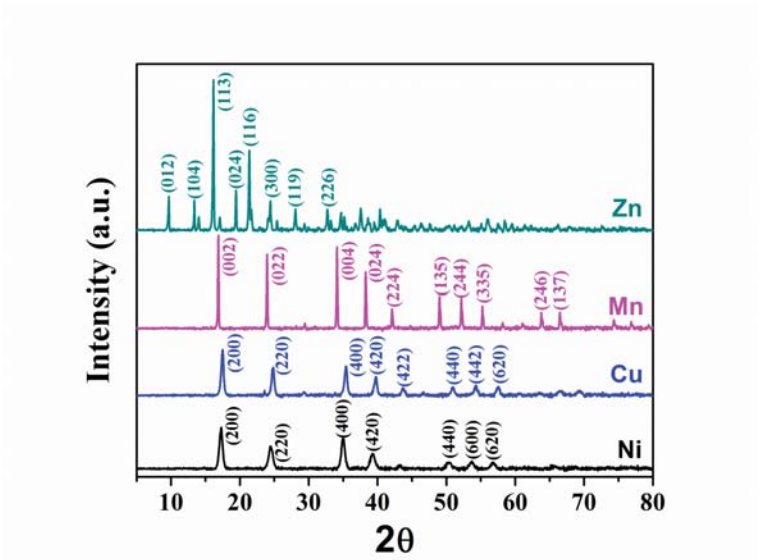


**Figure 1.** XRD pattern of as-prepared MHCF (M = Mn, Ni, Cu and Zn)

*3.3. Morphological analysis*

To investigate the surface morphology of the as-synthesized metal hexacyanoferrate (M = Mn, Ni, Cu and Zn) photo-catalysts, the field emission scanning electron microscopy (FESEM,Carl Zeiss-SUPRA 40) images were captured (Figure 2). From the FESEM of MnHCF, it can be seen that this is of cubic structure with an average length of 1um. The NiHCF and CuHCF are nano-sized particles. The FESEM image of ZnHCF suggests the cubic structure with an average length of 200 - 500 nm.

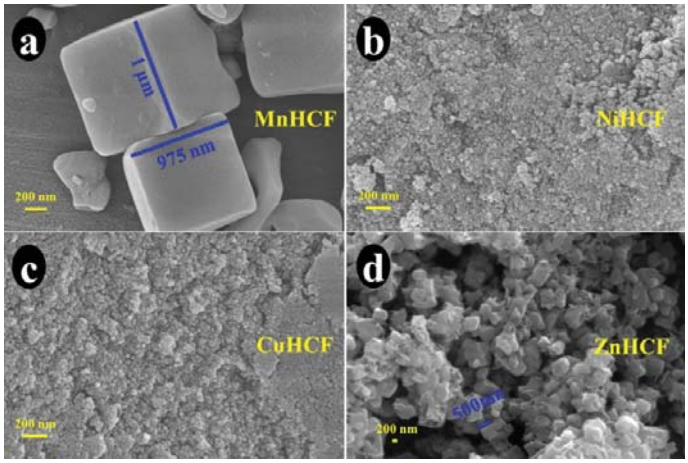


**Figure 2.** FESEM images of as-prepared metal hexacyanoferrate: MnHCF (a), NiHCF (b), CuHCF (c) and ZnHCF (d).

*3.4 Photocatalytic Reduction of Cr(VI)*

The photocatalytic reduction of Cr(VI) was performed by taking the aqueous dichromate solution containing the different as-synthesized catalyst (MHCF) under sunlight. A set of four beakers containing 25 mL $2\times10^{-4}$ M aqueous solution of $K_2Cr_2O_7$ with 25 mg of different MHCF (M = Mn, Ni, Cu and Zn) was taken and stirred for 1 h in dark condition to reach the adsorption−desorption equilibrium. One blank test was also performed without catalyst. After that all the beakers were put under sunlight for 2 h with occasional shaking. The solutions were centrifuged separately time to time and the UV-vis spectra were recorded.

Figure 3 shows the photocatalytic reduction of aqueous Cr(VI) under sunlight in the presence of the as-synthesized metal hexacyanoferrate, MHCF (M = Mn, Ni, Cu and Zn). The diversity in the efficiency of different metal hexacyanoferrate may be a result of several factors, such as composition, particle size, morphology, crystallinity, crystal defects, specific surface area, band gap, state of dispersion, adsorption capacity for Cr(VI), etc. [15]. These factors are strongly coupled with each other and hence it is hard to identify the specific function and influence of a single parameter in the photocatalytic activity of different metal hexacyanoferrates. From the Figure 3, it can be seen that as-synthesized zinc hexacyanoferrate nanocubes reveal superior photocatalytic activity when compared to other catalysts. With increasing exposure time, the main absorption band of Cr(VI) cantered at 363 nm notably decreases due to decreasing the concentration of Cr(VI). It is calculated that the as-prepared zinc hexacyanoferrate nanocubes exhibit excellent photochemical reducing capability. The photo-catalytic activity i.e., reducing capability of the material is calculated (Equation 1) by monitoring the decrease in the absorption intensity which is directly proportional to the Cr(IV) concentration. A decrease in absorption intensity from 1.02 to 0.33 at 365 nm implies 68% reducing capability of the as prepared ZnHCF within 2 h.

$$\text{Catalytic activity (\%)} = \frac{|(Final\ absorption\ intensity - Initial\ absorption\ intensity)|}{Initial\ absorption\ intensity} \times 100\ \% \qquad (1)$$

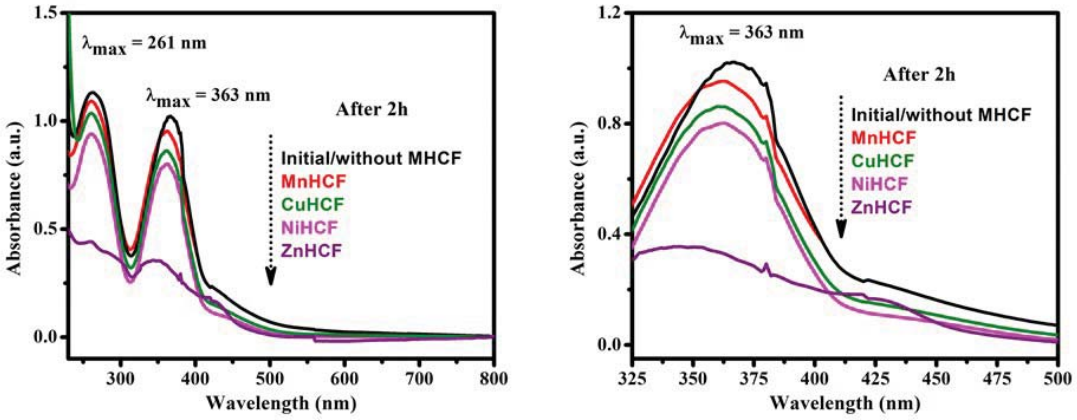


**Figure 3.** Photocatalytic reduction of 25 mL of $2 \times 10^{-4}$ M aqueous solution of dichromate under sunlight in the presence of different MHCF (M = Mn, Ni, Cu and Zn) (25 g)

The reduction of Cr(VI) to Cr(III) is mainly carried out by the photoexcited electrons and therefore, good electron−hole pair separation is attained in this reduction process. The better photocatalytic activity of the as-prepared ZnHCF catalyst for the reduction of Cr(VI) under sunlight can be explained by taking into consideration of some unique properties of Zn which is responsible for the exceptional behaviour of ZnHCF. Zinc has a completely filled valance shell *3d* orbitals and a narrow band gap. Due to highly dispersive nature of conduction band, the $d^{10}$ electronic configuration supports photo-generated electron-hole separation. On photo-irradiation with sunlight, MHCF semiconductors absorb light and electrons from valence band are excited to conduction band, generating the holes in the valance band. These photoexcited electrons in conduction bands of the semiconductors reduce Cr(VI) to Cr(III) with a visual color change of the solution from leuco to colorless. The probable reaction pathway for the photocatalytic reduction of Cr(VI) under sunlight over MHCF in aqueous solution is as follows:

$$MHCF + hv \rightarrow MHCF\ (e^- + h^+)$$
$$2H_2O + 4h^+ \rightarrow O_2 + 4H^+$$
$$Cr_2O_7^{2-} + 14H^+ + 6e^- \rightarrow 2Cr^{3+} + 7H_2O$$

## 4. Conclusion

In summary, four different metal hexacyanoferrates, MHCF (M = Mn, Ni, Cu and Zn) were synthesized via a simple and cost effective precipitation method. The as-prepared MHCF were characterized using XRD analysis and the morphology was investigated with FESEM images. The ZnHCF semiconductor exhibited more superior catalytic property for visible-light-driven photoreduction of Cr(VI), with excellent photochemical reducing capability of about 68%. Thus the as-synthesized metal hexacyanoferrates show promising applications in the field of environmental photocatalysis.

**References**

[1] Liu J, He X, Lin X, Chen W, Zhou Q, Shun W and Huang L 2015 Ecological effects of combined pollution associated with e-waste recycling on the composition and diversity of soil microbial communities *Environ. Sci. Technol.* **49** 6438–6447.

[2] Turpeinen R, Kairesalo T and Häggblom M M 2010 Microbial community structure and activity in arsenic-, chromiumand copper-contaminated soils *FEMS Microbiol. Ecol.* **47** 39–50.

[3] Liu F, Zhang W, Tao L, Hao B and Zhang J 2019 Simultaneous photocatalytic redox removal of chromium (vi) and arsenic (iii) by hydrothermal carbon-sphere@nano-$Fe_3O_4$ *Environ. Sci. Nano* **6** 937-947.

[4] Hsu C L, Wang S L and Tzou Y M 2007 Photocatalytic reduction of Cr(VI) in the presence of $NO_3^-$ and $Cl^-$ electrolytes as influenced by Fe(III) *Environ. Sci. Technol.* **41** 7907−7914.

[5] Bhaumik M, Maity A, Srinivasu V V and Onyango M S 2011 Enhanced removal of Cr(VI) from aqueous solution using polypyrrole/$Fe_3O_4$ magnetic nanocomposite *J. Hazard. Mater.* **190** 381−390.

[6] Testa J J, Grela M A and Litter M I 2004 Heterogeneous photocatalytic reduction of chromium(VI) over $TiO_2$ particles in the presence of oxalate: Involvement of Cr(V) species *Environ. Sci. Technol.* **38** 1589−1594.

[7] Joshi K M and Shrivastava V S 2011 Photocatalytic degradation of Chromium(VI) from wastewater using nanomaterials like $TiO_2$, ZnO, and CdS *Appl. Nanosci.* **1** 147-155.

[8] Dinda D, Gupta A and Saha S K 2013 Removal of toxic Cr(VI) by UVactive functionalized graphene oxide for water purification *J. Mater. Chem. A* **1** 11221−11228.

[9] Mondal C, Ganguly M, Pal J, Roy A, Jana J and Pal T 2014 Morphology controlled synthesis of $SnS_2$ nanomaterial for promoting photocatalytic reduction of aqueous Cr(VI) under visible light *Langmuir* **30** 4157-4164.

[10] He Y, Zhang P, Wang M, Wang F, Tan D, Li Y and Feng X 2019 Nano-sandwiched metal hexacyanoferrate/graphene hybrid thin films for in-plane asymmetric micro-supercapacitors with ultrahigh energy density *Mater. Horiz.* **6** 1041-1049.

[11] Bors R, Yun J, Marzak P, Fichtner J, Scieszka D and Bandarenka A S 2018 Chromium(II) hexacyanoferrate-based thin films as a material for aqueous alkali metal cation batteries *ACS Omega* **3** 5111-5115.

[12] Sitnikova N A, Komkova M A, Khomyakova I V, Karyakina E E and Karyakin A A 2014 Transition metal hexacyanoferrates in electrocatalysis of $H_2O_2$ reduction: an exclusive property of Prussian Blue *Anal. Chem.* **86** 4131-4134.

[13] Jassal V, Shanker U, Kaith B S and Shankar S 2015 Green synthesis of potassium zinc hexacyanoferrate nanocubes and their potential application in photocatalytic degradation of organic dyes *RSC Adv.* **5** 26141-26149.

[14] Jassal V, Shanker U and Shankar S 2015 Synthesis characterization and applications of nano-structured metal hexacyanoferrates: a review *J. Environ. Anal. Chem.* **2** 2380-2391.

[15] Zhang Y C, Li J, Zhang M and Dionysiou D D 2011 Size-tunable hydrothermal synthesis of $SnS_2$ nanocrystals with high performance in visible light-driven photocatalytic reduction of aqueous Cr(VI) *Environ. Sci. Technol.* **45** 9324-9331.

*Proceedings of International Conference on Energy and Sustainable Develeopment*
*Jointly organized by Jadavpur University and The Institution of Engineers, India*
*February 14-15, 2020*

# Investigation of the electrochemical performance of pristine CuO and $MnO_2$@CuO nanocomposite in redox mediated electrolyte

Manas Mandal[1,2], Radha Nagaraj[3], Krishna Chattopadhyay[4], Malay Chakraborty[2], Sujit Chatterjee[2], Debasis Ghosh[3], Swapan Kumar Bhattacharya*[2]

[1]*Department of Chemistry, Sree Chaitanya College, Habra, WB – 743268, India*
[2]*Physical Chemistry Section, Department of Chemistry, Jadavpur University, WB – 700032, India*
[3]*Centre for Nano & Material Sciences, JAIN University, Bangalore 562112, India*
[4]*School of Chemical Sciences, IACS, Kolkata, WB – 700032, India*

{Corresponding author's email: skbhatt7@yahoo.co.in}

***Abstract* - We have demonstrated a simple and cost effective precipitation approach to fabricate CuO nano-needle electrode and evaluated its electrochemical performance in a redox electrolyte (0.3 M $K_3[Fe(CN)_6]$ and 2 M KOH mixed solution). A high specific capacitance of 2519 F/g was recorded from galvanostatic charge-discharge cycle at 8 A/g. However, the electrode suffered from poor rate capability. The CuO nano-needles were further modified with $MnO_2$ nanosheets by a hydrothermal method, and the $MnO_2$@CuO electrode is able to deliver a high specific capacitance of 112.5 F/g even at very high current of 50 A/g. The physiochemical properties and the electrochemical performance of the CuO and $MnO_2$@CuO nanocomposites have been analyzed in detail.**

***Keywords - $MnO_2$@CuO; Redox electrolyte; Supercapacitor***

## INTRODUCTION

Enormous energy consumption by our electronically biased modern daily life triggers the scientists for searching a sustainable and renewable energy resource for future energy storage. Recently, electrochemical capacitors, also known as ultracapacitor or supercapacitors (SCs), have attracted remarkable attention in light of their unique properties of high power density, moderate energy density, long cycle life, fast charging capacity and green environmental protection [1]. The transition metal oxides, hydroxides, sulfides are commonly used as the pseudocapacitive electrode materials due to multiple oxidation states of the metal ions [2]. To enhance the efficiency of the electrode materials, the idea of incorporating combinatorial transition metal oxides with multiple electroactive redox sites, have been developing. Not only the choice of electrode materials but also the surface architectures of the electrode materials, electrolyte, separator, *etc.* can alter the efficiency of supercapacitor [3]. Recently, in terms of modification of electrolyte, addition of a foreign redox system into the mother electrolyte solution as an additional source of pseudocapacitance is being taken into consideration [4].

Herein, pristine CuO nano-needle and $MnO_2$ nanosheet wrapped CuO nano-needle were synthesized by the precipitation method followed by a simple and facile hydrothermal technique and the electrochemical properties were studied in terms of cyclic voltammetry (CV), galvanostatic charge–discharge (GCD) and electrochemical impedance spectra (EIS) in redox $[Fe(CN)_6]^{3-}/[Fe(CN)_6]^{4-}$ mediated electrolyte.

### *A. Experimental*

Copper(II) nitrate trihydrate, potassium hexacyanoferrate(III), sodium hydroxide, potassium permanganate were purchased from Merck, India. All the reagents were directly used for the experiment without doing any purification.

#### *1. Synthesis of CuO*

A large number of synthesis routs have been developed for the preparation of CuO with different morphology [5-6]. Herein, the co-precipitation method was followed for the synthesis of CuO. Briefly, 30 mL 0.1 M aqueous $Cu(NO_3)_2$ solution was added drop wise in 20 mL 0.1 M aqueous $K_3[Fe(CN)_6]$ solution with continuous stirring. The tawny brown colored precipitate of $Cu_3[Fe(CN)_6]_2$ was formed immediately. After one hour continuous stirring, the solution was kept for 12 h in undisturbed condition. Then 1 M NaOH was added slowly the mixture solution with continuous stirring. The prompt color change from tawny brown to deep brown was recognized. The solid product was washed with water for several times and dried at 60 °C in hot air oven.

#### *2. Synthesis of $MnO_2$@CuO composites*

The as-prepared 35 mg CuO was dispersed in 35 mL 0.025 M $KMnO_4$ aqueous solution. Then the solution was transferred in 50 mL stainless steel autoclave and was kept in furnace for 3 h at 180 °C. After cooling at room temperature, the solid brown product was carefully washed in succession with water and absolute alcohol for several times. The desired material was obtained after drying at 60 °C for 12 h.

### *B. Characterizations*

The chemical and structural analysis of the as-prepared electrode material were carried out by X-ray diffraction (XRD, Rigaku ULTIMA-III x-ray diffractometer) with Cu Kα radiation (λ = 1.548 Å) analysis, Fourier transform infrared (FTIR, NEXUS 870 Thermo-Nicolet) spectroscopy. From the field emission scanning electron microscopy (FESEM, Carl Zeiss-SUPRA 40) and

Gmail Manas Mandal <manasmandal26@gmail.com>

# Important: Revision Requested - Manuscript Number: 14-ES-09-40 / Handbook of Porous Carbon Materials / Springer Natutre Publications

**Dr. Preetam Bhardwaj** <pbhardwaj105@gmail.com> 21 December 2021 at 20:44
To: Manas Mandal <manasmandal26@gmail.com>, Krishna Chattopadhyay <krishchem001@gmail.com>, Amrita Jain <ajain@ippt.pan.pl>, skbhatt7@yahoo.co.in
Cc: Prashant Sonar <sonar.prashant@qut.edu.au>, Nirmala Grace <anirmalagladys@gmail.com>, Arghya Chakravorty <arghya.kgp.ac@gmail.com>

Date: 21-12-2021

**MANUSCRIPT ID: 14-ES-09-40**

**TITLE: "Porous Carbon Materials for Supercapacitor Applications"**

Book: Handbook of Porous Carbon Materials/Springer Nature

Dear Authors,

Greetings from the Editorial Team/ Handbook of Porous Carbon Materials/Springer Nature

We are pleased to tell you that we have provisionally accepted your book chapter Manuscript for publication in the "Handbook of Porous Carbon Materials"/Springer Nature. Any further comments from the referees/Editorial Board can be found below and/or attached to this message.

Our editorial team will now perform some final checks to ensure that we have everything we need to publish your submission.

These checks will enable our production team to publish your submission as quickly and efficiently as possible. Once this is confirmed, your manuscript will be formally accepted and we will inform you of this via email.

**Referees/Editorial Board Comments to Authors:-**

**Authors are requested to submit Figure Rights Link permission form with following details:**

**1. Title of new book: Handbook of Porous Carbon Materials**

**2. Lead author or Author or Corresponding Editor: Prof. A. Nirmala Grace**

**3. Publisher: Springer Nature**

**4. Expected publication date: March 2022**

**5. Expected Page Numbers or Number of Pages: 1000**

Kindly submit the Figure Rights Link permission form with above mentioned details as soon as possible.

If you have already submitted the figures copyright forms please ignore the above comments.

**Thank you for your fine contribution.**

Warm Regards & Best Wishes,

Sincerely,
Editorial Team
Book: Handbook of Porous Carbon Materials
Springer Nature Singapore Pte. Ltd.; 152 Beach Road, #21-01/04 Gateway East, Singapore 189721, Singapore

[Quoted text hidden]

--
**Dr. Preetam Bhardwaj**, (B.E., M.Tech, PhD)
Research Faculty, (Emp. ID. 16438)
Centre for Nanotechnology Research,
School of Electronics Engineering,
VIT, Vellore - 632014, Tamil Nadu, India
Email: pbhardwaj105@gmail.com, preetam.bhardwaj@vit.ac.in
**Phone (Whats-App) : +91 9541891115**
**Mobile: +91 7082599121, +91 9536940290**
ORCID: https://orcid.org/0000-0002-4210-9050
**Researcher Id** M-7790-2019
Vidwan Profile URL: https://vidwan.inflibnet.ac.in/profile/237139
**Microsoft Academic Research Id:** 3016412680
Google ID: https://scholar.google.co.in/citations?user=CHcQafsAAAAJ&hl=en

Emergent Materials (2020) 3:347–367
https://doi.org/10.1007/s42247-020-00090-5

REVIEW

# Journey from supercapacitors to supercapatteries: recent advancements in electrochemical energy storage systems

Dipanwita Majumdar[1] · Manas Mandal[2,3] · Swapan Kumar Bhattacharya[2]

Received: 9 June 2019 / Accepted: 20 March 2020 / Published online: 13 May 2020


**Abstract**
Generation, storage, and utilization of most usable form, viz., electrical energy by renewable as well as sustainable protocol are the key challenges of today's fast progressing society. This crisis has led to prompt developments in electrochemical energy storage devices embraced on batteries, supercapacitors, and fuel cells. Vast research and development are being executed worldwide on each of these systems. Although fuel cells and batteries possess higher energy density but excessive installation cost, bulkiness, low power capabilities, and short life time are major limitations till date. The performances of supercapacitors at present lie in-between these batteries and conventional capacitors, hence serve as supporting or secondary devices for uninterrupted power supply systems. Nonetheless, supercapacitors possess some indigenous qualities such as light weight, easy portability, high cycle life, and low maintenance requirement with the potentiality for high specific and energy densities. These attractive features have proposed scientific challenges that have promoted the urge for replacing conventional massive, low-lasting batteries. In recent past, nano-composite materials have been developed with improved energy density to replace the "first-generation supercaps." Moreover, hybridizing with high energy battery materials can successfully solve the existing limitation of the available supercapacitors without sacrificing their cycling performances substantially. Thus, a novel concept of "supercapatteries" (supercapacitors + batteries) has emerged combining the merits of the charge storage mechanisms of both batteries and electrochemical capacitors so as to attain improved electrochemical performances. At the same time, scientists are trying to pursue cost effective designing methods without compromising with device efficiencies. The paper outlines the progress of supercapacitor technology with special emphasis on the tuning of nature, composition, electronic, and structural designing of electrode materials and electrolytes, cell fabrication along with other related parameters that may assist in enhancing the overall electrochemical device performances.

**Keywords** Supercapatteries · Electrochemical energy storage · Supercapacitors · Electrode materials · Electrolytes · Nano-morphology

## 1 Introduction

Adverse environmental impacts of present day fossil fuels along with their restricted accessibility have stimulated serious concerns leading to extensive research to focus on discovering adequate alternatives of energy storage and conversion from various renewable as well as sustainable energy sources [1, 2]. In this circumstance, developments in electrochemical energy storage (EES) devices are enormously significant to store the electrical energy when generated in excess and to meet the ever rising demands of non-stop energy delivery [3, 4]. Till date, heavy weight and voluminous batteries are the primarily accepted and extensively employed electrochemical energy storage devices owing to their unique capability to provide high energy density (energy stored per unit volume)/specific energy (energy stored per unit mass) (30–300 Wh $kg^{-1}$) [4–6]. However, short life span, low specific power, pollution, and toxicity issues especially regarding their recycling and disposal after usage are the main drawbacks. But, lack of appropriate alternatives is the main cause for overlooking their

✉ Dipanwita Majumdar
wbesdmajumdar@gmail.com

✉ Swapan Kumar Bhattacharya
skbhatt7@yahoo.co.in

[1] Department of Chemistry, Chandernagore College, Hooghly, WB 712136, India

[2] Department of Chemistry (Physical Chemistry Section), Jadavpur University, Kolkata, WB 700032, India

[3] Department of Chemistry, Sree Chaitanya College, Habra, WB 743268, India

ChemPubSoc Europe
DOI: 10.1002/celc.201801761
CHEMELECTROCHEM Reviews

# $V_2O_5$ and its Carbon-Based Nanocomposites for Supercapacitor Applications

Dipanwita Majumdar,*[a] Manas Mandal,[b, c] and Swapan K. Bhattacharya[c]

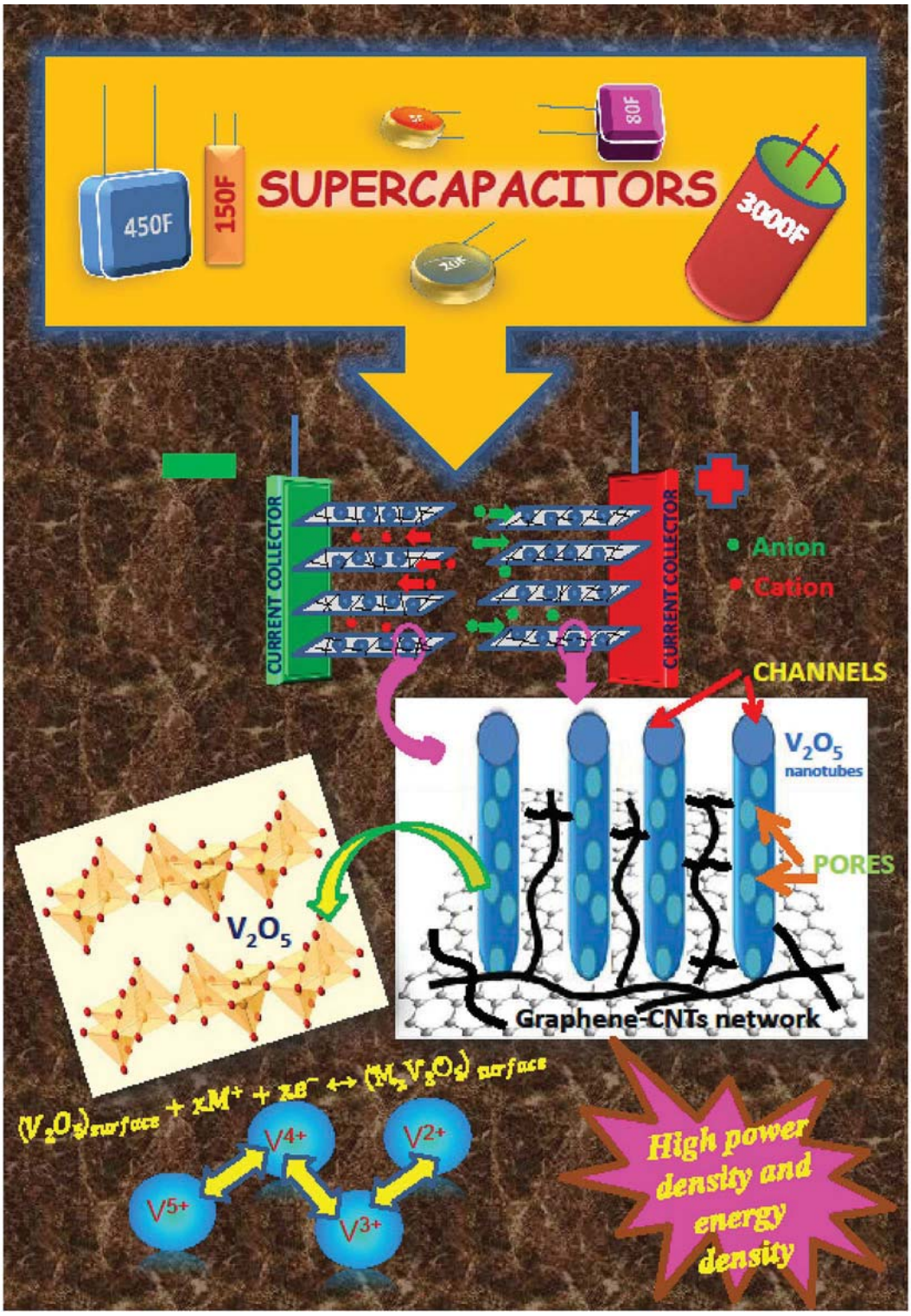

Vanadium pentoxide ($V_2O_5$) is renowned among the highly efficient supercapacitor electrode-materials for high power and energy densities, excellent specific capacitance, prolonged cycle lives, variable oxidation states of V, reversible nature of interconversions, theoretical importance, etc. Various synthetic methodologies and morphologies, formation of composites, and doping for tuning properties are the additional causes of interest. Different synthetic techniques like sol-gel, solvothermal, electro-deposition, electro-spinning, atomic layer deposition, etc. are employed to prepare $V_2O_5$-based electrode materials with merits and demerits. High rate of material agglomeration and poor conductivity limit its usage in pristine morphology. Accordingly, the impact on charge storage behavior of $V_2O_5$ on blending with various carbon-based systems has been explored for materials like activated carbons, conducting polymers, carbon nanotubes and functionalized graphene systems as binary/ternary composites. The aim has been to optimize the key factors such as reduced nanostructure lumping, minimal interfacial resistance and ultrafast charge diffusion across hollow porous structures which may eventually lead to the theoretically expected high specific capacitance (> 1000 F $g^{-1}$). In this review, we have discussed on the recent progress in the research of $V_2O_5$-based materials and highlighted on the correlation between morphology and electrochemical performances. In the course, we have attempted to delineate the advantage-disadvantages of different composite morphologies that may help to outline the present status and future aspects of these materials that the authors believe will be of first-hand assistance especially to the beginners in the field of research.

## 1. Introduction

### 1.1. Supercapacitors as Energy Storage Devices

Development of renewable, sustainable and environment benign devices for superior chemical energy storage and conversion to useful electrical energy has been the most demanding among the different motivating topics and cultivating areas to the scientists and technologists engaged in harvesting of energy for solving critical issues of energy crisis and environmental pollution since last two decades.[1–2] An essential answer to this problem is to store energy "electrochemically" as it is convenient, controllable and sustainable. It faces lower installation cost compared to other renewable energy production and storage techniques.[3] There are various types of electrochemical energy generation and storage technologies, namely, fuel cells, batteries, supercapacitors, etc. that have been intensively studied for the last three decades.[4–5] Fuel cells are considered as open systems with anode and cathodes merely act as media for charge-transfer while active masses (fuel), generally delivered from external sources (air/fuel tanks, etc.) experience the cell redox reactions. On the other hand, batteries and supercapacitors are treated as closed systems where the "active masses" of the electrodes most often actively participate in the redox reaction and responsible for charge storage behavior. However, the fundamental difference lies – unlike batteries and fuel cells that involve generation of electrical energy from chemical energy through redox reactions at the electrodes; the supercapacitors may not necessarily involve redox reactions (pseudocapacitors) but often utilize simple electrical double layers (electrical double layer capacitors) for electrochemical energy storage purposes.[4]

"Supercapacitors", also commonly addressed as ultracapacitors or electrochemical capacitors, have been accorded great importance due to their superior power density compared to batteries as well as appreciable energy density than common capacitors along with a long cycle life and enhanced energy utilization efficiency.[6–7] They are being designed for wide-applications in electrical vehicles to portable micro-electronic devices.[8–9] If secondary batteries are conjoined with supercapacitors in electronic devices, it extends the batteries' period of occupation, reduces the volume of devices and prolongs the batteries' longevity and reduces voltage instability.[10]

A typical supercapacitor set-up comprises of electrodes, a separator and an electrolyte (Figure 1); where the electrode material plays the main role in controlling the overall device performance.[11–12] It is indeed a very critical task to search smart electrode materials with excellent execution of desired efficiency. The basic working principle declares that electrode materials and electrolyte should have effective contacts, so that faster transport of ions/charges occurs in the electrode bulk portion as well as at the electrolyte-electrode interfaces so as to achieve excellent electrochemical properties.[13–14]

[a] *Dr. D. Majumdar*
*Department of Chemistry*
*Chandernagore College*
*Hooghly, Pin-712136, WB, India*
*E-mail: wbesdmajumdar@gmail.com*
[b] *M. Mandal*
*Department of Chemistry*
*Sree Chaitanya College*
*Habra, 24PGS(N), Pin-743268, WB, India*
[c] *M. Mandal, Prof. Dr. S. K. Bhattacharya*
*Department of Chemistry (Physical Chemistry Section)*
*Jadavpur University*
*Kolkata-700032, WB, India.*

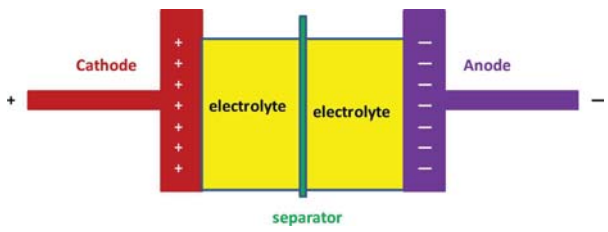


**Figure 1.** Fabrication-design of a typical supercapacitor.

Journal of ELECTRONIC MATERIALS, Vol. 45, No. 7, 2016
DOI: 10.1007/s11664-016-4493-6


# A Novel Asymmetric Supercapacitor Designed with $Mn_3O_4$@Multi-wall Carbon Nanotube Nanocomposite and Reduced Graphene Oxide Electrodes

MANAS MANDAL,[1] DEBASIS GHOSH,[1] KRISHNA CHATTOPADHYAY,[2] and CHAPAL KUMAR DAS[1,3]

1.—Materials Science Centre, Indian Institute of Technology Kharagpur, Kharagpur 721302, India. 2.—Department of Chemistry, Indian Institute of Technology Kharagpur, Kharagpur 721302, India. 3.—e-mail: chapal12@yahoo.co.in

We demonstrate a straightforward process for the synthesis and fabrication of a hybrid-type asymmetric supercapacitor (ASC) by combining $Mn_3O_4$ nanoparticle-supported multi-wall carbon nanotube ($Mn_3O_4$@MWCNT) composite as positive and reduced graphene oxide (rGO) as negative electrodes. A controlled hydrothermal synthesis of $Mn_3O_4$ in the presence of MWCNT resulted in a well-distributed $Mn_3O_4$ nanoparticles on the MWCNT backbone in the $Mn_3O_4$@MWCNT composite. The structure and morphology of the as-prepared materials have been investigated by x-ray diffraction, Fourier transform infrared spectroscopy, field-emission scanning electron microscopy, transmission electron microscopy, Brunauer–Emmett–Teller analysis and x-ray photoelectron spectroscopy measurements. The electrochemical characterizations were carried out in terms of cyclic voltammetry, galvanostatic charge–discharge (GCD) and electrochemical impedance spectroscopy analysis. The constructed ASC with 1 M KOH-supporting electrolyte was able to provide high-specificity capacitance of 173.36 F/g at 2 mV/s scan rate and high-energy density of 26.8 Wh/kg accompanied by high cycle stability with 79.3% capacitance retention over 3000 GCD cycles.

**Key words:** Asymmetric supercapacitor, composites, $Mn_3O_4$, reduced graphene oxide, pseudocapacitance

## INTRODUCTION

A sustainable and renewable energy resource is required as an alternative to the world's growing energy needs without causing any environmental detriment.[1] Solar energy and wind energy as renewable sources have attracted global attention, but these are unreliable energy sources due to their uncertain and intermittent behavior.[2] Recently, electrochemical capacitors, also known as supercapacitors (SCs), have drawn tremendous attention with their great potential application in the field of energy storage due to their unique properties of high power density, long cycle life, low maintenance cost and green environmental protection.[3,4]

Although SCs deliver very high power density (~10 W/kg to $10^4$ W/kg), they suffer from lower energy density (~0.2 Wh/kg to 10 Wh/kg) compared to conventional batteries (~10 Wh/kg to 200 Wh/kg).[5] The energy density ($E$) is related to the operating voltage ($V$) and capacitance according to the following equation: $E = 0.5CV^2$. To achieve high energy density along with high power density and long cycle life, efforts have been devoted to developing asymmetric supercapacitors (ASCs) by combining a battery-like Faradaic electrode (as energy source) and a capacitive electrode (as power source).[6] So far, various redox active metal oxides or hydroxides, such as $Mn_3O_4$,[7,8] $Fe_3O_4$,[9] $Co_3O_4$, $Co(OH)_2$,[10] $Ni(OH)_2$[11,12] and their composites with

(Received September 9, 2015; accepted March 24, 2016; published online April 12, 2016)

ACS APPLIED BIO MATERIALS

www.acsabm.org

Review

# Smart Metal–Organic Frameworks for Biotechnological Applications: A Mini-Review

Krishna Chattopadhyay,* Manas Mandal, and Dilip Kumar Maiti*

Cite This: *ACS Appl. Bio Mater.* 2021, 4, 8159–8171

Read Online

ACCESS | Metrics & More | Article Recommendations

**ABSTRACT:** In this pandemic situation it is evident that viruses and bacteria, more specifically, multiple drug resistant (MDR) bacteria, endanger human civilization severely. It is high time to design smart weapons to combat these pathogens for the prevention and cure of allied ailments. Metal–organic frameworks (MOFs) are porous materials designed from metal ions or inorganic clusters and multidentate organic ligands. Due to some unique features like high porosity, tunable pore shape and size, numerous possible metal-ligand combinations, etc., MOFs are ideal candidates to design "smart biotechnological tools". MOFs construct promising fluorescence based biosensing platforms for detection of viruses. MOFs also exhibit excellent antibacterial activity due to their ability for sustained release of active biocidal agents. There are several reviews that summarize the antibacterial applications of MOFs, but the biosensing platforms based on MOFs for detection of viruses have scarcely been summarized. This review carefully covers both the aspects including virus detection (nucleic acid recognition and immunological detection) with underlying mechanisms as well as antibacterial application of MOFs and doped MOFs or composites. This review will deliver valuable information and references for designing new, smarter antimicrobial agents based on MOFs.

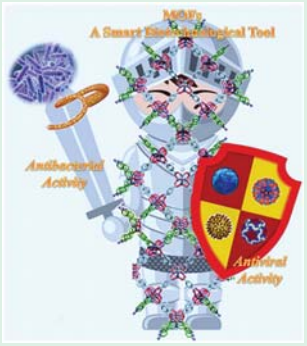


**KEYWORDS:** *antimicrobial, MOFs, pathogens, biosensor, biotechnological, bactericidal*

## INTRODUCTION

In this postpandemic situation, it is clear that the fast changing nature of pathogens and their resistance to existing drugs are the most serious threats to modern civilization. Drug resistance can grow through different mechanisms such as a change in the metabolic pathway or the target site of an antibiotic, less drug accumulation in a cell, or drug inactivation. For this reason, it is an ultimate necessity to develop new smart materials for faster detection and easy eradication of the pathogens.

Metal–organic frameworks (MOFs) constitute a new class of developing functional materials with versatile applications. MOFs are constructed from metal ions or inorganic clusters as nodes and organic ligands as linkers which form one, two, or three-dimensional (1D, 2D, or 3D) extended coordination networks. This class of compounds is exceptional with respect to high porosity, structural tunability, large internal surface area, and excellent thermal stability. The pore size, shape, and surface area of the MOFs can be tuned according to requirements with proper choices of organic linkers, metal ions, and reaction conditions.[1−3] MOFs have promising applications in the field of ion exchange, gas adsorption, storage of small molecules,[4−9] gas separation,[10] heterogeneous catalysis,[11−16] luminescence,[17−19] and magnetism.[20−22] Recently, MOFs have been extensively used for sensing various biomolecules such as antibodies and nucleic acids.[23−29] Due to their construction, composition, and large internal surface area, MOFs can act as reservoir for antimicrobial agents. This property makes MOFs a new class of high-performance material having potential biotechnological application.[30−33]

The common techniques used for detecting harmful viruses include serological tests,[34] cell culture,[35] reverse transcription polymerase chain reaction (RT-PCR),[36,37] polymerase chain reaction (PCR),[38,39] enzyme-linked immunoassay (ELISA),[40,41] fluorescence resonance energy transfer (FRET) assays,[42] high-quantity sequencing,[43] nucleic acid augmentation tests,[44] antigen tests,[45] IgA antibody tests,[46] combined IgM-IgG antibody tests[47] and electrochemical sensors, etc. These processes are time-consuming and require sophisticated instrumentation and complicated manipulations. Nanoscale MOFs are promising candidates to be employed as platforms for detection of nucleic acid by fluorometric methods.[48−51] MOFs are chosen for this work because of their structural diversity, unlimited number of metal–ligand combinations, easy synthesis and characterization, and low cost. The first work on nucleic acid detection using a Cu(II)-MOF was reported by the Chen group in 2013.[52] Afterward, various other MOFs, including UiO-66-$NH_2$ (UiO = University of

Received: September 15, 2021
Accepted: October 23, 2021
Published: November 6, 2021

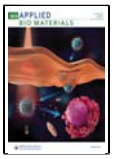





https://doi.org/10.1021/acsabm.1c00982
*ACS Appl. Bio Mater.* 2021, 4, 8159–8171

Applied Surface Science 541 (2021) 148450

Contents lists available at ScienceDirect

Applied Surface Science

journal homepage: www.elsevier.com/locate/apsusc

Full Length Article

# Visible light assisted photo-electrocatalytic oxidation of methanol using low Pt content NiO-rutile $TiO_2$ ternary heterojunction

Malay Chakraborty [a], Kamal Kanti Bera [a], Manas Mandal [a,b], Kalyan Ghorai [a], Nayim Sepay [a], Mahima Ranjan Das [c], Sreya Roy Chowdhury [a], Arup Gayen [a], Swapan Kumar Bhattacharya [a,*]

[a] Physical Chemistry Section, Department of Chemistry, Jadavpur University, Kolkata 700032, India
[b] Department of Chemistry, Sree Chaitanya College, Habra 24PGS (N) - 743268, India
[c] Department of Physics, University of Burdwan, Burdwan 713104, India

ARTICLE INFO

*Keywords:*
Ternary hetero-junctions
Photo-catalysis
Methanol oxidation
Mechanism

ABSTRACT

Platinum decorated binary hetero-junctions of NiO and $TiO_2$ of various mole-ratios have been synthesized for use of these as anode catalysts in the oxidation of methanol in alkali. The as synthesized composites are characterized by X-ray diffraction, spectroscopic and microscopic investigations. The ternary composite having 25.3 mass% of Pt deposited on the binary composite containing 34.36 mass% NiO and 40.34% $TiO_2$ is found to be the best catalyst both in dark and illuminated condition. The peak current density in cyclic voltammetry, the charge transfer conductance, and the steady chronoamperometric current density are increased by about 1.8, 4, and 1.5 times respectively, on the illumination of anode, in comparison to these in the dark. The electrochemical impedance spectroscopy (EIS) and photo responsive current measurements indicate that mixing of NiO with $TiO_2$ demonstrates a superior photo-electro catalytic performance for methanol oxidation plausibly due to enhancement of the electron-hole separation efficiency. Product analysis by HPLC reveals that the formation of formaldehyde, sodium formate, and methyl formate is facilitated on illumination while additional carbonate is formed in the dark.

## 1. Introduction

Direct methanol fuel cell (DMFC) is considered as a promising power source for application in cars and portable electronic devices because of high energy density [6.09 kWh $Kg^{-1}$], low volume occupancy, low cost, advantage in handling, transport, and storage [1–7] of fuel, methanol. The smart application of DMFC at a marketable price remains still an issue due to its limitations like sluggish anode kinetics, instability of catalyst, etc. [8–13]. To date, the most frequently used catalyst material is based on Pt in DMFC but it is less abundant and very costly. In addition, Pt catalyst tends to get poisoned by strongly adsorbed CO like intermediates. This leads to the rapid deactivation of Pt catalyst during electro-chemical methanol oxidation reaction (MOR). To mitigate the above poisoning and cost effect, many efforts have been committed in developing generation of Pt-based binary and ternary catalysts. A common strategy is allowing Pt to combine with other relatively oxophilic metals such as Ni, Sn, Ir, Ru, Au, etc. [14–18]. The utilization of the second metal in such alloys can generate oxygen-containing species such as M–OH (adsorbed $OH^-$) which promotes the oxidation of strongly adsorbed intermediates like $CO_{ad}$ to $CO_2$ [19–20]. Another strategy is to prepare composite catalysts by coupling Pt with different oxides (Such as $CeO_2$, $SnO_2$, $MnO_2$, $TiO_2$, ZnO, $Bi_2O_3$, etc.) which can be employed both as support carrier and rescuer from poisoning to improve electrocatalytic activity and stability [21–23]. $TiO_2$ being a semiconductor has low electric conductivity which can be overcome by making a thin film and using high conductivity carbon materials as inert support [24]. As one of the most studied oxides, $TiO_2$ has also found wide applications especially in photo-catalytic activity like water splitting, dye decomposition reaction, etc. assisted by visible-UV light [25–30]. When irradiated with sunlight, $TiO_2$ nanoparticles can only absorb in the UV part of light, a small portion of solar spectrum (5% in the sunlight) [31,32]. To increase absorption capability and co-catalytic activity and stability, several composites of $TiO_2$ with carbon materials, polymers have been used along with Pt [33–35]. Since the catalytic performance of semiconductor oxides can be improved by exposing the electrode to UV–visible light, a recent trend has been developed to oxidize the fuels in presence of light and thus photo-assisted fuel cells are constructed [33,34]. Recently, it is reported that coupling $TiO_2$ with NiO ($E_g$ = 3.4

* Corresponding author.

https://doi.org/10.1016/j.apsusc.2020.148450
Received 14 February 2020; Received in revised form 26 October 2020; Accepted 9 November 2020
Available online 13 November 2020

JMEPEG (2020) 29:8036–8048
https://doi.org/10.1007/s11665-020-05261-3


1059-9495/$19.00

# Synthesis and Characterization of CuO-NiO Nanocomposites for Electrochemical Supercapacitors

*Sujit Chatterjee, Apurba Ray, Manas Mandal, Sachindranath Das, and Swapan Kumar Bhattacharya*

Submitted: 17 March 2020 / Revised: 19 August 2020 / Accepted: 8 October 2020 / Published online: 6 November 2020

**The CuO nanostructures and CuO-NiO nanocomposites of various compositions were successfully synthesized by simple hydrothermal method followed by calcination for investigation of their pseudocapacitive performances. The UV-vis spectroscopy, x-ray diffraction, field emission scanning electron microscopy (FESEM) and high-resolution transmission electron microscopy were used to characterize the as-synthesized electrode materials. Among these different CuO-NiO nanocomposites, CuO($x$)NiO($100 - x$), that's with equal mole ratio, CuO(50)NiO(50) exhibits the highest specific capacitance of 35.63 F $g^{-1}$ at current density of 0.3 A $g^{-1}$. In addition, it shows excellent cycling stability with capacity retention of 85.7% at 1000th cycle at current density of 10 A $g^{-1}$. The morphology of CuO(50)NiO(50) nanostructures as determined by FESEM and HRTEM studies, revealed aggregated three-dimensional (3D) hierarchical networks due to aggregation of various parallel 2D thin nanosheets. The supercapacitive activity of the synthesized CuO and CuO-NiO nanomaterials was found to follow the order: CuO(50)NiO(50) > CuO(20)NiO(80) > CuO(100) > CuO(80)NiO(20).**

**Keywords** energy storage, hydrothermal synthesis, nanocomposites, pseudocapacitors

## 1. Introduction

Of late significant investigations are made to develop sustainable and renewable energy storage devices with high energy, power and reliability to meet the challenges of fossil fuel depletion, global warming, atmospheric pollution, needs in medical and electronic equipments, use of intermittent energy sources, etc. (Ref 1-4). Electrochemical capacitors or supercapacitors have been considered as the most promising energy storage device for sustainable development of human beings than others like lithium-ion batteries, owing to their fast charging-discharging rate, high power density, excellent cyclic stability, safe operation and wide range of working temperature (Ref 5, 6). These may be utilized as primary storer of non-conventional energy like wind, sunlight, etc., and auxiliary (secondary) storer with batteries and fuel cells implanted in cars, mobiles, cordless tools etc., where high power is needed for limited span of time at least occasionally (Ref 7, 8). In general, supercapacitors can be classified into three categories: electrochemical double layer capacitors (EDLCs), pseudocapacitors and hybrid capacitors based on energy storage mechanism (Ref 9, 10). The energy storage mechanism in EDLCs is only non-faradic process. No redox reaction occurs between the electrode and electrolyte. Pseudocapacitors store charges mainly by reversible faradic redox reactions, where the combination of both faradic and non-faradic processes occur in hybrid supercapacitors (Ref 2, 11-13). The most significant component of electrochemical supercapacitors is active electrode material (Ref 14, 15). Therefore, to design and fabricate low price and environment friendly novel active electrode materials for high-performance supercapacitors is a crucial task. Nowadays, nickel oxide and copper oxide both are emerging electrode materials among various metal oxide pseudocapacitor electrode materials such as $RuO_2$ and $IrO_2$ etc., for pseudocapacitor application owing to their low cost, enormous thermal stability, natural abundance and eco-friendliness. Despite nickel oxide and copper oxide both have high theoretical value of capacitance (2573 and 1800 F $g^{-1}$, respectively), their low electrochemical active surface area, poor electrical conductivity, and poor cycling stability limit their wide application in high-performance supercapacitors (Ref 16-19).

Mixed transition metal oxide (MTMO) is considered promising candidate for wide applications in catalysis, electrocatalysis, sensing, charge storing, etc., (Ref 20-26). MTMO nanocomposites improve the electrochemical performance by enhancing the electrochemical active surface area and charge transfer efficiency. Moreover, when a semiconductor metal oxide nanomaterial of narrow band gap is mixed with that of broad band gap, the composite may exhibit enhanced physiochemical properties compared with each single material. Among the various transition metal oxides, p-type CuO semiconductor oxide has narrow band gap ($E_g$ = 1.2 eV), while *p*-type NiO semiconductor oxide has a wider band gap in the range of 3.6-4.0 eV (Ref 27). Homogeneous precipitation, co-precipitation, sol-gel, thermal decomposition and hydrothermal methods have been successfully employed for the synthesis of mixed metal oxides nanoparticles (Ref 12, 28-30). The physiochemical properties of these nanocomposites largely depend on their size, shape, surface area and porosities. It is reported that the lattices of NiO in NiO-based nanocomposites could produce more electrochemical active sites for supercapacitive activity (Ref 19, 31). For example, Li et al. (Ref 32)

**Sujit Chatterjee, Manas Mandal,** and **Swapan Kumar Bhattacharya**, Department of Chemistry, Jadavpur University, Kolkata 700032, India; and **Apurba Ray** and **Sachindranath Das**, Department of Instrumentation Science, Jadavpur University, Kolkata 700032, India. Contact e-mail: skbhatt7@yahoo.co.in.